Experiments on Film Cooling of Gas Turbine Vane Passage Surfaces: The Effects of Various Distributions of Combustor Coolant and Endwall Injection Coolant

A THESIS

SUBMITTED TO THE FACULTY OF THE

UNIVERSITY OF MINNESOTA

BY

Kedar Prasad Nawathe

IN PARTIAL FULFILLMENT OF THE REQUIERMENTS

FOR THE DEGREE OF

MASTER OF SCIENCE

Professor Terrence W. Simon, Adviser

August 2019

Acknowledgements

Although this thesis bears only my name, this work was simply not possible without the help of a lot of people. First of all, I would like to thank Prof. Terry Simon for trusting in me for working on this project. His sound advice, approachable nature and the skill of explaining complex concepts in a way that my brain could comprehend have helped me the most. I am really grateful for getting to work with such an awesome adviser.

I would like to thank Solar Turbines, Inc. for providing financial support for my graduate studies. I would particularly like to thank Dr. Yong Kim for providing crucial details and valuable insight that helped me in creating accurate experimental test conditions.

As manufacturing various equipment was a significant part of this project, the College of Science and Engineering Shop played an important role. Specifically, I would like to thank Ron Bystrom and Peter Ness for their help in manufacturing as well as their suggestions.

My research group has been an integral part of this project. I am grateful to Dr. Mahmood Alqefl, as his thorough knowledge of the test facility has been instrumental while designing the experimental cases of my studies. I am indebted to Rui Zhu and Enci Lin for their help in taking the tedious measurements as well as for providing input on the interpretation of the results. I want to thank Pingting Chen, whose observant nature has been very helpful in deciphering some of the measurements. Also, I am grateful to Alex Li for his help in data taking and for the knowledge I gained from all our conversations.

Finally, I want to thank my parents for helping me through the difficult parts of this journey and for believing in me, even when I did not. I would like to thank my sister and role model, Mugdha, who, unbeknownst to her, has taught me a lot. I would also like to thank her husband, Aditya, as his advice has been really helpful in making my grad school life easier.

To my late grandfather, Shripad Belapurkar

And to my niece, Charvi

Abstract

The efficiency of gas turbines is known to increase with the exit temperature of the combustor gases. However, this temperature is limited by the melting point of various equipment downstream of the combustor. To increase this limit, coolants injected at different locations form low-temperature films on the surfaces of these regions to avoid melting and thermal stress damage. This injection significantly changes the flow field in the vane passage. Therefore, there is a need to study the aerodynamic and thermal effects of combustor, transition duct and passage coolant injection, which can assist the designers of gas turbines to employ better cooling schemes with minimal use of coolant, thus increasing the efficiency and durability of turbines.

The study presented in this thesis discusses experimental tests performed to understand the coolant effectiveness for cooling the endwall and vane surfaces of a nozzle guide vane cascade. The test section contains an engine representative combustor-turbine interface along with a contoured endwall. High turbulence intensity as well as high Reynolds numbers are achieved in the facility to closely simulate engine conditions. In addition to recording the surface effectiveness values, in-field thermal and aerodynamic measurements were taken. It has been previously discovered that the effusion and louver coolants, used to cool the combustor section, can also be credited in cooling the endwall and the vane surfaces. Therefore, this study is helpful to understand the effects of changing the mass flow ratios of different coolants injected upstream of the passage. Especially, louver coolant injection in the combustor transition duct region, due to its location and injection angle, is suspected to provide significant passage endwall cooling. In-field measurements provide insight to the coolant transport through the passage and its interaction with the mainstream. As the net combustor coolant momentum is higher

than the film coolant momentum, the changes in the flow field due to its injection are more significant and are sustained to the end of the passage, giving more streamwise coverage than with a conventional film cooling setup. The film coolant mass flow ratio is varied in this study to see how the interaction of different coolants changes with changes of their injected momentum.

The measurements reveal that the upstream coolant flow helps in keeping the film coolant attached to the endwall for most of the passage and also keeping the film thickness fairly uniform in the pitchwise direction. An increase in louver coolant mass flow rate shows higher endwall cooling effectiveness. The velocity contours show that a dominant vortex is present due to combustor coolant injection and that the passage vortex was, although present, diminished due to this other vortex. While changing the louver coolant mass flow rate did not change the intensity of these vortices, changes in the film coolant mass flow rate increased the intensity of the dominant vortex near the pressure surface. Also, the presence of this new vortex helps in film cooling the pressure surface, a region where, conventionally, the least amount of coolant coverage is recorded.

Table of Contents

List of Figures

List of Tables

Nomenclature

Symbols

A, B, n	Hotwire calibration constants [ ]
C	Vane true chord length [cm]
C_{ax}	Vane axial chord length [cm]
Cp	Pressure coefficient [ ]
E(ω)	Energy density spectrum [$m^2 \cdot s^{-2}$.Hz]
Lu	Energy length scale of turbulence [cm]
u_{rms}	Root mean square of velocity fluctuations [ms^{-1}]
g	Acceleration due to gravity [ms-2]
H	Inlet passage height [cm]
Hc	Height of the combustor exit [cm]
u(t)	Instantaneous velocity [ms^{-1}]
u'(t)	Instantaneous fluctuation about time-averaged mean velocity [ms^{-1}]
MFR	Ratio of coolant mass flow rate to mainstream mass flow rate [ ]
I	Momentum flux ratio of film coolant to mainstream [ ]
N	Sample size [ ]
P	Cascade pitch (spacing between successive vanes) [cm]
Ps	Static pressure [Pa]
Pt	Total pressure [Pa]
Q	Volumetric flow rate [$m^3 s^{-1}$]
Re	Reynolds number [ ]
S	Vane or approach plane span [cm]
T	Absolute temperature [K]
Tu	Turbulence intensity [%]
$\overline{U}$	Time-averaged mean velocity in axial direction [$m.s^{-1}$]
U_0	Approach flow velocity [ms^{-1}]
V	Velocity component [m/s] or Voltage [V]
X	Passage axial coordinate [m]
Y	Passage pitchwise coordinate [m]
Z	Passage spanwise coordinate [m]
[Variable]	Measured or calculated with respect to a "variable"

Greek

ρ	Density [kg/m3]
Δ	Difference operator
ε	Turbulent kinetic energy dissipation rate [m^2s^{-3}]
η	Endwall adiabatic effectiveness [ ]
ω	Frequency of energy density spectrum [Hz]
ωs	Sampling frequency [Hz]
Λ	Turbulence integral length scale [m]
λ	Taylor microscale [cm]
α	Pitch angle
θ	Recovery temperature coefficient [ ]
μ	Dynamic viscosity [Nsm^{-2}]
ν	Kinematic viscosity [m^2s^{-1}]
Ω	Vorticity [s^{-1}]
γ	Yaw angle

Subscripts

i	Located at passage inlet plane
ave	Average
e	Located at passage exit plane
W	Located at wall (z=0)
F	Film coolant flow property
C	Combustor coolant OR coolant
chord	Based on vane true chord length
exit	Passage exit
∞	Mainstream flow property
X	Located at passage axial coordinate [m]
Y	Located at passage pitchwise coordinate [m]
Z	Located at passage spanwise coordinate [m]
s	Relative to streamwise direction [m] OR sample
sp	Stagnation pressure

Chapter 1. Introduction

1.1. Motivation

For more than a century, gas turbines have been an important source for providing clean and efficient energy. But the efficiencies were not always high and considerable research was put into understanding and improving these turbines. Even today, some of the most prominent research in the turbomachinery field involves increasing the efficiency of turbines. As the efficiency of gas turbines increases with an increase in the combustor exit temperature, temperatures as high as possible, are preferred. But the turbines and their neighboring components should be able to sustain these high temperatures. To run the turbines beyond their melting temperatures, an effective cooling scheme is required. One of them is to inject some of the air from the compressor onto the hot surfaces to continuously cool them. The coolant injection takes place at different locations, providing cooling for multiple components. Although each of the coolant injection schemes is designed with a specific component in mind, they tend to provide cooling to multiple regions. Therefore, studying the interaction between multiple coolant streams and their combined effects on cooling the hot surfaces is important.

One of these hot surfaces is the endwall of the turbine. Cooling the endwall is a bit challenging, owing to the complex flow field in the endwall region due to the presence of the secondary flows. These flows are generated due to the vanes and the cross-pitch pressure gradients. The film coolant, introduced upstream of the vane passage, interacts with these secondary flows and the coolant skews toward the suction surface, decreasing the cooling near the pressure surface. Therefore, a detailed study of the coolant flow physics is required for performing efficient cooling.

1.2. Objective

This study focusses on cooling of a contoured endwall and vane surfaces located in the first stage of a high-pressure turbine. Previous studies on this cascade for the same combustor-turbine interface revealed that the coolant streams injected in the upstream combustor region provide significant cooling to the endwall as well as the vane surfaces. However, these measurements were done for only a particular mass flow rate of the injected air. To understand how the changes in coolant flow rates affect the cooling effectiveness, a set of studies changing the louver coolant (designed to cool the combustor liner) as well as the film coolant (designed to cool the endwall) were conducted. The flows are given in terms of mass flow rate to mainstream flow rate ratios (termed mass flow ratios, or MFRs). In addition to analyzing the changes in the endwall cooling effectiveness, there was an interest in understanding which of the coolant injection locations provided better overall results. As there are multiple coolant flows injected with different momenta, their interactions are likely to change appreciably with changes in their flow rates. Hence, in-field measurements were taken to explain the coolant interaction and coolant transport in the passage. While in-field velocity measurements were used to understand the secondary flow system, in-field thermal measurements were taken to show the effects of these secondary flows on coolant movement in the passage.

Chapter 2. Background

Fluid flow in the vane passage has always been complex and is further affected by various coolant injection schemes designed in the past few decades. To explain the methods behind the design of the current test facility and to show the state of the art, the background on vane aerodynamics and film cooling techniques is given. The various topics are addressed one by one below:

2.1. Vane Passage Secondary Flow Physics

Due to the vane geometry, a system of secondary flows is generated in the vane passage. Explanations for some of the most important features seen in these systems are given in this section. A brief introduction to the formation of the horseshoe vortex is given first, as it is one of the oldest documented features in the passage flow. Sedney and Kitchens [1] were among the first to give a visualization of the horseshoe vortex (shown in fig. 2.1.1). When a flow approaches an obstacle mounted on a wall, the mainstream stagnates over a line of symmetry on the leading edge converting its dynamic pressure into a static pressure rise. However, in the boundary layer of the wall, the velocity and the dynamic pressure are lower than the mainstream and thus, the stagnation pressure in the boundary layer is much lower than in the mainstream. This creates a pressure gradient that drives the flow from the mainstream toward the wall. This flow, after reaching the boundary layer, turns away from the obstacle and moves in the opposite direction to the mainstream, creating a recirculation zone just upstream of the obstacle. This one major recirculation zone creates more secondary recirculation zones. Figure 2.1.1 shows the formation of the recirculation zones upstream of an obstacle. Goldstein and Karni [2] studied a similar flow approaching a cylindrical obstacle mounted on a wall. They also found the vortex

originating upstream of the recirculation zone and moving around the obstacle as shown in fig. 2.1.2, giving a horseshoe shape to the flow near the obstacle when viewed from above. They also observed that, although there was only one dominant vortex, other small-sized vortices were present.

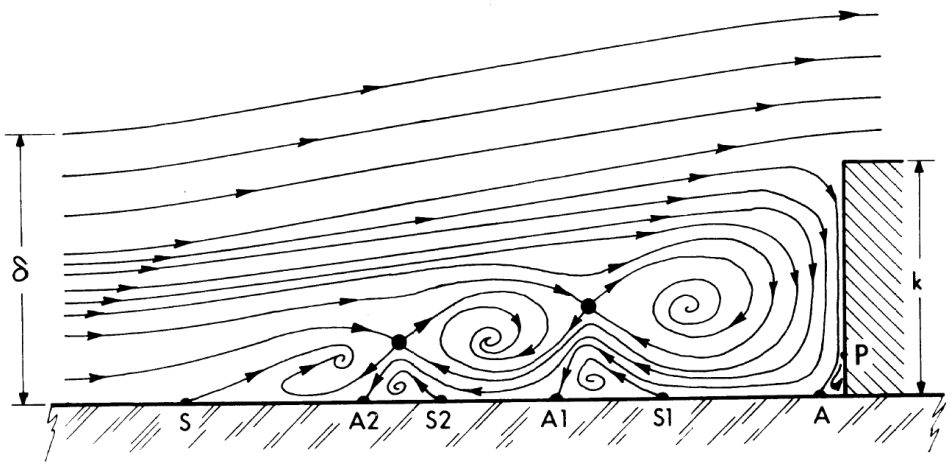

Figure 2.1.1 Formation of recirculation zones upstream of an obstacle [1]

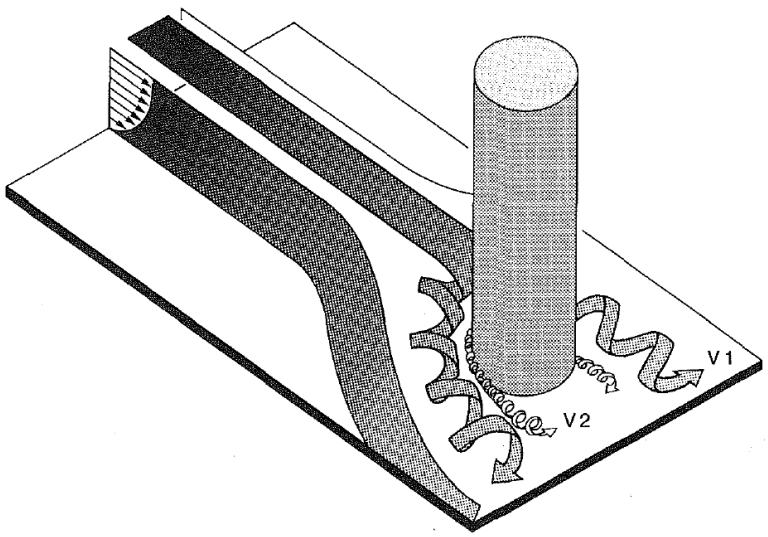

Figure 2.1.2 Formation of horseshoe vortex around a cylindrical obstacle [2]

When the flow upstream of the vane passage approaches the turbine vane leading edge, a similar situation to the one described above is created and a horseshoe vortex is

expected. In the case of a turbine cascade, the obstacle is the vane leading edge and the boundary layer that creates the stagnation pressure gradient is on the endwall. Langston [3] did a detailed study of flow physics and found that the horseshoe vortex generated at the leading edge has two legs, one each going over the pressure and the suction sides, as shown in fig. 2.1.3. But, as the vortex moves downstream, it experiences the inherent pressure gradient between the pressure surface and the suction surface (due to curvature of the blade). This gradient causes the horseshoe vortex present on the pressure side to migrate toward the suction side. This vortex is called the passage vortex, which is an evolution of the horseshoe vortex in the passage. It was seen that the passage vortex, after reaching the suction surface merges with the suction leg of the horseshoe vortex (which remains on the suction surface since its generation). This was confirmed later by Sharma and Butler [4]. Also, Langston found that the pressure gradient between the pressure and suction surfaces causes a cross-stream flow on the endwall (indicated in fig. 2.1.3), called 'endwall cross-flow.' It can be seen in the figure that the orientation of this cross-flow is such that it helps the passage vortex to move toward the suction surface.

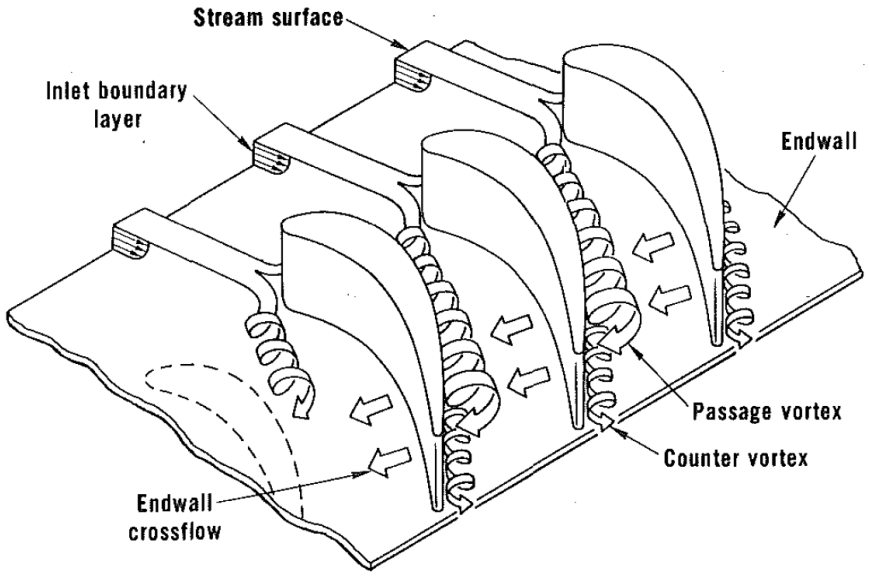

Figure 2.1.3 Secondary flow system in vane passages [3]

Goldstein and Spores [5], in a similar study, found the passage vortex. They discovered that after the pressure leg of the horseshoe vortex reaches the suction side, it lifts off the endwall and moves along the suction surface (labeled vortex 3 in fig. 2.1.4). However, unlike Langston, they found that the suction leg of the horseshoe vortex and the passage vortex did not merge together but rather moved alongside on the suction surface (see vortices 2 and 3 in fig. 2.1.4). In general, the results found by authors of [3], [4] and [5] were comparable. Wang et al. [6] performed extensive flow visualization to study turbine passage flow models that confirmed the findings of the earlier models. Their interpretation of the flow pattern is show in fig. 2.1.5. This is one of the most comprehensive and accepted vane passage flow field descriptions.

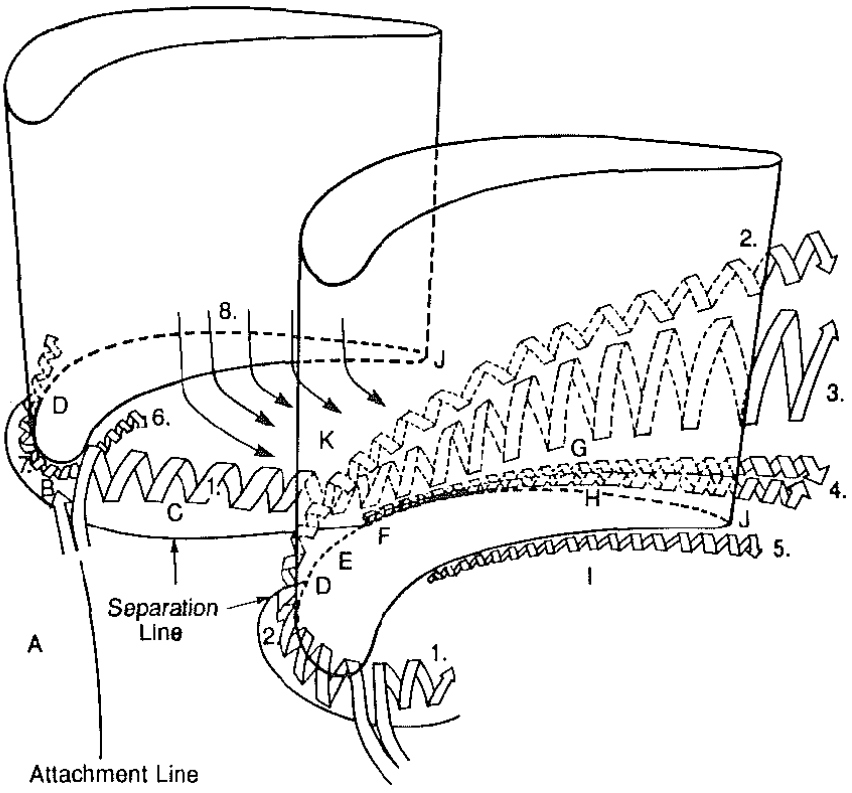

Figure 2.1.4 Interpretation of Goldstein and Spores of the passage flow field [5]

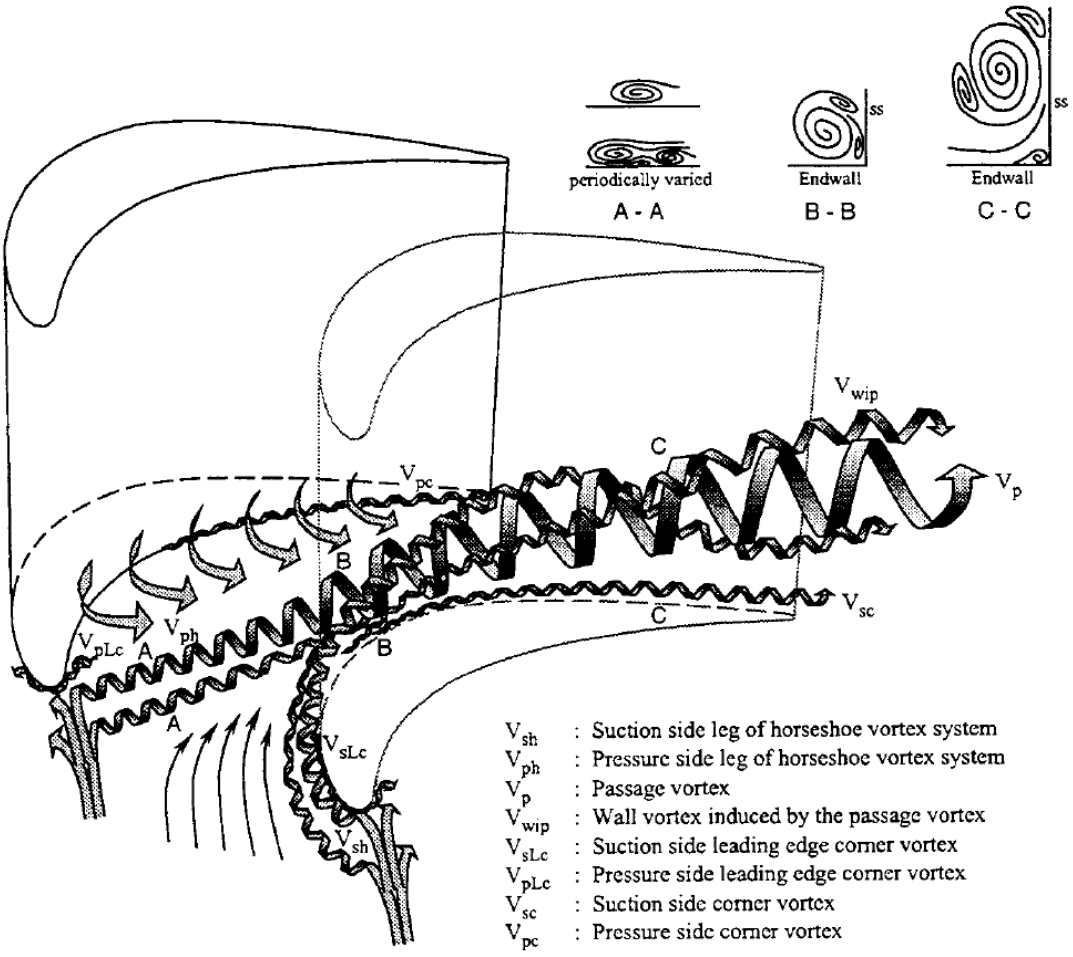

Figure 2.1.5 Most comprehensive secondary flow field in the vane passage by Wang et al. [6]

2.2. Secondary Flow Suppression

The vortices explained in the earlier sections are detrimental to turbine performance. They can cause pressure losses and flow separation in the passage and thus, should be avoided. A detailed discussion on various losses present in vane passages is given by Denton [7]. One of the ways to suppress the secondary flows, namely the passage vortex strength, is to contour the endwall. This contouring can be an axisymmetric one or a more complex three-dimensional one. It was found that the secondary flow losses are highly dependent on cascade geometry and, therefore, a single contouring method cannot be established. A good compilation of various endwall contouring methods was done by Burd

[8]. Figure 2.2.1 shows the various endwall contours studied. Ewen et al. [9] reported an increase in efficiency by using a contoured endwall. Morris and Hoare [10] studied multiple endwall contours (fig. 2.2.1 (A), (C) and (D)) having various airfoil aspect ratios. They are compared with a flat endwall on fig. 2.2.1 (B). It was found that the endwall having symmetric-cubic profiling located downstream of the most curved part of the vane yielded a reduction of secondary flow losses of up to 25% for small aspect ratios and small inlet boundary layer thicknesses. Kopper [11] studied a cascade having one contoured endwall and one flat endwall, finding that the aerodynamic loss reduction was up to 17%, compared to a cascade having both flat endwalls. It was found that the contouring of one of the endwalls helped in reducing secondary flow losses on the flat (opposite) endwall.

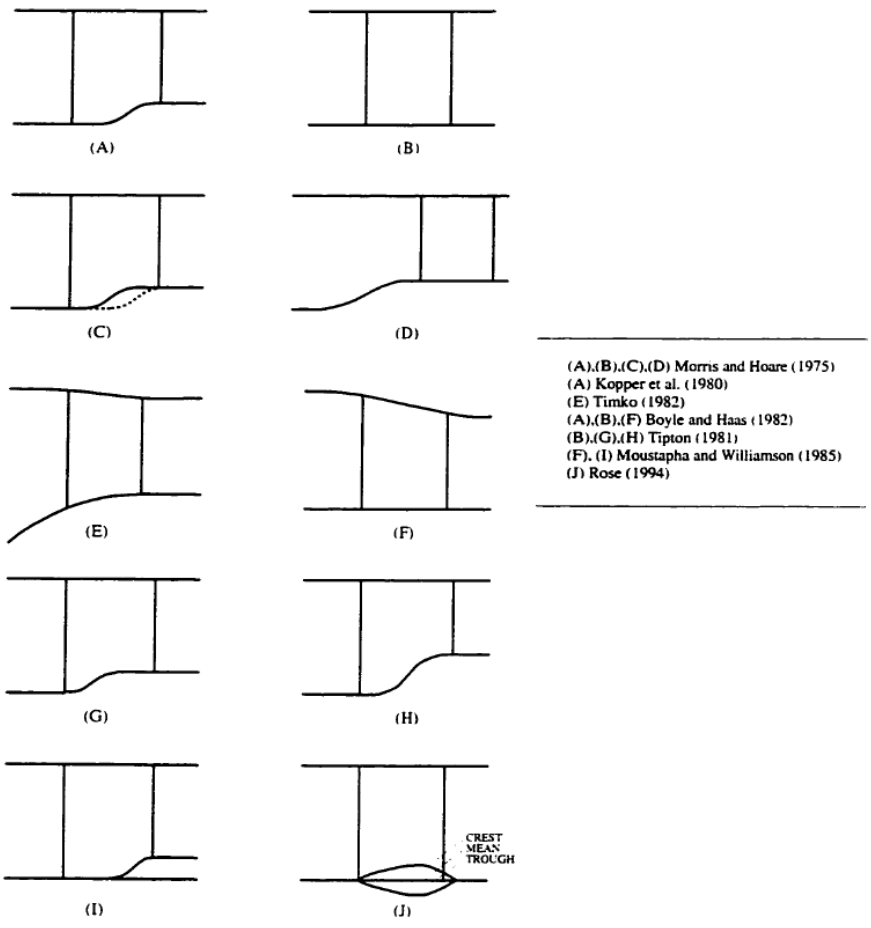

Figure 2.2.1 Various endwall contours compiled by Burd [8]. Originally extracted from [10,11,12,13,14,15,16]

Burd and Simon [17] studied an endwall similar to that studied by Kopper and found that the passage vortex strength was reduced near the contoured endwall, more so than on the flat endwall. Piggush and Simon [18], who used an endwall that had contouring smoother than those of the studies presented earlier, also reported a larger passage vortex near the flat endwall. Most of the contouring studies have used axisymmetric endwall contouring and have found that contouring significantly helps suppress secondary flows.

2.3. Effects of Coolant Blowing on Secondary Flow Physics

As explained in chapter 1, the endwall and vane surfaces must be cooled as the combustor exit temperatures are higher than the endwall material melting points. Therefore, coolant injection is done to form a protective film on the surfaces to be cooled. But it is important to understand how the coolant flow is affecting the secondary flows and whether it increases or decreases losses in the passage.

Flat Endwall Studies

The effect of the film coolant injection on secondary flows was first studied by Blair [19] who found that heat transfer was affected by the corner vortex, but the secondary flow field remained relatively unaffected by injection. Sieverding and Wilputte [20] found that endwall coolant flows affected secondary flows and that three cooling air parameters were significant: the coolant to mainstream flow pressure ratio, the coolant to mainstream mass flow ratio and the angle between coolant flow and main flow. Goldman and McLallin [21] discovered that the blowing ratio of coolant was the deciding factor in whether secondary flows will be suppressed significantly, or not. Their findings show that coolant injected at pressures higher than that of mainstream, with an angle of 15° to the mainstream is optimum for reduction of secondary flow losses.

Biesinger and Gregory-Smith [22] did an extensive analysis of loss reduction due to coolant blowing. They found that a low blowing ratio of coolant increased the flow of low-velocity coolant near the wall, increasing the strength of the horseshoe vortex and, in turn, of the passage vortex, proving to be detrimental to the turbine efficiency. When the blowing ratio is increased, the vorticity of the injected coolant, which is in the opposite direction of the secondary flow vorticity, reduces the losses due to secondary flows. At the same time, coolant having blowing ratios higher than a certain value creates significant secondary flows by itself, which persist until the end of the passage. Thus, the coolant itself becomes a source of secondary flow. Also, a low angle of injection is more effective in reducing secondary flows because it keeps the injection flow close to the endwall. The injection momentum required to decrease the secondary flows is higher than what is generally required for cooling the endwall and the authors claim that the reduction in the secondary flows is offset by this additional injection momentum but expect that the succeeding blade row will benefit from a uniform exit flow of the first row.

Friedrichs et al. [23] found that injection done upstream in the passage can significantly change secondary flows and reduce losses caused by it. The spanwise location until which secondary flow effects are seen is also reduced with coolant injection. Also, they found that the optimum coolant supply pressure occurs when the streamwise component of the coolant velocity matches with the mainstream velocity. It was also found that losses from individual rows cannot be added proportionately. It showed that coolant flows from different rows interacted with each other and with the mainstream. Papa et al. [24] discovered that blowing ratios of coolant injection less than 1.0 can reduce the size the passage vortex. But, as the passage vortex is not eliminated, the coolant still transports itself from pressure surface to the suction surface, depriving coolant coverage on the endwall near the pressure surface. For a blowing ratio of 1.5, the flow structure changes

significantly due to coolant penetrating the mainstream, giving high cooling effectiveness values on the endwall near the pressure side as well as near the suction side.

Generally, it was found that the secondary flow system is affected when the injected coolant has moderate blowing ratios. The effect was positive in that it reduced the intensity of the passage vortex. A higher-than-mainstream coolant injection pressure and low angle of injection provides optimum results.

Contoured Endwall Studies

Burd and Simon [25] studied the aerodynamic effects of coolant injection in a vane passage with a contoured endwall. Similar to flat endwall studies presented in the preceding section, it was found that moderate injection flow rates helped in suppressing secondary flows near the contoured endwall more so than with the flat endwall located at the opposite end of the vane span that has no film injection. They claimed that the bleed flow was providing additional streamwise momentum thinning the boundary layer and thereby affecting the secondary flow formation and growth near the endwall. Also, they found the total pressure loss remained about the same in the injection cases when compared to a no-injection study, showing that the injected coolant does not cause a significant negative effect on passage flow.

Piggush and Simon [18] studied upstream and slash-face (on the endwall between the vanes) blowing over a contoured endwall. In their parametric studies, they found that the overall total pressure loss was increased. This increase was seen mainly on the contoured endwall and was due to slash-face blowing. El Gabry, et al. [26] also studied the effects of blowing through upstream slots, slash-face slots, in-passage holes on the endwall and holes on the vane surfaces. They found that, while the endwall cooling flows influenced the flow field, the vane cooling flows did not have much effect. Schuepbach et al. [27]

found that injection of coolant increased aerodynamic losses. But they found that this negative effect was lower on the contoured endwall than on the flat endwall, showing that careful profiling of the endwall can limit the losses. Recently, Alqefl et al. [28] computationally studied the effects of slot film cooling injection on passage aerodynamics. They found that film cooling injection did not play a role in affecting passage losses and flow structure.

From the studies mentioned, it can be concluded that if the endwall contour profile is chosen correctly, cooling injection can have no or very limited detrimental effect on pressure losses in the passage. Also, a contoured endwall is prone to lower losses than those for a flat endwall in cases of coolant injection.

2.4. Effects of Coolant Blowing on Endwall Cooling Effectiveness

Film cooling is widely used to cool endwalls. The effect of the coolant on the flow field was explained in the preceding section. The present section will document the cooling effectiveness reported by various studies conducted on flat and contoured endwalls.

Flat Endwall Studies

Blair [19] performed a study on observing endwall cooling effectiveness of coolant injected upstream of the vane passage and found that the coolant was skewed toward the suction surface in the latter part of the passage, providing non-uniform cooling on the endwall. Takeishi et al. [29] studied a similar cascade but added injection rows in the vane passage to counter this coolant skewing toward the suction surface. This helped in cooling the endwall more effectively in the downstream part of the passage and also to reduce secondary flow effects generated by upstream coolant jets. However, the coolant spread still had some pitchwise non-uniformity. The coolant row locations and effectiveness contours are shown in fig. 2.4.1.

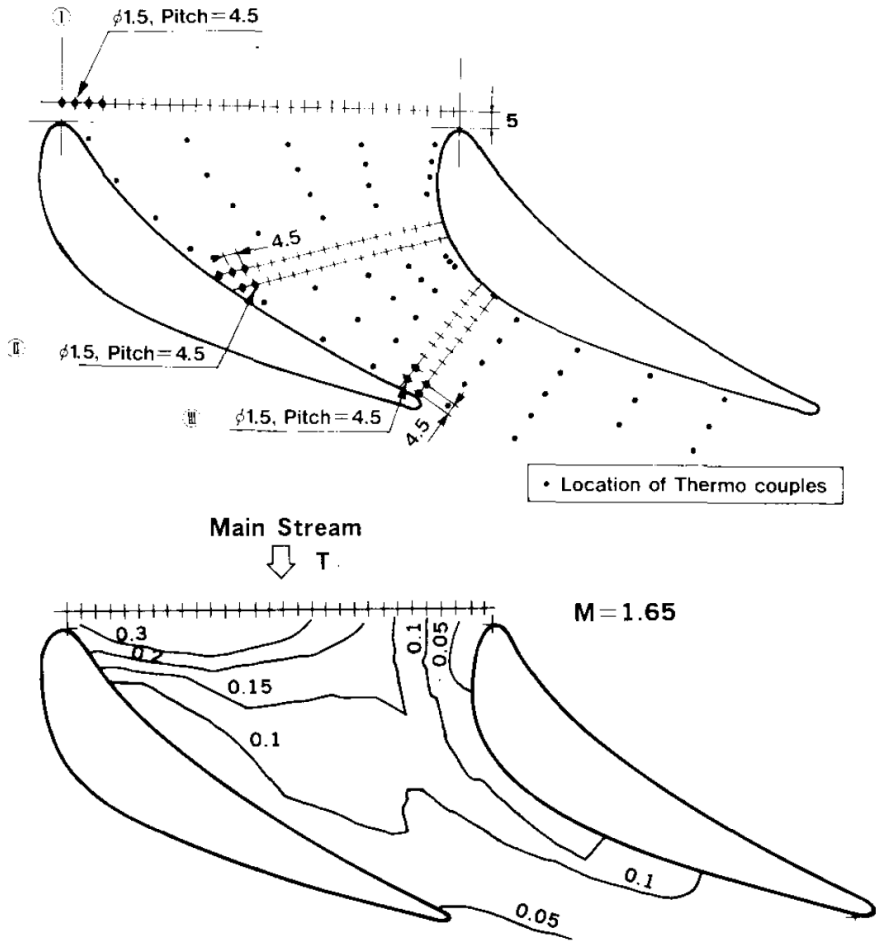

Figure 2.4.1 Employing multiple cooling rows throughout the vane passage. Top: Thermocouple and cooling rows location. Bottom: Cooling effectiveness contours [29]

Based on the flow behavior near the endwall, Jabbari et al. [30] chose the film cooling hole configuration shown in fig. 2.4.2 (a). This was designed based on flow visualization results and uncooled endwall heat transfer measurements. The results are shown in fig. 2.4.2 (b). It was found that a lower blowing ratio helps in cooling the mid-passage region while a higher blowing ratio was helpful in cooling the latter part of the endwall. Also, when the passage vortex is present (near the mid-passage region), the coolant flow moves toward the suction side while, near the trailing edge, the effect of the passage vortex is not present and thus shows the coolant to be flowing along the mainstream direction. The preceding

two studies show that the location of film cooling holes and the blowing ratio are important for high endwall cooling effectiveness.

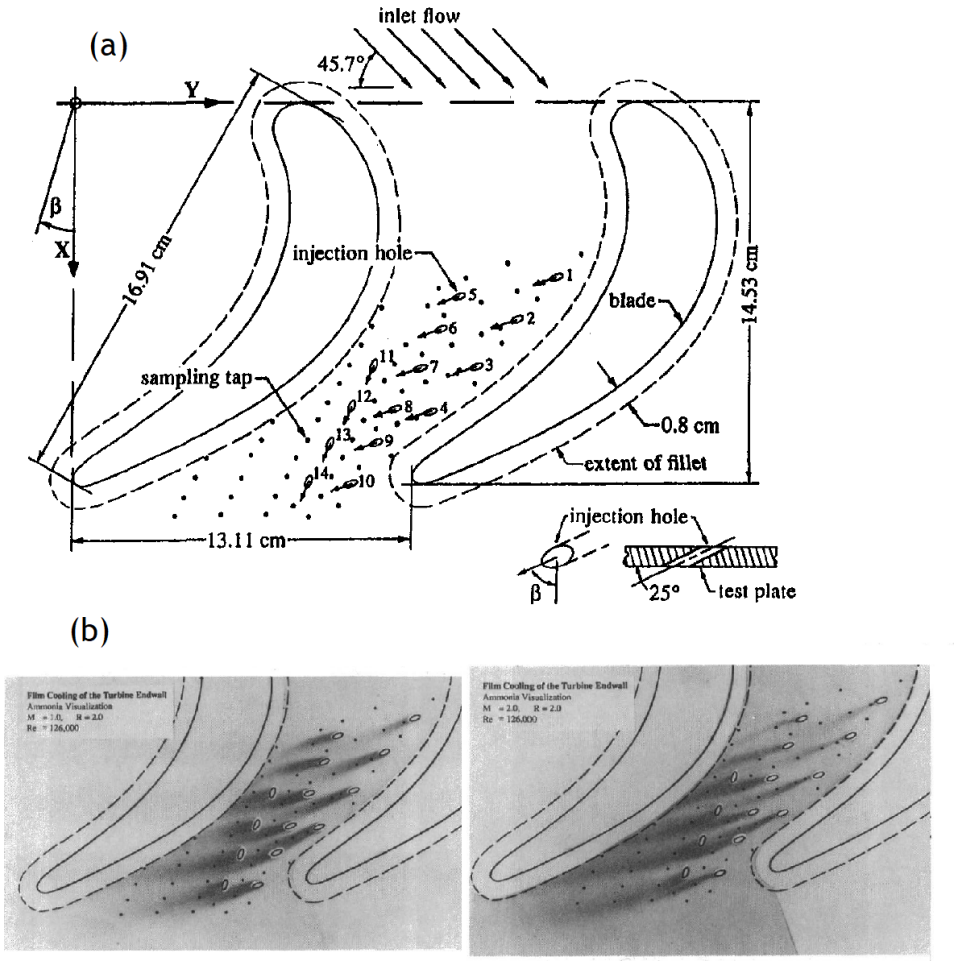

Figure 2.4.2 Cooling hole configuration studied by Jabbari et al. (a) Location and orientation of cooling holes, (b) Effectiveness results of blowing ratios (M) of 1.0 (left) and 2.0 (right) [30]

Thrift et al. [31] studied both the effect of changing the mass flow ratio (MFR) and the injection angle on cooling the endwall using upstream slot cooling. They found that an injection angle of 45° provided better cooling effectiveness than that from 90° angle injection. Also, it was found that the closer the slot is to the vane passage, the higher is the effectiveness. An increase in MFR from 0.3% to 1% (while keeping the momentum flux the same by changing the slot width) showed better cooling effectiveness on the endwall. Their results are shown in fig. 2.4.3.

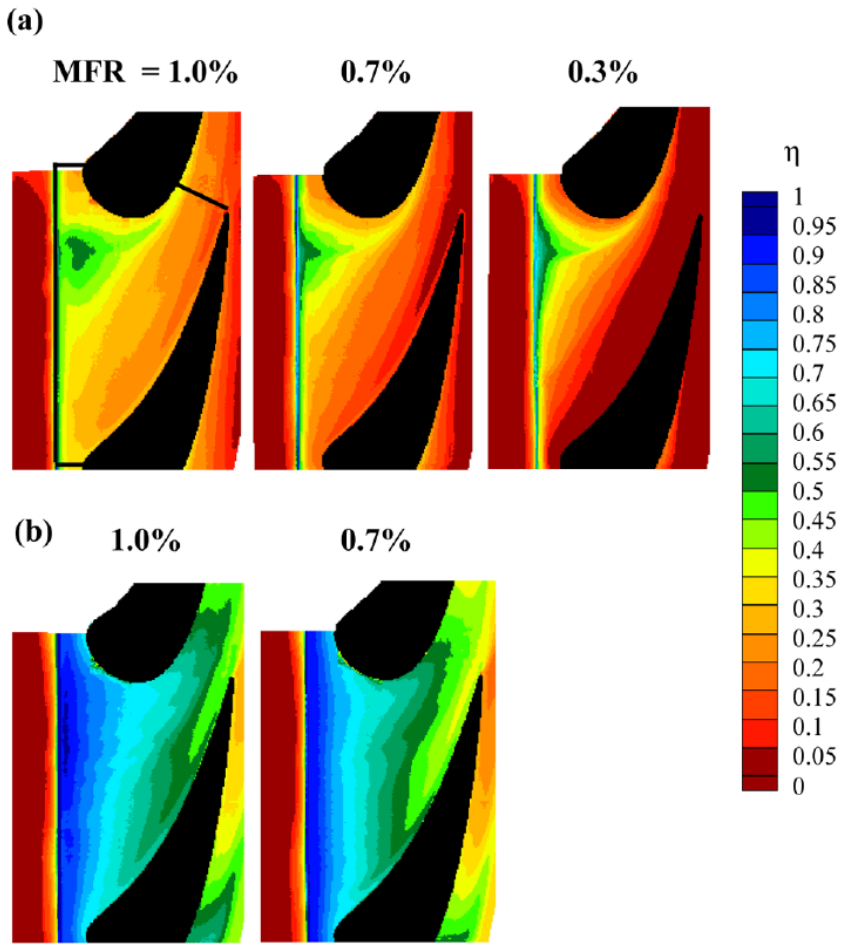

Figure 2.4.3 Parametric study on endwall cooling effectiveness performed by Thrift et al. (a) Cases with 90° slot orientation, (b) Cases with 45° slot orientation [31]

Contoured Endwall Studies

Burd and Simon [25,32] studied the endwall cooling effectiveness due to upstream slot injection on a contoured endwall. They found that at low injection MFR, the film coolant was concentrated toward the suction side of the endwall due to the secondary flows, also spreading on the suction surface. An increase in MFR helped the coolant to partially overcome the endwall cross-flow and spread over a greater region on the endwall. An even greater increase made the coolant completely overcome the endwall cross-flow and the passage turning, which resulted in significant coolant remaining near the pressure surface region of the endwall. Erickson and Simon [33] compared two different contoured

endwalls: dolphin nose shape and shark nose shape. They measured the cooling effectiveness of coolant injected from an upstream disc cavity in a rotor cascade at the exit of a first stage nozzle guide vane. They found that irrespective of the mass flow ratio of the coolant, the dolphin nose contoured endwall had higher effectiveness values than on the shark nose contoured endwall.

Recently, Ornano and Povey [34] studied the effects of changing the momentum flux ratio of coolant injected upstream of the vane passage. The experiment also simulated the injection of effusion coolant flows that are present to cool the combustor sections. They found that increases in the momentum flux significantly increased the coolant coverage on the endwall, but only up to a certain value. Beyond that, the increase was minimal. They hypothesized that the increase is due to suppression of the passage vortex by coolant streams, although aerodynamic data to support this claim were not presented.

2.5. Effects of Including Combustor Coolant Flows

Most of the studies presented in the preceding sections considered a uniform flow profile approaching the vane passage. However, in actual engines, multiple coolant streams, designed for cooling the combustor liner have changed both thermal and velocity profiles of the flow upstream of the passage. Therefore, it is important to consider the effects of these upstream elements while measuring the cooling effectiveness in the vane passage.

Colban et al. [35, 36] were among the first to document the cooling effectiveness and in-field flow measurements in a first stage nozzle guide vane having combustor coolant features simulated upstream of the passage. The endwall in this study was flat. They compared two cases: one having the features of the combustor coolant and the other without them (like the conventional studies). They found a large vortex rotating in the direction opposite to the passage vortex rotation direction (see fig. 2.5.1). However, an in-

depth explanation for the formation of this vortex was not given. Computationally, this vortex was observed by Hermanson and Thole [37].

Recently, Saxena et al. [38] and Alqefl [39] simulated the thermal profiles upstream of the

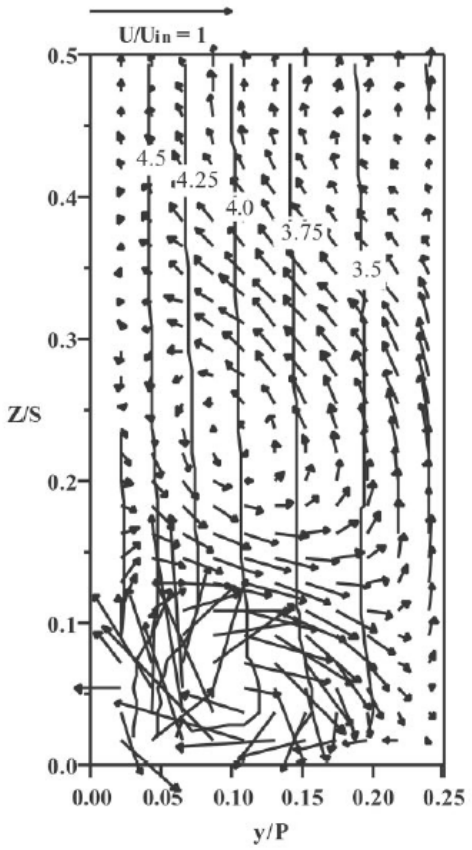

Figure 2.5.1 Counter-rotating vortex in the study by Colban et al. [35]

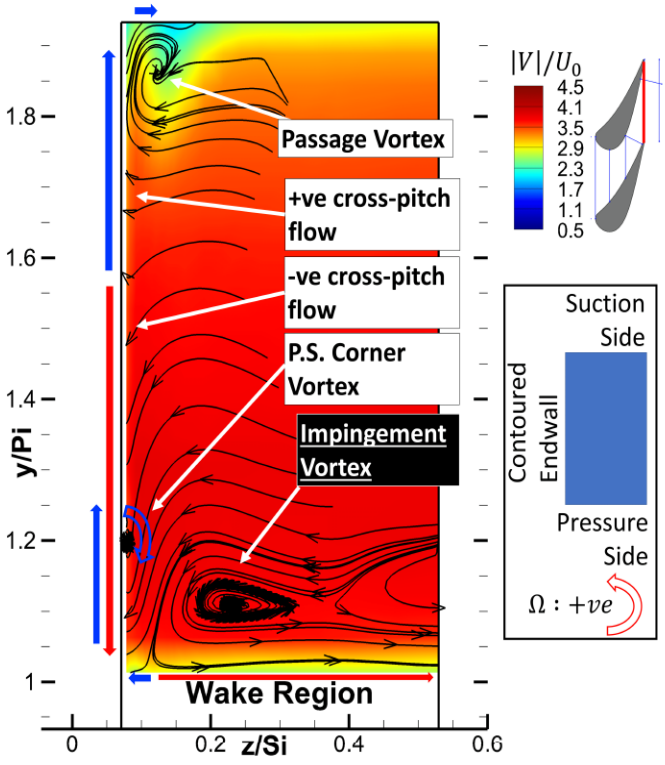

Figure 2.5.2 Counter-rotating vortex in the study by Alqefl [40]

passage to include the combustor coolant effects. In this study, the turbulence level and length scales were matching the exit of a low-NO_x combustor. They took endwall surface measurements and thermal and aerodynamic in-field measurements. They found that the endwall cooling effectiveness was only weakly dependent on mass flow ratio of film coolant and also suggested that the combustor coolant plays an important role in cooling the endwall. Also, they found that contouring of the endwall accelerated the boundary layer, thereby reducing the passage vortex intensity. However, in this study, the

aerodynamic aspects of the combustor coolants were not present and, hence, the second vortex observed by Colban et al. was not seen.

A more comprehensive study on the aero-thermal effects of combustor coolant on endwall cooling was done by Alqefl [40]. In addition to the contoured endwall and film coolant injection, the test facility introduced combustor coolant streams. The turbulence levels and length scales were matched with actual engines to make an accurate imitation of the engine conditions. The combustor coolant MFR was fixed and measurements were taken for multiple cases of different film cooling MFR values. The second vortex reported by Colban et al. was observed in every case measured in the Alqefl et al. study (see fig. 2.5.2 for a sample velocity field). The vortex was called the ‘impingement vortex’. The same facility was used for measurements taken in the current study and this vortex is expected. It will be discussed extensively. Therefore, an explanation on its formation, as documented by Alqefl, is necessary. There are three mechanisms by which this vortex is formed, which are discussed below:

1. *A difference in approach flow angles:* The combustor coolant flow, introduced upstream of the passage, is axially injected while the mainstream flow has started to turn due to passage turning downstream. As the combustor coolant momentum is significant, the coolant flow, instead of turning like that of the mainstream, migrates beneath the mainstream near the pressure surface. Therefore, a difference in the flow angles causes a swirl that forms the vortex upstream of the leading edge.
2. *Modified velocity profile at the leading edge:* In the conventional cascade approach flow, a generic turbulent boundary layer velocity profile is used. However, when multiple coolant streams at different velocities are injected near the contoured endwall, the velocity profile can have multiple peaks near the endwall. Therefore, when the flow stagnates on the leading edge, the additional dynamic pressure of the flow near the

endwall can actually cause multiple pressure gradients on the leading edge: one leading the flow from a local peak to the endwall, similar to what is seen in conventional cascades, and another driving the flow from a local peak toward the mid-span. The latter flow rolls up around the leading edge forming the impingement vortex. This vortex splits into two legs as it moves downstream, one each along the pressure surface and suction surfaces. The pressure leg was observed to be the dominant vortex in the study.

3. *Continuous impingement of injected coolant:* As the axially injected coolant has momentum high enough to resist the passage turning, it continuously impinges on the pressure surface over the majority of the passage until the energy of the coolant is dissipated by shearing with the mainstream. This impinging helps in preventing the impingement vortex from migrating to the suction side.

Alqefl reported significant increases of cooling effectiveness on the endwall due to the inclusion of combustor coolants far upstream of the passage. He also discovered that the impingement vortex helped in keeping the coolant uniformly distributed in the pitchwise direction as the passage vortex was not present to migrate the flow toward the suction surface. The third mechanism of formation of the impingement vortex also suggests that the pressure surface, a region which is known to have low coolant effectiveness, is getting good coolant coverage due to the impingement vortex.

2.6. Phantom Cooling of Vane Surfaces

When a coolant is introduced in a vane passage to cool a particular surface but ends up cooling some other surface/surfaces as well, the cooling on the additional surface is known as second-order cooling, or phantom cooling. Based on the observations made by Alqefl [40], it is implied that the combustor and film coolants may be cooling the vane surfaces

in addition to the endwall. Therefore, a review of the phantom cooled vane surfaces is given in this section. Although the phenomenon has been known for a long time, not many studies have been done in this area and knowledge about this subject is limited.

Roback and Dring [41,42] in their two-part paper studied the accumulation of coolant on the suction and pressure surfaces. They found that coolant accumulation was dependent on coolant-to-mainstream velocity ratio. For coolant velocities lower than the mainstream velocity, the coolant accumulated on the suction surface while, for higher coolant velocities, the coolant accumulated on the pressure surface. Zhang et al. [43] studied phantom cooling of the suction surface by upstream coolant injection intended for endwall cooling. They varied the diameter of the cooling holes and the mass flow ratio, keeping the blowing ratio the same. It was found that an increase in diameter until a certain value increased cooling effectiveness, both on the endwall and the suction surface. Li et al. [44] studied suction surface cooling on a similar cascade. They found that when the coolant-to-mainstream velocity ratios were from 0.4 to 0.6, higher suction surface phantom cooling effectiveness (from 0.08 to 0.1) was achieved for about 20% of the span, away from the endwall, as shown in fig. 2.6.1. An increase in the mass flow ratio had a positive effect on phantom cooling of the suction surface. However, the pressure surface phantom cooling was much less than the suction surface cooling, especially in cases having velocity ratios less than 1.

Some numerical simulations were conducted for studying phantom cooling on the suction surface. Du et al. [45,46] studied the effects of upstream slot geometry, coolant slot injection angle (with respect to pitch direction) and turbulence intensity on suction surface phantom cooling. They computed suction surface effectiveness for a contoured upstream slot but found it to be less than with a straight (conventional) upstream slot. They found that, while the changes in turbulence intensity did not affect the cooling effectiveness,

changes in injection angle had a significant impact. As expected, when the injection direction is axial, the suction surface had coolant coverage for most of the passage while the pressure surface, due to the passage vortex, had negligible cooling.

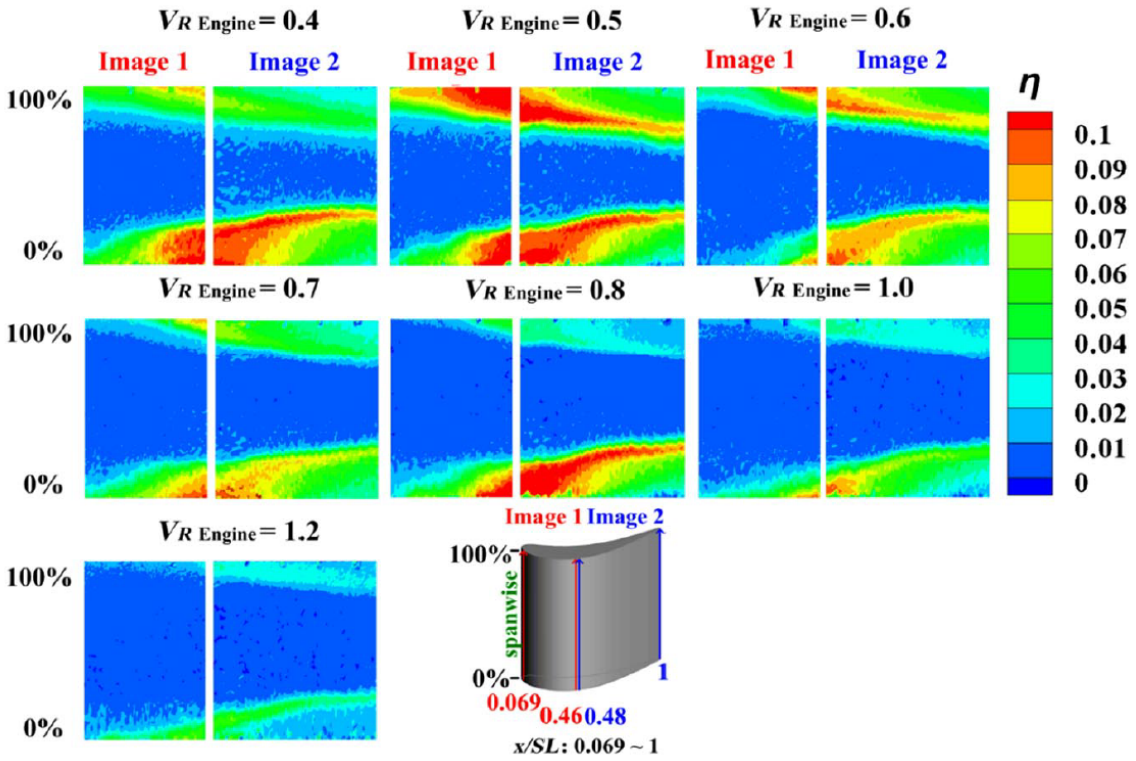

Figure 2.6.1 Phantom cooling of suction surface for different velocity ratios [44]

2.7. Summary

Flow through a vane passage is three-dimensional. The secondary flows formed due to the passage geometry are detrimental for the performance of the turbine. The most significant secondary flows are the horseshoe vortex, its evolution into a passage vortex and the cross-pitch flow along the endwall. To decrease the effects of the secondary flows near the endwall, a contoured endwall profile is employed, which has shown very good results. Additionally, these flows are affected by the introduction of various coolant streams present in the vane passage. Based on the literature, the geometry of endwall

contouring, as well as the geometry of the region upstream of the passage decide whether the coolant flows affect secondary flows positively or negatively. The literature has ample evidence on how the cooling of endwall is affected by changes in film coolant injection parameters. However, in-passage measurements documenting the interaction of the coolant streams with these secondary flow systems are limited. Therefore, knowledge of coolant transport through the passage is also limited. Even fewer studies are present that document the influence of combustor coolant injected far upstream of the passage on coolant coverage on the endwall. A large vortex rotating in the opposite direction to that of the passage vortex, formed due to the combustor coolant injection, was found which changed the coolant coverage on the endwall as well as the typical understanding of the coolant transport in the passage. Also, the effects of changes in the combustor coolant flow rates on the endwall cooling have not been documented. Hence, taking thermal measurements on the endwall for various combustor coolant flow rates was one of the main objectives of the current study. Additionally, as the flow field is affected significantly by this new vortex, studying its trend due to changes in the combustor flow rates is also important. Therefore, detailed thermal and aerodynamic measurements were taken in the current study to understand how coolant transport is affected by coolant flow rate variations and to provide support to the endwall cooling effectiveness values observed. As the film coolant is also present in the study, a set of cases having different film cooling mass flow rate was also considered for the above measurements. Finally, as it was suspected that the vane surfaces were getting significant coolant coverage, detailed thermal measurements on these surfaces were also taken to study the phantom cooling of these surfaces.

Chapter 3. Test Facility Description

The experiments were conducted at the Fluid Mechanics and Heat Transfer Laboratory at the University of Minnesota. The current test facility is the result of efforts by Burd [8], Oke [47], Piggush [48], Erickson [49], Ayaskanta [50], Saxena [51], Alqefl [52,40] and the present author. Each of these authors has contributed in building a different part of the test facility or modifying an existing part to satisfy the experimental requirements. The test facility in its current state is shown in fig. 3.1.1. The air is introduced in the facility through multiple blowers, passed through a turbulence generator and a nozzle, followed by the combustor-turbine region and finally egressed into the atmosphere through the diffuser. Each equipment item in this test facility is explained in the order in which the air flows through the facility.

3.1. Main Flow Supply

The experiments require high Reynolds number, between 380,000 and 450,000, to simulate real engine conditions. Therefore, powerful blowers are required to generate the required Reynolds number at the required flow rate. There are four blowers used in the wind tunnel to create the main flow: two main blowers and two auxiliary blowers. They are indicated in fig. 3.1.1. At the entry to the wind tunnel, a general-purpose centrifugal blower of type 183 ACF, with rated power of 5 HP (3.7 kW), manufactured by New York Blower takes in air from the room. At this blower's outlet, a rectangular angle duct is attached, which changes the direction of the flow by 90° making it parallel to the mainstream direction (x direction). Then, the flow enters an axial blower. This blower is manufactured by Joy Manufacturing Company and is of type 29-17-17770AP, rated 7.5 HP (5.6 kW). The frequency (rotational speed) of the blower can be changed using a speed controller.

The frequency range is 0-70 Hz, with 0.1 Hz increments. The current experiments were run at 64 Hz as any higher frequency can cause damage to the motor of this blower.

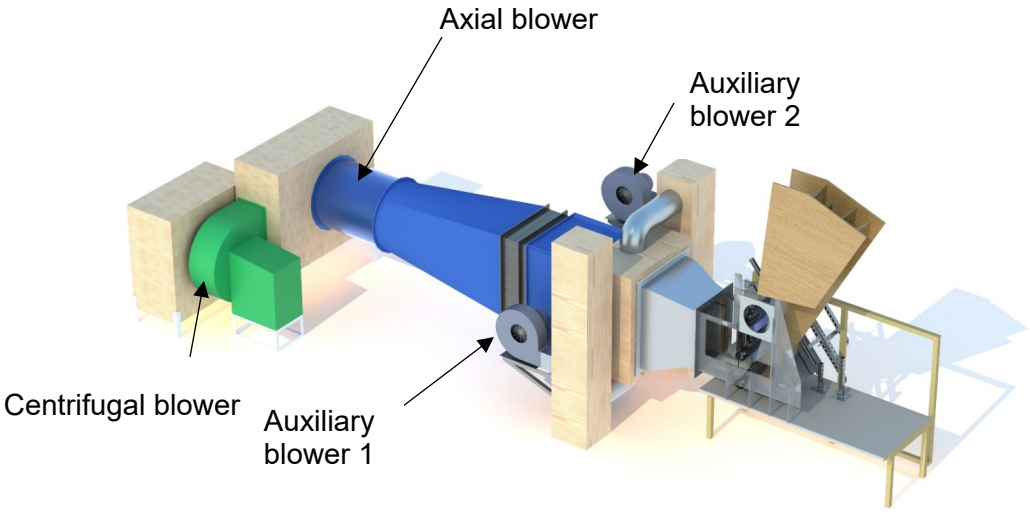

Figure 3.1.1 Test facility overview [52]

The flow at the exit of the axial blower is then directed to a long, round-to-square transition duct. At the end of this section is a heat exchanger. It was built as a part of an earlier study and is not used in the current experiments. However, as removing it requires a major modification, it was not done. The heat exchanger is followed by a series of screens that, with the heat exchanger, break down the flow turbulence and swirl. Downstream is a turbulence generator. It's design and operation are explained in the following section. There are two auxiliary blowers present as an input to the turbulence generator. These are of model 4c330, manufactured by Dayton Electric Manufacturing Company. They each have a power rating of 5 HP (3.7 kW), combining to provide about 60% of the main flow.

Filters are attached at the inlet of all four blowers to ensure that the air inside the tunnel does not contain debris. This is very important as the debris can easily cause harm to the measuring instruments, namely breaking of hot-wires and clogging of pressure measuring tubes.

3.2. Turbulence Generator

For the current study, turbine entry flow must have characteristics of a flow exiting a dry, low-NO_x type combustor. This combustor is characterized by high turbulence intensity and large turbulence length scales. Imitating these characteristics is important as high mainstream turbulence has a significant impact on endwall heat transfer [53,54]. The current turbulence generator has been designed originally by Erickson [49] and slightly modified by Saxena [51]. For the current study, no further changes were made to this equipment. Hence, only important information about the turbulence generator is given here. Interested readers are directed to the above theses for a detailed explanation of the turbulence generator.

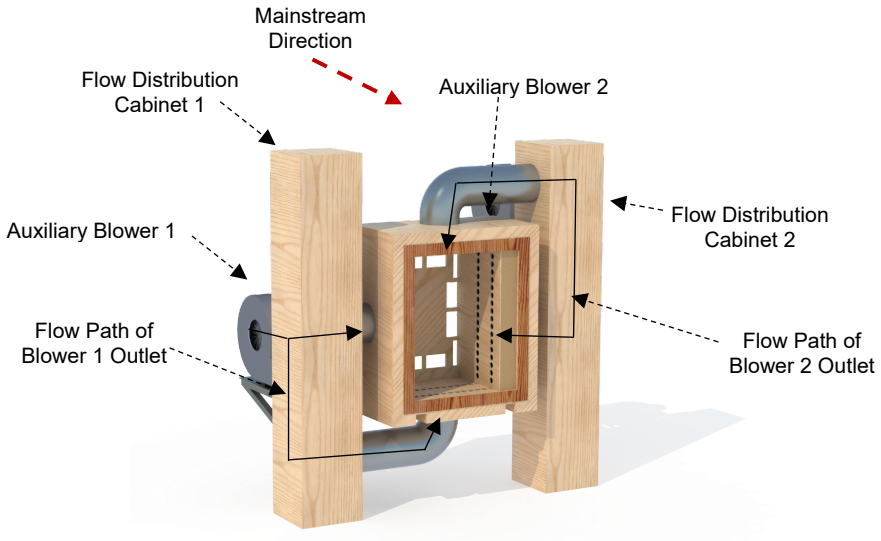

Figure 3.2.1 Turbulence generator [52]

The turbulence generator is made of a large mixing volume with two separate flows injected in the form of jets, called 'core flow jets' and 'cross-flow jets.' They enter the mixing volume through several holes in the front, top, side and bottom walls. The main flow enters the mixing volume through the front wall while the auxiliary blowers blow air through the

side, top and bottom walls into the mixing volume. Figure 3.2.1 shows the auxiliary blowers and the path of the air blown through them.

The core flow jets are formed by the main flow. The main flow, generated by two powerful blowers upstream, is made to pass through 12 rectangular slots present around the four edges of the rectangular mixing volume entrance. These are designed to give turbulence length scales in the order of 24-47% of the actual vane chord length. The design specifications of the turbulence generator are given in fig. 3.2.2. The cross-flow jets, generated by the auxiliary blowers, are first blown into two flow distribution cabinets (indicated in fig. 3.2.1). These cabinets have two exits to the mixing chamber that would introduce two flow streams perpendicular to each other and through discrete circular holes. Passing the core flow through the slots gives rise to turbulence. The turbulence is generated by the shear layers of the mixing jets with adjacent wakes created by the slot spacings and by creation of large recirculation zones. To further increase the turbulence levels, cross-flow jets, introduced through 2 discrete rows of holes, are blown normally to the core flow in the mixing chamber. These cross flows enhance mixing of the flow inside the mixing chamber and generate the necessary small-scale and large-scale turbulence features. The flows become a series of jets that maintain the turbulent shear layers necessary to preserve turbulence. The needed turbulence could not be simulated using stationary turbulence grids.

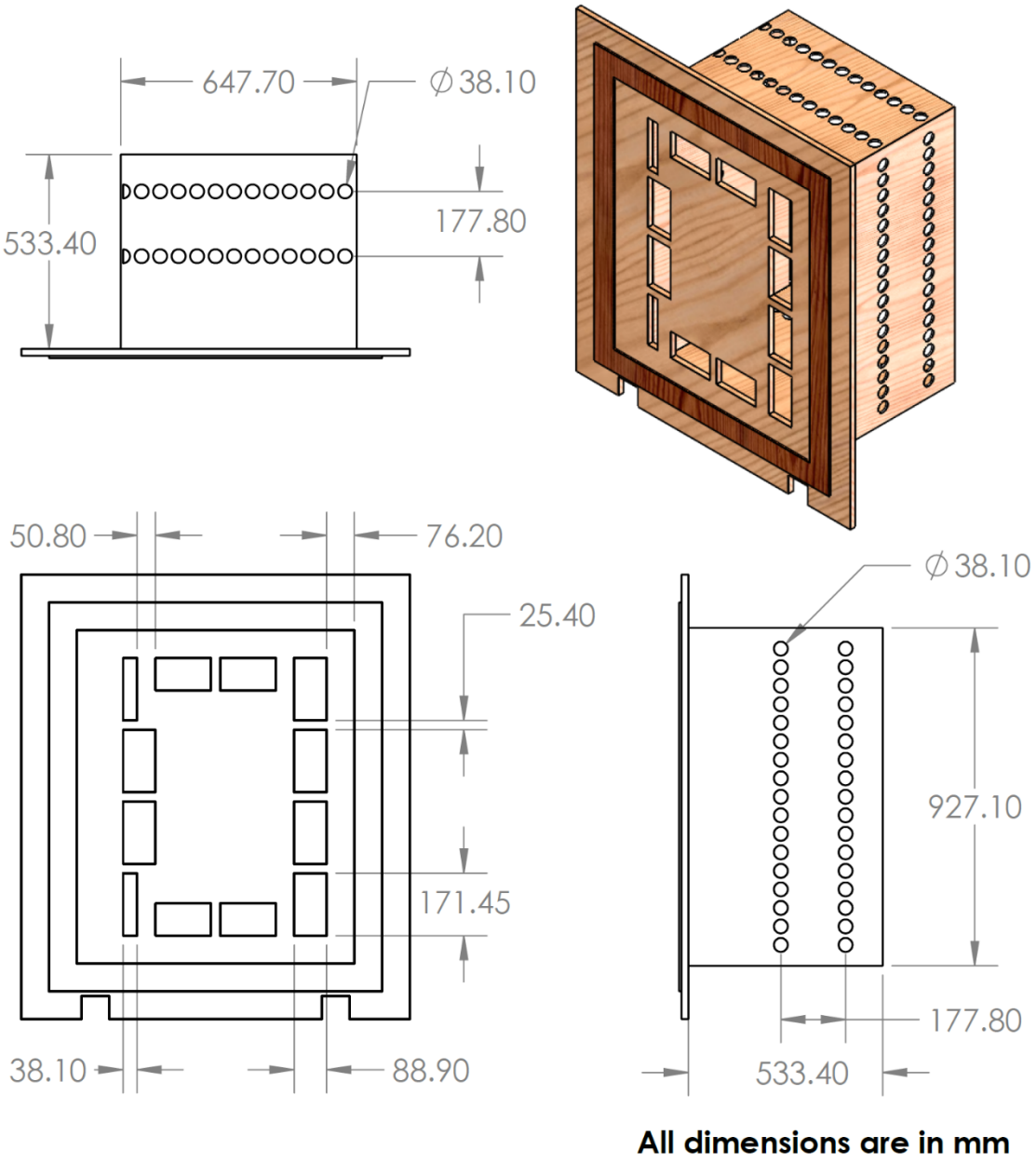

Figure 3.2.2 Turbulence generator design specifications [52]

3.3. Nozzle

A nozzle is situated downstream of the turbulence generator to facilitate the change of cross-sectional area between the turbulence generator and the test section entrance. The nozzle is contracting the flow, creating a uniform velocity profile. Engines also have an

area contraction at the exit of the combustor. Therefore, the nozzle simulates the last stage of the combustor.

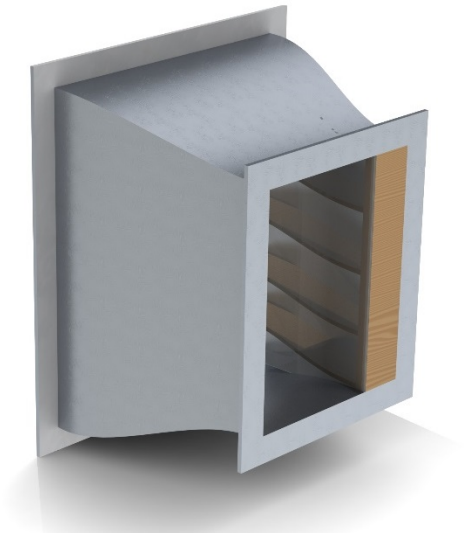

Figure 3.3.1 Wind tunnel nozzle [52]

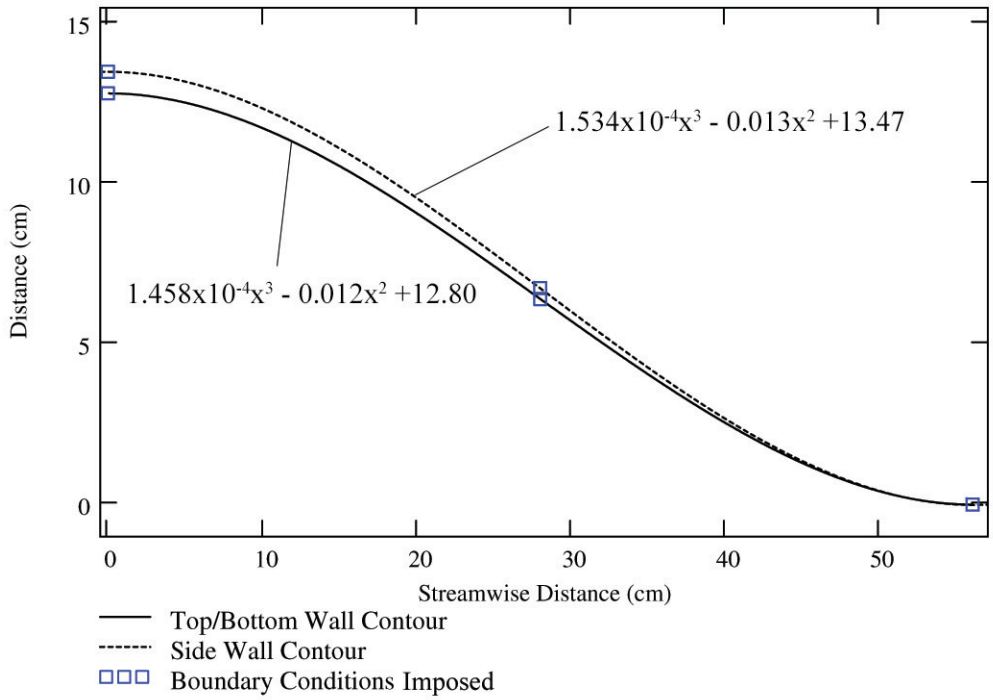

Figure 3.3.2 Nozzle contours [49]

The nozzle is shown in fig. 3.3.1. As was the case with the turbulence generator, it was originally designed by Erickson [49] and later modified slightly by Saxena [51]. The original contour of the nozzle was defined in such a way that the first and second derivatives of the contour curves are zero at the ends of the nozzle. The resulting third-order polynomial curve is shown in fig. 3.3.2. The small modification made by Saxena to adhere to her test facility requirements resulted in a slightly modified contour curve. There were no changes made in the nozzle for the current study.

3.4. Test Section

The flow exiting the nozzle, which simulates the combustor exit, enters the test section. This section imitates the region near the nozzle guide vane of a gas turbine between the last flat edge of the combustor liner and the trailing edge of the first stage nozzle guide vane. The test section includes the following design features: (i) combustor-turbine interface cavity, (ii) contoured endwall alongside the vanes, (iii) coolant injection holes at three locations upstream of the vanes, and (iv) two coolant plenums located upstream of the injection holes. These features are indicated in fig. 3.4.1, which shows the top and front views of the test section.

The walls of the test section, which come into direct contact with the main and coolant flows, are made of acrylic plastic (for visual access) and PVC plastic or wood, to maintain adiabatic wall conditions. The only exception is the aluminum rotating disc used to put the probe into the test facility and move it within the test facility. The purpose of this disc is explained later in this chapter. The aluminum disc is a good conductor of heat, but as it is located on the opposite side of the contoured endwall (where no measurements are taken), the effects of this heat transfer on the measurements are negligible.

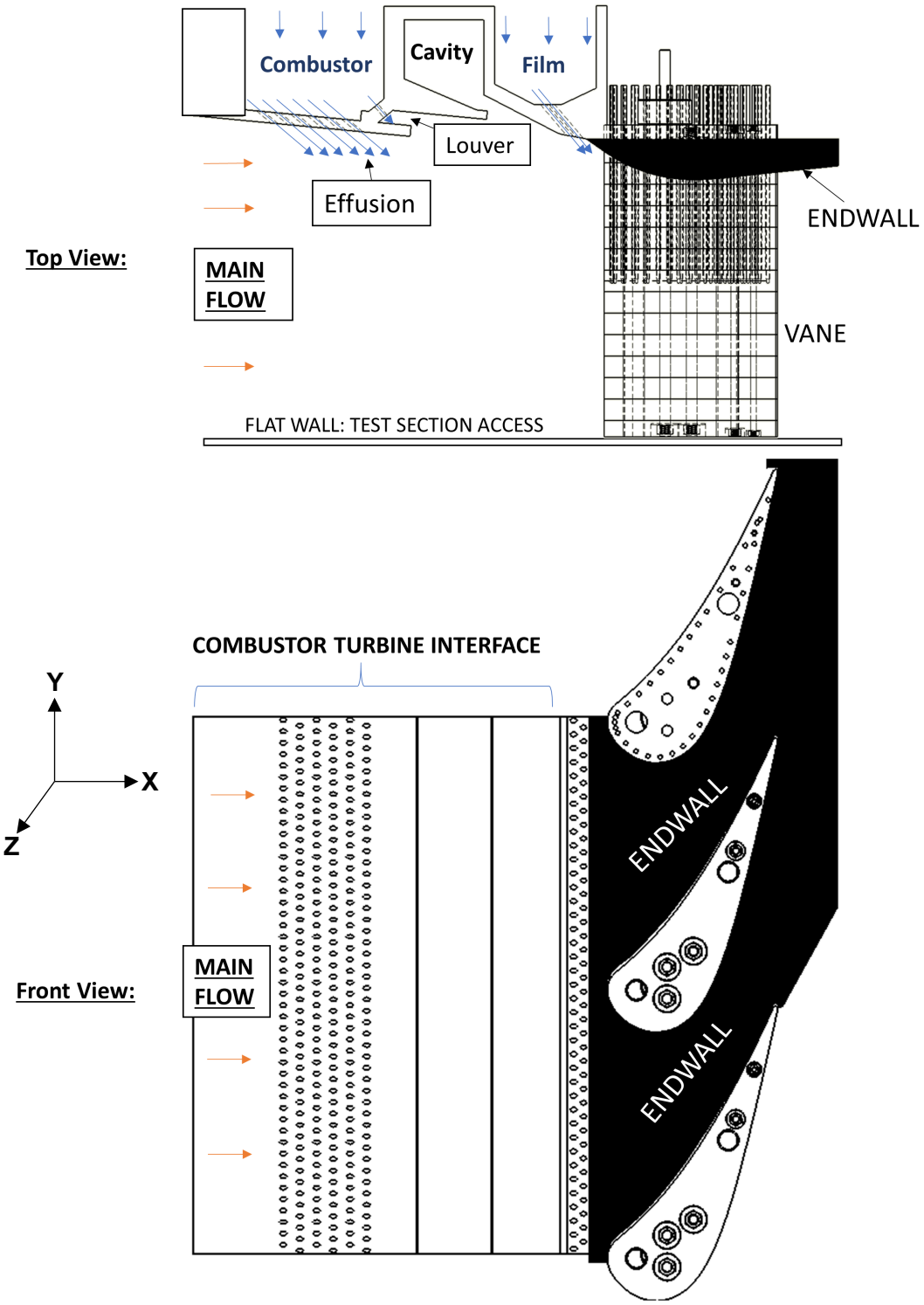

Figure 3.4.1 Test section overview, (Top) Top view, (Bottom) Front view [40]

3.4.1. Combustor-turbine Interface

The flow upstream of the vanes must be carefully simulated to match the engine conditions. In the engine, the hot gases exiting the combustor have a coolant present along the combustor walls. This coolant is injected in the engine to protect the walls from damage due to high temperatures. These coolant flows create low-temperature regions near the walls while the core is maintained at a high temperature by combustion. Thus, in addition to turbulence matching, the aerodynamic and thermal profiles of the passage inlet flow must be correctly simulated. In the test, it is the dimensionless temperature profile that is simulated. Figure 3.4.1 shows the combustor-turbine interface with its neighboring components while fig. 3.4.2 shows the dimensions of the interface. The interface consists of two combustor walls followed by a combustor-turbine cavity. The first combustor wall has an angle of 5° with the mainstream, as recommended by the industry (Solar Turbines, the sponsors of this project). Downstream of this wall is another combustor wall stepping down from this wall. The cavity, which marks the transition between combustor and turbine, is located at the downstream end of this wall. In the engine, the leakage flow through this cavity is low and therefore, no flow is supplied through this cavity in the test. Also, the cavity has a large volume to imitate the flow recirculation and mixing seen in the real engine. Alqefl [52] numerically showed that some flow in the pitchwise direction is present, where flow enters the cavity from one cross-span location and exits from another, driven by the spanwise static pressure gradient.

The combustor liner coolants are also introduced through discrete holes on the combustor-turbine interface, as shown in fig. 3.4.1. Two coolant streams are used to cool the combustor walls. The first one is called effusion coolant and is released through three sets of staggered rows having discrete holes. This coolant is used to cool the combustor wall exposed to the hot gases. The second is called louver coolant, released through a single

row of discrete holes beneath the combustor wall to cool the overhanging back side of the combustor wall. Both coolants are supplied using a single plenum, as shown in fig. 3.4.1. The coolant supply is metered using a laminar flowmeter upstream of the plenum. The meter is manufactured by Meriam (Model 50MC2-4). The flow is provided by a blower manufactured by Twin City Fans (Model 19N4 TBNA), having a rated power of 5 HP (3.7 kW). The flow rate through the blower can be managed using a speed controller (GDP333) manufactured by MagneTek. The intake to this blower is air from the room. To measure the coolant effectiveness, the coolants are marked by heating above the mainstream temperature. Therefore, a series of resistance heaters are attached inside the coolant supply duct upstream of the laminar flowmeter. Their total maximum power is 4.4 kW and this power is controlled using a variable autotransformer.

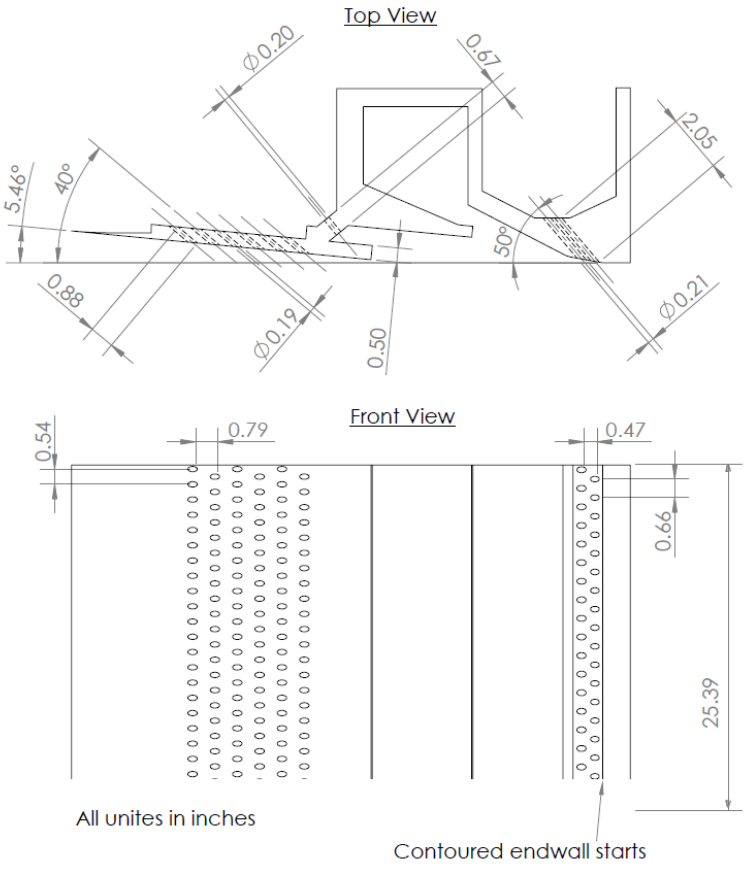

Figure 3.4.2 Combustor-turbine interface [40]

The interface was originally designed for the study presented in Alqefl [40]. It was manufactured of PVC plastic in the College of Science and Engineering Machine Shop. While the original interface was designed and manufactured by Alqefl, the assembly of the interface and supply ducts in the test facility, was performed by Alqefl and the author of the current study. Because it is very important to get the angle of the interface with the mainstream accurate, a considerable amount of time was spent on getting the interface correctly in place. The uncertainties in distances and angles of the assembly are given in table 3.4.1. The geometric uncertainties in the manufacturing of the interfaces, based on the CNC machine used were 0.1 mm in distance and 0.01° in angle.

Table 3.4.1 Geometric uncertainties in combustor-turbine interface

	Uncertainty in Length in Three Directions			***Uncertainty in Angle***
	Spanwise	***Pitchwise***	***Streamwise***	
Effusion cooling hole array	*5 mm*	*2 mm*	*2 mm*	*1°*
Film cooling hole array	*0.5 mm*	*2 mm*	*1 mm*	*1°*

Modification of the Original Combustor-turbine Interface

Alqefl's study involved the combustor coolant flow coming at the same flow rate for all cases. However, the current study required a change of flow rate *only* through the louver cooling holes. Therefore, to increase the flow only through the louver cooling holes, the cooling holes were enlarged so that the ratio of the resistance provided by the effusion cooling holes to the resistance provided by the louver cooling holes was correct; as such, the percent flow passing through the louver coolant rows was increased to the desired amount while the flow passing through the effusion cooling rows remained the same. The percentages of total combustor coolant passing through the effusion coolant rows and louver coolant rows, for various cases, are shown in table 3.4.2.

Table 3.4.2 Combustor coolant flow distribution and corresponding louver coolant holes diameters

Case	***Percent of combustor coolant passing through***		***Louver coolant hole diameter (in)***
	Louver coolant holes	***Effusion coolant holes***	
1	*7.36*	*92.64*	*0.2*
2	*16.49*	*83.51*	*0.3125*
3	*23.48*	*76.52*	*0.375*

While the original interface provided 7.36% of the flow through the louver cooling holes, the two new cases required 16.49% and 23.48%. The two larger louver cooling hole diameters corresponding to these cases were provided by the industry (Solar Turbines) based on the mainstream pressure, existing diameters of the louver and effusion coolant holes and the required flow rates of the louver coolant and effusion coolant. They are also recorded in table 3.4.2.

As the combustor-turbine interface was already in place, removing it would have been a major effort. Also, as some cases from Alqefl [40] were to be used as comparison for this study, as little change to the test facility as possible was desired. Therefore, enlarging of coolant holes had to be done from the region that is accessible for modification. A jig was designed to enlarge these holes. This jig would have holes with the same diameter as the louver coolant holes required for the new cases. The idea of the jig was to attach it on to the overhanging part of the combustor wall and drill through the overhanging combustor wall and then drill through the wall having the louver cooling holes, from the mainstream side of the test facility. This would create a row of unwanted holes in the front combustor wall that would later be filled with air-hardening clay and a thin, clear tape to keep the clay in place. The jig-interface assembly is shown in fig. 3.4.3.

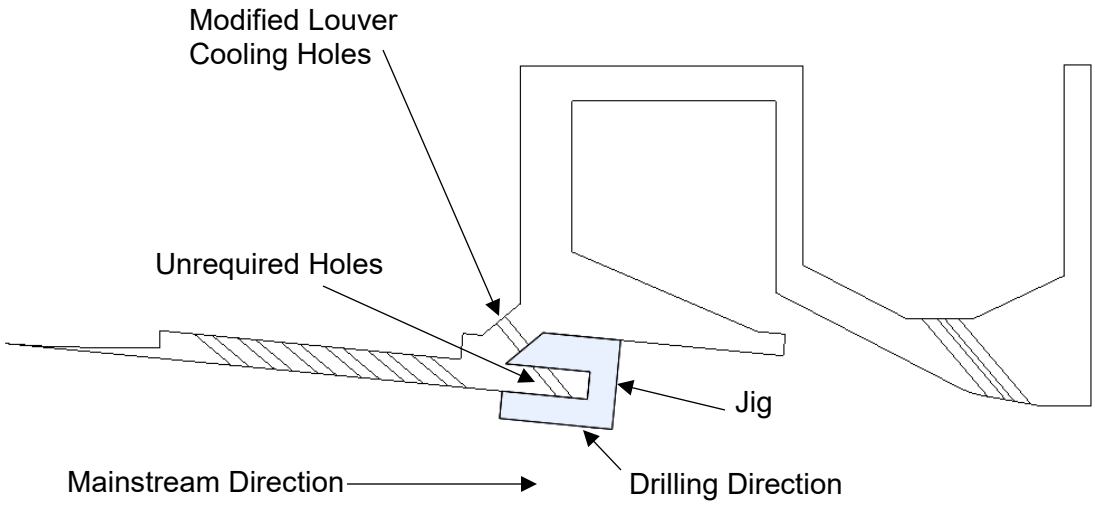

Figure 3.4.3 The jig-interface assembly

The jig was manufactured by the College of Science and Engineering machine shop. The working material is aluminum. The jig was manufactured first with the enlarged diameter required for case 2. After using it to drill the holes in the interface, it was enlarged further for the diameter required for case 3. The design of the jig, having the louver coolant hole diameter of case 2, is shown in fig. 3.4.4 and 3.4.5.

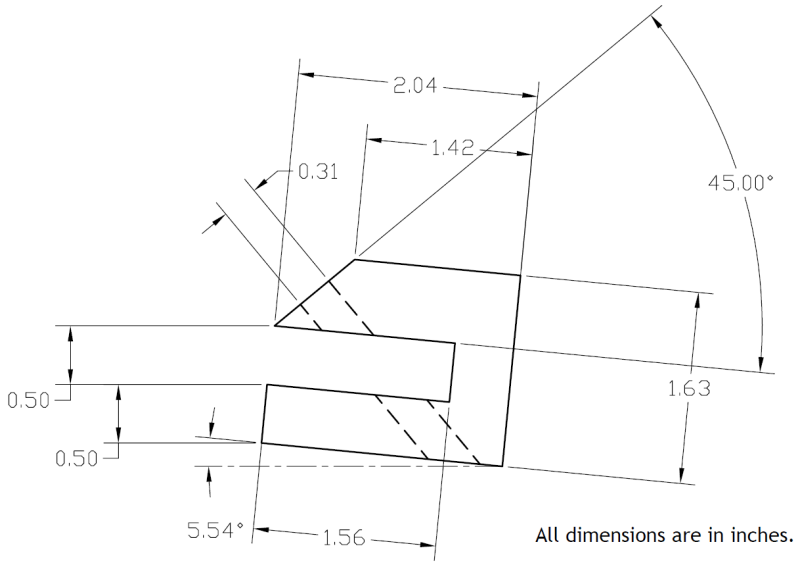

Figure 3.4.4 Top view of the jig

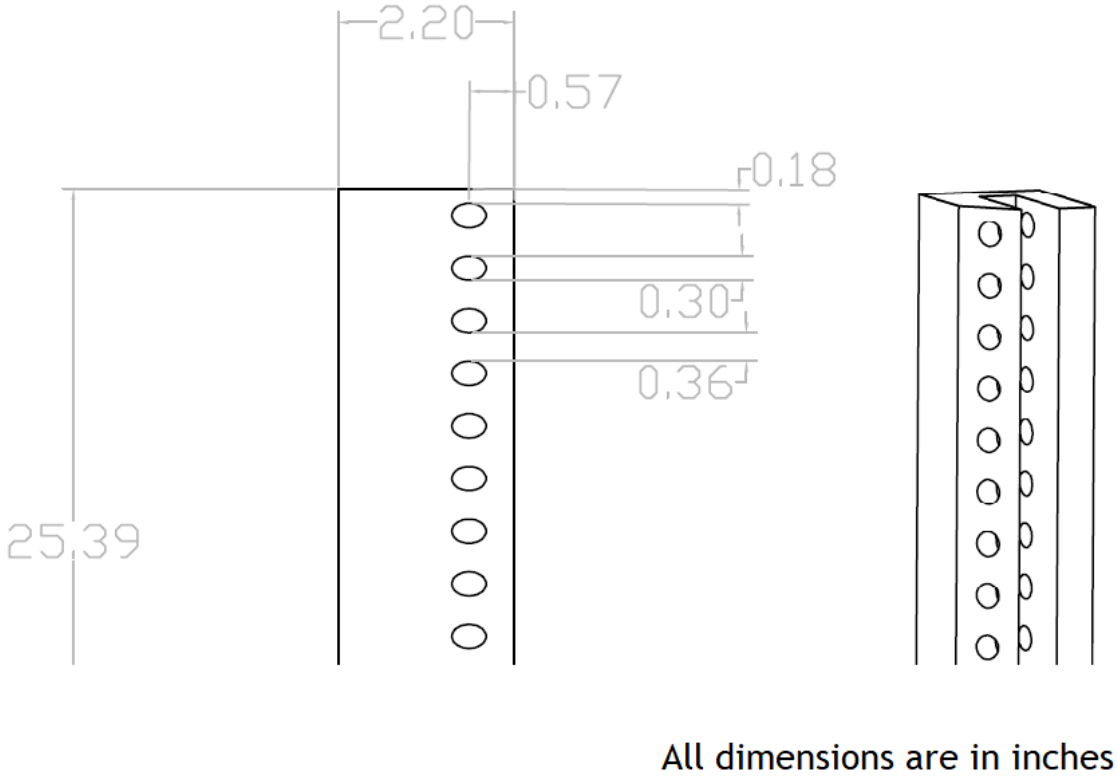

Figure 3.4.5 (Left) Front view of the jig, (Right) Isometric view of the jig

3.4.2. The Endwall Region

Film Cooling Supply

Film coolant is supplied by a pair of staggered rows of discrete holes, located immediately upstream of the vane passage. These are designed for a single purpose: to provide coolant to the endwall. The film coolant holes have a different diameter, length to diameter ratio and injection angle compared to the combustor coolant holes. Figure 3.4.2 shows the location of film cooling rows and other equipment in the test facility and shows dimensional specifications of the endwall region near the film cooling holes. The high length-to-diameter ratio causes a significant pressure drop across the holes and, therefore, the flow coming out of every hole in the mainstream has the same velocity distribution. The angle

of injection is very close to the departure angle of the endwall, making the film coolant a wall jet.

Like the combustor coolant, a second plenum and duct system are designed for delivering film coolant. The blower used for film coolant was manufactured by Cincinnati Fans (Model HP-4C22), rated 5 HP (3.7 kW). The flowmeter and the speed controller used for film coolant supply are of the same make and model as the ones used for the combustor coolant supply. Two resistance heaters, totaling a power of 1.7 kW, were used to heat the coolant to mark it at the same temperature as the combustor coolant.

Endwall Contouring

The hub endwall is one of the most important regions in the cascade and significant measurements are taken on and near this region. This endwall was manufactured by Saxena [51] and has not been changed for the current study. The endwall has an axisymmetric contour, i.e. the shape of the endwall is invariant over the pitch (y) direction, only changing in the axial (x) direction (see fig. 3.4.1 for axes references). The actual contouring was given by Solar Turbines, shown in fig. 3.4.6. Moving streamwise, the contour first contracts, decreasing the vane span, before expanding again in the latter portion of the passage. The inlet vane span (at $X/C_{ax} = 0$) is longer than the outlet vane span (at $X/C_{ax} = 1$) leading to net acceleration due to contouring, in addition to acceleration created by the turbine shape. Contouring is present on only one side of the passage, while the other side has a flat endwall. The flat endwall region is not simulated according to the actual engine and no passage measurements are taken in that region.

Medium density fiberboard (MDF) was used to manufacture the contoured endwall. As the endwall must be adiabatic, MDF was chosen because it has a low thermal conductivity of 0.15 $W.m^{-1}.K^{-1}$. The endwall was fabricated as a single piece with recesses for vanes cut

into it. The machining was done on a CNC machine to have good accuracy for the vane-shaped recesses and the contoured shape of the endwall. After machining, the surface was sealed with polyurethane sealant and painted to close the pores in the MDF.

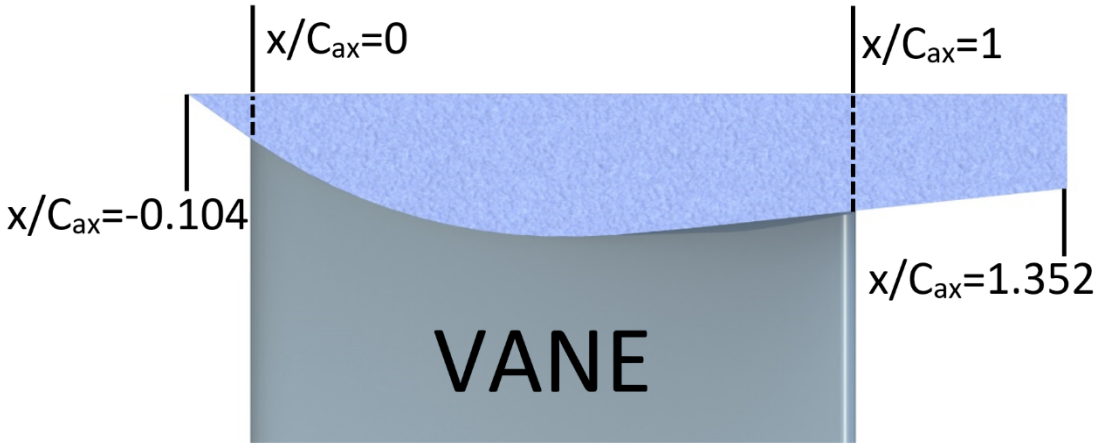

Figure 3.4.6 Contoured endwall in reference to the vanes

Once the endwall was manufactured, the vanes were installed in the recesses on the endwall. The gaps between the vanes and the endwall were sealed with self-adhesive pliable caulk sealant. This created a round fillet of 0.3 cm radius between the vane surface and the endwall. Then, the vane-endwall assembly was put into the test section. It was supported by a wooden frame, which, in turn, was supported with a structure of Unistrut® frames bolted to the workbench that carries the test section.

3.4.3. Cascade

First stage, high pressure nozzle guide vanes were used in this study. The cascade used in this study is the same as the one used in studies by Saxena [51] and Alqefl [52,40]. The vanes are stationary and are a reasonable imitation of the actual vanes. The cascade features are discussed in detail below:

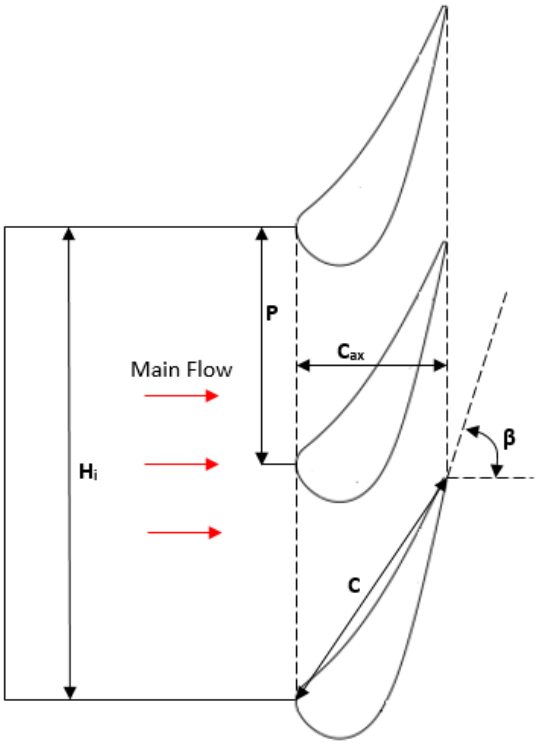

Figure 3.4.7 Layout of the vane cascade [51]

2-D Cascade Layout

The nozzle guide vanes are used to turn and accelerate flow coming from the combustor in the direction aligned with the rotor inlet. This cascade has three vanes and two vane passages, as shown in fig. 3.4.7. The leading edges of the top and bottom vanes are also the top and bottom walls of the test facility. Table 3.4.3 lists the geometric parameters of the cascade. The vanes, although of transonic design, are modified for low Mach number experiments. The cascade is scaled up by a factor of 4.91 to achieve the necessary Reynolds number, matching that of the engine. The scaling was decided by comparing the vane pitches of the actual vanes to the experimental vanes. The vanes have a Zweifel coefficient of 0.91, indicating moderate loading. The aspect ratio of the vanes is a bit lower than that of the engine, making the pressure distribution profile slightly more prone to secondary flow effects. The span of the vane changes in the axial direction, because one

end of the span has a flat endwall while the other has a contoured endwall. Two bleed slots are present across the spanwise direction just upstream of the vane passage and along the top and bottom walls of the test section. These are adjustable and set in such a way that periodicity between the two passages is achieved (see section 6.2 for the periodicity results).

Table 3.4.3 Cascade vane geometric specifications

Scale Factor (with respect to actual engine size)	4.91
Vane True Chord Length (C)	36.54 cm (14.38 in)
Vane Axial Chord Length (C_{ax})	20.53 cm (8.08 in)
Cascade Pitch (P)	32.25 cm (12.70 in)
Vane Inlet Span (S_i)	33.72 cm (13.28 in)
Vane Exit Span (S_e)	31.3 cm (12.32 in)
Vane Aspect Ratio, Inlet (S_i/C)	0.922
Vane Aspect Ratio, Outlet (S_e/C)	0.857
Space-Chord ratio (P/C)	0.883
Vane Inlet Angle (α, angle between cascade centerline axis and camber line at leading edge)	0˚
Vane Outlet Angle (β, angle between cascade centerline and camber line at trailing edge)	72.33˚
Inlet Passage Height (H_i)	64.50 cm (25.39 in)
Vane-Endwall fillet radius	0.3 cm (0.12 in)

The Vanes

The profile of the vanes was provided by Solar Turbines and the manufacturing was done by Saxena [51]. The vanes are made of acrylic plastic because it can be machined easily and has a low thermal conductivity of 0.19 $W.m^{-1}.K^{-1}$. Horizontal and vertical CNC milling machines were used alongside Mastercam software for accurate manufacturing. Forty-five identical small slabs having the vane profile were built. Each vane was made up of

fifteen of these slabs attached together as shown in 3.4.8. Seven of the fifteen vane slabs on each vane were drilled to make a hole (diameter = 0.508 mm) in the spanwise direction, to the midway point of the span, along the contour of the vane. These are used as pressure tap channels. At the mid-span, these channels had a hole drilled perpendicular to them and to the surface, toward either pressure or suction surface (depending on location). These are the pressure taps used to measure the static pressure distributions along the vane surfaces. A special jig was 3-D printed to ensure that the perpendicular holes are aligned correctly along the vane surfaces. The jig and the locations of the pressure taps are shown in fig. 3.4.9 and 3.4.10, respectively.

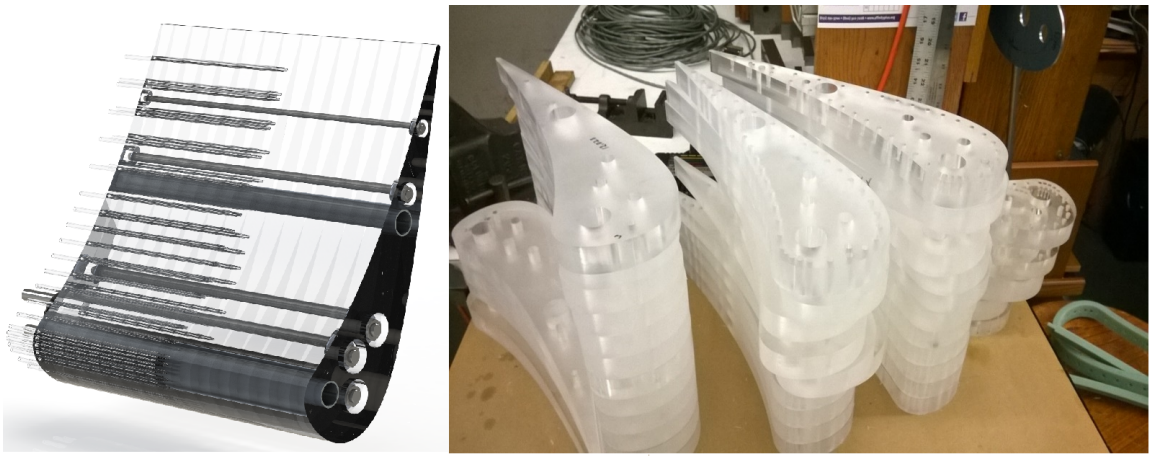

Figure 3.4.8 Vane assembly with the vane slabs (Left) Model, (Right) During assembly [51]

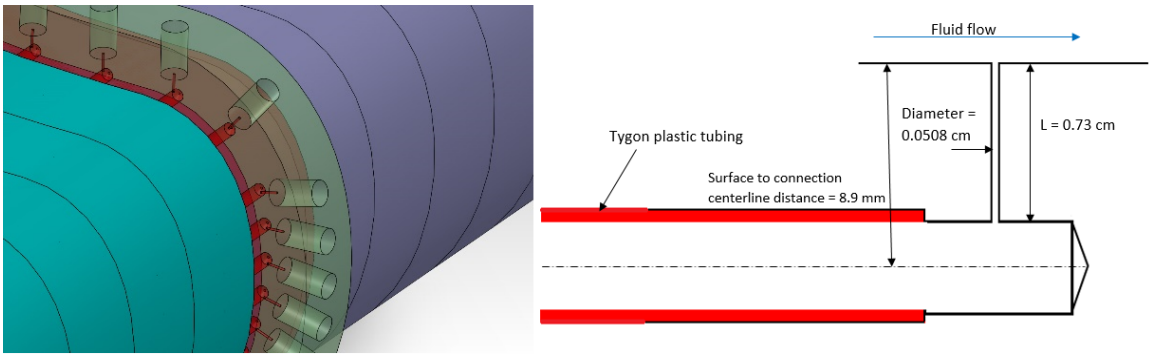

Figure 3.4.9 Jig for drilling holes on vane surfaces (Left) In reference to the vane surface (Right), dimensional specifications [51]

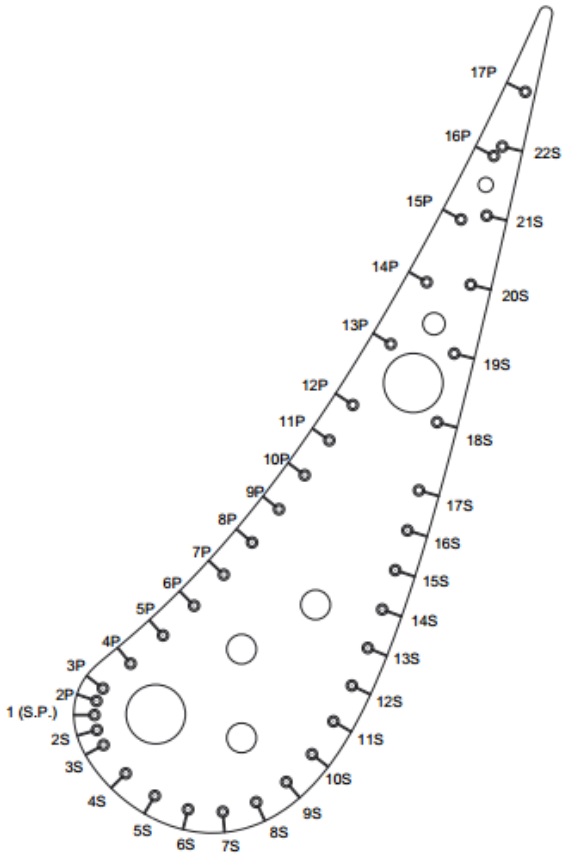

Figure 3.4.10 Static pressure tap locations along the vane surfaces [51]

3.4.4. Test Section Access

The test section can be accessed from the flat endwall side of the cascade. As seen in fig. 3.4.11, the flat endwall consists of four removable panels, one movable-hole panel and a rigid wall supporting these panels. The panels' dimensions are calculated such that the movable-hole panel can fit into any region where the remaining four panels could reside. All the panels can be slid into grooves on the supporting wall and are held together using toggle clamps. Additionally, tape segments to prevent leakage are put where the panels mate with each other or with the supporting walls. All panels and walls are acrylic plastic to have visual access and to prevent significant heat transfer through them.

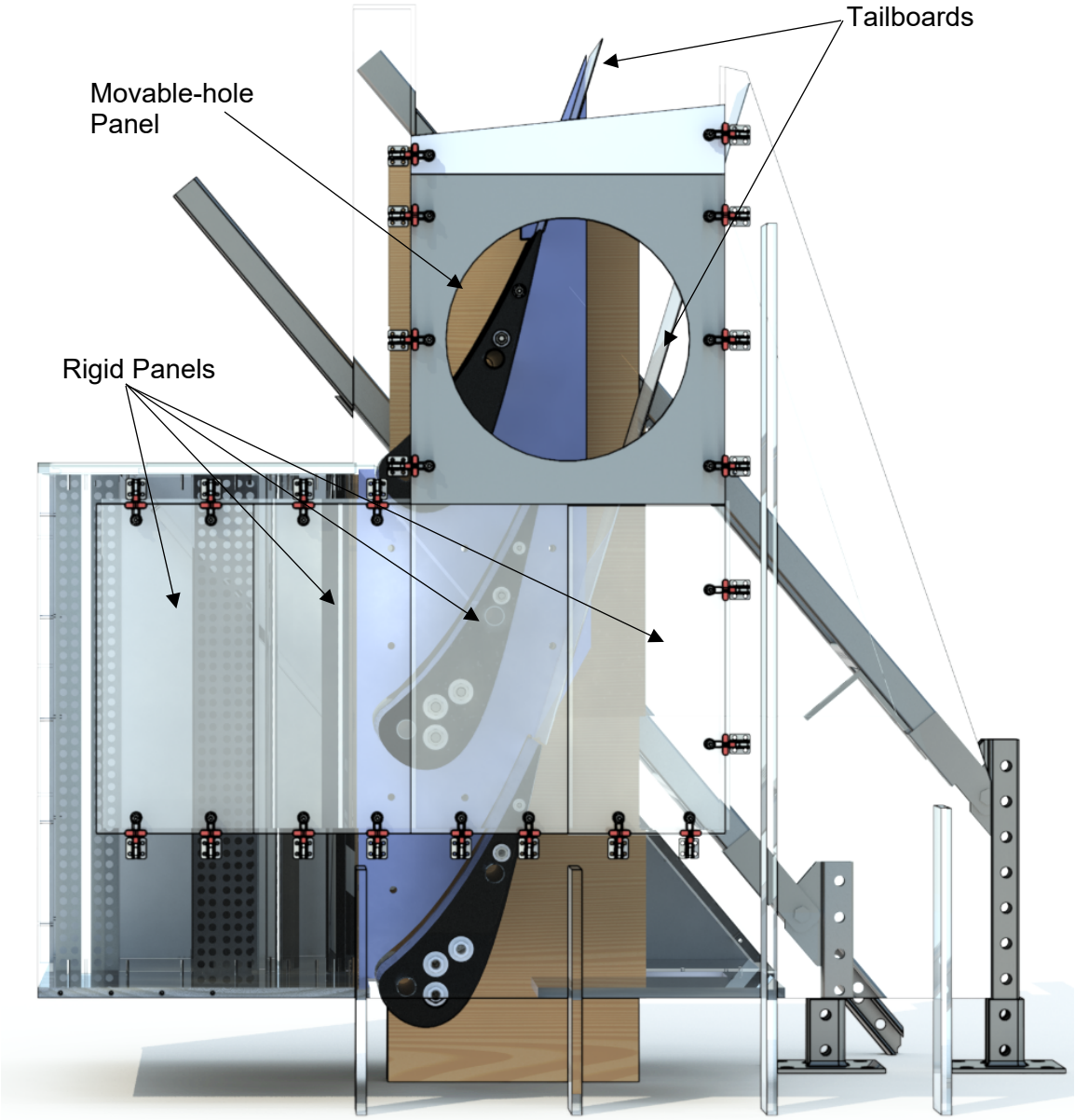

Figure 3.4.11 Test section access region. Four rigid panels and the movable hole panel are indicated [52]

The movable-hole panel was designed by Piggush [48]. The purpose of this panel is to allow the probe, which passes through a hole in this panel, to go inside the test section to have wide access to points within the passage. All thermal and aerodynamic measurements in the passage were taken by using this panel. This panel is shown in 3.4.12. The panel has two discs which can rotate freely due to ball bearing rings situated

along their circumferences (indicated in the figure). The probe hole is located at a circumferential point of the smaller disc. The diameter of the inner disc is equal to the sum of the radius of the larger disc and the diameter of the hole. This is done so that the hole can pass through the center of the larger disc, meaning that it can reach any point on the larger disc. The panel is made with aluminum for rigidity and the discs are made of acrylic plastic.

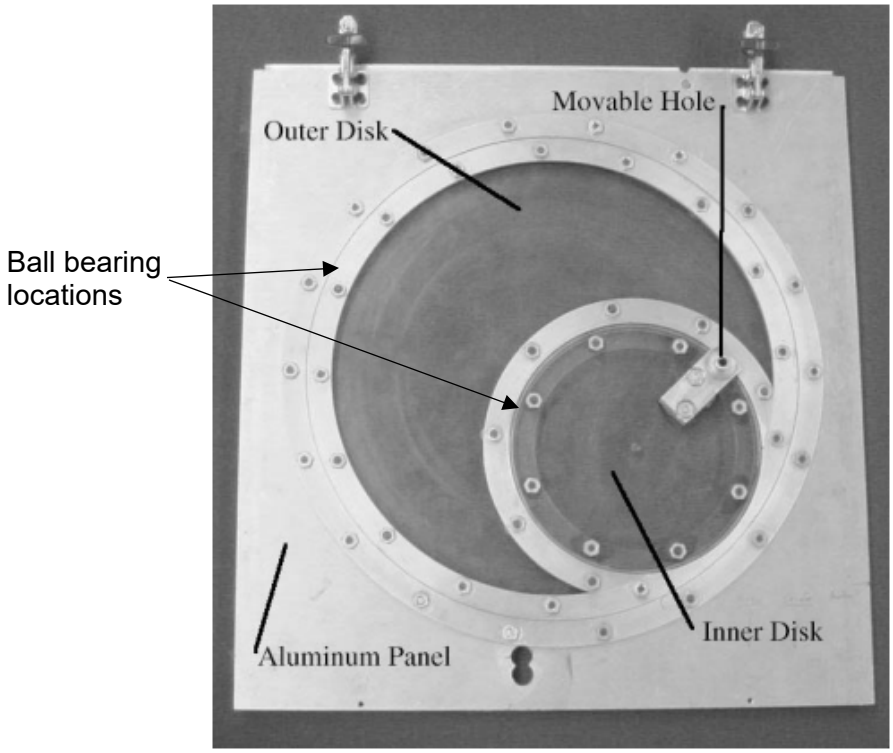

Figure 3.4.12 Movable-hole panel [48]

3.5. Exit Flow Management

3.5.1. Tailboards

The flow coming out of the cascade must be diffused carefully upon departure, as it will reduce the pressure rise requirements of the wind tunnel fans and increase flow velocity. For diffusing, the flow exiting the cascade is directed by the tailboards toward a multi-vane

diffuser, as indicated in fig. 3.4.11. The tailboard ends are attached to the trailing edges of the top and bottom vanes. The contoured endwall seamlessly merges with the diffuser endwall to form a continuous wall. On the flat endwall side, the acrylic walls create a flat surface up to the upstream edge of the diffuser endwall. The tailboards are made of thin acrylic plastic sheets (thickness = 0.635 cm/0.25 in) and are sealed on the sides using fillets of weather-proof sealing material. The tailboards' profiles were found experimentally by an iterative process, moving them until flow periodicity between the two passages was achieved.

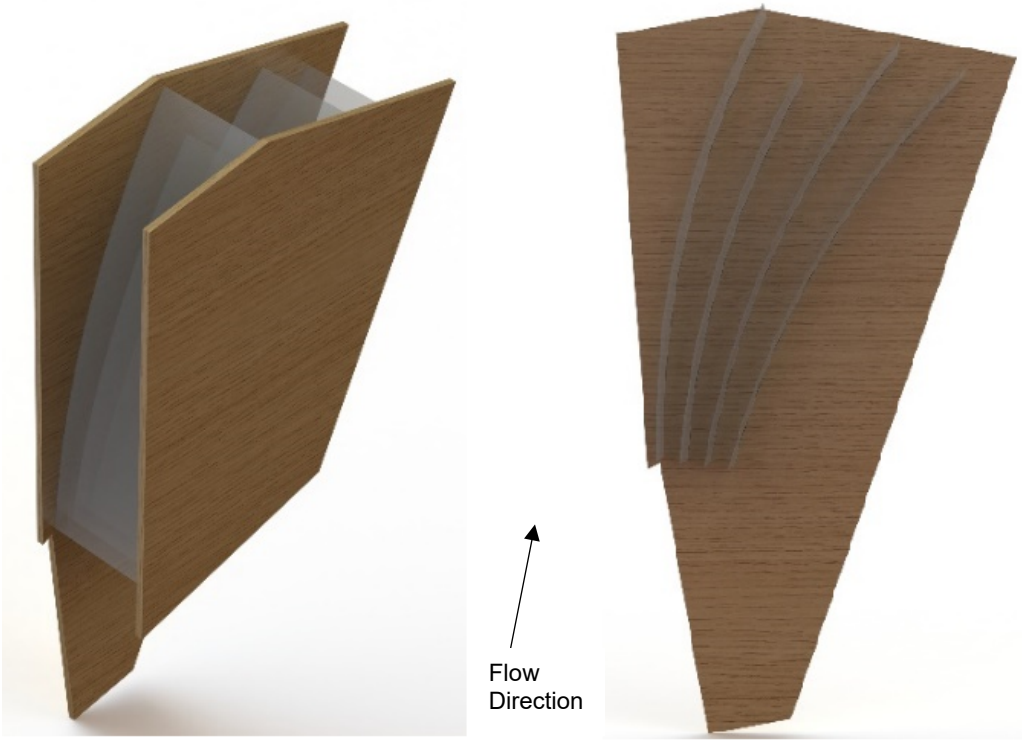

Figure 3.5.1 Different diffuser views [52]

3.5.2. Diffuser

The flow directed by the tailboards must be diffused properly. Ideally, a long, straight, single channel diffuser can be used to diffuse the flow. But, due to space constraints in the room, a short, three-channel, curved diffuser was designed and manufactured by

Alqefl [52] by performing a 2-D CFD analysis. The analysis is not repeated here. The diffuser is shown in fig. 3.5.1. It was found that the diffuser outlet-to-inlet ratio is 2.9. The diffuser vanes were made of acrylic sheets, having thickness of 0.238 cm/0.094 in. The diffuser endwall is made of two thin wooden sheets joined together. The upper sheet has grooves of the thickness of the diffuser vane such that the diffuser vane can be slid into this groove and held securely. During the current study vibrations caused one of the diffuser vanes to come out of the groove. Therefore, thin steel reinforcements were manufactured and attached at the upstream portion of the diffuser vanes to dampen vibrations and secure the diffuser vanes in place.

Chapter 4. Measurement Techniques

This section documents details of the instruments used for taking measurements. The quantities measured and the theory behind the instrument, including calibration methods and results are explained in detail. The instruments are grouped by the type of measured quantity and location of the measurements.

4.1. Temperature Measurements

This section explains the instrument used for the taking thermal measurements in this study. As one of the main objectives of this study is to measure the cooling effectiveness over various surfaces in the cascade and to study the temperature distributions in the flow, in-field temperature measurements are crucial. For this study, thermocouples are used to measure all temperatures required in this study. The working principle of a thermocouple is based on the Seebeck effect. The Seebeck effect states that when two dissimilar metals are joined and the junction is heated relative to the other ends, an electromagnetic field is generated, giving rise to a potential difference. This potential difference is directly related to the temperature between the junction and other end. The value of this potential difference, in Volts, is usually very small but, it can be used to accurately measure the temperature of the heated end, or junction.

The thermocouples used in this study are of type E (chromel-constantan). These have a temperature range of 3-1150 K. As the study involves a temperature range from ambient temperature to about 25°C higher (295-318 K), this thermocouple type is very suitable. The two ends of each thermocouple are known as the hot and cold junctions. The hot junction is kept where the temperature is to be measured while the cold junction is kept in an ice bath. In this study, an actual ice bath is not used. Instead, compensation for the

cold junction is provided inside the data acquisition (DAQ) unit, Agilent 34970A. This function helps to directly convert the voltage generated in the thermocouple to temperature, based on the data provided by NIST, documented in Burns, et al. [55]. A calibration of the thermocouples used in the study was also done using the conventional ice bath and thermometer setup. It was found that the cold junction compensation provided in the DAQ unit was giving very close results when compared to the conventional calibration procedure. The difference in temperature measured by these two methods was found to be within 0.024°C. Also, as the study requires a difference in temperatures to calculate the dimensionless recovery temperatures and cooling effectiveness, a small inaccuracy in the absolute temperature measurements will have no significant effect on the calculated quantities. As the measurements were taken continuously for 5 days every week, for 3 weeks, using an ice-bath was not practical, especially since the temperature uncertainty of using the DAQ cold junction was low. The DAQ cold junction temperature is common to all the measurements.

4.2. Aerodynamic Measurements in the Vane Passage

Information relating to the instruments used for measuring pressure and velocity magnitudes and directions inside the vane cascade passages is documented in this section. The pressure measurements at the static pressure taps on the vane surfaces are taken using an inclined manometer. For velocity measurements, a five-hole pressure tube, usually referred to as the five-hole probe, is used. The various instruments used for aerodynamic measurements are explained below.

4.2.1. Inclined Manometer

The theory behind a manometer is based on the fact that pressure causes a force on a surface. This force will lead to the displacement of the manometer fluid, on the surface to

which the pressure is applied. In cases of incompressible fluids (in this case, water or oil), the pressure applied can be directly related to the displacement of the fluid. A manometer has two vertical tubes that are connected at the bottom and contain same fluid. Different pressures can be applied to the top ends of these two tubes. When the pressure on each end is the same, the liquid levels are the same in both tubes. When unequal pressures are applied on these ends, the net pressure force causes a displacement. This displacement is directly proportional to the difference in pressures applied in the two ends. They are related as shown below:

$$\Delta P = \rho * g * \Delta y \qquad Equation\ 4.1$$

Where ΔP is the pressure difference in the two tubes of the manometer, ρ is the density of the fluid used in the manometer and Δy is the difference between the heights of the fluid columns in the two tubes. None of the measurements in the study (other than for describing thermodynamic properties) require an absolute pressure. The cascade measurements are taken with a reference pressure inside the tunnel and, therefore, changes in ambient pressure do not affect any quantities calculated from the measured pressure differences. This study uses an incline-type manometer, shown in fig. 4.2.1. These manometers, due to their geometry, provide large displacements of fluids for small pressure differences, increasing the accuracy of the measurement. A manometer used in this study is manufactured by Dwyer Co. and the model number is 246. It contains the Dwyer red gage oil having a specific gravity of 0.86. However, the scale printed on the manometer is made in such a way that it shows the displacement in terms of 'inches of water' instead of actual inches. The range for the pressure measurement is from 0 to 6 inches of water column (0-1494 Pa) which is enough for the present pressure measurements. A displacement precision of 0.25 mm (0.01 inches) of water column is reported by the manufacturer.

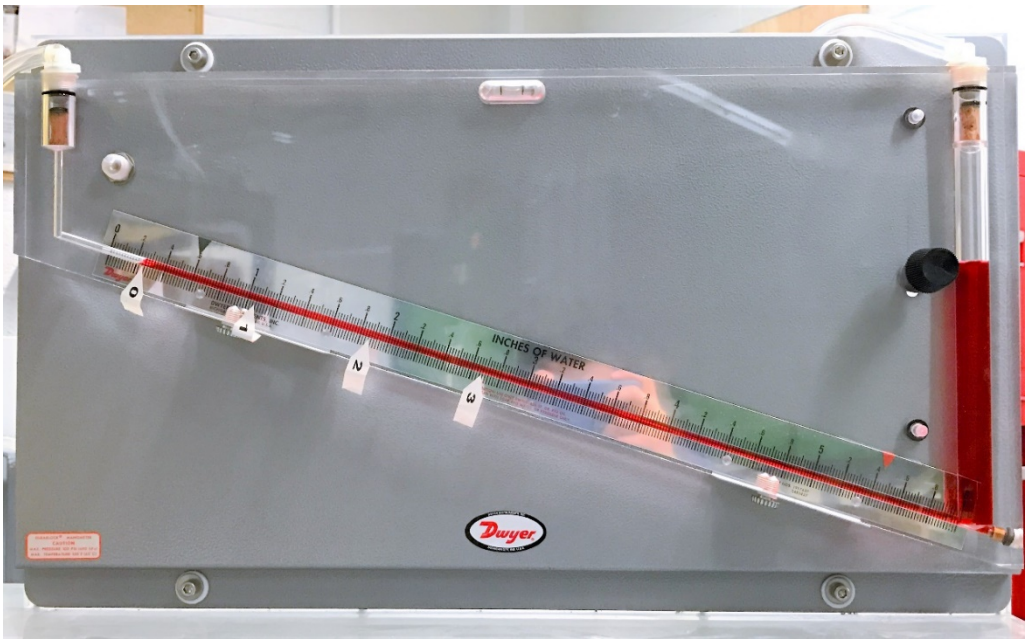

Figure 4.2.1 Inclined manometer used in this study [52]

4.2.2. Pressure Transducers

As manometers require manual collection of the measured data, they are not very convenient for taking a large volume of data. However, as they are accurate, they can be used to calibrate other pressure measuring devices. Pressure transducers, one of such devices, are used in this study. Pressure transducers are faster and more precise than manometers and the measured data can be directly stored in a computer using a data acquisition unit. The pressure transducer contains a diaphragm, which is made of magnetically permeable stainless steel. When pressure is applied on this diaphragm, it becomes deformed. This deformation gives rise to a change in magnetic reluctance and this reluctance changes the inductance of a coil that is embedded in the diaphragm. This leads to a change in voltage of the circuit connected to transducer. This change is a function of the pressure and therefore, the voltage generated by the transducer and the pressure applied to the transducer can be correlated. The pressure transducers used in this study were manufactured by Validyne Engineering Corp. and the model number is

DP15. As the five-hole probe requires five different pressures to be measured for each measurement, five transducers were calibrated. This calibration was done by Alqefl [52] and as the same five-hole probe and the same transducers were used for this study, the calibration was not repeated for this study. Only the results of the earlier calibration are reported here. For a detailed explanation of the calibration procedure, the readers are directed toward Alqefl [52].

A sample transducer calibration curve is shown in fig. 4.2.2. The calibration was done for the same range of pressures as the range of the manometer (6 inches/15 cm of water column). The pressure-voltage relationship appears to be linear as the coefficient of the second-degree term in the trendline equation is very close to zero. Hysteresis error can be seen by comparing the slopes of the negative part of the curve with the positive part of the curve. They appear to be identical, indicating no presence of hysteresis and that the diaphragm is in fine working order and has not been damaged.

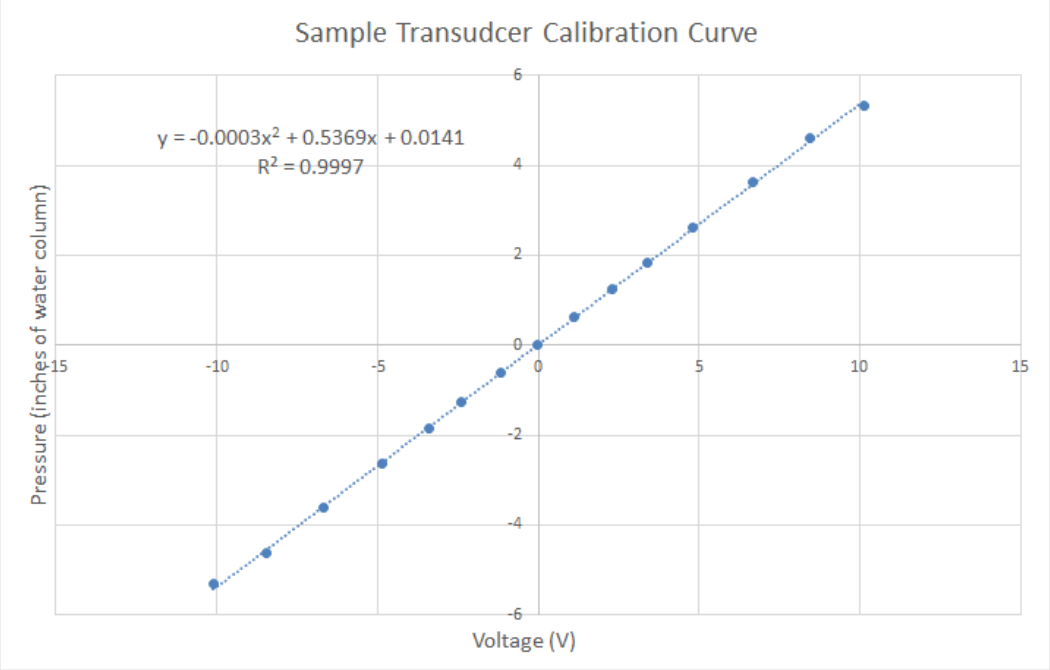

Figure 4.2.2 The calibration curve for one of the transducers used in this study [52]

4.2.3. Five-hole Pressure Tube

The five-hole pressure tube is used to measure the flow velocity as well as the flow angles, which can be used to calculate the flow components. As the name implies, the five-hole probe has five holes at the tip of the probe, as shown in fig. 4.2.4. The center hole (1) measures the total pressure of the flow hitting the tip of the probe only when the flow has no angle. For cases having non-zero flow angles, the calibration results are used to convert the pressure measured by the center hole into the total pressure of the flow. The holes (2) and (3) are used to measure the 'pitch' angle of the flow. Pitch is the angle that the flow makes with the x-z plane (see fig. 4.2.3). The holes (4) and (5) are used to measure the 'yaw' angle which is the angle the flow makes with the x-y plane (see fig. 4.2.3). The directions will become clearer once the results are plotted and discussed. The differences between the pressures seen at the opposite flanking holes ((2) and (3) for pitch angle and (4) and (5) for yaw angle) are used to calculate the respective flow approach angles. Therefore, measurements from the center hole of the five-hole probe and the flanking holes, provide enough information to calculate all components of the velocity in the passage. The method of calculation of the flow components using the measured data is given in section 5.2.

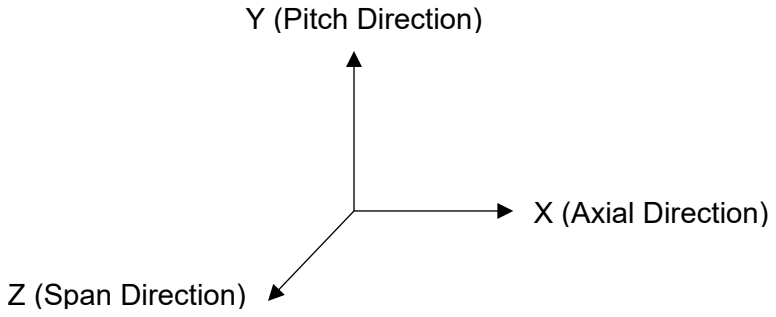

Figure 4.2.3 Test section axes. The main flow moves in the positive axial direction

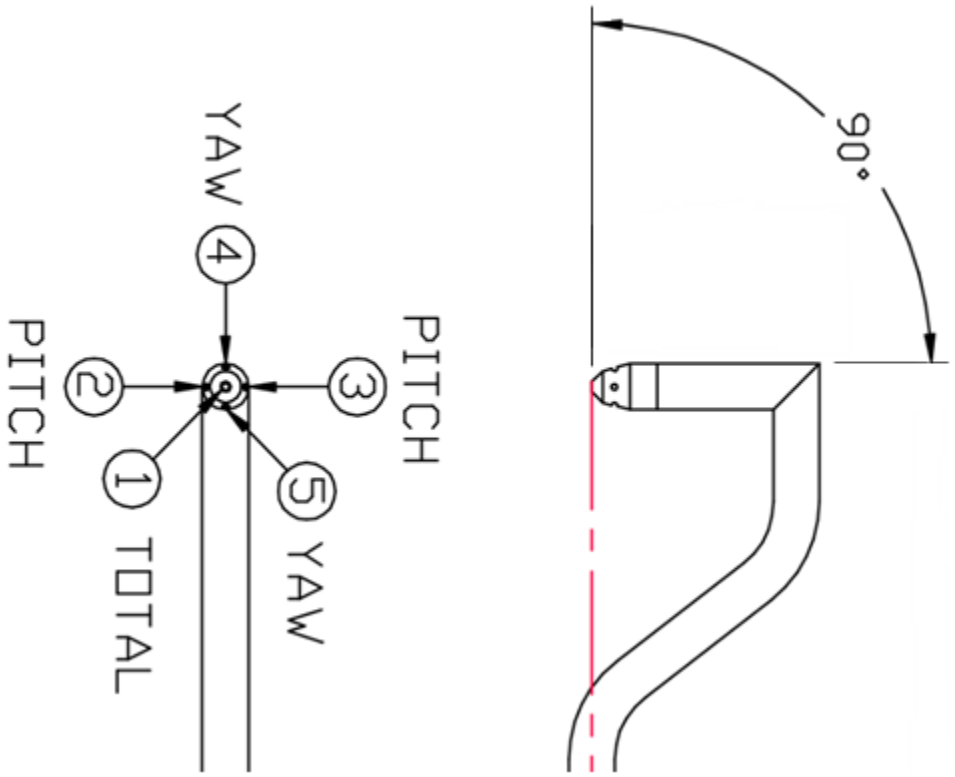

Figure 4.2.4 Schematic of the conical five-hole probe used in this study (provided by United Sensors Corp.)

The paper by Treaster and Yocum [56] was used to calibrate the five-hole probe. The 'non-nulling' technique is used for calibration. In this technique, the flow is kept at the same angle and the probe angle is changed in pitch and yaw directions so that the probe will see the flow coming from different angles as it is moved. When all the data are recorded, a contour fit is employed to relate the angles with the pressures measured by the five holes of the probe. Treaster and Yocum gave pressure coefficients which can be related to the pressures measured by the probe. These are given below:

$$Cp_{total} = \frac{P_1 - P_{total}}{P_1 - P_{ave}} \qquad Equation\ 4.2$$

$$Cp_{pitch} = \frac{P_2 - P_3}{P_1 - P_{ave}} \qquad Equation\ 4.3$$

$$Cp_{yaw} = \frac{P_4 - P_5}{P_1 - P_{ave}} \qquad Equation\ 4.4$$

$$Cp_{static} = \frac{P_{ave} - P_{static}}{P_1 - P_{ave}} \qquad Equation\ 4.5$$

Where

$$P_{ave} = \frac{P_2 + P_3 + P_4 + P_5}{4} \qquad Equation\ 4.6$$

The pressure coefficients can be calculated for all measured combinations of yaw and pitch angles. The subscript of each coefficient tells the parameter that has been non-dimensionalized. The denominators of the pressure coefficients contain the P_{ave} term, which reaches singularity for higher angles (typically >30°). Therefore, the definition of P_{ave} was modified by Hall and Povey [57] to give better results for higher flow angles as shown below:

$$P_{ave} = \frac{1}{2}\{\min(P_2, P_3) + \min(P_4, P_5)\} \qquad Equation\ 4.7$$

This definition of the P_{ave} was used in this study as higher flow angles were expected. Using this definition also yielded much smoother curves as the gradients of the contours of the pressure coefficients were much lower with it.

Calibration Technique

The five-hole probe used for this study was of the conical type. It was manufactured by United Sensors Corp. The length of the probe is 76.2 cm and the diameter of the probe is 2.41 mm. The diameter of the sensing holes is 0.305 mm. The flanking holes are located equidistantly from the center hole.

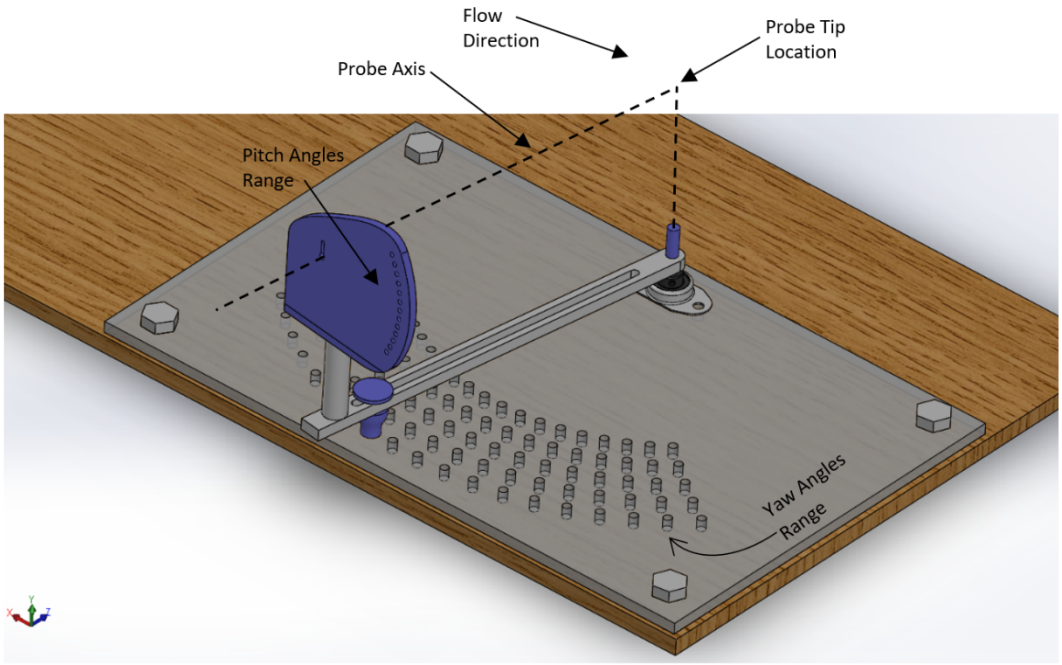

Figure 4.2.5 Five-hole probe calibration setup. Original drawing referenced from [52].

Figure 4.2.5 shows the schematic of the calibration rig that was used to 3-D print the rig. A detailed description of the calibration rig can be found in Alqefl [52]. Only a brief review is given here. The locations for varying the pitch and yaw, the axis along which the probe is aligned, and the flow direction are indicated in fig. 4.2.5. A leaf blower is used to create a flow having approximately the same velocity as the exit velocity of the tunnel (~52 m/s). This flow is made uniform by using a nozzle at the exit of the leaf blower. The probe tip is located as shown in the figure. When the probe tip is aligned at the shown location, it also aligns at the center of the flow coming from the leaf blower.

As stated earlier, the probe is calibrated using the non-nulling technique. Therefore, the probe was calibrated for a range of pitch and yaw angles. The angle ranges of the rig are ±45° with 1° increments and ±35° with 5° increments for yaw angle and pitch angle, respectively. However, the calibration was done for a ±35° range with 5° increments for both pitch and yaw angles. Two additional yaw angles, +2° and -2°, were added for better accuracy in the low-angle region. Therefore, a total of 255 probe positions (17 yaw angles

X 15 pitch angles) were measured for calibration. As the five-hole probe has a slow response, every time a new location is reached, ~30 seconds were spent for the pressure in the tygon tubes, connected to the five-hole probe, to stabilize. After that, pressures were measured for ~20 seconds and then averaged.

The data recorded are in Volts. Therefore, the transducer correlations are used to convert them into pressures. After that, pressure coefficients are found using equations 4.2 through 4.7. The yaw angle is a function of Cp_{pitch} and Cp_{yaw} and, therefore, a 3-D contour was plotted using the curve-fitting tool in MATLAB. Similarly, for pitch angle, a similar contour is plotted with the same independent variables, i.e. Cp_{pitch} and Cp_{yaw}. As expected, the pitch and yaw angles increase with increases in Cp_{pitch} and Cp_{yaw}, respectively.

Also, both the total pressures and the static pressures are functions of the pitch and yaw angles, the pressure coefficients, Cp_{total} and Cp_{static}, are also functions of Cp_{pitch} and Cp_{yaw}. As Cp_{total} will be a maximum when the flow angle is zero, both Cp_{pitch} and Cp_{yaw} become zero when Cp_{total} has its maximum value. A similar observation is made for Cp_{static}. The contours for all four pressure coefficients are shown in fig. 4.2.6 through 4.2.9. Generally, all contours look smooth and the extrapolation does not look to be wrong. Still, any data having pitch or yaw angles more than 35° were excluded from the results, allowing a lower maximum uncertainty value.

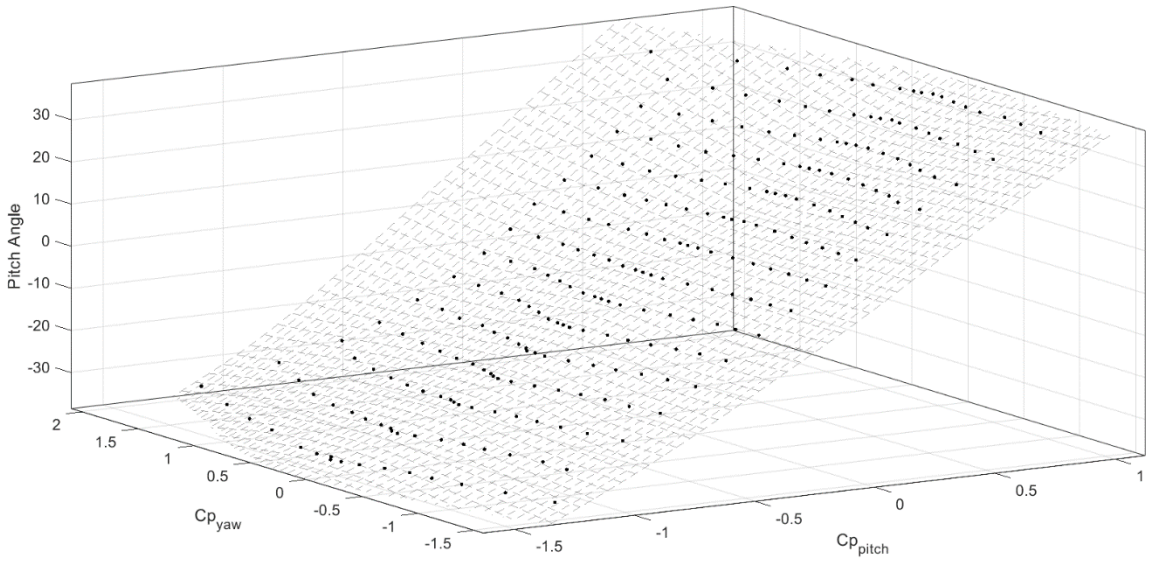

Figure 4.2.6 Contour fit for pitch angles as a function of Cp_{pitch} and Cp_{yaw}

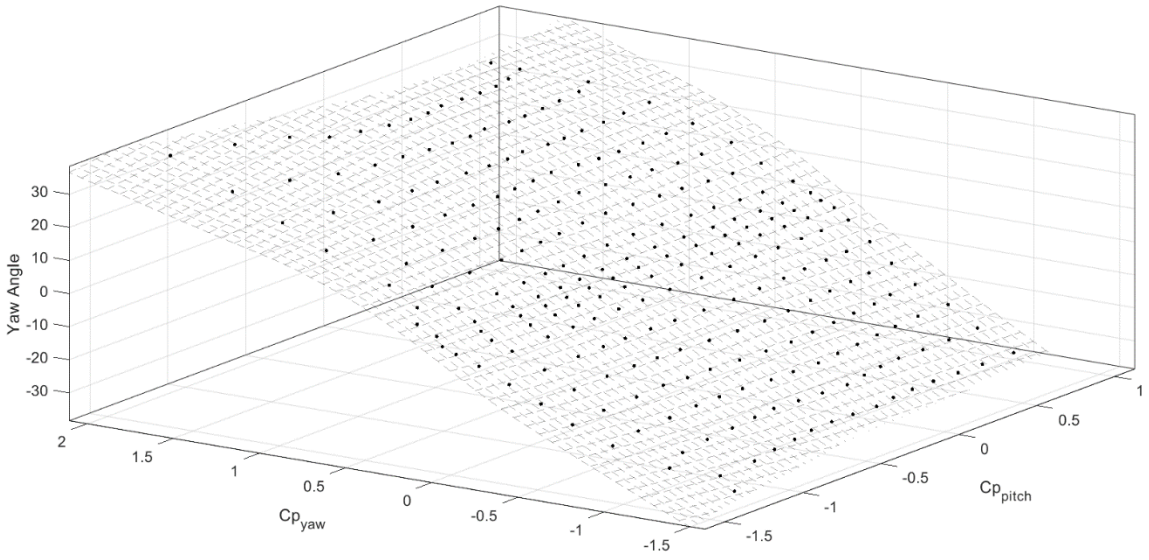

Figure 4.2.7 Contour fit for yaw angles as a function of Cp_{pitch} and Cp_{yaw}

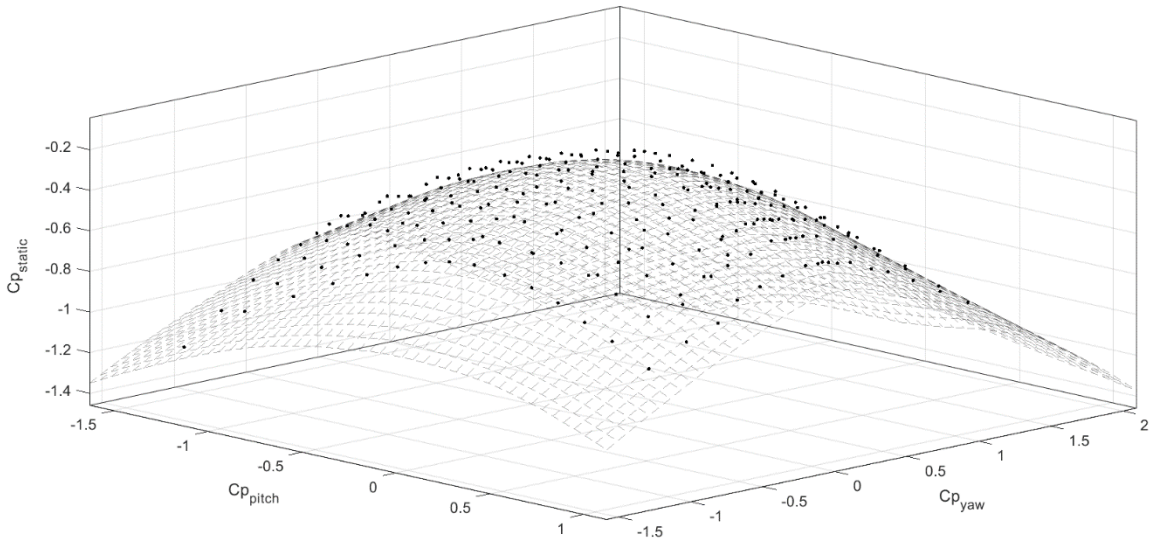

Figure 4.2.8 Contour fit for Cp_{static} as a function of Cp_{pitch} and Cp_{yaw}

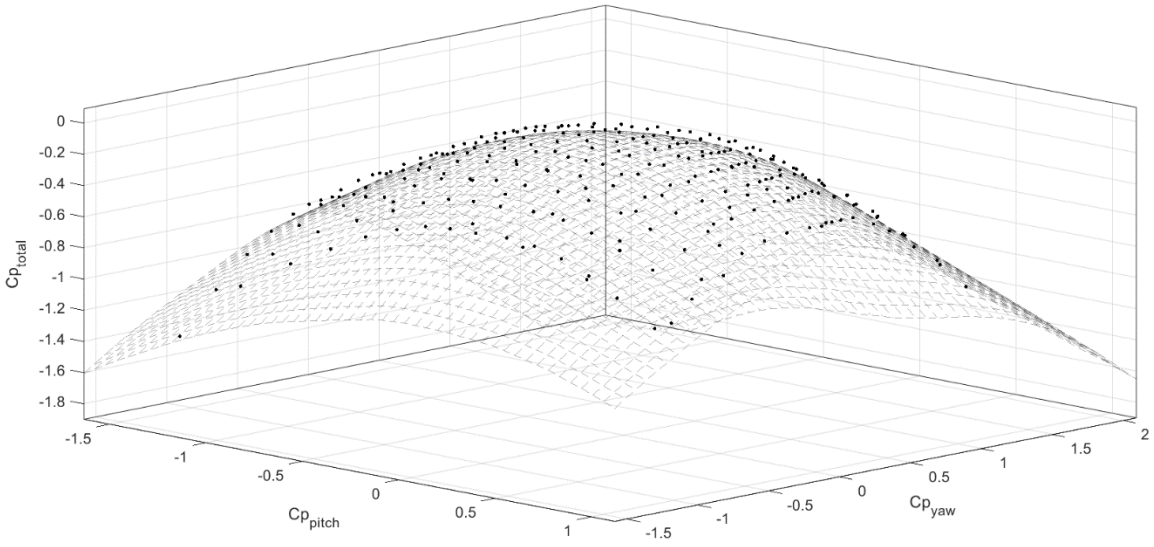

Figure 4.2.9 Contour fit for Cp_{total} as a function of Cp_{pitch} and Cp_{yaw}

4.3. Aerodynamic Measurements Upstream of the Vane Passage

The measurements required upstream of the passage are: (i) Temperature measurement for the approach flow thermal profile, (ii) The flow rates of combustor coolant and film coolant, (iii) High-frequency velocity measurements of the approach flow for turbulence intensity and turbulence length scale calculations. Out of these, the temperature measurements are done by the same thermocouples as introduced in section 4.1 and,

hence, are not discussed again. The remaining two types of measurements are done by a laminar flowmeter and hot-wire anemometry, respectively, as explained in the following sections.

4.3.1. Laminar Flowmeter

As both combustor coolant and film coolant flow rates are changed for this study, the flow must be metered accurately. In a laminar flowmeter, the flow is passed through thin tubes that make the flow laminar. This conversion makes the flow a Hagen-Poiseuille flow, which has an exact analytical solution for velocity distribution. Therefore, the velocities and, by extension, the flow rates, calculated from pressure drops measured across a laminar flowmeter are very accurate. The solution is dependent on the tube diameter, pressure gradient and the viscosity of the fluid, all of which are either known or can be measured. The downside of using a laminar flowmeter is that a significant pressure drop is experienced across the flowmeter. However, this was met by using high pressure-high flow rate blowers in the coolant flow supply lines.

The laminar flowmeter used in this study was the Model 50MC2-4 manufactured by Meriam. There are two pressure taps, one each at the entry and exit of the flowmeter, to measure the pressure drop. The necessary equation required to calculate the flow rate was supplied by the manufacturer as Q, in cubic feet per minute, as a function of pressure drop across the flowmeter, ΔP, in inches of water column, and viscosity, μ, in $N.s.m^{-2}$. This equation is:

$$Q = (-0.0692834 * \Delta P^2 + 50.0651 * \Delta P) * \frac{\mu_{std}}{\mu_f} \qquad Equation\ 4.8$$

Where μ_{std} is the dynamic viscosity of the working fluid (air) at 21°C while μ_f is the dynamic viscosity in lab ambient conditions. The air temperature and humidity in the lab were measured using an HH311 Humidity-Temperature Meter, purchased from Omega

Engineering. From this information, dynamic viscosity for lab ambient conditions is calculated. The uncertainty in the flow rate calculated by equation 4.8 is reported by the manufacturer to be 0.72%, given for a 95% confidence level.

Flow rates are based on mass flow ratios (MFR). The mass flow ratio of the combustor coolant is defined as the ratio of the combustor coolant flow rate to the mainstream flow rate. It is usually expressed in percentage. In this study, the MFR values of combustor coolants were provided by the industry and the flow rates of the coolants ($Q_{combustor}$) were calculated based on the given values as shown below:

$$(MFR)_{combustor} = \frac{Q_{combustor}}{V_0 * A_m} \qquad Equation\ 4.9$$

V_0 is the velocity magnitude of the mainstream at a location upstream of injection of combustor coolant and A_m is the cross-section area at the location where V_0 is measured. Their multiplication gives the flow rate of the mainstream at a location upstream of combustor coolant injection. This value is used as a mainstream flow rate reference for defining the combustor coolant MFR.

For the film cooling flow rate, a similar formula is written based on the film cooling MFR values provided by the industry. In this case, the mainstream flow contains combustor coolant flow as well. Therefore, the equation changes from equation 4.9, slightly.

$$(MFR)_{film} = \frac{Q_{film}}{V_0 * A_m + Q_{combustor}} \qquad Equation\ 4.10$$

For film cooling MFR, the reference flow rate consists of the mainstream flow rate and the combustor coolant flow rate introduced upstream of film coolant injection. Although a mass flow ratio term is present in these equations, density terms are not seen. That is because both mainstream and coolant flows have the same working fluid, air, and are at very similar

temperatures. Therefore, the density ratio of the mainstream fluid to coolant flows is practically 1.0, eliminating the term from the equations.

Additionally, the momentum flux ratio for the film coolant flow, I, is defined as:

$$I = \frac{V_c^2}{V_0^2} = (MFR)^2 * \frac{A_m^2}{A_c^2} \qquad Equation\ 4.11$$

Where V_c is the velocity magnitude of the film coolant injection and A_c total cross-section area of the film coolant holes.

4.3.2. Hot-wire Anemometry

To characterize the approach flow velocity and turbulence, high-frequency velocity measurements are required. This is not possible with the slowly responding five-hole probe. Therefore, hot-wire anemometry is used to measure the flow velocity of the approach flow.

The hot-wire anemometry is based on using the heat transfer characteristics of the hot-wire to measure the velocity of the flow moving around it. There are three types of hot-wire anemometers: constant temperature type, constant current type and constant voltage type. This study uses the constant temperature type hot-wire anemometry. In this type, a very thin wire is connected in an electrical circuit that is used for sensing the velocity. As the name suggests, the temperature of this wire is kept constant. The circuit maintains the electrical resistance of the wire constant, but it is a function of wire temperature. Therefore, when the hot-wire is kept in a flow of a particular velocity, the current required to keep the wire temperature constant must be established so that the power is that required to match the convective heat transfer rate between the fluid and the wire. This current change is effected by changing the voltage applied to the circuit. This change in voltage, therefore,

is a function of the change in velocity. A correlation can be found between these two quantities. This correlation was first found by King [58] and is shown below:

$$u^n = A * V^2 + B \qquad Equation\ 4.12$$

Where 'u' is the flow velocity ($m.s^{-1}$), 'V' is the voltage (V) and n, A and B are curve-fit constants which are based on the type of hot-wire used. Theoretically, the value of 'n' should be 0.5, but practically, it lies between 0.45 and 0.5.

Instrumentation

The hot-wire anemometer used in these experiments was a Constant-Temperature Anemometer (CTA), Model 1750, manufactured by TSI Inc. The hot-wire probe used was a Standard Boundary Layer Probe, Model 1218, also manufactured by TSI, Inc. The probe measures the major component of velocity. The boundary layer probe was chosen because, as the name suggests, it can be used to take velocity measurements very close to a wall (the combustor wall in the case of this experiment). The boundary layer probe is shown in fig. 4.3.1. The figure shows that the probe has a protective stem going perpendicular to the flow direction. It is designed to leave a 0.13 mm clearance between the hot-wire and the wall when the stem is just touching the wall. This ensures that the fragile hot-wire is protected from breakage. The constant temperature at which the hot-wire is maintained is 250°C. This temperature is suggested by TSI Inc. because it optimizes the sensitivity and lifespan of the hot-wire.

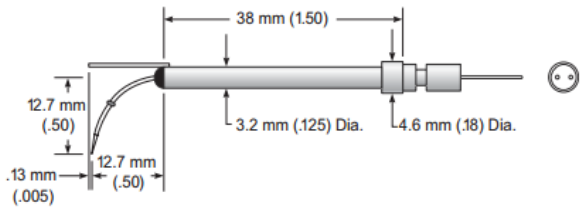

Figure 4.3.1 Dimensions of the model 1218 standard boundary layer hot-wire probe used in this study [59]

Calibration Setup

The calibration setup for calibrating the hot-wire should provide flow of a uniform velocity profile, little to no turbulence and an accurate method to predict the flow velocity. Such a device was designed and documented in Wilson [60]. Figure 4.3.2 shows a schematic of the calibration system.

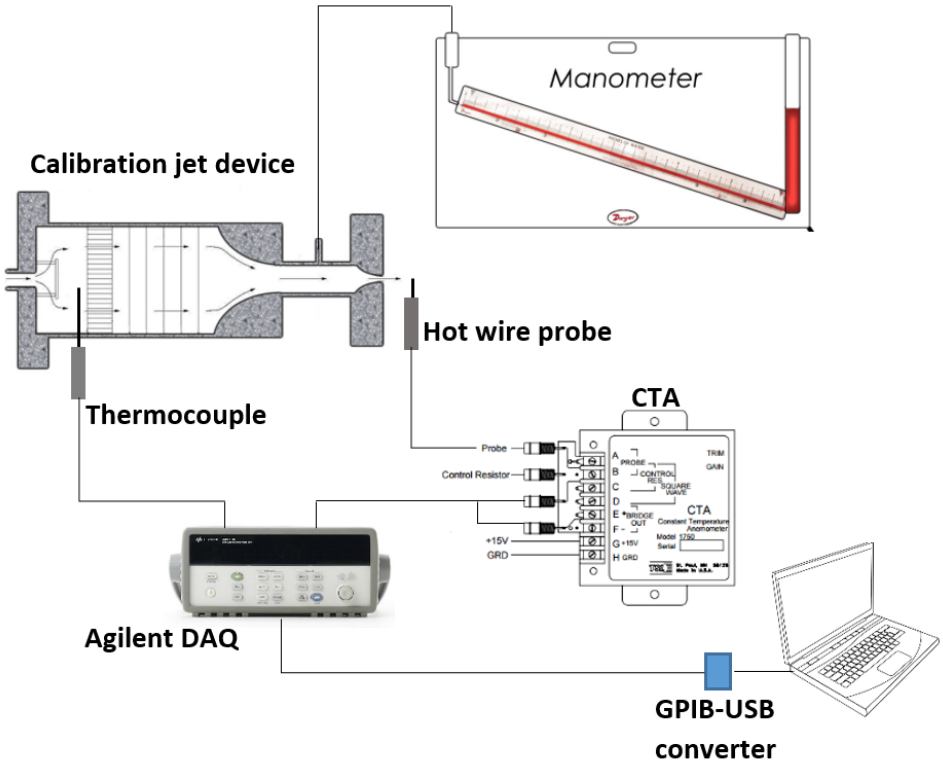

Figure 4.3.2 Hot-wire calibration setup [52]

The flow for the calibration jet is generated by using pressurized air. The flow velocity is controlled using a series of coarse and fine valves. These are followed by flow straighteners and then a porous, sintered plate that makes the flow uniform downstream. Downstream of that, a series of screens are present, at the end of which, an elliptical profile contraction nozzle is attached. This is done to dampen the turbulence of the flow and accelerate it. Another elliptical profile contraction nozzle is located slightly downstream of this location. This nozzle makes the flow uniform so that when the flow

exits this nozzle (which is also the exit of the whole calibration setup), the velocity has a flat profile.

Between the two elliptical contractions mentioned above is a chamber in which a pressure static tube and a thermocouple are introduced in the flow. The static pressure of the calibration jet is measured by the pressure static tube while the total pressure of the calibration jet is computed from the ambient pressure, as the jet is exiting into the atmosphere with minimal losses between the chamber and the ambient. This information can be used to calculate the dynamic pressure that can be used to calculate the jet velocity. Very small corrections for non-ideal behavior are given with the facility. The fluid properties required for this calculation can be found using the temperature and room humidity measurements taken simultaneously.

Keysight 34465A data acquisition unit is used to collect and store the data. The static pressure tube is attached to the inclined manometer (explained in section 4.2.1) on one of its ends while the other end is kept open to the atmosphere, to measure the dynamic pressure of the flow. Temperature is measured using a type-E thermocouple (explained in section 4.1).

Procedure and Results

The first step in the anemometer calibration is to check whether the anemometer is giving a correct response. This is done by giving a pulse wave of 1 kHz frequency and checking the anemometer's response on an oscilloscope. Once the response is satisfactory, the next step is to set the temperature of the hot-wire to 250°C. As the wire resistance is constant, the resistance of the connecting cable is varied until the desired hot-wire temperature is reached. When no sluggish response or ringing is observed, the anemometer performance can be considered to be optimum. For the calibration, the hot-

wire probe is held at the center of the exit of the nozzle of the calibration setup, with the hot-wire perpendicular to the incoming flow. The valves controlling the pressurized air in the calibration setup are used to vary the velocity of the flow. The range for the dynamic pressures for which the calibration was done is 0-1.32 inches of water column (0-329 Pa), with increments of 0.06 inches of water column (15 Pa). This pressure range corresponds to a range of velocity of 0-24 $m.s^{-1}$. As the approach flow is known to have an approximate velocity of 14 $m.s^{-1}$, this velocity range is appropriate. For every measurement point, the data were collected for 25 seconds with 2kHz frequency. Simultaneously, the temperature was measured for fluid property evaluation.

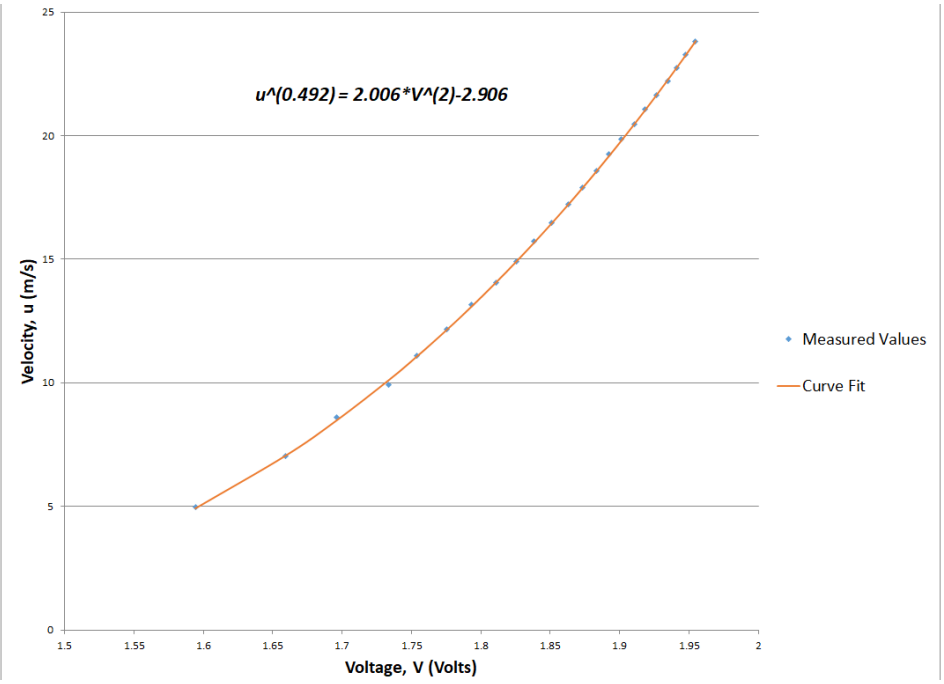

Figure 4.3.3 Calibration curve for the hot-wire used in this study

The voltage measured for each data point is plotted against the velocity calculated from the measured pressure. The plot is shown in fig. 4.3.3. The constant 'n' from equation 4.12, is 0.492, very close to the ideal value of 0.5. The curve-fit, done using a least-square fit method, shows good agreement with the measured values. The uncertainty in velocity was found to be 3.8% within a 95% confidence interval (see Appendix A for calculations).

Chapter 5. Experimental Procedure

The aim of this experiment is to find how the interactions between mainstream and coolant streams affect coolant coverage on the endwall and vane surfaces; essentially, how cooling effects change when the flow rates of the coolant streams are changed. Therefore, an extensive set of thermal and aerodynamic measurements in the vane passage is required. This chapter will explain the cases that were chosen for this study, as well as the locations where the measurements were taken.

5.1. Experimental Cases

It is suspected that, in the engine, three coolant streams are helping cool the endwall. These are: effusion coolant, louver coolant and film coolant. Their injection locations and functions are already outlined in chapter 3. The engine-representative mainstream to coolant mass flow rate ratio (MFR) for the combustor coolant (which consists of effusion coolant and louver coolant) is 5.03%, out of which, 4.66% is the effusion coolant while 0.37% is louver coolant. In this study, the louver coolant flow rates are changed while keeping the effusion coolant flow rate constant. There is a total of 3 louver coolant flow rates considered: 0.37%, 0.92% and 1.43%. Out of these, the case with 0.37% was already recorded and discussed by Alqefl [40] but the results are discussed in this study while making a direct comparison with the remaining two cases.

Originally, it was decided that for the 0.92% and 1.43% cases, three film cooling flow rate cases each, would be considered. These flow rates are 0% (i.e. no film coolant injection), 1% and 1.5%. However, after the data for the cases with louver cooling MFR of 0.92% were recorded and analyzed, it was found that a film cooling flow rate rising to 1.5% was reducing cooling performance. Therefore, for the cases with louver cooling MFR of 1.43%,

the case having the film cooling MFR of 1.5% was replaced with a case having the film cooling MFR of 0.5%, a decision that proved correct after analyzing those results.

Table 5.1.1 presents the test matrix and the nomenclature of all the cases studied. The case nomenclature is based on the film cooling MFR and the louver cooling MFR as these two parameters were changed in the study. The letter 'L' corresponds to louver coolant and the two numbers next to it correspond to the louver cooling MFR. For example, L09XXX will correspond to a case having louver cooling MFR of 0.92%. Similarly, the letter 'F' corresponds to the film coolant and the two numbers next to it correspond to the film cooling MFR. For example, XXXF05 corresponds to cases having film cooling MFR of 0.5%. Additionally, when a family of cases involving the same coolant MFR is to be referenced, it is referred to using a partial nomenclature. For example, if all cases having louver cooling MFR of 1.43% are to be referenced, they will be called the 'L14' cases and if all cases involving film coolant MFR of 0% are to be addressed, they will be called the 'F00' cases. This method is used for brevity.

Table 5.1.1 Test matrix and case nomenclature

<table>
<tr><th rowspan="2">Louver Cooling MFR</th><th rowspan="2">Type of Measurements</th><th colspan="4">Film Cooling MFR</th></tr>
<tr><th>0% (F00)</th><th>1% (F10)</th><th>1.5% (F15)</th><th>0.5% (F05)</th></tr>
<tr><td rowspan="2">0.37% (L04) *</td><td>Thermal</td><td rowspan="2">L04F00</td><td rowspan="2">L04F10</td><td rowspan="2">L04F15</td><td rowspan="4">Not Considered</td></tr>
<tr><td>Aerodynamic</td></tr>
<tr><td rowspan="2">0.92% (L09)</td><td>Thermal</td><td rowspan="2">L09F00</td><td rowspan="2">L09F10</td><td rowspan="2">L09F15</td></tr>
<tr><td>Aerodynamic</td></tr>
<tr><td rowspan="2">1.43% (L14)</td><td>Thermal</td><td rowspan="2">L14F00</td><td rowspan="2">L14F10</td><td rowspan="2">Not Considered</td><td rowspan="2">L14F05</td></tr>
<tr><td>Aerodynamic</td></tr>
</table>

* Recorded and discussed in Alqefl [40]

5.2. Aerodynamic Measurement Procedure

The aerodynamic data consist of measuring the flow velocity as well as the flow angles, in the vane passage. These data are important to understand the coolant transport through the passage so that it can be correlated with the coolant effectiveness measurements. The aerodynamic data are recorded at four axial planes and one streamline-normal plane in one of the vane passages. The locations of these planes are shown in fig. 5.2.1. The plane direction is coming out of the paper in the spanwise direction (Z) while the vertical direction is the pitch-wise direction (Y) and the horizontal direction is axial (X). The flow direction is from left to right. The measurements in the span direction are taken for one-half of the span length at the axial location of the plane being measured. A total of 21 data points was measured for every spanwise row, while the number of data points in the pitch direction varied from 13 to 20 based on the axial location of the plane. The axial locations of the planes and the number of data points recorded on that plane are documented in table 5.2.1.

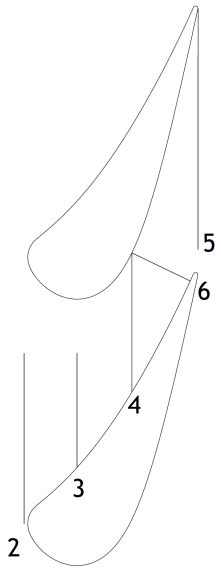

Figure 5.2.1 Aerodynamic measurement planes location. Plane numbers are displayed near the suction surface.

Table 5.2.1 Aerodynamic measurement planes information

	Axial Planes				Stream-Normal Plane
Plane Number	2	3	4	5	6
Location (x/C_{ax})	-0.02	0.289	0.612	1.02	0.612
Measurement Points	13	13	17	20	16

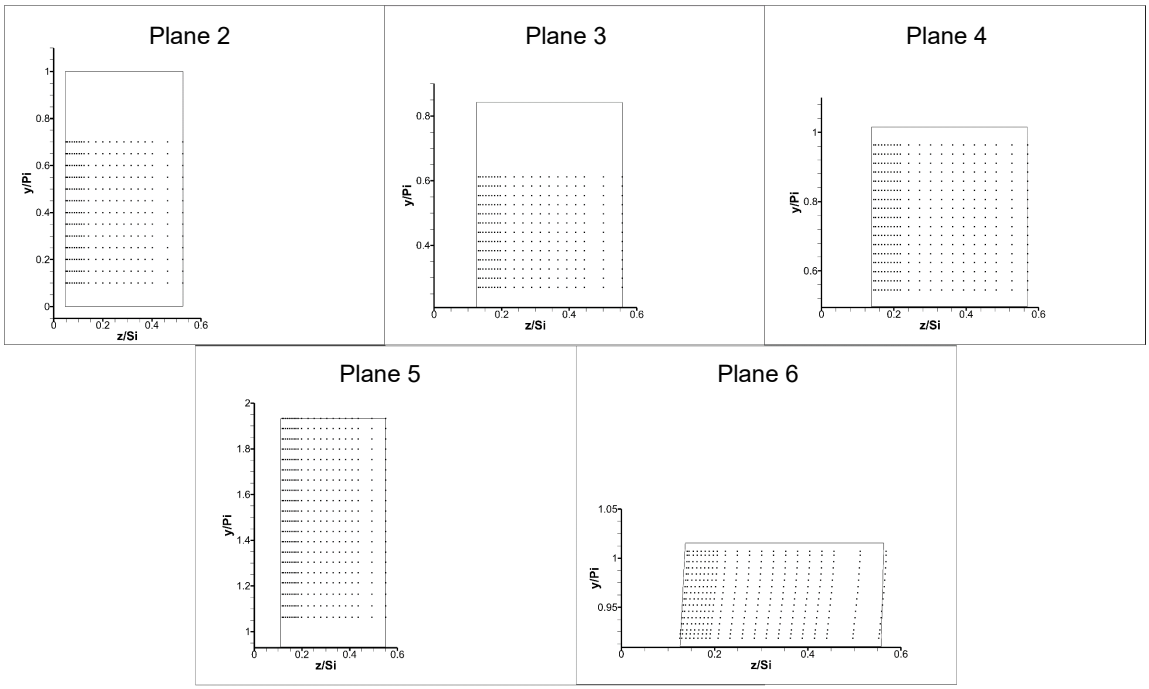

Figure 5.2.2 Measurement grid for aerodynamic measurements

The actual locations where the data were taken for each plane, are shown in fig. 5.2.2. The z and y axes are non-dimensionalized by the inlet span (Si) and inlet pitch (Pi), respectively. The five-hole probe does not give correct results when it is very close to the wall because the pressure sensed in the flanking hole nearest to the wall is affected by the proximity to the wall. Hence, the first span point for the velocity measurements starts slightly away from the endwall, as well as from the pressure and suction surfaces. Also, for planes 2 and 3, some data near the suction surface are not taken, as shown in fig. 5.2.2. This is a test facility limitation in that the five-hole probe cannot reach these data points. Additionally, for plane 2, some data points very close to the leading edge (y/Pi = 0)

are not shown. These data were recorded, but as the flow in this region is highly variable, the five-hole probe readings were considered to not be correct. Therefore, these data were chosen to not be plotted in the results section. Similarly, for the exit plane (plane 5), the flow near the pressure surface is part of the wake region and therefore, doesn't reflect the flow physics of the actual engine. Therefore, these data also are not plotted. Based on Alqefl [40] results, which had the same cascade and the same locations, the data not plotted for planes 2 and 5 had not revealed any important information; therefore, they were not presented in this this study as well.

Using the calibration results of the five-hole probe presented in section 4.2.3, the pressures recorded by the five holes of the five-hole probe can be converted into velocity. The Cp_{pitch} and Cp_{yaw} values, calculated from the pressures measured, can be used to calculate Cp_{static} and Cp_{total}, using the contour-fits shown in fig. 4.2.8 and 4.2.9. These two coefficients give total pressure (P_t) and static pressure (P_s), which can be used to calculate the velocity magnitudes by the following formula:

$$V = \sqrt{\frac{2 * (P_t - P_s)}{\rho}} \qquad Equation\ 5.1$$

The next step is to calculate the flow angles used to calculate the velocity components. The pitch (α) and yaw (γ) angles are calculated by first calculating the pressure coefficients and then using the contour-fit. The velocity component equations, which were proven in Treaster and Yocum [56] are used, although the nomenclature for the flow angles used in their paper is opposite to that of the nomenclature used in the current study. The equations for velocity components in the current test section reference co-ordinates are given below:

$$V_X = V * \cos(\alpha) * \cos(\gamma) \qquad Equation\ 5.2$$

$$V_Y = V * \cos(\gamma) * \sin(\alpha) \qquad Equation\ 5.3$$

$$V_Z = V * \sin(\gamma) \qquad Equation\ 5.4$$

It is known that the vane passage has several vortices. Therefore, vorticity plots are required to determine coolant transport. In order to plot the vorticity, secondary flows are needed. Secondary flow at a location can be defined as any deviation of flow at that location from the bulk-flow streamline at that streamwise location. This requires determining the streamlines. The coolant streams affect the area near the endwall and the vane surfaces, predominantly. Hence, the flow near the mid-span, mid-pitch location is expected to remain relatively unaffected by coolant flows. In other words, with the exception of the flow near the endwall, the bulk flow will follow the passage turning. Therefore, flow vector measured at a mid-pitch, mid-span location at a streamwise location can represent the streamline at that streamwise location. Secondary flows will be defined as the velocity vectors that have deviated from this streamline.

Equations 5.2 through 5.4 give the velocity components with respect to the test section co-ordinate system (X=axial, Y=pitchwise, Z=spanwise). The velocity vector with respect to this co-ordinate system is known from the measurements. The secondary flow components of this velocity vector are found by considering a modified co-ordinate system that is defined based on the streamline vector (see X_S and Y_S in fig. 5.2.3).

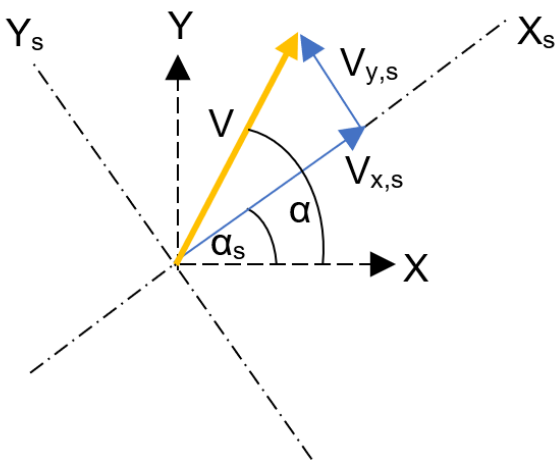

Figure 5.2.3 Streamline coordinates for secondary flow analysis

Figure 5.2.3 shows how the velocity vector at any measurement location is used to calculate the flow deviation in the axial (X) and pitch-wise (Y) directions. While 'X' and 'Y' represent the coordinate system of the test facility, 'X_s' represents the direction of the mid-span, mid-pitch velocity vector and 'Y_s' represents the direction perpendicular to the streamline vector on the X-Y plane. Also, 'α' represents the pitch angle of the velocity vector under consideration from the test facility axes while 'α_s' represents the pitch angle of the velocity vector at the mid-span, mid-pitch location with respect to the test facility axes. Therefore, to calculate the secondary flow velocity vector of the given velocity ('V' in the figure), the equations 5.2 through 5.4 are modified as follows:

$$V_{X,S} = V * \cos(\alpha - \alpha_s) * \cos(\gamma - \gamma_s) \qquad Equation\ 5.5$$

$$V_{Y,S} = V * \cos(\gamma - \gamma_s) * \sin(\alpha - \alpha_s) \qquad Equation\ 5.6$$

$$V_{Z,S} = V * \sin(\gamma - \gamma_s) \qquad Equation\ 5.7$$

In this way, the secondary flow velocities are calculated and used to plot vorticity contours. There is a chance that the mid-span, mid-pitch velocity vectors may not be exact representations of the streamlines at a particular plane and this would mean that some

features may not be precisely represented according to the above definition on the velocity vector and vorticity plots. However, Alqefl [40] calculated the secondary flow vectors with a variety of streamline pitch and yaw angles in the vicinity of flow angles for the mid-pitch and mid-yaw velocity vectors for every plane. He found that none of the aerodynamic plots showed any new features and the clarity of existing features didn't change much, with changes in the reference streamline angle. Therefore, he concluded that using the angles of the mid-span, mid-pitch velocity vectors, as reference angles for presenting secondary flow vectors, was justified. The uncertainty in the absolute velocity was found to be 2.5% and the uncertainty in the pitch and yaw angles was found to be 2°, within a 95% confidence interval (see Appendix A for detailed calculations).

5.3. Thermal Measurement Procedure

The thermal measurements involve two different types of data analyses. The first are the temperature recovery measurements taken in the passage (henceforth called in-field measurements) and the second are the surface cooling effectiveness measurements taken on the endwall and vane surfaces (henceforth called surface measurements). Both types require data taken by the same instrument, the thermocouple, but the dimensionless quantities derived from these measurements have slightly different meanings. Therefore, they are explained individually in the following sections.

For identifying the cooling effectiveness of the coolant streams, the injected coolant is heated about 15°C above the temperature of the mainstream. Here, the coolant is only used as a marker and no heat flux measurements are taken. The coolant and mainstream temperatures are used to calculate a non-dimensional cooling effectiveness. All coolants are to be at the same temperature during the experiments, the maximum difference between coolant streams was 0.15°C. As absolute temperatures are not used for the

calculations, the uncertainty is calculated for the dimensionless temperature parameters. This uncertainty is 8.5% within 95% confidence interval (see Appendix A for detailed calculations).

5.3.1. Surface Thermal Measurement Procedure

To adequately capture the cooling effectiveness on the endwall, a suitable measurement grid is required. As one of the cases considered in this study was part of Alqefl [40] study and because the results found in that study showed the major features distinctly, the measurement locations of Alqefl's study were used in the present study. Although Alqefl did not study the vane surface effectiveness, it was assumed that a measurement grid having the same axial locations as those for the endwall measurement grid and the same number of span-wise locations as for the thermal in-field measurements (explained in the following section) was suitable.

Endwall Measurement Grid

Each axial location considered for measurement is called a 'station.' A total of 14 stations were considered for this study. Out of these stations, 12 have measurement locations in the pitch direction ranging from the suction surface to the pressure surface (i.e. across the whole passage pitch) while two measurement stations were added later. Those have points near the suction surface, as some flow features were suspected to have been missed due to a lack of data in that region. The stations are shown in fig. 5.3.1 (a) and their information is tabulated in table 5.3.1. In the table, the measurement points correspond to the number of points in the pitch (Y) direction. The station angle in the table is related to the in-field thermal measurements as is explained in the following section.

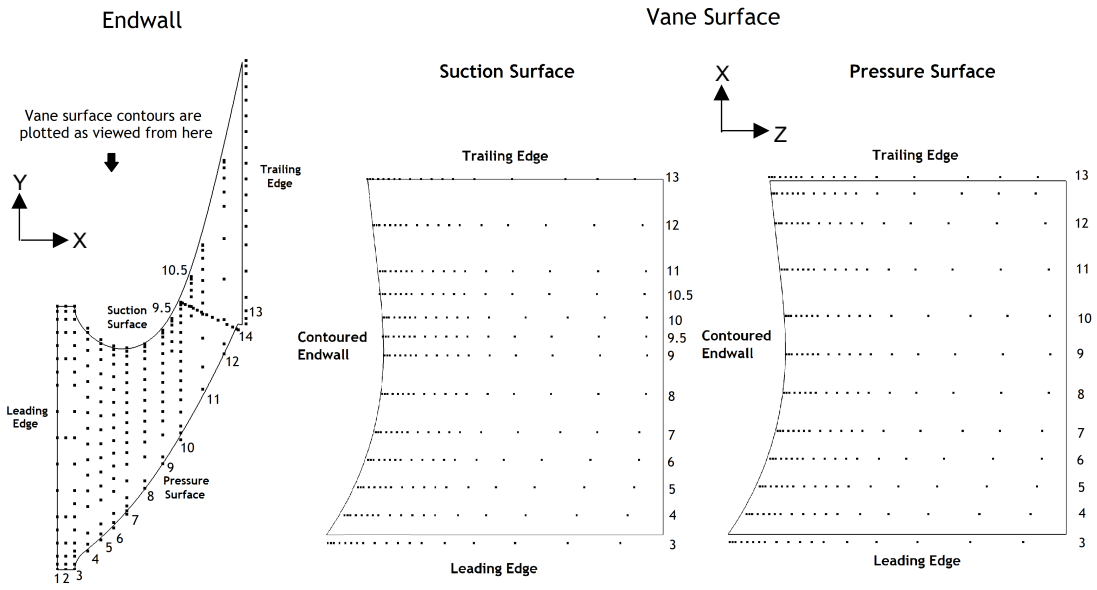

Figure 5.3.1 Surface effectiveness measurement locations: (L-R) (a) Endwall, (b) Vane suction surface, (c) Vane pressure surface. Station numbers are also noted for every axial location

Vane Surface Measurement Grid

As stated before, axial locations for the surface measurements are the same as for the endwall measurements. For each axial location, 18 points in the spanwise (z) direction (see figs. 5.3.1 (b) and (c)) are considered. For these measurements, it can be seen that the furthermost point away from the endwall in the spanwise direction is not at the same location for all stations. This is because the measurements were taken to the local mid-span of every station. As the local mid-span location changes due to the contoured endwall, the last data point also changes. The outermost boundary near the mid-span of the surfaces is drawn to include the furthermost point away from the endwall (which is present on station 9). Although, this means that most of the data very close to this boundary are extrapolated, it was found that the effectiveness near this location is already very close to zero and thus, has little importance.

Table 5.3.1 Endwall measurement stations information

	Endwall Measurement Stations							
Station	1	2	3	4	5	6	7	8
	(Plane 1)		(Plane 2)				(Plane 3)	
Location (x/C_{ax})	-0.104	-0.052	-0.02	0.056	0.134	0.212	0.289	0.397
Measurement Points	20	13	22	17	17	17	19	16
Station Angle	0°							

	Endwall Measurement Stations							
Station	9	9.5	10	10.5	11	12	13	14
			(Plane 4)				(Plane 5)	(Plane 6)
Location (x/C_{ax})	0.504	0.552	0.612	0.677	0.742	0.871	1.02	0.612
Measurement Points	16	5	17	7	12	11	19	14
Station Angle	0°							64.25°

Surface Effectiveness Calculation

Surface temperatures were taken from measurements in the near-wall, zero-temperature-gradient region. These temperatures are non-dimensionalized to calculate the adiabatic cooling effectiveness, η, using the following formula:

$$\eta = \frac{T_{(x,y)} - T_\infty}{T_C - T_\infty} \qquad Equation\ 5.8$$

Where $T_{(x,y)}$ represents the near-surface data measured by the thermocouple at location (x,y), T_∞ is the temperature of the mainstream and T_C is the coolant temperature at injection.

5.3.2. In-field Thermal Measurement Procedure

As finding the relationship between coolant transport and coolant coverage is the aim of this study, all planes where the aerodynamic data were taken (shown in fig. 5.2.1) were locations where thermal measurements were taken. Studying multiple planes throughout

the passage show how the coolant loses its effectiveness as it moves through the passage. An additional plane called plane 1, located at x/C_{ax} = -0.104, was also considered for thermal measurements. The information of all thermal planes is documented in table 5.3.1. A total of six planes, corresponding to stations 1, 3, 7, 10, 13 and 14 were measured. Figure 5.3.2 shows the axial locations of the planes. The solid black lines represent the plane locations. The grey centerlines show the locations of additional stations where surface measurements were taken for reference. For each plane, the measurements were taken up to 32% of the span, measured from the contoured endwall. That is where the thermocouple temperature becomes equal to the mainstream temperature i.e. the recovery coefficient drops to zero. However, near the pressure side, for higher film coolant MFR values, we see that the coolant spreads up to the mid-span. So, that region has measurements taken up to 50% of the span. Figure 5.3.3 shows the actual measurement locations for all thermal planes.

The loss of coolant effectiveness can be quantified by calculating a non-dimensional temperature recovery coefficient, θ. This is calculated by the same equation that was used for calculating the cooling effectiveness. But its physical significance is different. While the cooling effectiveness is measured on the surfaces and represents how effectively the surfaces are cooled, the recovery coefficient shows the cooling ability of the coolant (concentration of coolant) at the measured location compared to its cooling ability at the injection location (entirely coolant). The equation for calculating the recovery coefficient is:

$$\theta = \frac{T_{(x,y)} - T_{\infty}}{T_C - T_{\infty}} \qquad Equation\ 5.9$$

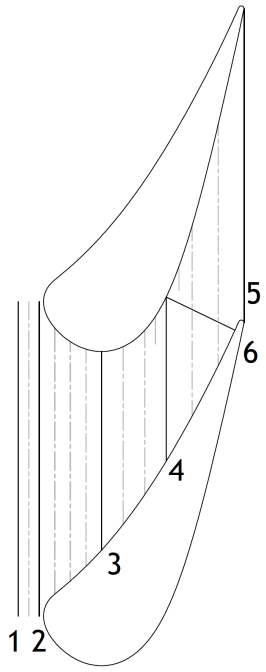

Figure 5.3.2 Thermal measurement planes locations. Plane numbers are displayed near the suction surface.

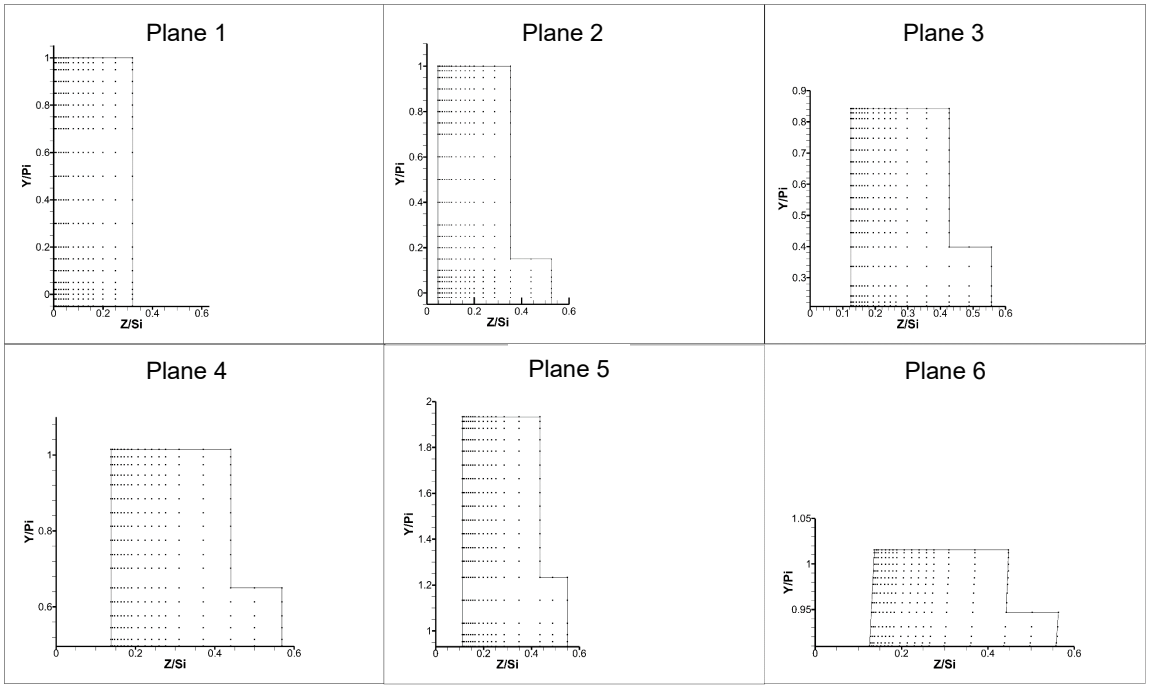

Figure 5.3.3 Measurement grid for thermal measurements. Note the additional data points in span (z) direction near the pressure surface

Chapter 6. Test Section Qualification

Test section qualification is important as it verifies whether the experiments are being conducted under suitable conditions. Therefore, verification is done before doing the actual experiments. For the current test facility, the qualification procedures performed are listed below:

1. Measuring the cascade Reynolds number of the flow upstream of the measurement region to ensure that the high Reynolds number conditions, like the engine, are met
2. Adjusting the tailboards in a way that matches static pressure profiles of the vane surfaces of the two passages to ensure periodicity
3. Reporting the approach flow velocity contours and turbulence features to verify that they match the engine conditions, as we know them
4. Qualifying the adiabatic endwall characteristics and documenting the thermal profile of the approach flow

6.1. Cascade Reynolds Number

Having a high Reynolds number at the passage inlet is a feature of the engine requiring matching. Achieving similar values is important as the viscous effects at Reynolds numbers higher than 350,000, based on the vane chord length, are minimal. The design Reynolds number of the engine is ~400,000. The first step in measuring the Reynolds number is measuring the flow velocity. The velocity is calculated by measuring the dynamic pressure of the flow using a pitot static tube. The pitot static tube can measure both the static pressure as well as the total pressure of the flow. If the two ends of this tube are connected to a manometer, the manometer will show the dynamic pressure. This can be used to compute the velocity. The dynamic pressure measurement was made at

the passage exit. Then, the ratio of the passage exit area and the approach plane area was used to calculate the flow velocity at the approach plane. The fluid properties were calculated based on the temperature measurements (explained in section 6.4) taken at the same plane. The following equation was used to calculate the Reynolds number.

$$Inlet\ Re_{chord} = \frac{\rho * V * C}{\mu} \qquad Equation\ 6.1$$

Where 'ρ' is the density of the working fluid (air), 'V' is the flow velocity at the approach plane, 'C' is the vane true chord length and 'μ' is dynamic viscosity of the working fluid.

Results

The Reynolds number based on the calculations explained in the above paragraph was found to be 385,000. Later, when the aerodynamic measurements were conducted, five-hole probe measurements were taken at the exit plane and, based on the average velocity found in the exit plane, the cascade Reynolds number was calculated again. This came out to be 393,000. The two values are very close to each other, well above the 350,000 threshold and very close to the design Reynolds number. Therefore, the test section satisfies the Reynolds number requirement.

6.2. Vane Passage Periodicity

The current test section has two passages. In order to ensure that it can represent an annular rig, the flow going through both passages should be the same. This is tested by measuring the static pressures at the midspan along the vane surfaces and matching the respective pressure profiles of the suction and pressure surfaces. The downstream tailboards are adjusted until the two pressure profiles match.

Static pressure taps, installed at the mid-span location along the vane surfaces, are used to measure the static pressure profiles. Their positions are explained in section 3.4.3. The

taps are connected, using tygon tubes, to a pneumatic switchboard having individual switches for each pressure tap. When the switch for one of the taps is turned on, the pressure in the corresponding tygon tube is transmitted to one end of a DP 15 transducer (working principle explained in section 4.2.2). The other input to the transducer is a reference pressure. This reference is one of the static pressure taps. An ambient pressure reference is not used, as the ambient pressure can change while taking measurements. On the other hand, any transient changes inside the tunnel will be experienced by both the reference pressure tap and the airfoil surface pressure. Therefore, small changes in passage pressure will not affect the static pressure profiles.

The pressure profiles are measured for four surfaces: (1) suction surface of the top vane, (2) pressure surface of the middle vane, (3) suction surface of the middle vane, and (4) pressure surface of the bottom vane (see fig. 6.2.1 for vane geometry). The static pressure profiles of (1) and (3) and the static pressure profiles of (2) and (4) must match one another. The pressure data are non-dimensionalized to pressure coefficients defined as:

$$C_p = \frac{P_s(x) - P_{sp}}{0.5 * \rho * U_{exit}^2} \qquad Equation\ 6.2$$

Where P_s (x) is the static pressure tap located at the axial co-ordinate 'x,' P_{sp} is the vane stagnation pressure and U_{exit} is the passage exit velocity (measured by pitot static tube).

The pressure profile is presented in fig. 6.2.1. The profiles match except the region near X/C_{ax} = 0.6, which shows a slight mismatch. However, as the profiles near other locations show very good matches, the small local mismatch is considered to not very significant.

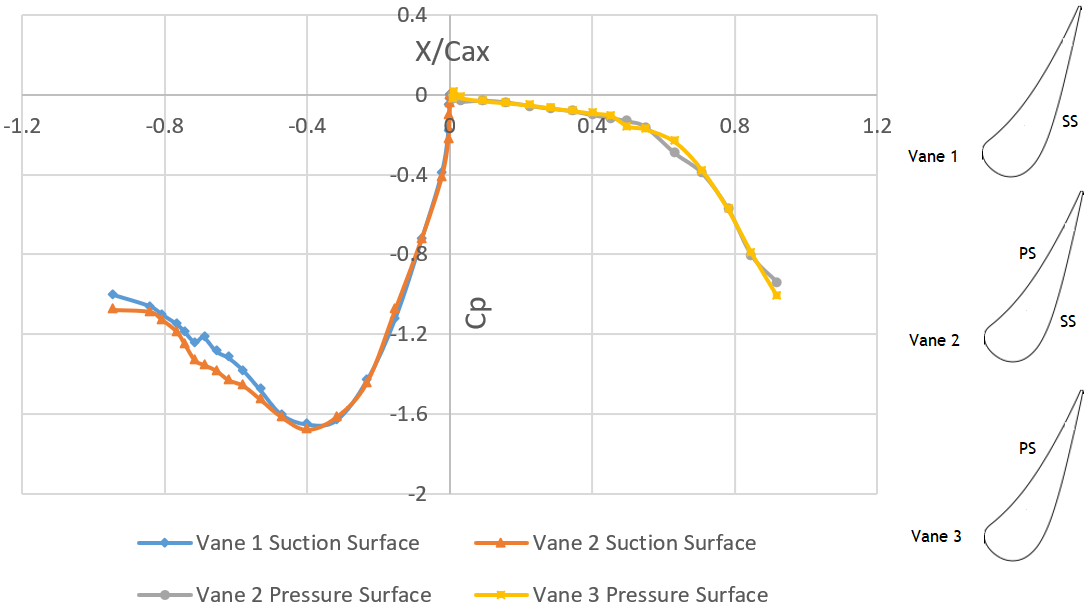

Figure 6.2.1 Static pressure profile of vane surfaces

6.3. Approach Flow Velocity and Turbulence Features

Characterizing mean velocity and turbulence is important as the turbulence influences the secondary flow and how the coolant transports in the passage. The approach flow plane is located 10 mm upstream of the end of the effusion wall (shown in fig. 6.3.1). This location was chosen because the flow is expected to have minimum three-dimensionality there as most of the flow will be axial. Also, as there are no sharp gradients in the geometry upstream, for some length, no separation is expected.

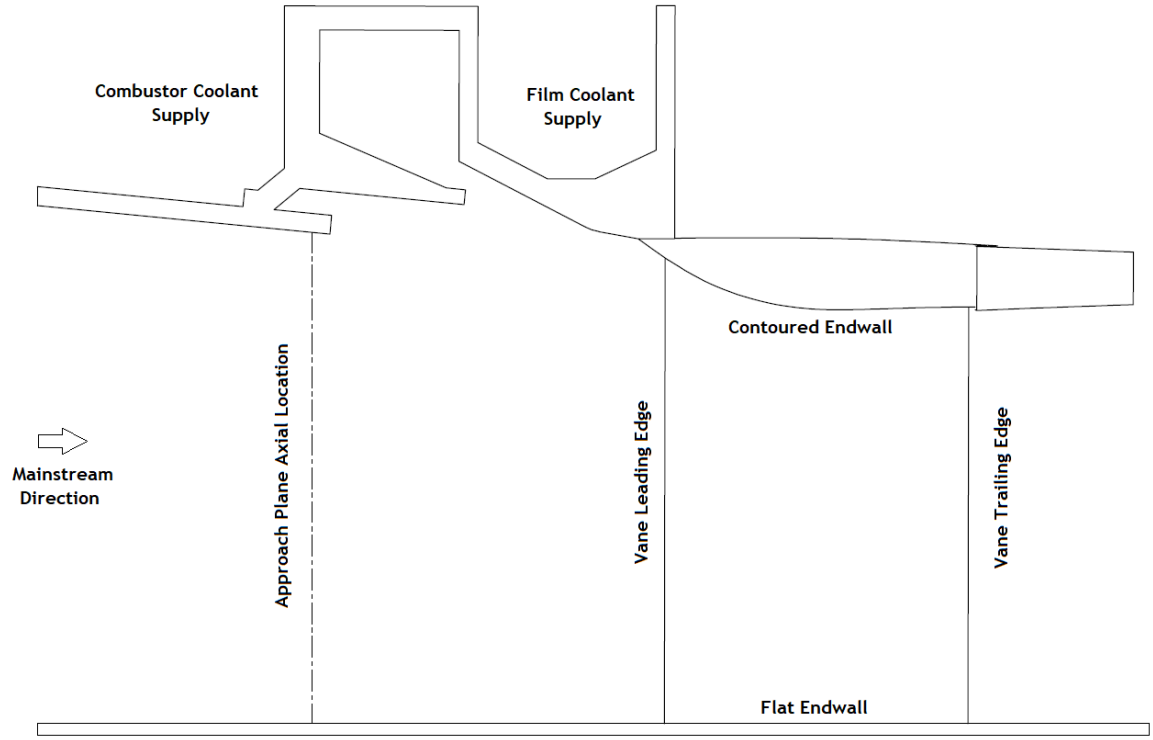

Figure 6.3.1 Axial location of the approach flow characterization plane

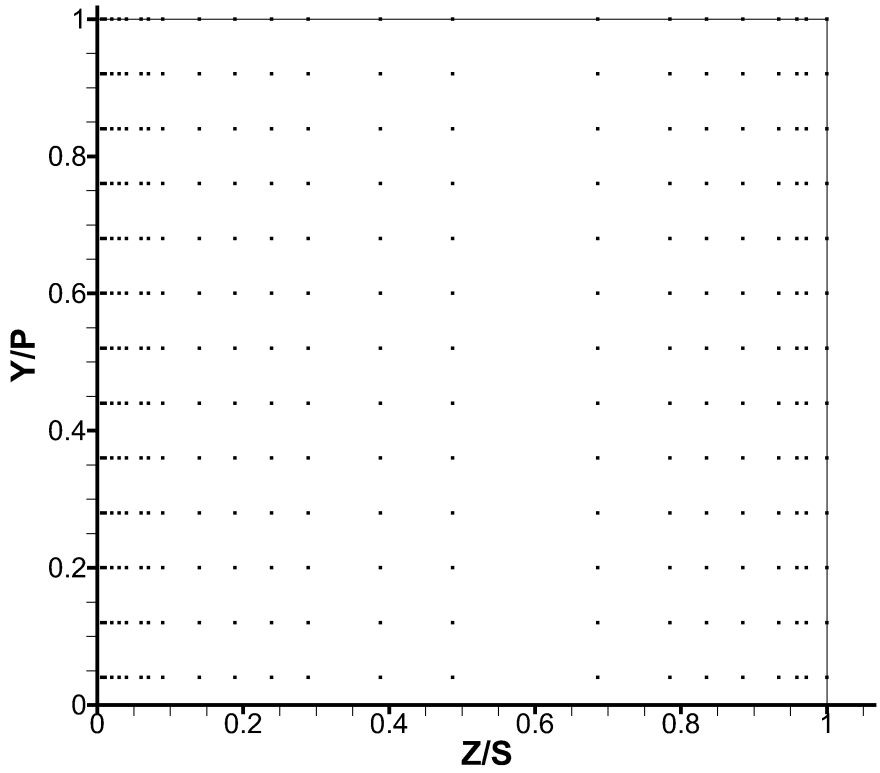

Figure 6.3.2 Velocity measurement locations for the approach flow characterization plane

6.3.1. Mean Velocity and Turbulence Intensity

Mean velocity is measured by hot-wire anemometry (instrumentation explained in section 4.3.2). The velocity measurement grid is shown in fig. 6.3.2. It consists of 14 pitchwise rows with every row having 23 span points. The measurements are taken for 1 pitch and for the whole span of the test facility. Each measurement is taken for 25 seconds with a frequency of 2 kHz using the Keysight 34465A data acquisition unit. Parameters calculated based on these measurements are mean velocity, '$\overline{U}$(y,z),' RMS fluctuation about mean velocity 'u_{rms}(y,z),' and turbulence intensity, 'Tu (y,z)' (in percent), at the chosen location (y,z). Equations for these parameters are:

$$\overline{U}(\mathrm{y},\mathrm{z}) = \frac{1}{N} * \sum_{1}^{N} u(y,z,t) \qquad Equation\ 6.3$$

$$u_{rms}(y,z) = \sqrt{\frac{1}{N} * \sum_{1}^{N} \left(u(y,z,t) - \overline{U}(\mathrm{y},\mathrm{z})\right)^2} \qquad Equation\ 6.4$$

$$Tu(y,z) = \frac{u_{rms}(y,z)}{\overline{U}(\mathrm{y},\mathrm{z})} * 100 \qquad Equation\ 6.5$$

Where 'N' is the number of samples collected over the recording time (25 seconds), 'u(y,z,t)' is the velocity at every measured coordinate (y,z) averaged over time 't'.

Results

Figure 6.3.3 shows the mean velocity contours. The core velocities are close to 14 m.s^{-1} while the velocities near the contoured endwall are elevated to be as high as 20 m.s^{-1}, due to the additional flow rate provided by the effusion coolant. Uniformity of velocities in the pitch direction as well as in the span direction at locations away from the endwall can be seen. This shows that the approach flow is satisfactory for the experiments.

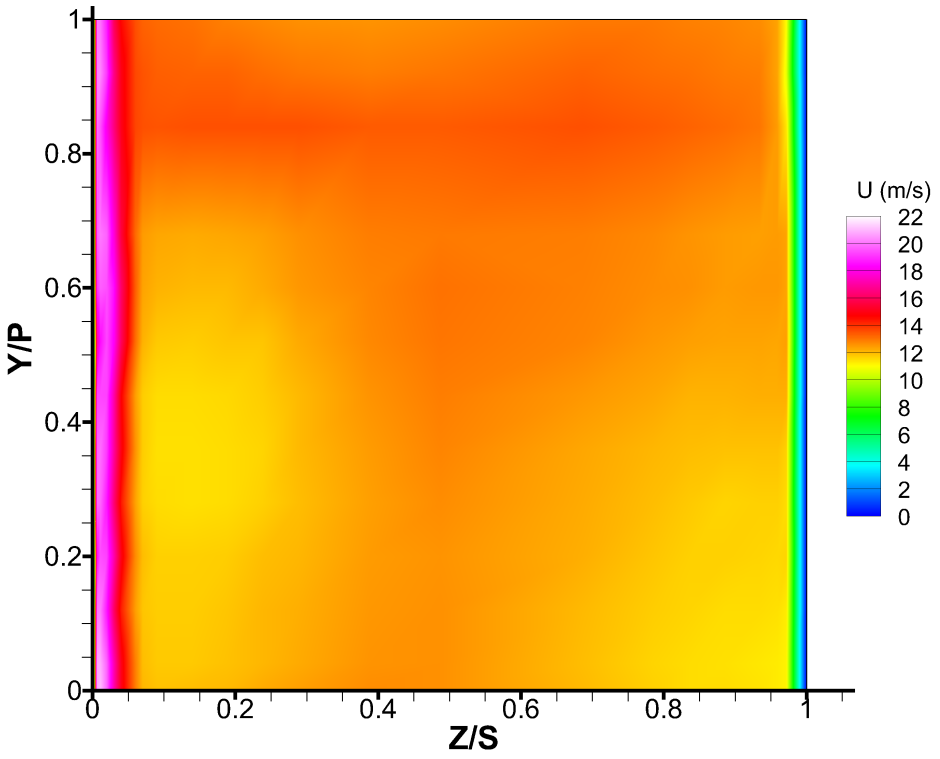

Figure 6.3.3 Mean velocity distribution of the approach flow characterization plane

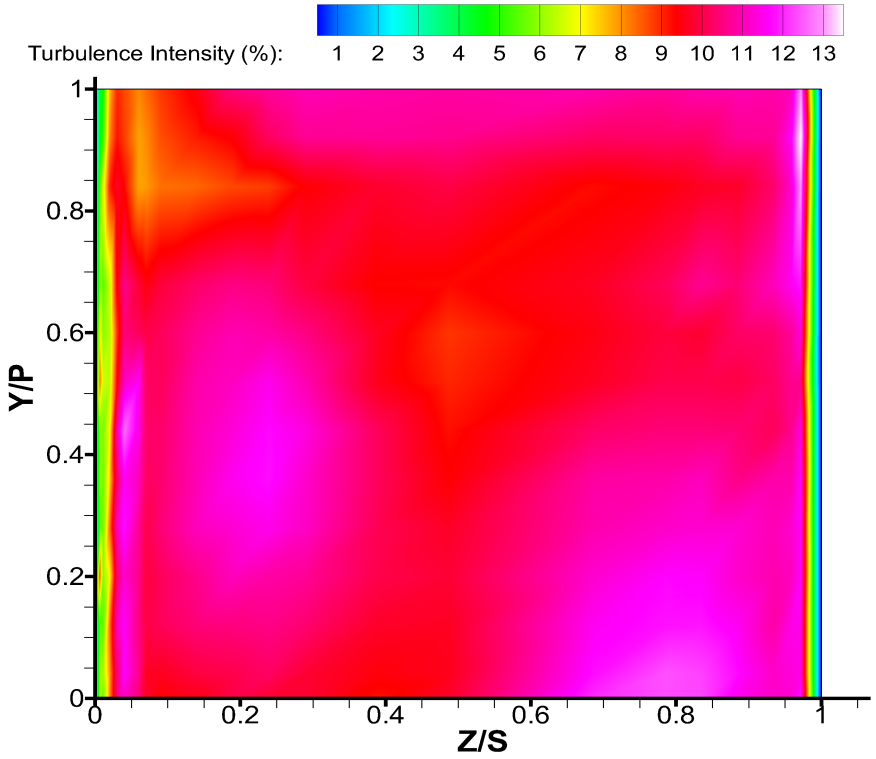

Figure 6.3.4 Turbulence intensity distribution of the approach flow characterization plane

The turbulence intensity contour is shown in fig. 6.3.4. Average turbulence intensity seen on the approach plane is about 10.2% with slightly higher values (around 13%) near the suction side. Also, near the contoured endwall, the turbulence intensity is decreased to around 7% due to the higher velocities in this region. Overall, the turbulence intensities are high enough, and satisfy the qualification requirements.

6.3.2. Energy Density Spectrum and Turbulence Length Scales Calculations

While turbulence intensity gives a very general idea of the turbulence present in the flow, it is not enough to characterize the turbulence sufficiently. In low-NO_x combustors, large eddies are generated that do not dissipate quickly and greatly affect the flow in the vane passage. This would change the coolant transport, greatly changing the coolant coverage when compared to a low-turbulence generator. Therefore, the turbulence generator was designed as explained in section 3.2. It is necessary to verify that the turbulence generated by it is according to the test condition requirements.

Using the high-frequency measurements taken by hot-wire anemometry, the turbulence kinetic energy spectrum can be easily plotted, and various turbulence length scales can be calculated. The hot-wire measurements are taken at 2 kHz for 25 seconds. Based on the previous experiments in this wind tunnel [51,52,40], this frequency is sufficient to capture the eddies in the inertial sub-range of the turbulence spectrum.

For the spectral analysis, the measurements taken at a single location over a time interval can be used to find the turbulence characteristics based on Taylor's 'frozen turbulence' hypothesis. The mean velocity can be calculated using equation 6.6, while the velocity fluctuations are calculated using equation 6.7.

$$\overline{U} = \frac{1}{N} * \sum_{0}^{N} u(t) \qquad Equation\ 6.6$$

$$u'(t) = u(t) - \overline{U} \qquad Equation\ 6.7$$

Where N is the number of samples taken (50,000) at the location chosen for turbulence measurements.

Next step is to convert the velocity fluctuations, which are in a time-domain, into a frequency-domain using a Fast Fourier Transform (FFT). MATLAB has a predefined function that can directly convert the velocity data into frequency domain data by FFT. The transformation is done using the following equation:

$$f_k[w_k] = \frac{1}{\sqrt{N}} * \left(\sum_{n=1}^{N} u'_n * \ e^{i\left(\frac{2\pi n}{N}\right)k} \right) \qquad Equation\ 6.8$$

Where, 'f_k' is the transformed coefficient indexed with k and is a function of 'w_k,' 'w_k' is fluctuation frequency, 'u_n' is velocity fluctuation about the mean, 'N' is the number of samples of u' over t=60 seconds, 'n' is 'u_n' sample number (n=1,2,3, … N).

The term 'f_k' is a complex number with its real part describing the amplitude and the imaginary part describing the phase difference between 'k' and the velocity fluctuation at time equal to 0 seconds (u'[0]). Based on this transformation, the energy density function E(ω) can be evaluated as follows:

$$E[w] = \frac{2\left(f_{real}[w]^2 + f_{imag}[w]^2\right)}{w_s} \qquad Equation\ 6.9$$

Where 'w_s' is the sampling frequency and 'w' is the fluctuation frequency defined as:

$$w = \frac{w_s k}{N} \qquad Equation\ 6.10$$

The frequency domain data obtained can be used to plot the kinetic energy density spectrum (EDS). This plot shows the quantity of kinetic energy present in the flow at different frequencies, on a log-log scale. Different eddy sizes, which represent various

turbulence length scales, can be calculated using this plot. Generally, the larger eddies occur at lower frequencies and smaller eddies occur at higher frequencies. This is expected as larger eddies take more time to pass over the hot-wire, thus decreasing their frequencies.

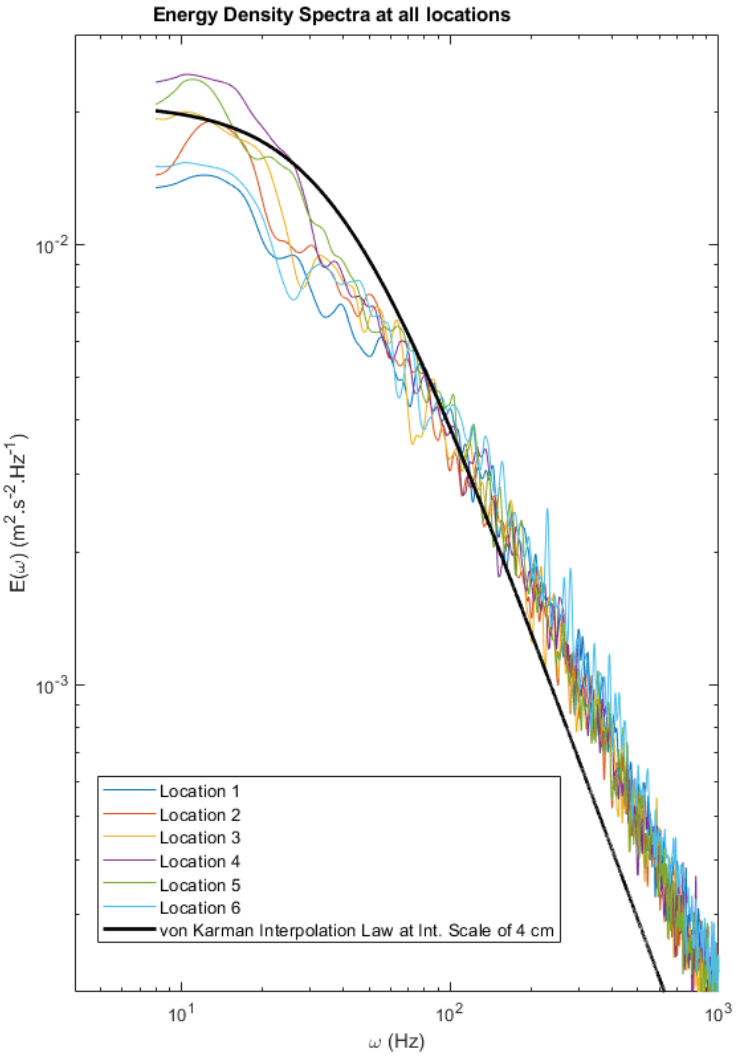

Figure 6.3.5 Energy density spectra measured at multiple locations on the approach flow characterization plane

For the current study, EDS is plotted in fig. 6.3.5. Spectra for many locations were studied and six random locations were chosen to plot the spectra in the figure. It can be seen that, except for very low frequencies, all spectra are generally in good agreement. At frequencies lower than 10 Hz, it is quite possible that the fluctuations recorded were due

to some unsteadiness present in the wind tunnel, rather than due to turbulence. Hence, data recorded for frequencies below 10 Hz were not plotted. Also, the low frequency data have very few realizations at those frequencies, so scatter is expected. A longer record would reduce this low-frequency variability, but more accurate characterization of this portion of the spectrum was considered to be unnecessary. An empirical spectrum was also plotted, based on the von Karman interpolation law, which is explained later. Based on the spectra, the turbulence length scales can now be determined.

Integral Length Scale, Λ

The integral length scale is defined as the size of the largest eddies present in the flow. On the spectrum, they are represented by the flat region in the low frequency region. The length scale is calculated using the following relation, given by Hinze [61],

$$\Lambda = \frac{\overline{U}}{4} * \lim_{\omega \to 0} \frac{E(\omega)}{u'^2} \qquad Equation\ 6.11$$

The limit in the above equation points out that only the region having very high energy should be considered. Therefore, only the measured points having frequency below 1 Hz are considered to get the E(ω). But, due to the number of such points being very low and the aforementioned unsteadiness present in the wind tunnel, the calculation involves significant uncertainty. Also, the value of the integral length scale is highly dependent on the location where the measurement was taken. The measurement points considered while plotting fig. 6.3.5 ranged from the center of the whole plane to near the endwall and the vane surfaces. For these locations, the calculated integral length scale varied from 3 cm to 8 cm.

To get a more certain number for the integral length scale, an empirical formula, known as the 'von Karman Interpolation Law' was used to calculate a spectrum. The relation to calculate E(ω) by this law is given below [62]:

$$E(\omega) = \frac{4 * u'^2 * \Lambda}{\bar{U} * \left\{1 + \left(\frac{8 * \pi * \omega * \Lambda}{3 * \bar{U}}\right)^2\right\}^{5/6}} \qquad Equation\ 6.12$$

The above equation requires integral length scale, Λ, as an input. The value of Λ is varied in equation 6.12 until a good fit was found with the middle frequency range of the measured spectrum. This region was chosen for fitting because the low frequency data has very few measured points while the very high frequency data may have aliasing error. The range of Λ, for which a good match was found for different locations, was 3 cm to 5 cm. The spectrum curve generated using an integral length scale of 4 cm is indicated by the black plotline in fig. 6.3.5. The von Karman interpolation law is more reliable than the measured values for the low frequency region of the spectrum. Therefore, instead of reporting the integral length scale calculated based on the measured values, a range is reported that was calculated based on the interpolation law. This range for integral length scale, Λ, is 3 cm to 5 cm. It should be noted that this was reported based on only some of the locations on the approach plane. Therefore, integral length scales beyond this range are still possible at some locations on the approach plane.

Energy Length Scale, Lu

The energy length scale represents an approximation of the size of the mean-energy-containing eddies in a turbulent flow. On the EDS plot, this region is seen where the kinetic energy starts dissipating. In this region, smaller eddies are feeding on the large eddies which have started to dissipate (~50Hz for this spectrum). To define the energy length scale, kinetic energy dissipation 'ε', must be defined. This term represents the rate at which

kinetic energy is converted into internal energy via viscous dissipation. For this region of the spectrum, also known as the inertial sub-range, Kolmogorov's famous 5/3^{rds} rule states that the kinetic energy, E(ω), is proportional to the -5/3^{rds} power of the wave number, k. The wave number is converted into the frequency, ω when the Fourier transformation is done. Therefore, in the frequency domain, the Kolmogorov relation looks as follows:

$$E(\omega) = \frac{18}{55} * A * \varepsilon^{2/3} * \omega^{-5/3} * \left(\frac{2 * \pi}{\bar{U}}\right)^{-2/3} \qquad Equation\ 6.13$$

The equation can be rearranged after taking a natural log on both sides,

$$\log\big(E(\omega)\big) = -\frac{5}{3} * \log(\omega) + \log\left(\frac{18}{55} * \left(\frac{2 * \pi}{\bar{U}}\right)^{-2/3} * A * \varepsilon^{2/3}\right) \qquad Equation\ 6.14$$

Where 'A' is a constant and equal to 1.62, according to Ames and Moffat [63].

As equation 6.14 is an equation of a line in the form '*y = m*x + c*', any one combination of E(ω) and ω can be used to evaluate the dissipation, ε. It was found to be 42.8 m^2.s^{-3}.

Now, the energy length scale, Lu, can be calculated using the relation given by Ames and Moffat [63]:

$$Lu = 1.5 * \frac{u'^3}{\varepsilon} \qquad Equation\ 6.15$$

It should be noted that the 5/3^{rds} law is not perfectly followed by the measured data (compare black plotline with all other plotlines in fig. 6.3.5), which means that the value of ε will vary slightly based on which combination of E(ω) and ω was chosen for evaluation of ε in equation 6.14. The values of Lu were calculated for each of the six locations. Although not exact, all locations showed the energy length scale to be in the vicinity of 8 cm. To calculate the uncertainty involved, ε must be calculated using all measured points in the inertial sub-range for all measured locations and an uncertainty band must be

established. This would take a significant amount of time and was not found necessary as the value of ε remained close to the one reported above for few different combinations of E(ω) and ω, and the calculated energy length scales were close to each other for all locations.

Taylor Microscale, λ

The energy length scale eddies were smaller eddies feeding on bigger, integral length scale eddies. These smaller eddies start dissipating and form even smaller eddies which dissipate into thermal energy due to viscosity. The eddy size of the smallest eddies, that dissipate into thermal energy, is defined as the Kolmogorov length scale. But these eddies exist at very high frequencies and the data measured at these frequencies contain alias error. Therefore, the Kolmogorov length scale is not computed. The eddies, which have their eddy sizes larger than the Kolmogorov length scale but smaller than the energy length scale, are characterized by the Taylor microscale, λ. The relation to calculate this length scale was given by Hinze [61] and is shown below:

$$\lambda = \sqrt{\frac{15 * \nu * u'^2}{\varepsilon}} \qquad Equation\ 6.16$$

The Taylor microscale was calculated to be 0.37 cm. Note that Taylor microscale and the Kolmogorov length scale are the only length scales which are directly influenced by viscosity.

The bulk flow properties and the turbulence characteristics are shown in table 6.3.1.

Table 6.3.1 Approach flow characteristics

Bulk Flow Characteristics		**Turbulence Characteristics**	
Mean Velocity, $\bar{U}$ ($m.s^{-1}$)	**12.6**	*Integral Length Scale, Λ (cm)*	**3-5**
Velocity Fluctuations, U_{rms} ($m.s^{-1}$)	**1.3**	*Energy Length Scale, Lu (cm)*	**8.2**
Turbulence Intensity, Tu (%)	**10.2**	*Taylor Microscale, λ (cm)*	**0.37**
Cascade Reynolds Number, Re_{chord}	**393,000**	*Dissipation, ε ($m^2.s^{-3}$)*	**42.8**

To get a sense of the turbulence length scales presented in table 6.3.1, a comparison is attempted with the results reported by Ames [64], whose setup is used as a basis to build the turbulence generator in the current facility and who claims that his setup gives a very good approximation of a combustor exit flow. This comparison is shown in table 6.3.2. Ames suggested that the exit height of the combustor, Hc, can be used to normalize the various length scales and, therefore, in table 6.3.2 the length scales are reported as percent of the height of the respective combustor. Although, Ames' setup had a slightly higher velocity and a higher velocity fluctuation level, the values in both setups are very close to each other. Hence, it can be said that the turbulence generator in the current facility produces turbulence similarly to that seen at the exit of an engine combustor.

Table 6.3.2 Comparison of turbulence characteristics

Facility	***H*** ***cm***	***$\bar{U}$*** ***$m.s^{-1}$***	***U_{rms}*** ***$m.s^{-1}$***	***Tu*** ***(%)***	***Λ*** ***cm***	***Lu*** ***cm***	***Λ/Hc*** ***(%)***	***Lu/Hc*** ***(%)***
Ames'	*42.54*	*19.3*	*1.6*	*8.3*	*2.08*	*4.34*	*4.89*	*10.20*
Current	*92.7*	*12.6*	*1.3*	*10.2*	*4*	*8.2*	*4.31*	*8.85*

6.4. Thermal Qualification Measurements

Thermal qualification consists of two measurements: the first is testing whether the contoured endwall is adiabatic and the second is to measure the thermal profile of the approach flow. All measurements are taken using thermocouples, as explained in section 4.1 and the data were measured using the Agilent 34970A data acquisition unit.

6.4.1. Contoured Endwall Adiabatic Performance

This measurement is taken to ensure that the temperature gradient is becoming zero very near the endwall. These measurements were performed as part of the experiments documented in Saxena [51] and were not repeated for this study as the same contoured endwall was used. The results are documented here for completeness.

To verify that no temperature gradient is present near the contoured endwall, thermal measurements from very near the wall up to 0.45 cm away from the endwall were taken at randomly chosen locations on the endwall. The film coolant supply at temperature, T_C (which is higher than the mainstream temperature, T_∞) was present to provide a temperature difference between the contoured endwall and the mainstream. The results for the tests were non-dimensionalized in terms of a recovery temperature as shown:

$$\theta_C = \frac{T - T_\infty}{T_C - T_\infty} \qquad Equation\ 6.17$$

Where 'θ_C' is the film coolant recovery temperature and 'T' is the temperature measured by the thermocouple away from the endwall. The results of this test are shown in fig. 6.4.1. They show that temperature gradients are zero near the wall, verifying that the endwall is adiabatic.

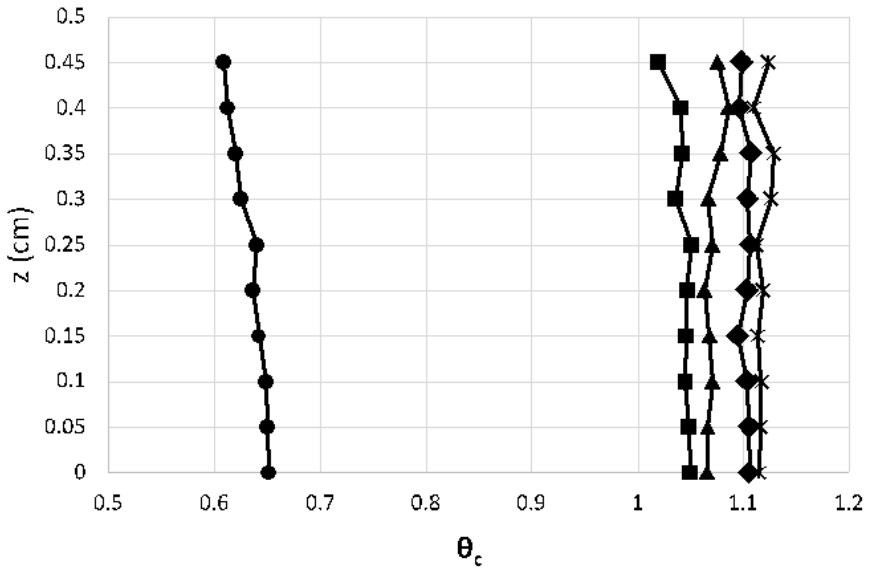

Figure 6.4.1 Temperature gradients away from the contoured endwall at randomly chosen locations [51]

6.4.2. Thermal Profile of Approach Flow

It is important to verify that both the effusion cooling holes and the film cooling holes are providing coolant uniformly over the pitch direction. The approach plane, located only a short distance downstream of the effusion cooling holes (x/C_{ax} = -1.19), is a perfect candidate to test this uniformity. Once again, the results are non-dimensionalized using equation 6.17. For these measurements, the mass flow ratio of the combustor coolant (the addition of effusion coolant and louver coolant) was 5.03%. The performance is expected to be similar for higher combustor coolant flow rate cases. The thermal contours are presented in fig. 6.4.2 with actual measurement locations shown by black dots. Note that measurements were taken only from the endwall to half-span (Z/S = 0.5) where the recovery temperature reaches values close to zero. As expected, a pitchwise-uniform coolant layer near the contoured endwall, characterized by high θ_C values, was observed. This is created only by the effusion coolant and expected to thicken downstream due to the addition of louver coolant. This contour ensured that there is no unexpected coolant transport present in the approach flow.

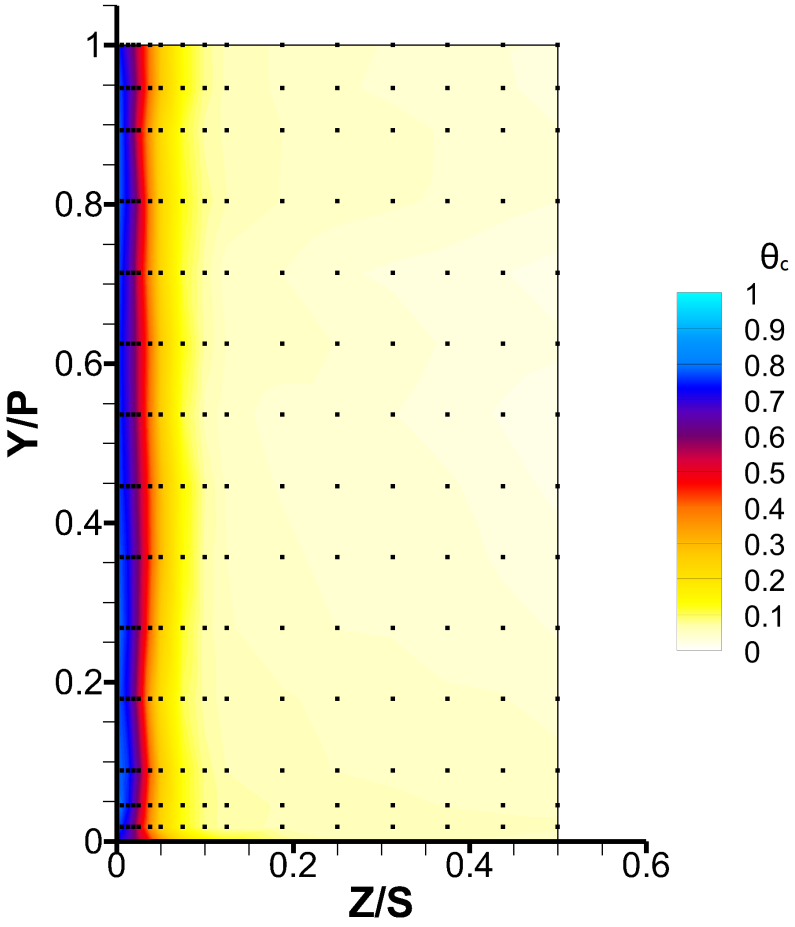

Figure 6.4.2 Thermal contours of the approach flow characterization plane

Chapter 7. Results and Discussion: In-field Measurements

7.1. Order of Presentation

The results section is presented in two chapters. This first chapter focusses on the in-field thermal and aerodynamic measurements taken for all cases (see chapter 5 for the case grid). Firstly, the effects of changing the film cooling mass flow ratio on coolant stream migration and interaction of coolant streams is explained. The second subsection studies the same parameters when the louver coolant flow rate is changed. For both sections, the planar data are presented with increasing axial distance of the planes. The nomenclature for the case names is explained in chapter 5 and used extensively in this and the following chapter.

7.2. Effects of Changing the Film Coolant Mass Flow Ratio

This section explains the results measured for the cases that had louver cooling MFRs of 0.92% and 1.43%. Results for louver cooling MFR of 0.37% have already been presented and discussed in Alqefl [40]. The remaining two louver coolant cases will be discussed independently as this section focusses only on the effect of film coolant on passage aerodynamics and heat transfer. Thermal contours, velocity contours and streamline traces are plotted for all the measured data. For planes downstream of plane 2, vorticity contours with secondary flow vectors are also plotted. Positive vorticity is in the counter-clockwise direction while negative vorticity is clockwise.

Plane 1

This plane is located upstream of the passage at the axial location where the endwall contouring starts (x/C_{ax} = -0.104). Only thermal measurements were taken for this plane. Figure 7.2.1 shows the thermal contours for all cases. Generally, a uniform distribution in the pitch direction can be seen along the contoured endwall for all cases. This establishes a pitchwise-uniform supply of coolant. The combustor coolant, being injected somewhat far upstream of plane 1 gets redistributed due to the pressure gradient present downstream in the passage. This creates a small concentration of coolant near y/Pi of 0.8. As the film coolant MFR is increased, more uniformity in the pitch direction can be seen very close to the endwall. This is because the momentum of the film coolant is able to overcome the effects of pitchwise pressure gradient downstream. The cases with film cooling present show a thin, highly-effective coolant layer on the endwall. This is possibly entirely film coolant, as the differences between the F00 and F10 cases are significant. However, for the cases with film cooling injection, the increase in thickness of this highly effective layer (or increase of effectiveness in this layer) with an increase of film cooling flow rate is minimal. This suggests that, although film coolant is necessary to provide good cooling to the endwall, an increase in its flow rate beyond a point does not grant any substantial improvement. Plane 1 helps in establishing a uniform temperature profile for the coolant streams.

Plane 2

Plane 2 is located just upstream (x/C_{ax} = -0.02) of the inlet of the vane passage. The thermal and velocity contours are presented in fig. 7.2.2 through 7.2.4. The aerodynamic measurement data for only between y/Pi of 0.7 and 0.1 are plotted. This is because the test section geometry prevented measuring aerodynamic data for y/Pi above 0.7. Between y/Pi of 0.1 and 0, the data were measured. However, due to the nearness to the stagnation

line, flow angles were much higher than could be measured by the five-hole probe. Hence, the measured data were not reliable and, therefore, were not plotted in any of the cases. The thermal data for these regions are plotted. They show the general coolant coverage.

The velocity contours for all cases have similar profiles. The velocities near the suction side are higher than those near the pressure side due to downstream passage turning. Near z/Si = 0.1, the velocities are higher than velocities that are farther in the span direction. These elevated velocities are due to the additional flow provided by the coolant, especially the effusion coolant. For this plane only, the secondary vectors are plotted using the angles measured with reference to the axial direction. This is done to show the velocity distribution when the flow is just entering the passage. The flow near the endwall is affected by the coolant flows. When compared to F00 cases, the other cases show more horizontal angles of the secondary velocity vectors, until z/Si of 0.15. This is because of the injection angle and the momentum of film coolant. For L09 cases, the decreases in angles with the horizontal are more significant when increasing from F10 to F15 than when increasing from F00 to F10. This shows that with film coolant MFR of 1.5%, the coolant, due to its added momentum, is more successful in penetrating the mainstream. As the L14 cases do not have a F15 case, the secondary vectors' angles do not change as much as seen in the L09 cases.

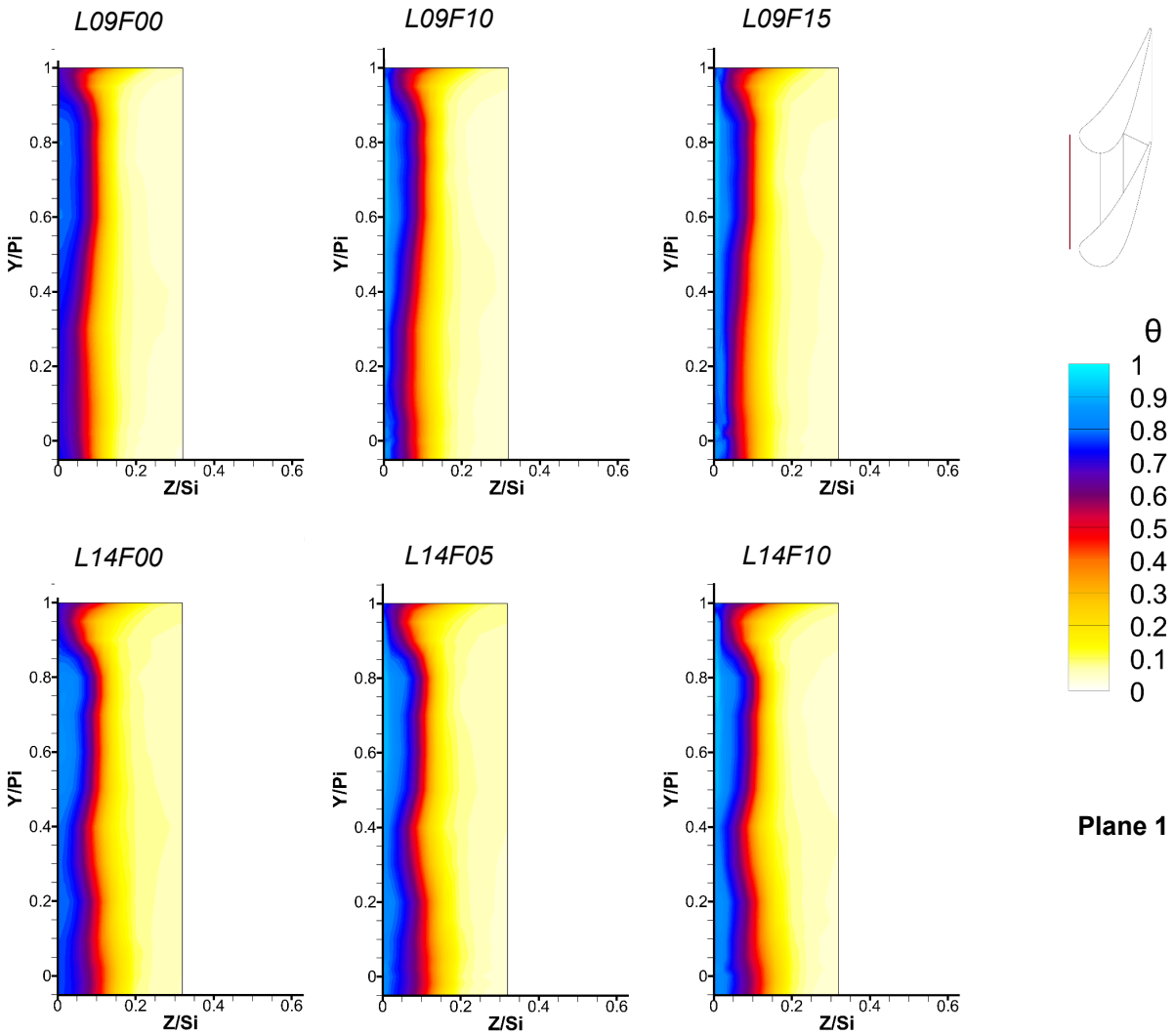

Figure 7.2.1 Thermal contours for L09 and L14 cases of plane 1

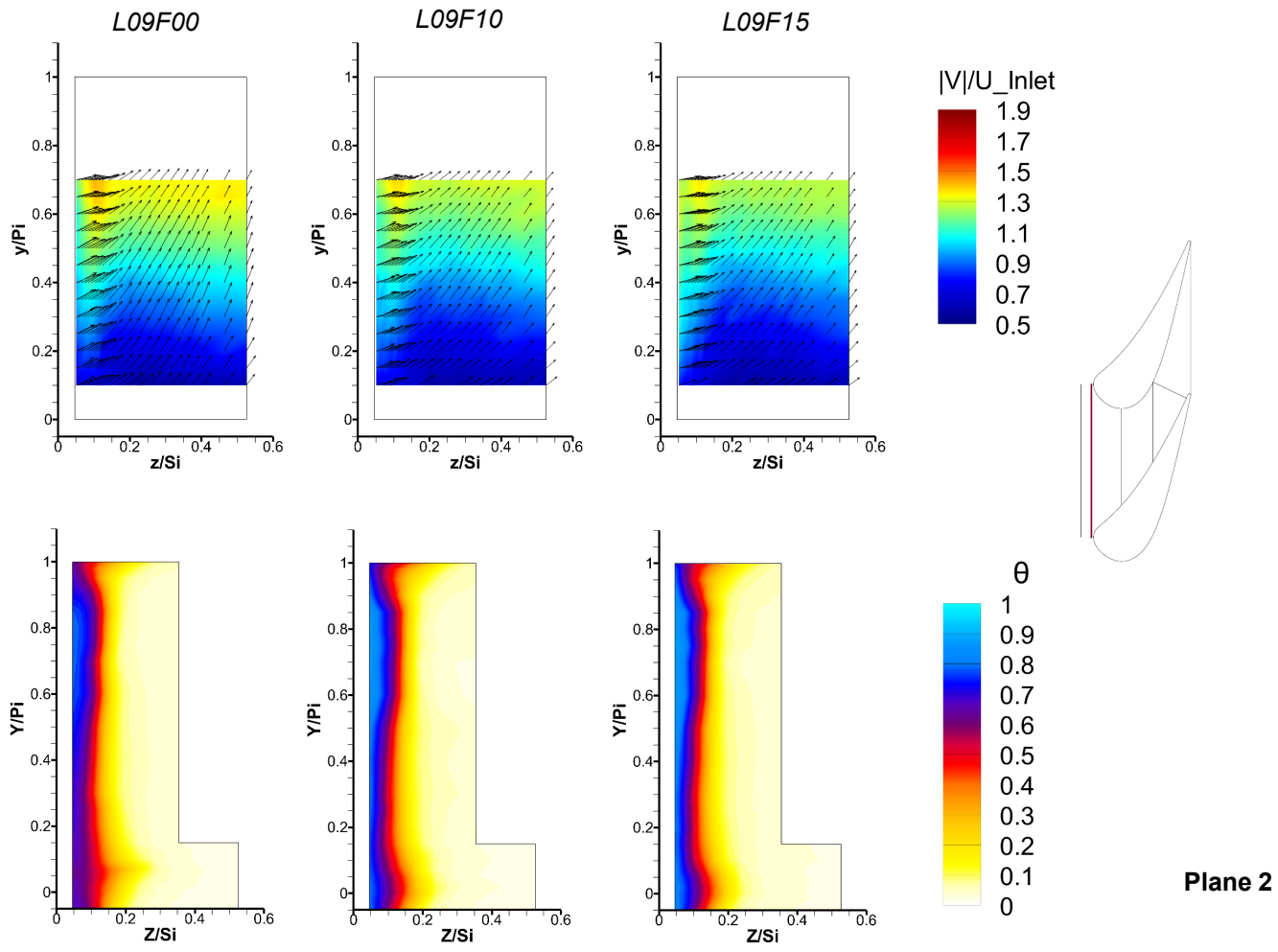

Figure 7.2.2 Thermal contours and velocity contours with secondary flow vectors for the L09 cases of plane 2

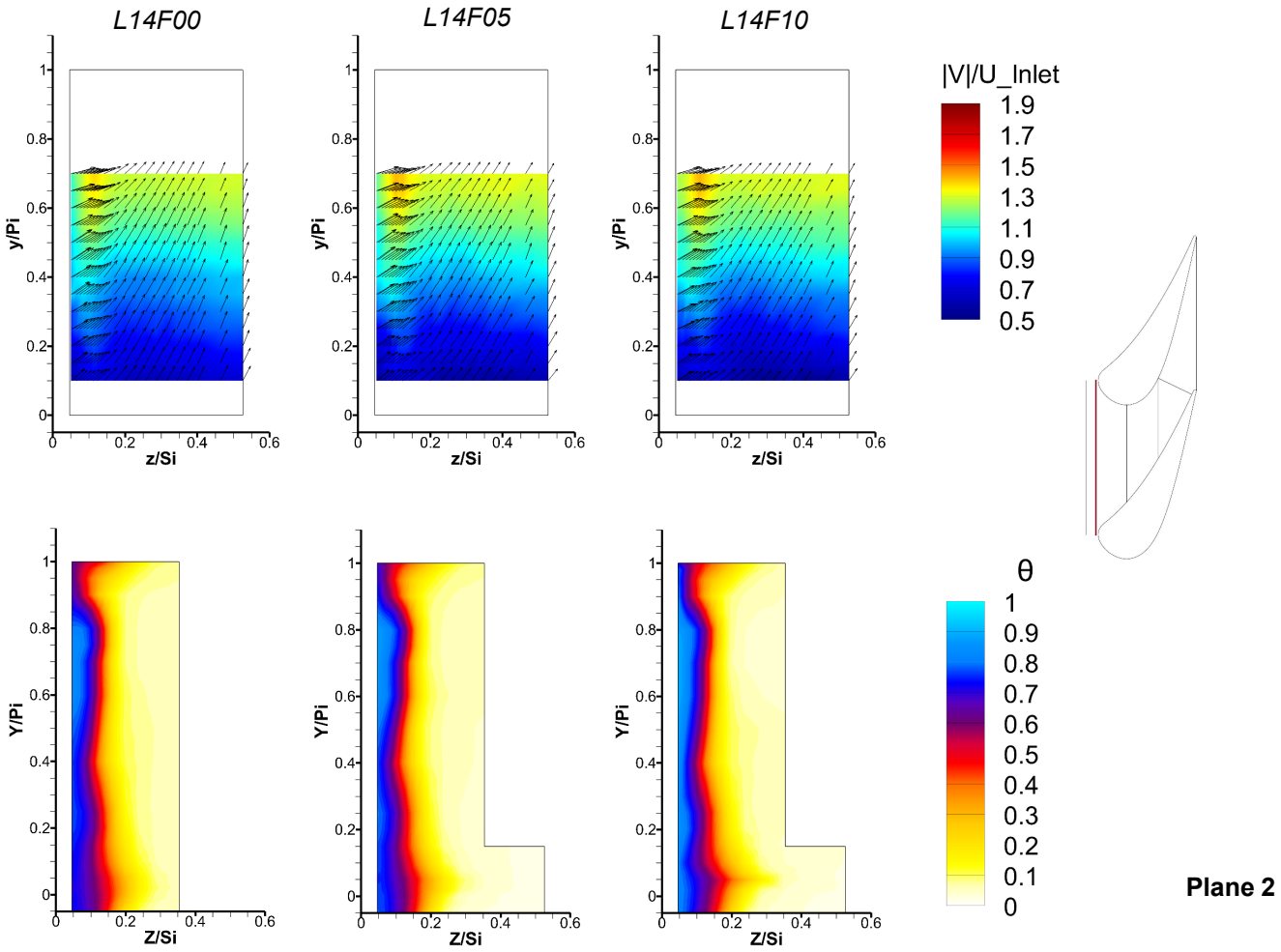

Figure 7.2.3 Thermal contours and velocity contours with secondary flow vectors for the L14 cases of plane 2

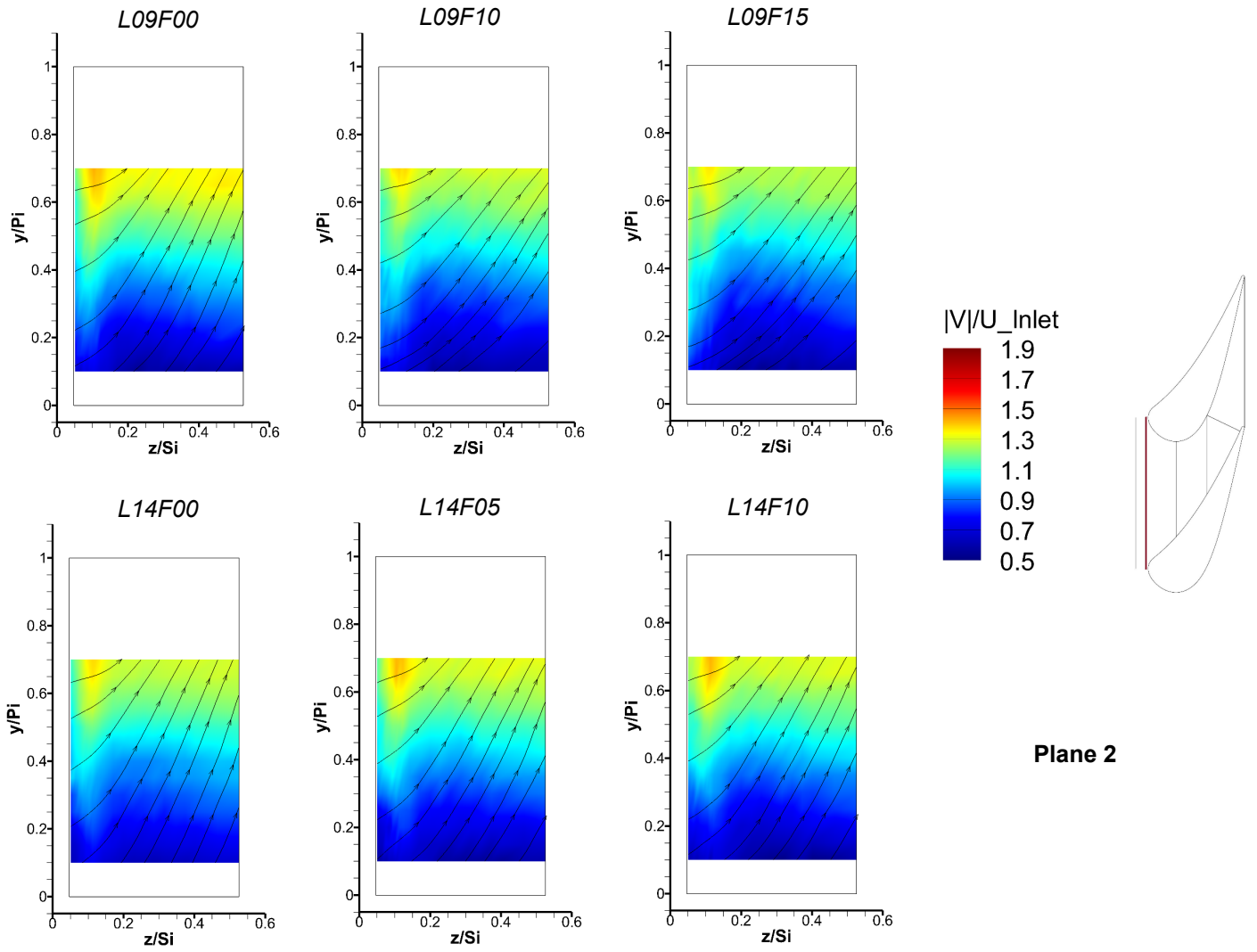

Figure 7.2.4 Velocity contours with streamline traces for L09 and L14 cases of plane 2

The thermal contours confirm some of the observations made from the velocity plots. They show good coolant effectiveness until z/Si of 0.15 which is the same distance over which the secondary vectors were affected by the coolant streams. Also, the spanwise distance to where the coolant shows good effectiveness is increased with an increase in film coolant MFR. This confirms that the mainstream penetration is increased with an increase in momentum of film coolant. Also, a small bulge in the coolant film near the stagnation line (y/Pi=0) can be seen for all cases. Confirmed by the secondary flow vectors, it appears that the coolant is hitting the stagnation line and then proceeding to move in the spanwise direction away from the endwall and toward the mid-span. This is because the coolant is spreading along the pressure side away from the endwall. This is an important observation because it is in the opposite direction to the direction generally observed. This phenomenon is explained and validated by the results presented for downstream planes. For L09F10 and L14F05, it can be seen that the pitchwise coolant distribution is skewing toward the suction side. This is due to film coolant starting to redistribute due to the pressure gradient downstream and its own low momentum. However, for L09F15 and L14F10, the coolant injection rate is higher and, thus, redistribution is less apparent.

The thermal measurements for planes 1 and 2 were taken for more than one pitch length (from y/Pi =1 to y/Pi = -0.05). This was done because, upstream of the cascade, a bleed slot, which affected the upper passage differently that the lower passage, was present. Therefore, the data above y/Pi = 0.95 were possibly affected by this feature. Some effects in that region should be neglected and the results for between y/Pi = 0 and y/Pi = -0.05 should be used as a substitution, for most proper characterization.

Plane 3

This plane is at x/C_{ax} = 0.289. The thermal and velocity contours are shown in figs. 7.2.5 and 7.2.7. Due to restrictions offered by the test facility, aerodynamic data are limited to

the region below y/Pi = 0.61. Usually, around this axial location, the flow starts migrating from the pressure side to the suction side due to the passage vortex (pressure side to suction side pressure gradient), which has been documented numerous times. However, the velocity contours show that the orientation of the secondary vectors is opposite to the direction a passage vortex would drive the flow. The secondary vectors show that the flow actually goes from suction side to pressure side and then runs along the pressure surface toward the midspan. This is caused by the presence of another vortex known as the 'impingement vortex.' It was studied in detail by Alqefl [40]. The mechanism was explained in chapter 2 but a brief overview is given here, as a reminder.

Alqefl gave three mechanisms that create and sustain the impingement vortex. They are listed below:

a. A swirl created due to the resistance offered by the coolant flow (especially by the combustor coolant) to the passage turning
b. A modified velocity profile at the passage inlet causing a circulation rotating in the opposite direction to that of the horseshoe vortex, causing most of the coolant to move toward the midspan rather than toward the endwall
c. Coolant impinging on the pressure surface continuously feeding the impingement vortex

As the test facility used for the current study is the same as the one used by Alqefl, the impingement vortex is expected in all cases of the present study. The resistance of the coolant flow to passage turning, the changes in the velocity profile and coolant run-up along the pressure surface are seen as far upstream as plane 2. Hence, the impingement vortex is expected in all planes after plane 2. Alqefl explains that the impingement vortex probably has two legs: a suction side leg and a pressure side leg. He further explains why the suction side leg is not strong enough for the flow to change significantly in direction.

Unless mentioned otherwise, any further mention of the impingement vortex refers to the above discussion about the vorticity of the pressure side of the passage.

Aerodynamic plots show that the velocity vectors indeed go from suction side to pressure side near the endwall and run along pressure surface. However, the center of the impingement vortex is not visible in any of the cases. As the downstream planes confirm the existence of this vortex, a plausible explanation is that the center lies beyond the region where data were taken. If true, this means that the center of the impingement vortex is affected by the combustor coolant MFR on plane 3. The streamline traces and the vorticity contours for all cases are plotted in figs. 7.2.6 and 7.2.8. These show that the angle (with respect to the spanwise direction) of coolant coming from the suction side and passing to the pressure side is becoming steeper as the film coolant MFR increases. These also show that, as the film coolant MFR increases, the size of the impingement vortex increases in the z direction. This confirms that the impingement vortex is strengthened by an increase in film coolant MFR.

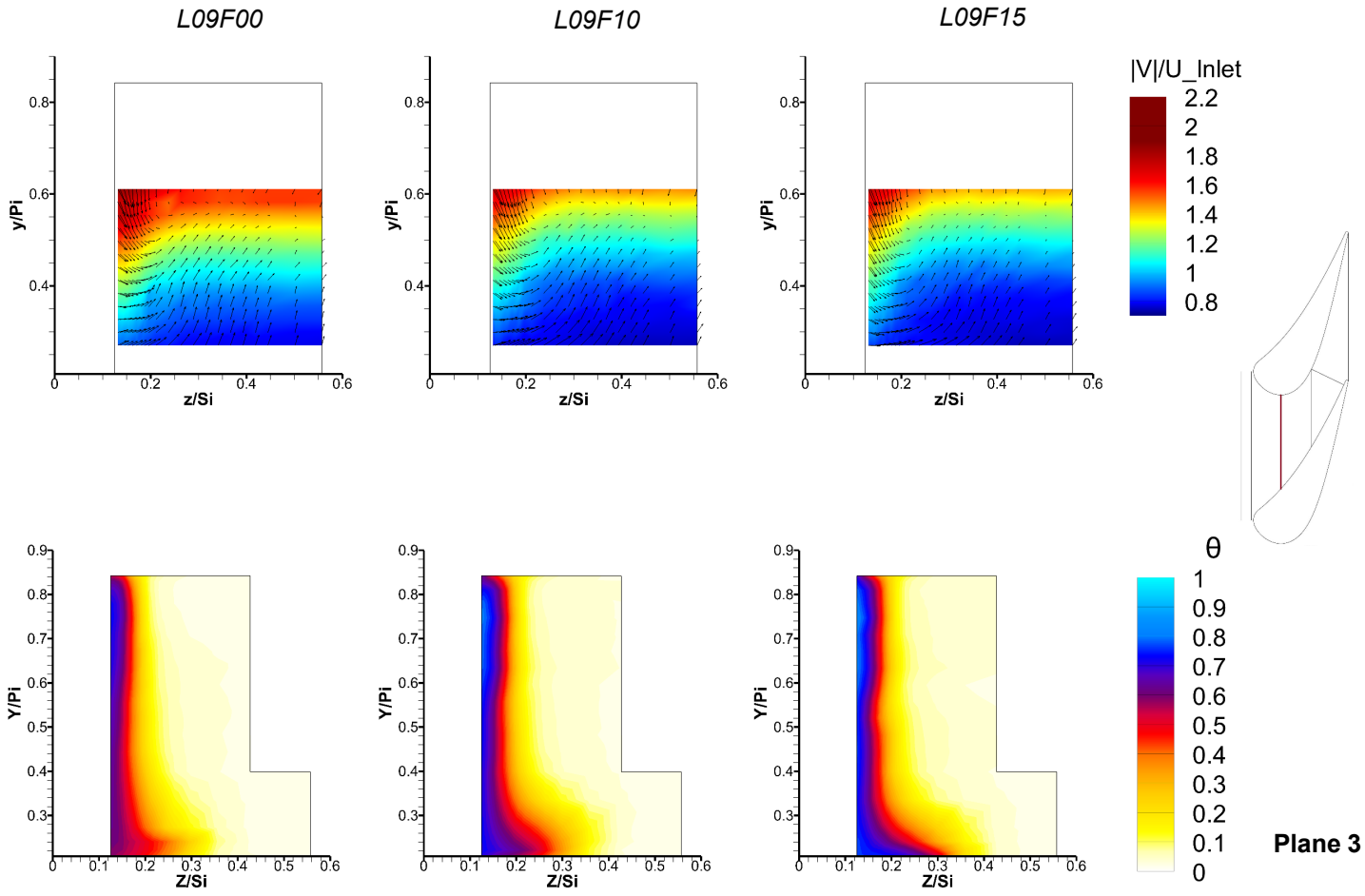

Figure 7.2.5 Thermal contours and velocity contours with secondary flow vectors for the L09 cases of plane 3

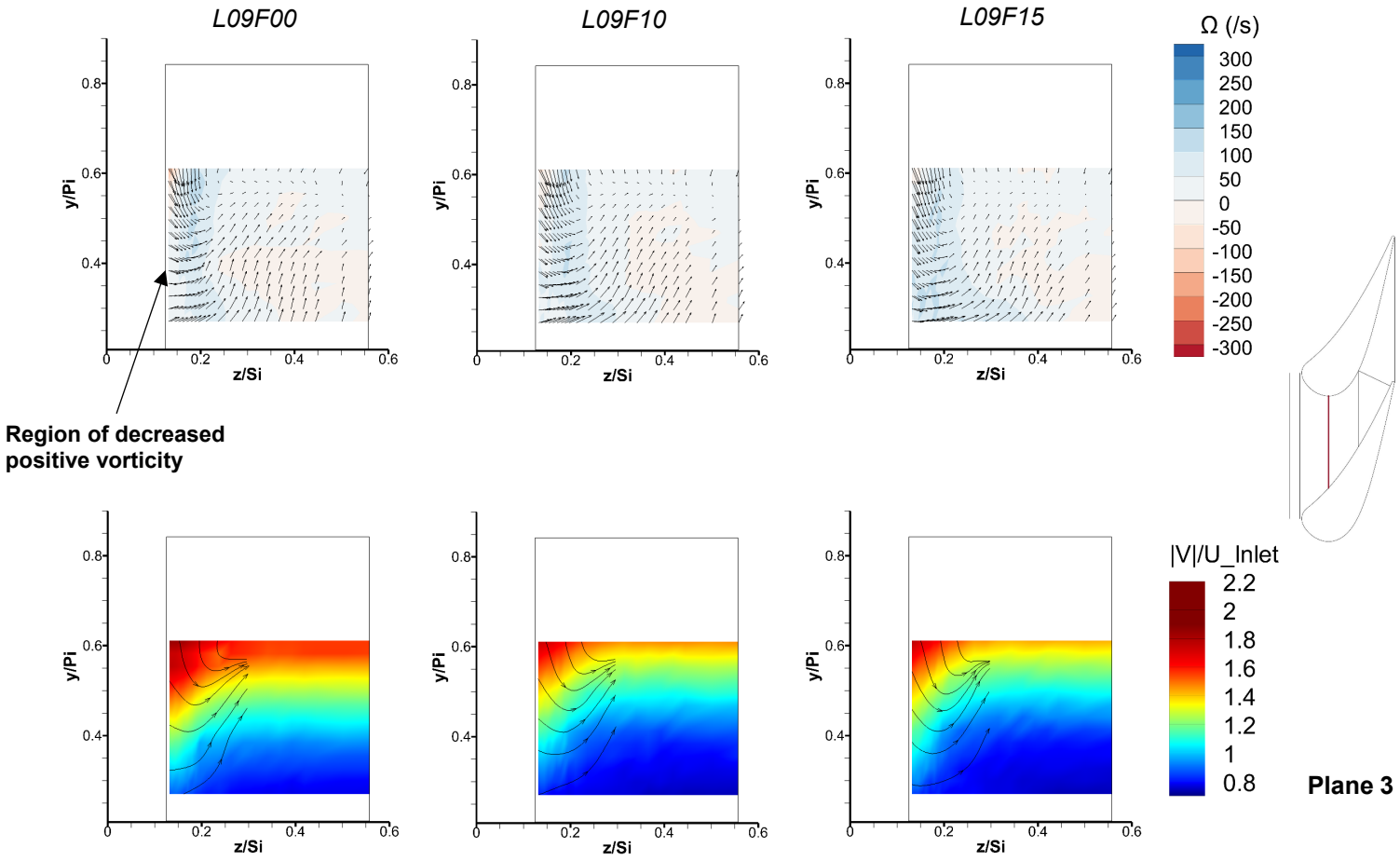

Figure 7.2.6 Vorticity contours with secondary flow vectors and velocity contours with streamline traces for the L09 cases of plane 3

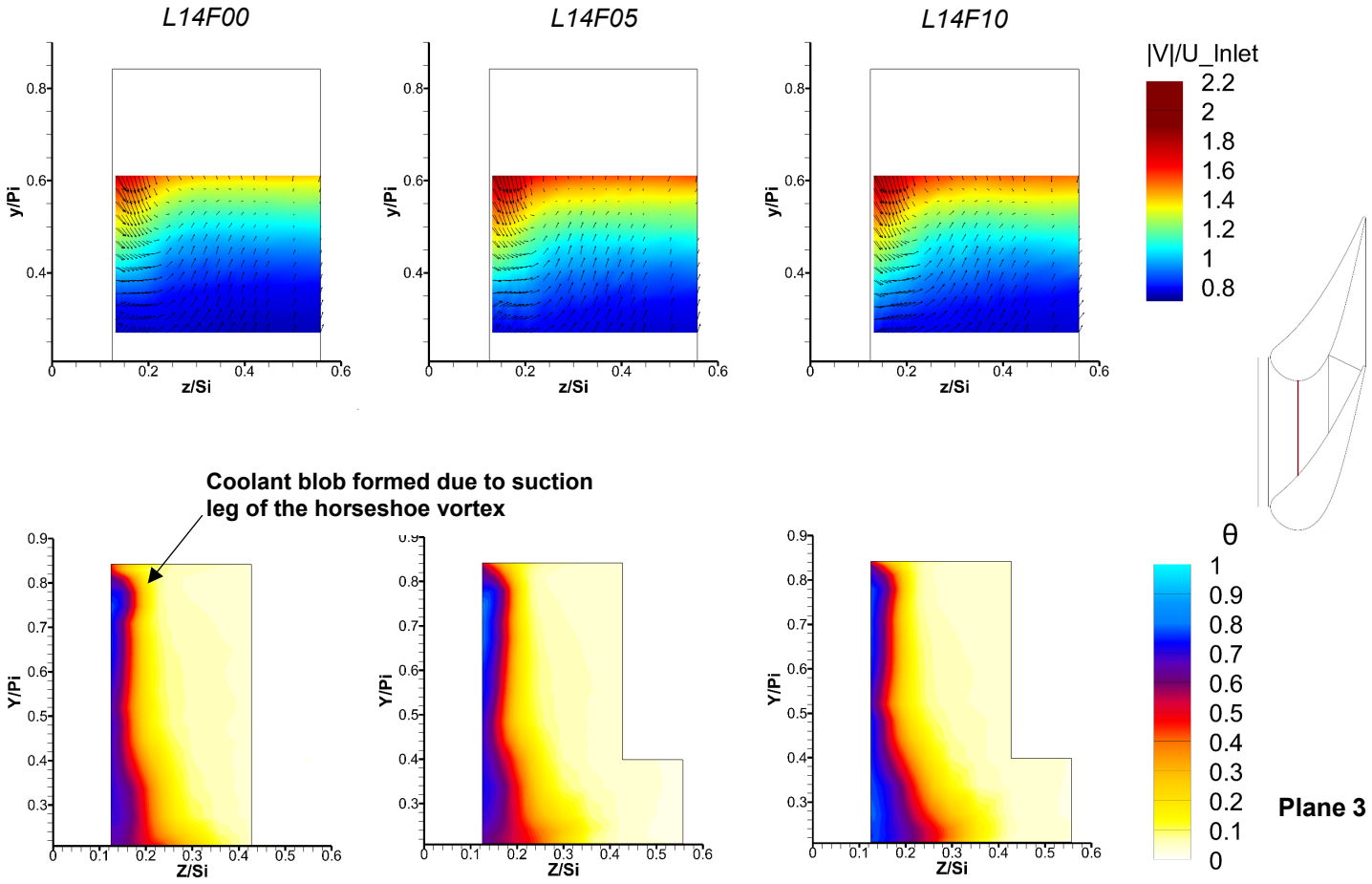

Figure 7.2.7 Thermal contours and velocity contours with secondary flow vectors for the L14 cases of plane 3

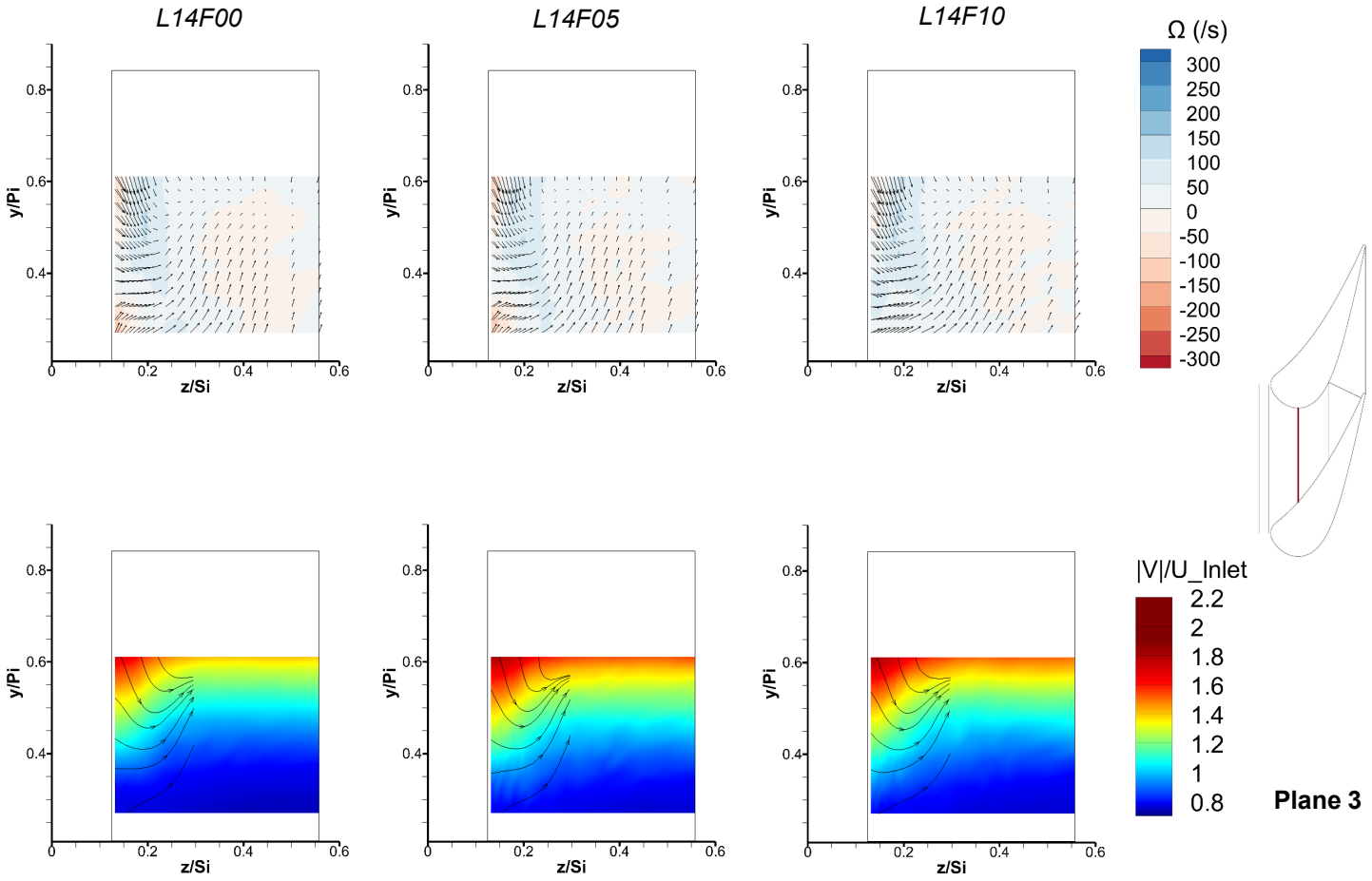

Figure 7.2.8 Vorticity contours with secondary flow vectors and velocity contours with streamline traces for the L14 cases of plane 3

In the L09 cases, a decrease in positive vorticity near the endwall can be seen (see fig. 7.2.6). This points to an effect, endwall cross-flow, that is opposing the effect of the impingement vortex. The velocity vectors do not show a change in their angles to point in the direction of the cross-flow, but the decreased positive vorticity in the endwall region of this plane and the negative vorticity seen in this region in the downstream planes confirm that this effect is indeed due to endwall cross-flow. For the L14 cases, the negative vorticity near y/Pi = 0.6 indicates that the cross-flow along the endwall is present (see fig. 7.2.8). The cross-flow near this region is apparently not much affected by the increase in film coolant flow rate. Another region affected by the endwall cross flow in the L14 cases is the pressure-side-endwall corner. For L14F00 and L14F05, a negative vorticity region is seen, which vanishes in the case of L14F10. This is likely because the momentum of the film coolant is able to overcome the cross-flow effect in the L14F10 case, causing it to remain relatively unaffected by both the impingement vortex and the endwall cross-flow. Also, the spanwise distances for which the impingement vortices exist are always around z/Si = 0.4. The flow beyond z/Si = 0.4 has very small secondary velocity vectors and mild negative vorticity, showing that they are relatively unaffected by coolant injection.

Thermal contours support the conclusions drawn above. Energizing of the impingement vortex can be seen by the increase in the horizontal distance for which the coolant spreads along the pressure surface. In the L09 cases, the spanwise distance for which the coolant spreads along the pressure surface increases from z/Si = 0.34 to z/Si = 0.42 for the F00 and F15 cases, respectively. Once again, the difference between the horizontal coolant spreading along the pressure surface for the F10 and F15 cases is minimal when compared to the differences between the F00 and F10 cases. This supports the statement that, although film coolant injection certainly strengthens growth of the impingement vortex, an increase of film coolant MFR beyond a certain value does not make an

appreciable further increase. For the L09 cases (see fig. 7.2.5), the coolant concentration along the endwall is surprisingly uniform in the pitch-wise direction, even in the region near the suction wall where velocity measurements could not be taken. This suggests that the effects of the impingement vortex are present for the whole pitch and that the passage vortex is not present in this plane. In contrast, for the L14 cases (see fig. 7.2.7), a coolant blob is present near the suction side, most notably for the F00 case. This would mean coolant circulation is present, possibly due to the suction leg of the horseshoe vortex. Even then, its effect seems to be very localized. For the F05 and F10 cases (fig. 7.2.7), the blob is flattened a bit, suggesting that horseshoe vortex effects may be suppressed by the higher film coolant flow rate. As the aerodynamic data in this location are not present, none of these conclusions, although seemingly logical, can be said with certainty.

Compared to results presented in Alqefl [40], the coolant near the endwall is losing its effectiveness at a much slower rate. For all cases, the coolant effectiveness is well over 0.7 at plane 3. The reason for this is that the combustor coolant (louver coolant, more specifically) is shielding the film coolant flow from mixing with the mainstream. It was observed earlier that the higher momentum of the higher film coolant flow rates penetrates the mainstream more effectively. This can be observed when cases L14F05 and L14F10 are compared (figs. 7.2.7). The cooling effectiveness is higher in the former case, even though film coolant injection is lower. This is because the F10 case has film coolant possibly tending to lift off the endwall and mix with the mainstream, resulting in decreased effectiveness near the endwall. This lift-off is further augmented as the louver coolant also has a higher MFR of 1.43%. However, for the L09 cases, the film coolant MFR increase leads to a further increase in effectiveness at the endwall. This is because of the lower MFR of the louver coolant, which does not have high enough momentum to penetrate to the mainstream, but has high enough momentum to prevent film coolant from penetrating

to the mainstream. This implies that louver coolant MFR of 0.92% is more effective in keeping film coolant on the endwall than is a louver coolant MFR of 1.43%, a hypothesis confirmed by the results measured on the downstream planes.

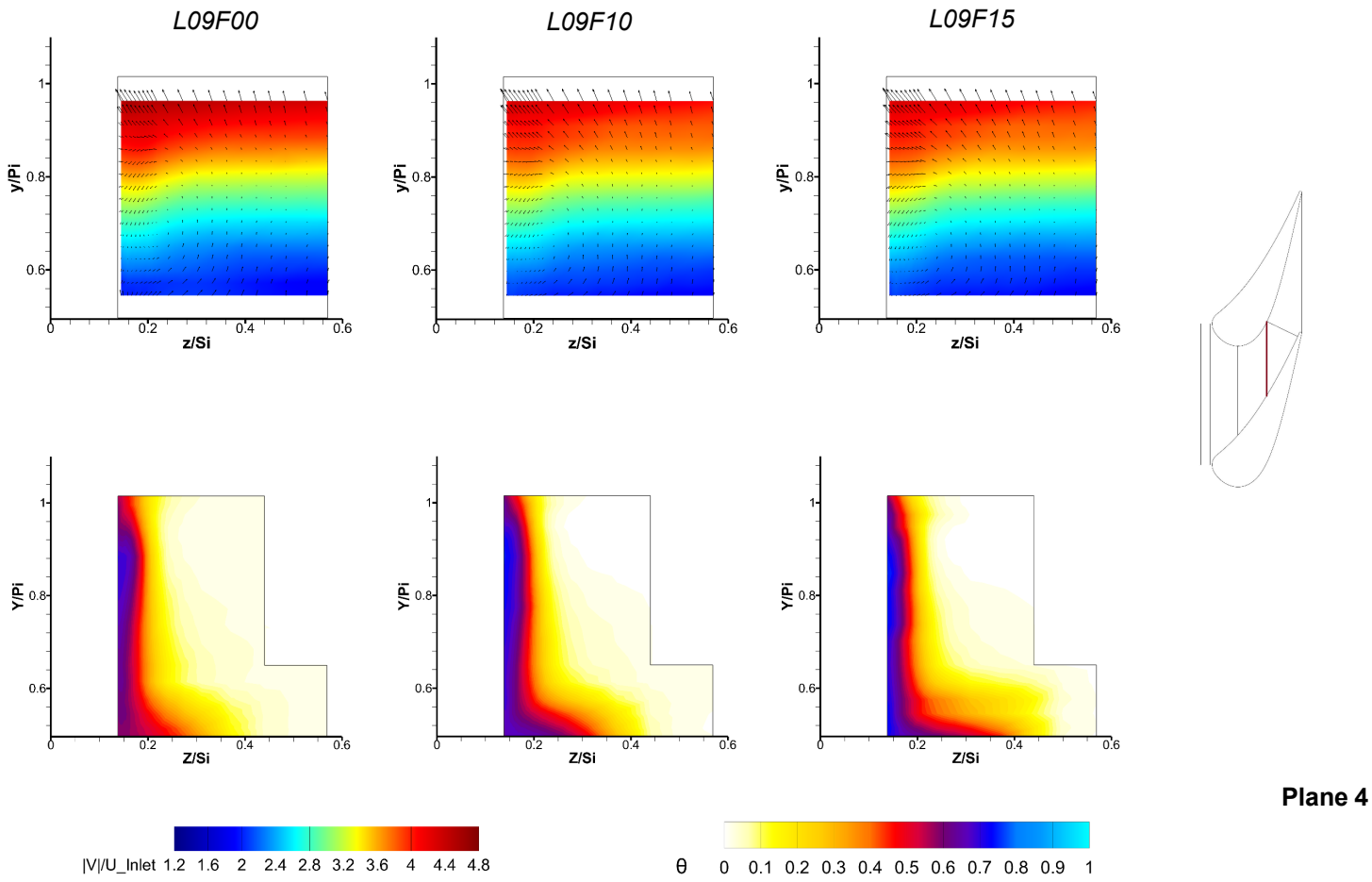

Figure 7.2.9 Thermal contours and velocity contours with secondary flow vectors for the L09 cases of plane 4

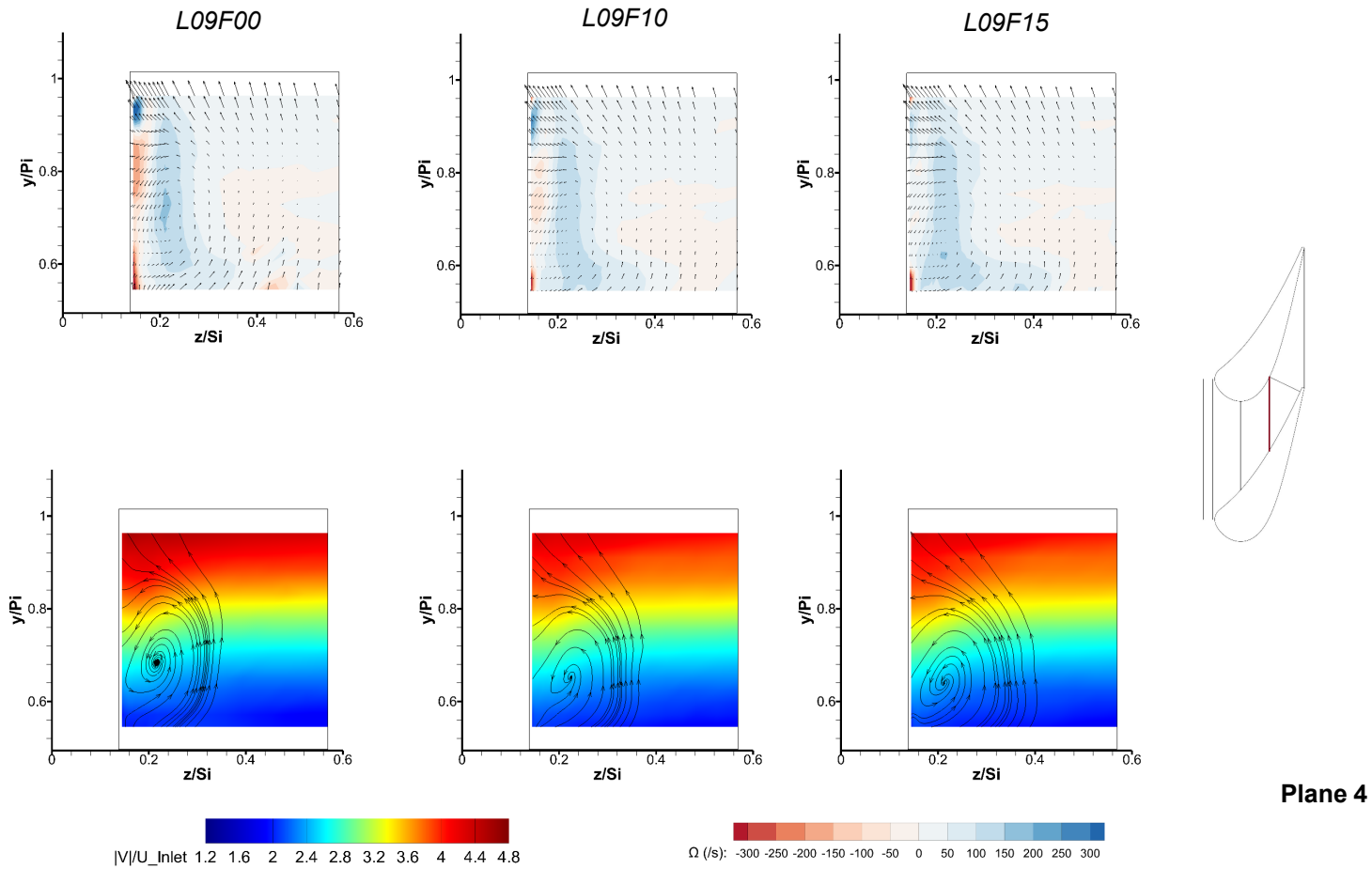

Figure 7.2.10 Vorticity contours with secondary flow vectors and velocity contours with streamline traces for the L09 cases of plane 4

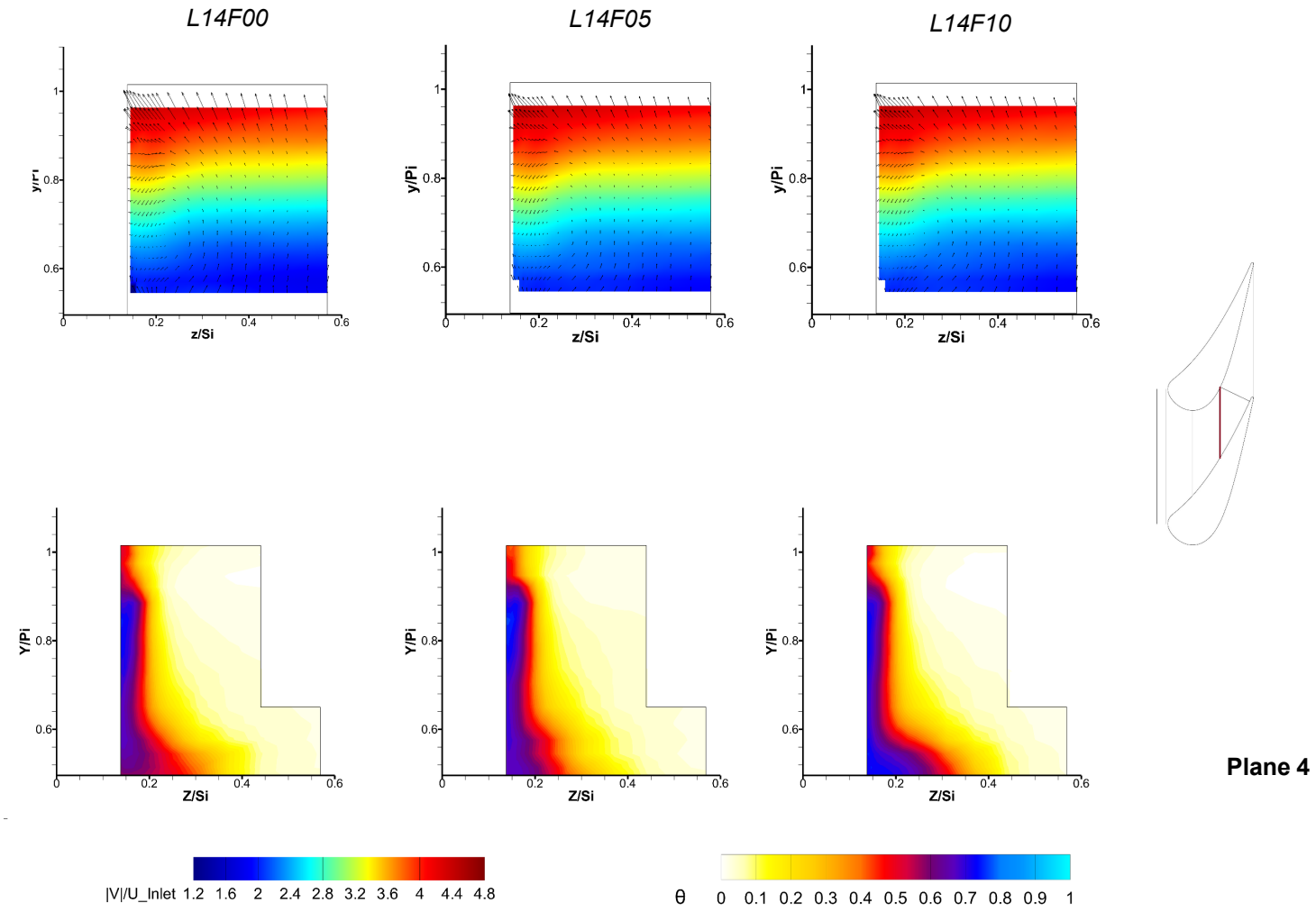

Figure 7.2.11 Thermal contours and velocity contours with secondary flow vectors for the L14 cases of plane 4

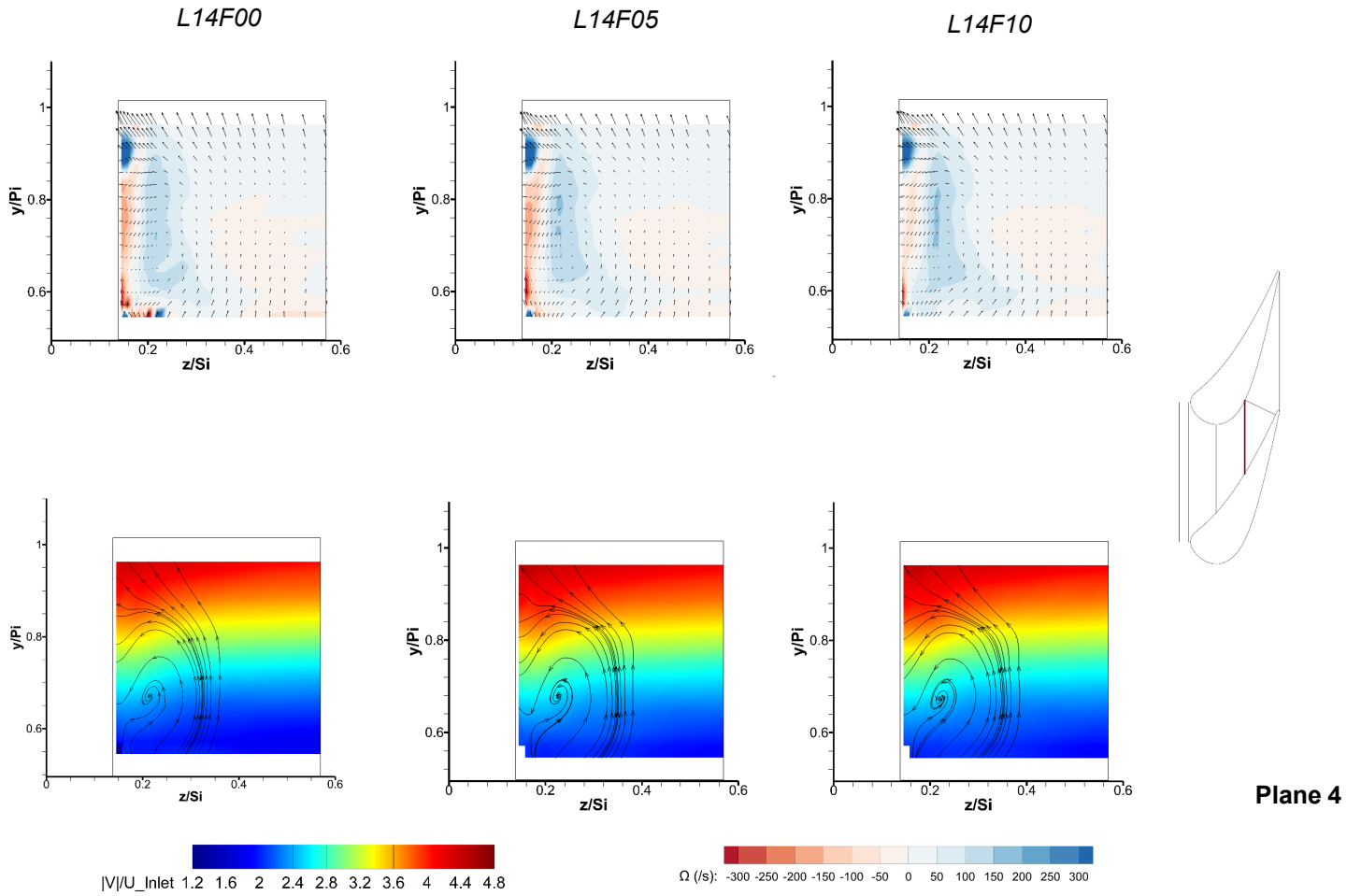

Figure 7.2.12 Vorticity contours with secondary flow vectors and velocity contours with streamline traces for the L14 cases of plane 4

Plane 4

The thermal and velocity contours for plane 4, located at x/C_{ax} = 0.612, are shown in figs. 7.2.9 and 7.2.11. As seen earlier, the absolute velocity profiles do not change with changes in film coolant MFR. Figures 7.2.10 and 7.2.12 show the streamline traces, indicating that the impingement vortex is present in all cases, with its center around y/Pi = 0.65 and z/Si = 0.21. For all cases, the vorticity plots show that the impingement vortex does not span the whole pitch distance (figs. 7.2.10 and 7.2.12). The plots show a small but intense vortex near y/Pi=0.9. This vortex has a direction that is opposite to the passage vortex seen in this region when combustor coolant is not present. The only other vortex in this region with counter-clockwise rotation is the suction leg of the horseshoe vortex (henceforth referred to simply as the horseshoe vortex). The plots show that, even as far upstream as plane 4, the movement of the pressure leg of the horseshoe vortex from pressure to suction sides (i.e. the passage vortex) is seriously hampered by the impingement vortex. Because the impingement vortex is usually some distance away from the endwall (due to coolant flowing somewhat away from the endwall), the suction leg of the horseshoe vortex is unaffected and is seen in this study. Note that this is opposed to conventional studies where the passage vortex overcomes the effects of the suction leg vortex. Also, the horseshoe vortex is not on the suction surface, probably because the flow below it tends to move toward the pressure side due to the impingement vortex, effectively pulling it down. Another feature that has not been observed clearly in these results, until now, is the endwall cross-flow. Vorticity contours show that a negative vorticity region is very close to the endwall. It is also noticeable that the horseshoe vortex is more dominant than the endwall cross-flow, as the cross-flow near the suction surface is decreased strongly by to this vortex.

When the horseshoe vortices for all L09 cases are compared, a considerable decrease in their intensities is seen when film coolant is introduced, and the decrease is even stronger with further increases in the film coolant flow rate. This, again, can be explained by the resistance provided by the film coolant momentum to horseshoe vortex rotation. For the L09F15 case, the horseshoe vortex has almost disappeared as the film coolant has overwhelmed its effect. For the L14 cases, the vortex strength does not decrease as much as in the L09 cases. This may be because an L14F15 case was not taken and the film coolant MFR of 1% (the value taken) may not be enough to resist the vortex and the coolant; instead, it is mixed by the vortex with passage flow.

For all cases, the streamlines show that for $0.85 < y/Pi < 0.82$, secondary flows seem to be impinging on the endwall. This is because the effects of the endwall cross-flow (which moves coolant from pressure to suction surfaces) and the horseshoe vortex (which moves coolant from suction to pressure surfaces) are being cancelled. An interesting observation is that at the pitch location, where the effect of the impingement vortex is completely diminished on plane 4 (around $y/Pi = 0.82$), is the same pitch location on plane 3 where the effect of the impingement vortex seems to have decreased completely. This shows that the impingement vortex resists passage turning and the pressure gradient present between the pressure and suction surfaces is overwhelmed by the impingement vortex. The passage vortex would be present in a conventional cascade and should have migrated toward the pressure surface by this axial location. Such is true for even the F00 cases, showing that the combustor coolant is solely capable of resisting the passage vortex.

The competing effects of horseshoe vortex and endwall cross-flow also explain the steep decrease of coolant coverage near the endwall around $z/Si = 0.92$. This is in the vicinity of the center of the horseshoe vortex, indicating mixing of the coolant, which decreases

its effectiveness. Both vorticity and thermal contours confirm this conclusion. Similarly, near the location of the center of the impingement vortex, the effectiveness value drops due to coolant mixing. This is evidenced by the thinning of the highly effective coolant layer near this region for all cases. However, the thickness of this dip does not change much with increases of film coolant MFR, implying that it is insensitive to changes in film cooling flow rate.

Two of the observations made in the upstream planes are again made for plane 4. The first is that the coolant spreading on the pressure surface increases with an increase in film coolant MFR, owing to strengthening of the impingement vortex. Also, the coolant layer is thicker for the L14F05 case than for the L14F10 case. This provides further proof that a lower film cooling MFR may be more beneficial than a higher one.

Plane 6

Plane 6 is a streamwise-normal plane, which starts at the same location on the suction side as does plane 4 (x/C_{ax} = 0.612). It has an angle of 64.25° with the pitch direction. Thermal and aerodynamic contours are shown in figs. 7.2.13 and 7.2.15, respectively, and figs. 7.2.14 and 7.2.16 show streamline traces and vorticity contours. The effects of the impingement vortex are visible in the streamlines, but the center is not clearly visible. This means that the center is probably very close to the pressure surface, an observation made by Alqefl as well for his cases with film coolant MFR below 1.5%. Also, the streamlines show a more pronounced effect of cross-flow over the endwall in the pitch-wise direction. Unlike plane 4, where a region of the flow near the endwall suggested a cross-flow from pressure to suction sides, plane 6 has cross-flow present for the whole pitch range. The vorticity contours show that secondary flows provide less cross flow for higher film coolant MFR cases, as evidenced by decreased negative vorticity near the endwall. This means

that, although the impingement vortex does not completely eradicate endwall cross-flow, it decreases cross-flow effects.

The horseshoe vortex is present also near the suction side-endwall corner for all cases. For every case, the intensity and size of this vortex match with features seen on plane 4, suggesting that the horseshoe vortex's effects have not diminished, even at the throat of the passage. However, small hints of passage vortex effects have started to show up on the endwall in all the L09 cases, as well as the L14F00 case, which can be seen in the form of the negative vorticity as well as having streamlines pointing toward the suction side. Based on the L09 cases, it seems that the decrease in the effect of the horseshoe vortex is related to the increase in the passage vortex strength, which is expected as these vortices act in opposite directions.

Since the velocity contours show that the impingement vortex is covering the whole pitch for plane 6, thermal contours were expected to show more uniform coolant coverage on the endwall. This is true for all except the F00 cases. In the F00 cases, the coolant layer thins beyond y/Pi = 0.93. This can be directly related to the strong negative vorticity seen on the pressure side between y/Pi = 0.13 and y/Pi = 0.20. The endwall cross-flow is causing the coolant away from the endwall to flow over the pressure surface toward the endwall and then up the endwall toward the suction side. This causes virtually no change on the endwall itself, but the area next to the endwall is deprived of coolant, causing thinning of the coolant film.

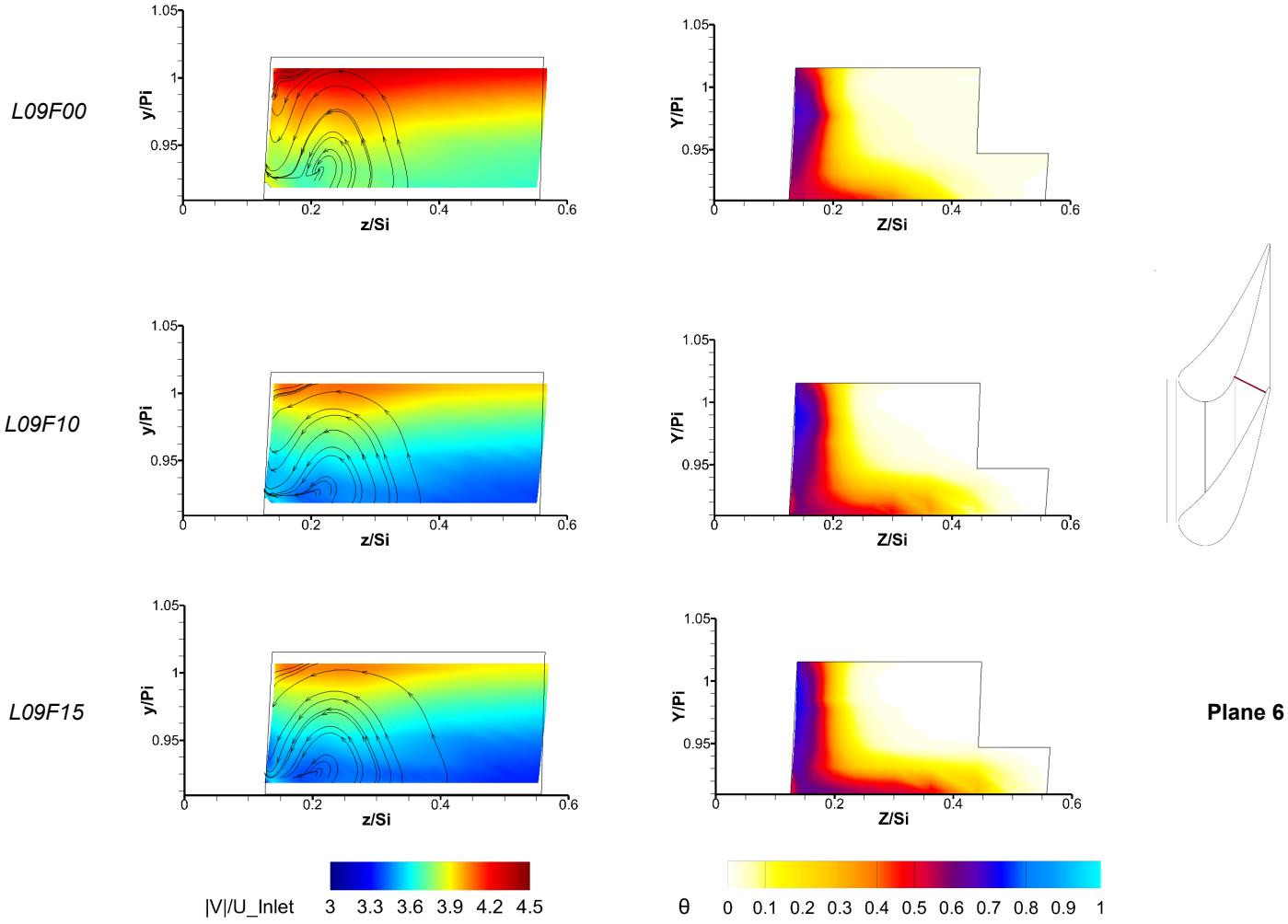

Figure 7.2.13 Thermal contours and velocity contours with secondary flow vectors for the L09 cases of plane 6

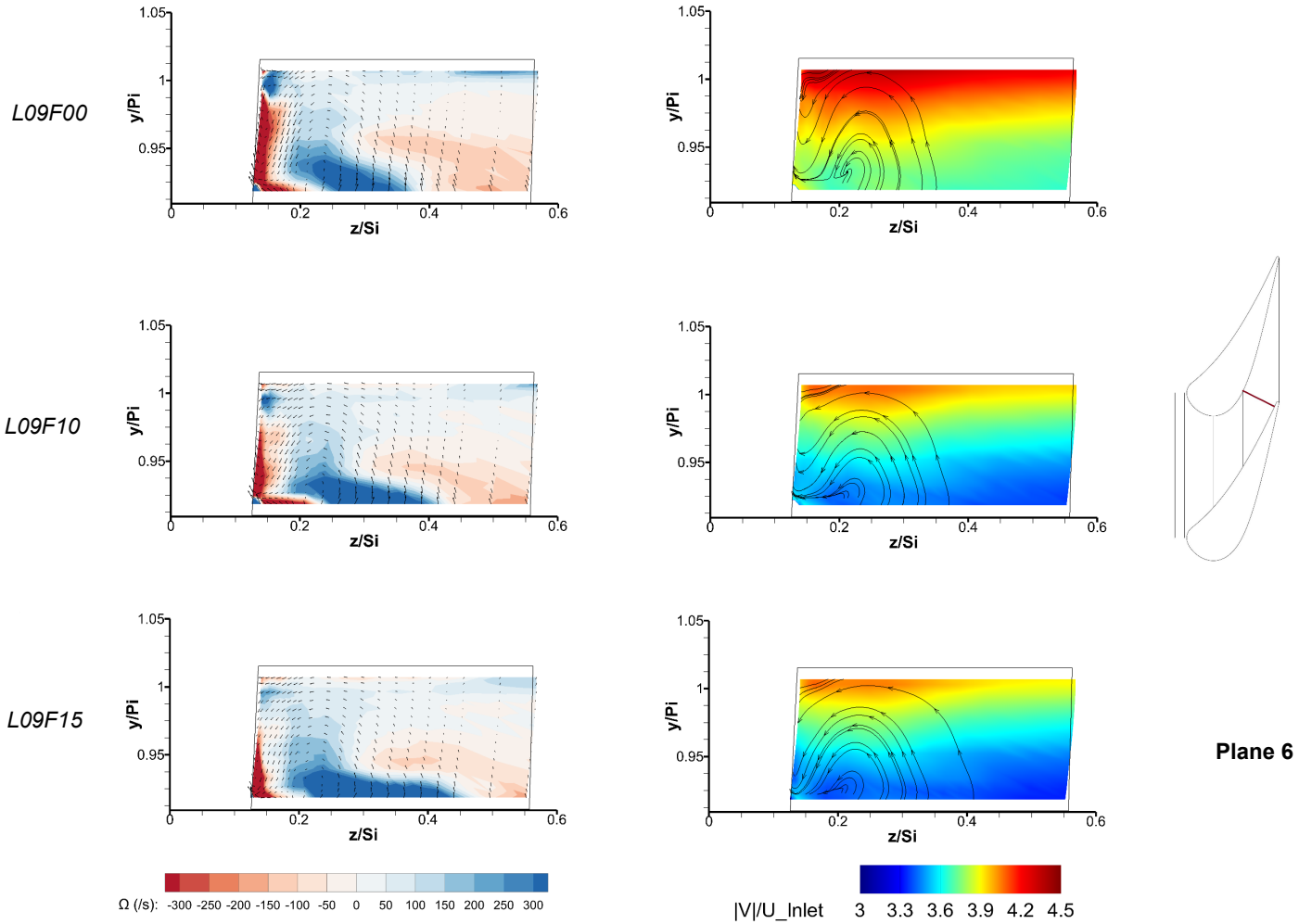

Figure 7.2.14 Vorticity contours with secondary flow vectors and velocity contours with streamline traces for the L09 cases of plane 6

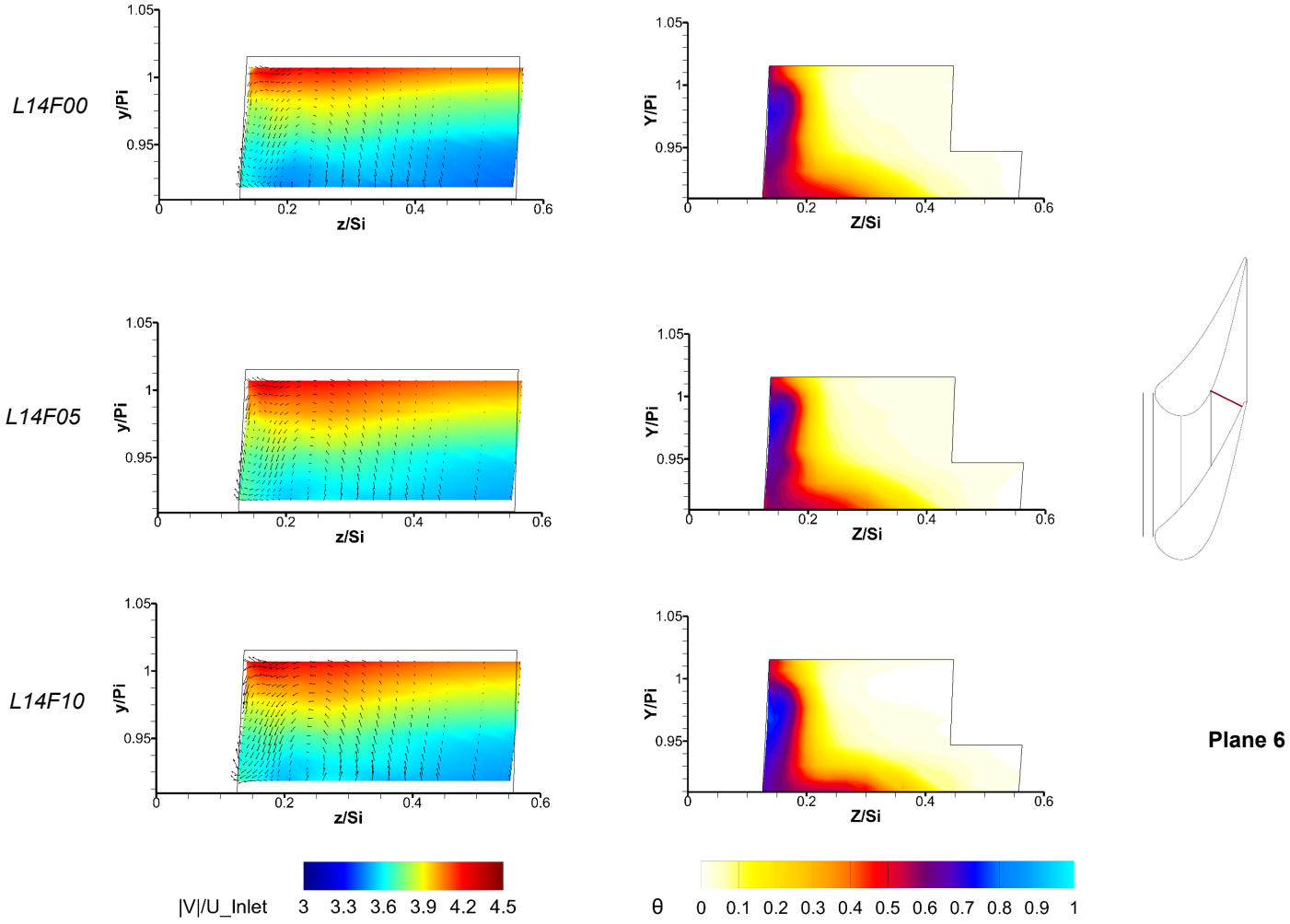

Figure 7.2.15 Thermal contours and velocity contours with secondary flow vectors for the L14 cases of plane 6

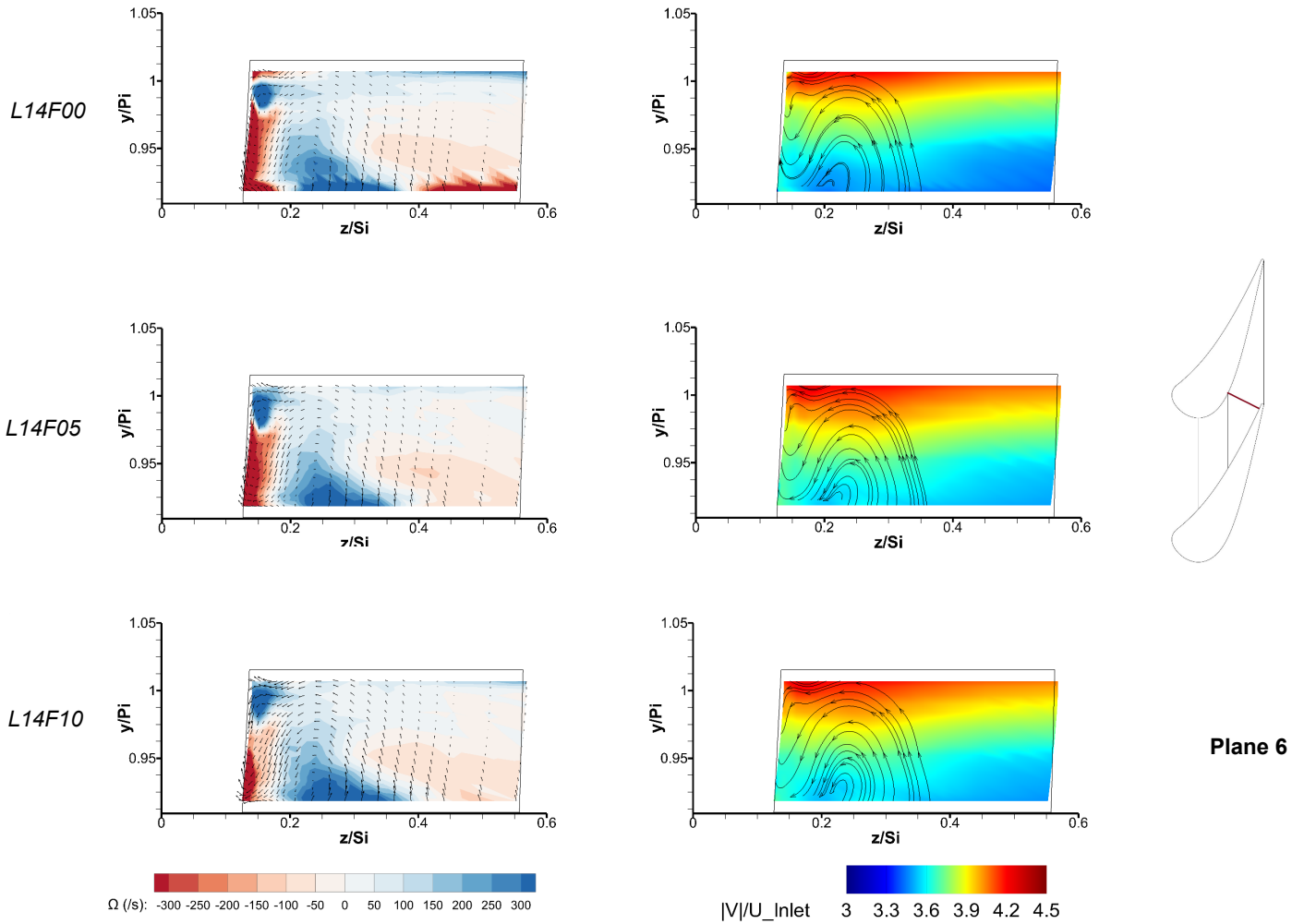

Figure 7.2.16 Vorticity contours with secondary flow vectors and velocity contours with streamline traces for the L14 cases of plane 6

Coolant spread along the pressure surface is seen to increase in the spanwise direction with increases in film coolant rate. This is corroborated directly by the vorticity contours in which the extent of the high positive vorticity region (corresponding to the impingement vortex) is the same as the extent of the coolant film along the pressure surface. This confirms that the film coolant energizes the impingement vortex.

Plane 5

Plane 5 is the passage exit plane. Thermal and aerodynamic contours are shown in figs. 7.2.17 and 7.2.19, while streamline traces and vorticity contours are shown in figs. 7.2.18 and 7.2.20. The region below y/Pi = 1.05 is in the wake region where the flow streams from pressure side and suction side of the vane passage, mix and disrupt the fluid mechanics. The facility was not designed to properly capture the turbine flow in this region. Hence, flow features are not precisely accurately documented for this region. Thermal contours in this region are plotted but it should be noted that the coolant distribution in this region may not reflect actual engine conditions due to different downstream conditions between the engine and the test facility. Most of the effects that have been seen in upstream planes are seen in the exit plane. Therefore, a brief explanation of each of them is given in relation to the contours at the exit plane.

The impingement vortex can be clearly seen in all cases. Its center is close to y/Pi = 1.05. Based on the direction of the vorticity contours, one can see that the vortex size in the horizontal direction is greater for higher film coolant MFR cases as the film coolant energizes the vortex. Also, although the vortex helps in not letting the coolant migrate toward the suction side, there is coolant mixing at the center of the vortex, which reduces coolant effectiveness. In the case of plane 5, coolant mixing is seen near y/Pi = 1.15 and z/Si = 0.3.

The impingement vortex has been the dominating vortex for most of the passage, even at the exit plane, to y/Pi = 1.7. It is mostly responsible for suppressing the secondary flows. However, the intensity of this vortex is substantially decreased at the exit plane. This, in turn, makes the passage vortex, which was not seen clearly upstream of the throat of the passage, to be more prominent and have a more pronounced effect on coolant distribution in the vane passage. Additionally, the horseshoe vortex has also diminished and is not seen at this plane. Its disappearance helps the endwall cross-flow to be more uniform in the pitch direction. The vorticity plots show a thin, yet strong, negative vorticity on the endwall. Near the suction side, however, the passage vortex causes negative vorticity to decrease in intensity but increase in size. The passage vortex is causing a decrease in the absolute velocity due to circulation near the suction surface, as evidenced by the velocity contours. The passage vortex strength decreases with increases of film coolant flow rate, as seen by the decrease in the negative vorticity near y/Pi = 1.9. But this decrease is not very substantial, possibly because the effects of the impingement vortex have waned so much by this point that even the highly energized impingement vortices (in the case of high film coolant MFRs) are not able to resist passage vortex effects.

In conventional cascades (no combustor coolant present), the effects of the endwall cross-flow and the passage vortex are considered undesirable as they create non-uniformity in coolant distribution in the pitch direction. However, with the passage vortex absent over most of the vane passage, the endwall cross-flow is instrumental in spreading the coolant evenly on the endwall, making it a desirable feature. Although the impingement vortex helps in resisting the passage vortex, it causes some additional mixing, which decreases the effectiveness. But, the endwall cross-flow is also restricted in the spanwise direction due to the impingement vortex, which is desirable in this cascade. This is true only when the cross-flow is more dominant than the coolant momentum. The cross-flow vorticity is

the least influential for the L14F10 case, among all the L14 cases. Also, the coolant effectiveness for the L14F10 case on the wall is actually less than that of the L14F00 case, which has no film coolant injection. The highly effective, thin coolant film formed on the endwall for all other cases is missing in the L14F10 case. This can be explained due to the higher momenta of both louver coolant and film coolant. The coolant streams are more successful in penetrating into the mainstream, losing their effectiveness due to mixing. This effect was seen mildly for all planes in this case but is very prominent on the exit plane. This mixing decreases the coolant effectiveness on the endwall for this case. This result shows also that excess coolant injection leads to reduced cooling.

Due to the impingement vortex, the pressure surface is provided with more coolant than in conventional cascades. This is clearly shown in all the thermal contours near the pressure surface. Also, it is, as before, explained in that the impingement vortex increases in strength with increases in film coolant flow rate. This shows coolant coverage for over a longer spanwise distance on the pressure surface. This is observed on the exit plane as well; however, as this is in the wake region, this result may not be seen exactly as in the real condition, due to the cascade geometry. Nonetheless, the upstream planes support the notion that the actual distribution for the exit plane near the pressure surface will be close to that seen in these contours.

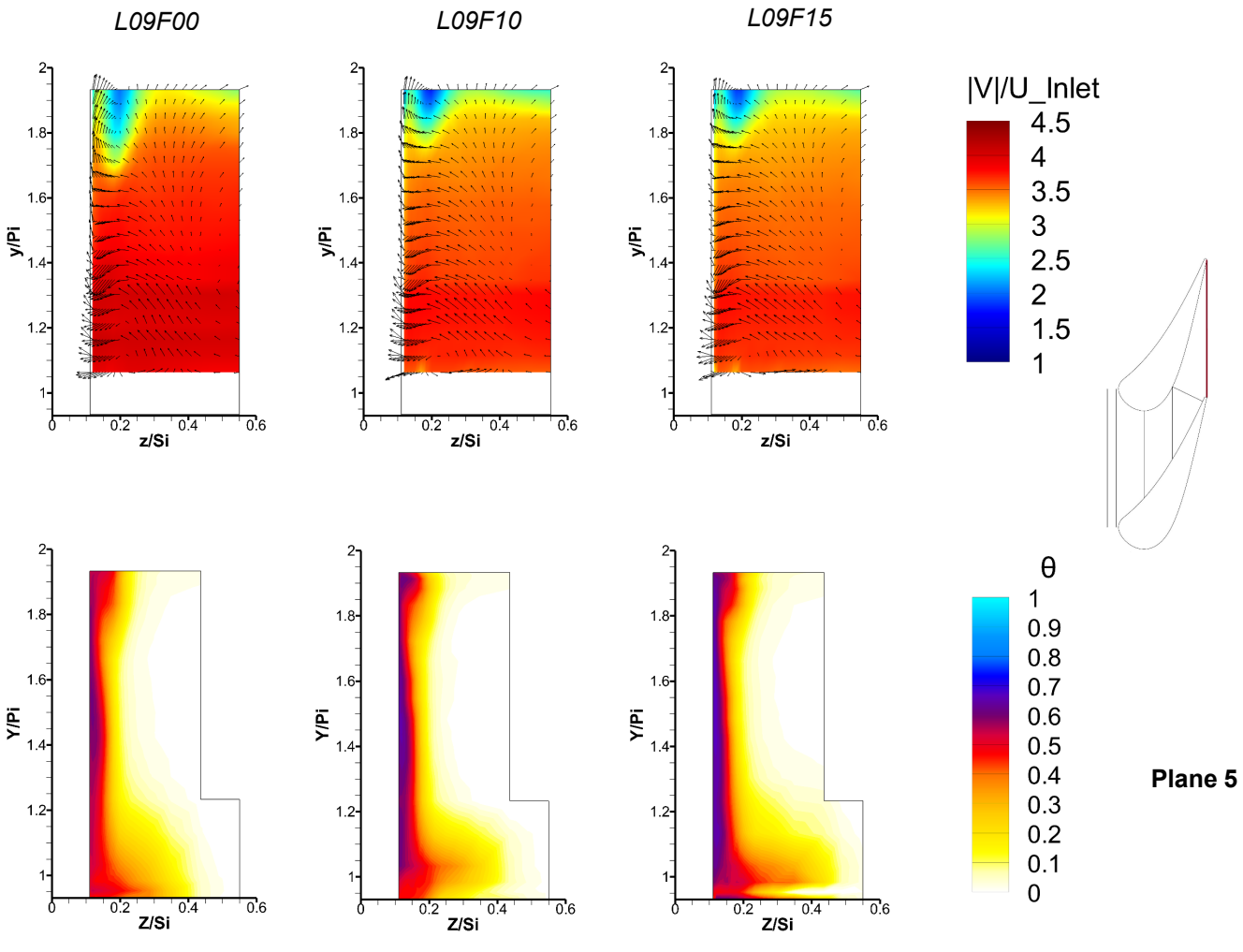

Figure 7.2.17 Thermal contours and velocity contours with secondary flow vectors for the L09 cases of plane 5

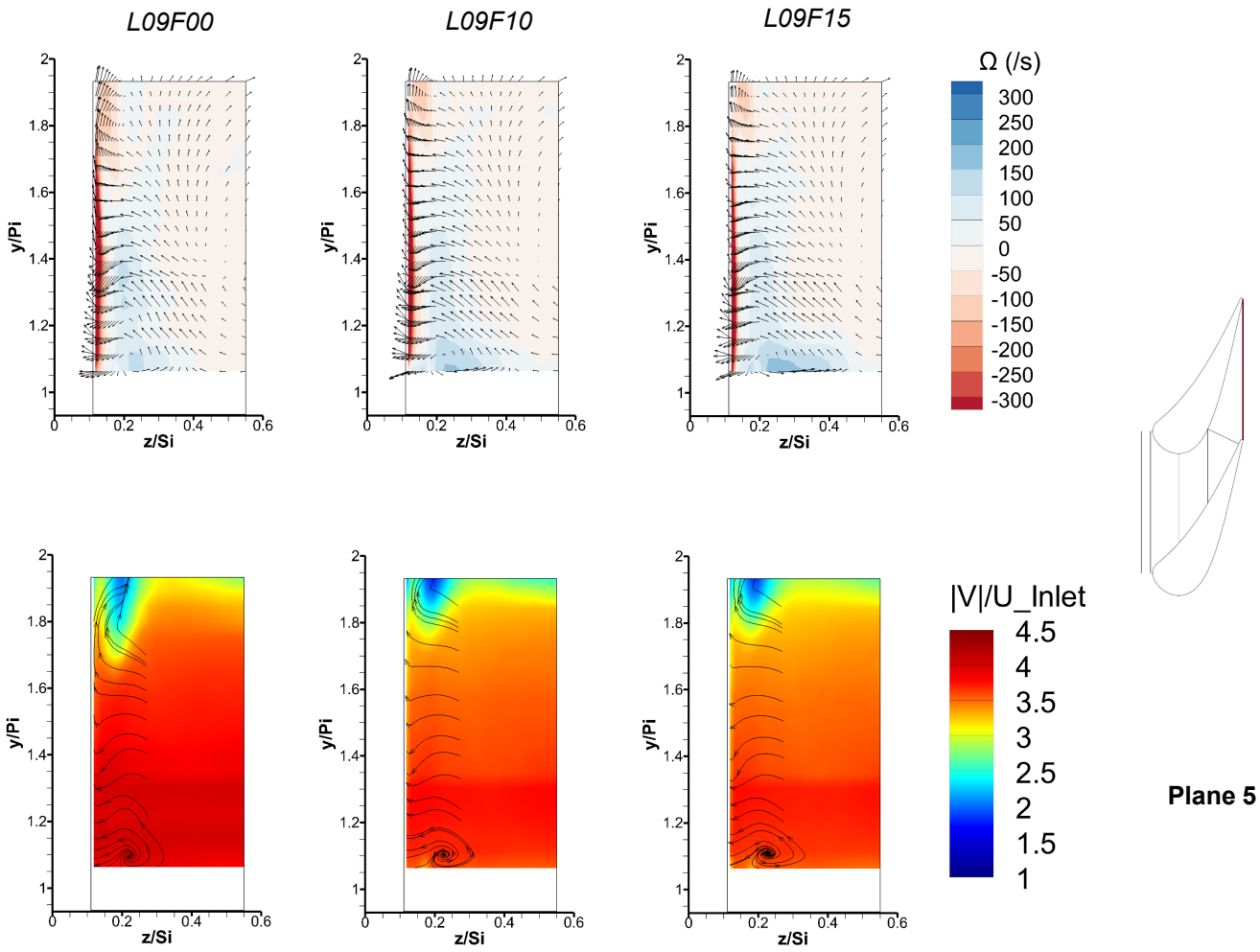

Figure 7.2.18 Vorticity contours with secondary flow vectors and velocity contours with streamline traces for the L09 cases of plane 5

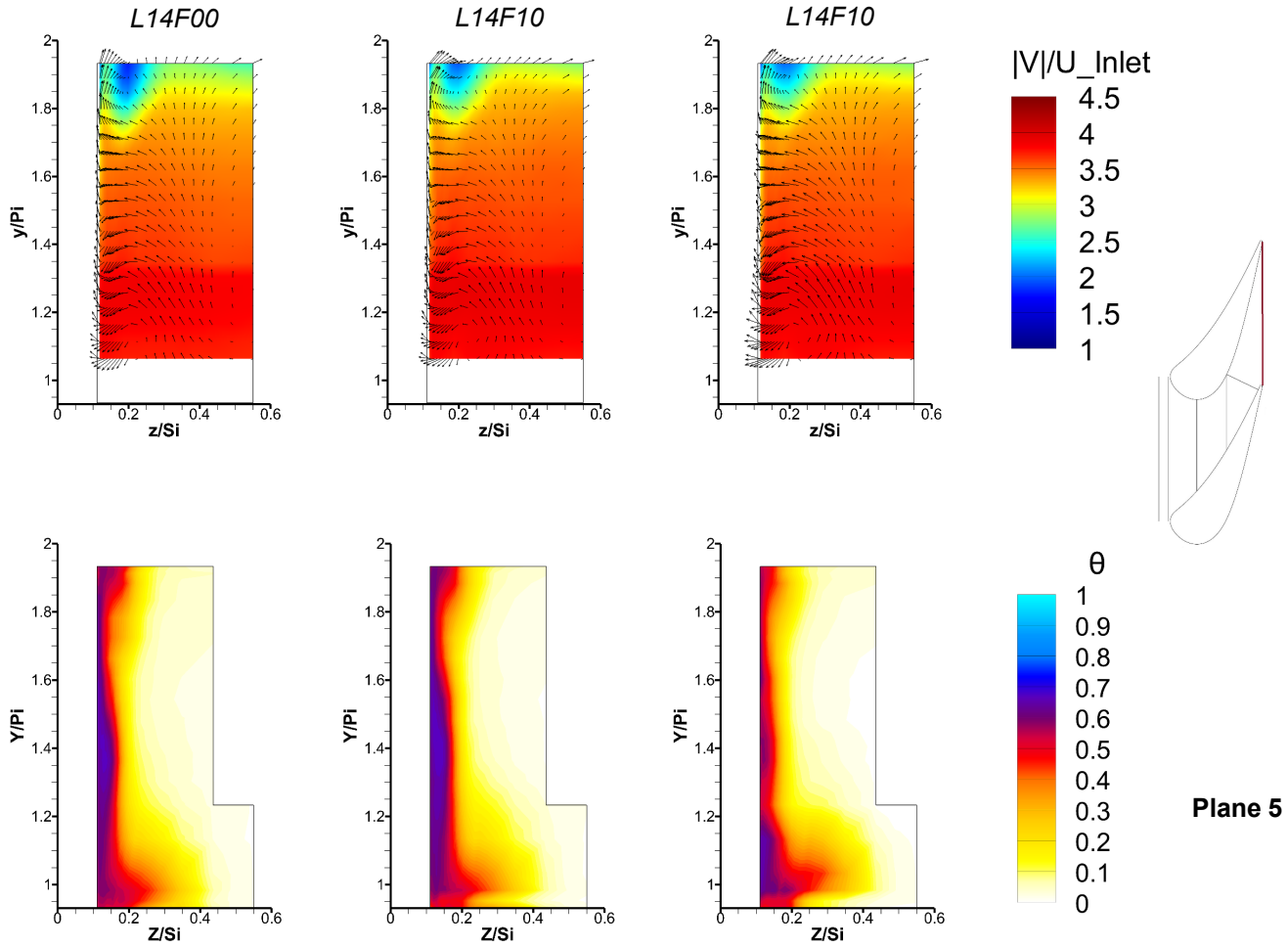

Figure 7.2.19 Thermal contours and velocity contours with secondary flow vectors for the L14 cases of plane 5

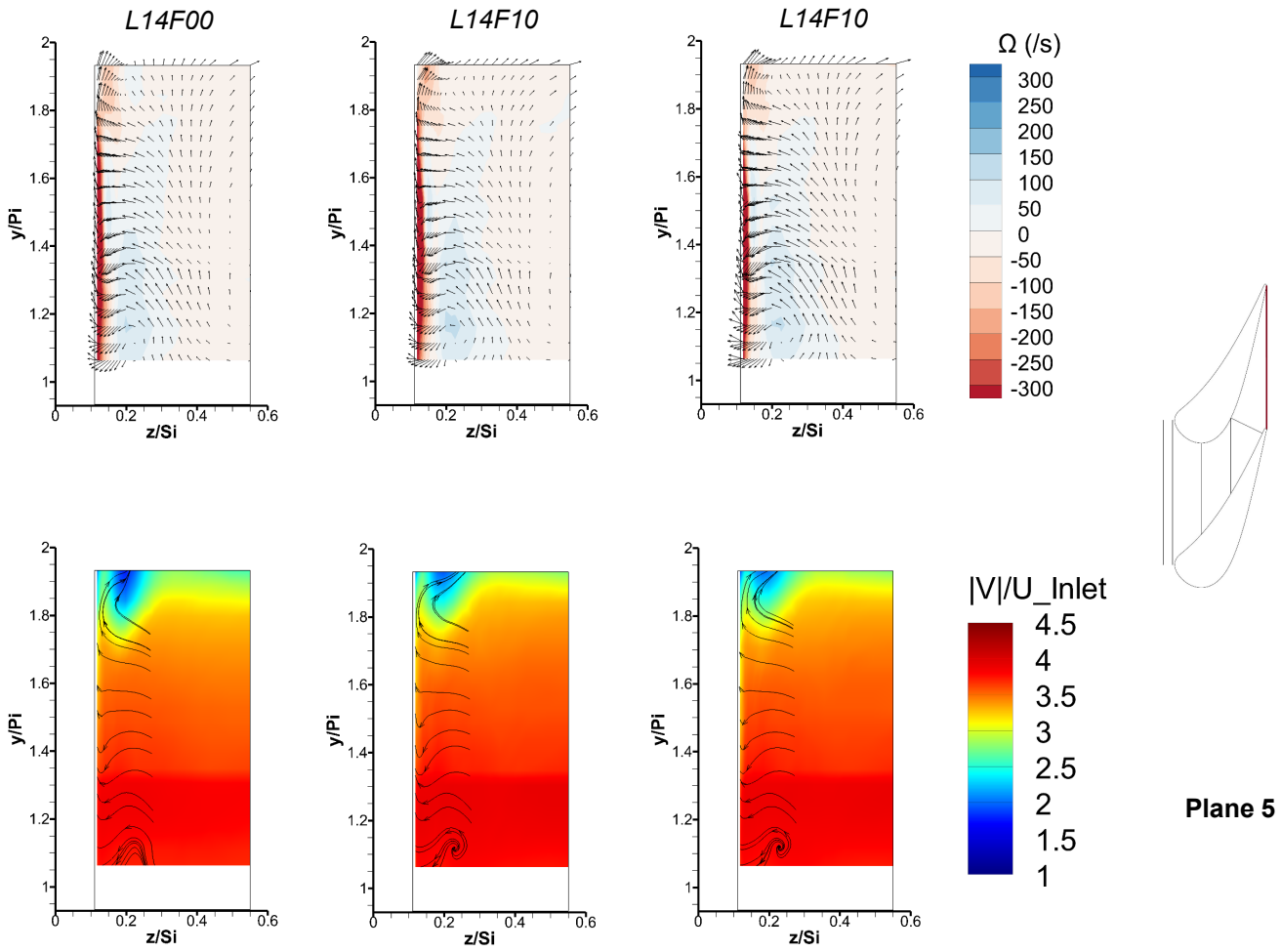

Figure 7.2.20 Vorticity contours with secondary flow vectors and velocity contours with streamline traces for the L14 cases of plane 5

7.3. Effects of Changing the Louver Coolant Mass Flow Ratio

For this section, the in-field measurements for three different louver cooling MFRs are discussed. The louver cooling MFRs are 0.37% (L04), 0.92% (L09) and 1.43% (L14). For every louver cooling flow rate, two conditions of film cooling flow rates are compared. One is no film injection (F00) and the other is an MFR of 1% (F10). The reason for this is that these two film cooling cases are the only cases for which data are available for a survey across all cases of various louver cooling flow rates. Also, this comparison is supported by a comparison between the different film cooling MFRs presented in section 7.2 and in Alqefl [40].

As thermal and aerodynamic contours for some of the following cases have been shown in earlier sections, the thermal and aerodynamic data are presented together. The contours shown in these plots are for the non-dimensional temperature recovery values, while the aerodynamic data are presented in the form of streamlines. This is done as such because the relationship between the vortices present in the passage and the coolant distributions have been made evident in the earlier section.

It should be noted that the L04 cases have been referenced directly in Alqefl [40] but the plotting graphics are not the same for the L09 and L14 cases (they were done as part of this study). Also, some annotations by Alqefl are also present on these contours. Therefore, all plots of this case are presented together in fig. 7.3.1. The changes from previous presentations are minor. Lastly, the co-ordinate system used by Alqefl was a bit different than that used for this study. Therefore, the absolute co-ordinates in the z/Si direction are shifted, slightly. However, as the scales of the plots are the same, making comparisons easy.

Plane 1

For this plane, the aerodynamic data were not measured. Figure 7.3.2 shows the thermal contours for the louver coolant cases. For F00 cases, a small blob of coolant is expected near the suction side as the combustor coolant redistributes itself by the streamwise position of plane 1, due to an elliptic (mathematical) effect of downstream passage turning. The blob increases in thickness (but not in size, in the pitch-wise direction) with increasing louver coolant flow rate; effectiveness of coolant coverage also increases. This is expected, as more coolant is present in higher louver cooling MFR cases for redistribution and the effusion coolant is probably shielding the louver coolant from mixing with the mainstream. This creates a small region of high coolant concentration near the suction side. Also, the coolant layer near the pressure side has increased in thickness in the spanwise direction. This is so because the higher louver coolant MFR cases, especially the L14F00 case, have enough momentum of coolant to penetrate into the mainstream. As this plane is upstream of the passage, this effect is apparent at the stagnation line and, with passage aerodynamics and endwall contouring, it is expected to become more prominent downstream.

The coolant blobs seen in the F00 cases are present also in the F10 cases. The non-uniformity of the coolant distribution in the pitch-wise direction decreases with an increase in louver coolant MFR. For the L04F10 and L09F10 cases, it is possible that the film coolant introduced just upstream of plane 1 has redistributed. However, in the case of L14F10, the high momentum of louver coolant is more successful in resisting this non-uniformity in the pitch-wise direction. And, as the film coolant is between the endwall and the louver coolant layer, it remains more uniform than in the L04 and L09 cases, creating a completely uniform layer of coolant on the endwall.

It has been established that on and very near the endwall, the coolant present is almost exclusively the film coolant. Therefore, it would have made sense that, for all the F10 cases, the region near the endwall would have similar levels of coolant effectiveness. But the coolant effectiveness increases with increases in louver coolant flow rate. The reason for this is that, for the L09 and L14 cases, the louver coolant is shielding the film coolant flow from mixing into the mainstream. Therefore, although the coolant near the endwall is of the same flow rate for all cases, more coolant is retained on the endwall for the higher louver coolant MFR cases. This is an important observation as this effect is seen in the whole passage, to some degree, and is important for endwall cooling.

Plane 2

Figure 7.3.2 shows thermal contours for the passage inlet plane. For the L04 cases, the streamline traces are not available. Therefore, only the thermal contours are plotted (fig. 7.3.1). The streamlines for the L09 and L14 cases show that secondary flows are hardly affected by changes in louver coolant MFR. The impingement vortex was in the passage for these cases, but its effects are not apparent on this plane. The streamlines are pointed away from the endwall, due to the injection angles of coolant flows. The blob near the suction side is present at this plane, but its size does not increase in any of the cases, suggesting that coolant migration from pressure side to suction side is being impeded. For most of the endwall for case L09F10 and for all of the endwall for case L14F10, coolant coverage is very uniform. This is surprising as this is not true for the L04F10 case. In the L04F10 case, coolant layer thinning from pressure to suction sides occurs with a slightly higher gradient than in the other cases and continues to Y/Pi = 0.05.

In fact, for the L14 cases, the coolant layer starts thickening again below the coolant blob seen at around Y/Pi = 0.7, but well above the pressure surface. Thermal contours for this case show two different blobs in regions 0.8>Y/Pi>0.6 and 0.3>Y/Pi>0.15. The upper blob

is due to redistribution of the combustor coolant upstream of the passage. This redistribution occurs due to the cavity between the combustor wall and the film cooling wall. Computational results regarding this redistribution were presented in the appendix of Alqefl [52]. The lower blob, on the other hand, possibly forms due to the higher momentum of the coolant streams. The coolant streams are trying to penetrate into the mainstream, causing them to go farther spanwise than seen in the L09 and L04 cases. This effect should be present for all pitch-wise locations but is apparent only in the regions noted because the other regions have other, more dominating, effects. The L14 cases have displayed this tendency at numerous locations downstream, as seen in the results presented in section 7.2 and this effect is not seen in cases L09 and L04. So, it is reasonable to assume that this is due to higher coolant momentum.

For both F00 and F10 cases, coolant spreads in the spanwise direction near the stagnation line (y/Pi = 0). The mechanism for this is the modified velocity profile along the spanwise direction, as explained in detail by Alqefl [40] and briefly discussed in an earlier section of this report. As expected, as the louver coolant flow rate is increased, the coolant runs farther along the pressure side, as can be seen in the contours. This creates a second bulge for the L04 and L09 cases and a third bulge for the L14 cases (indicated for the L14F10 case in fig. 7.3.2). Also, the thickness of the bulge, compared to the thickness of the coolant layer near y/Pi = 0.4 (where most of the effects of secondary flows are minimal), is decreased as the louver coolant MFR increases. This is expected because of the stronger non-uniformity in the pitch-wise direction for the lower-louver-coolant-MFR cases.

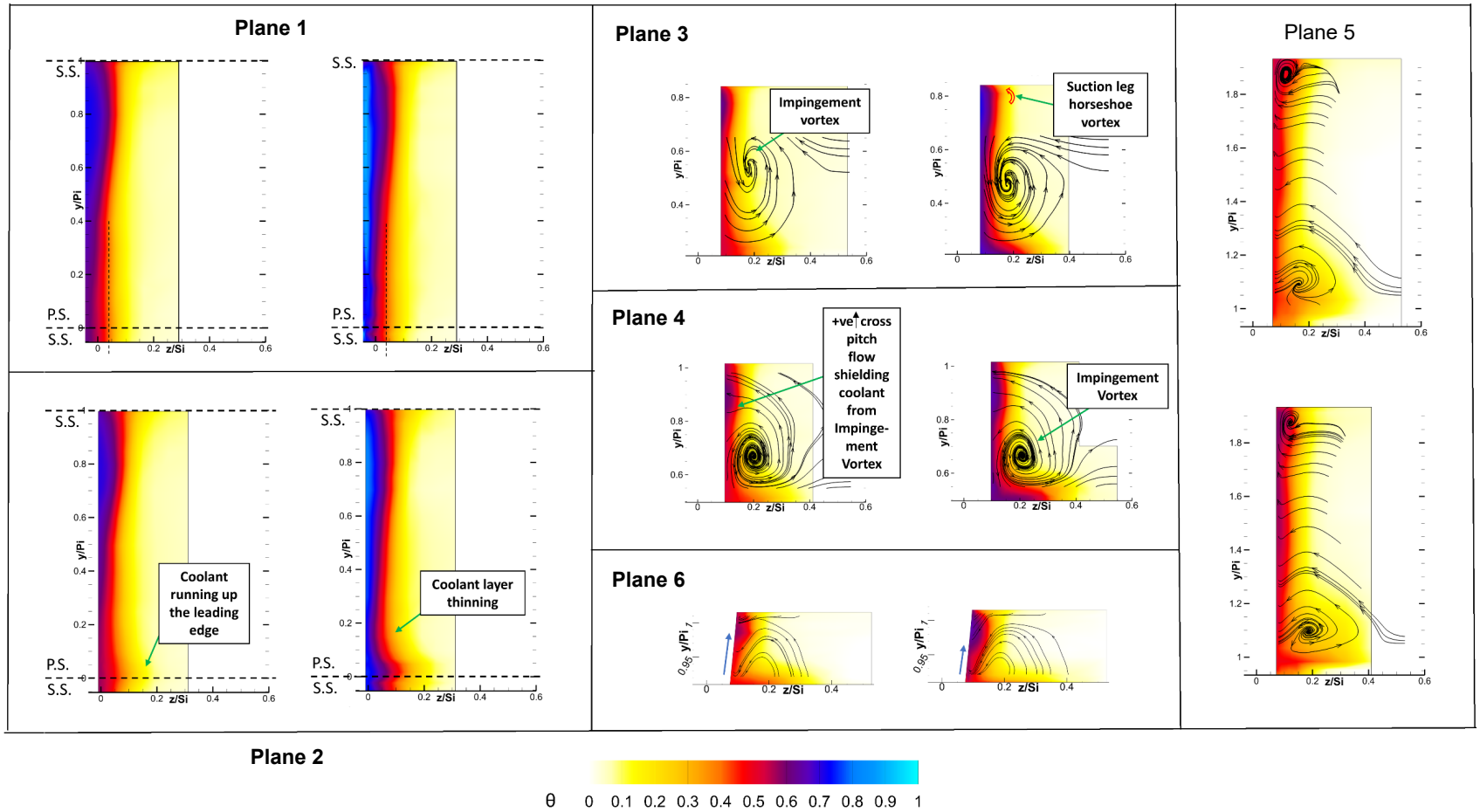

Figure 7.3.1 Available data for L04 cases. Referenced from Alqefl [40]. For planes 1 to 4 and 6 left case is F00 and right case is F10. For plane 5 upper case is F00 and lower case is F10.

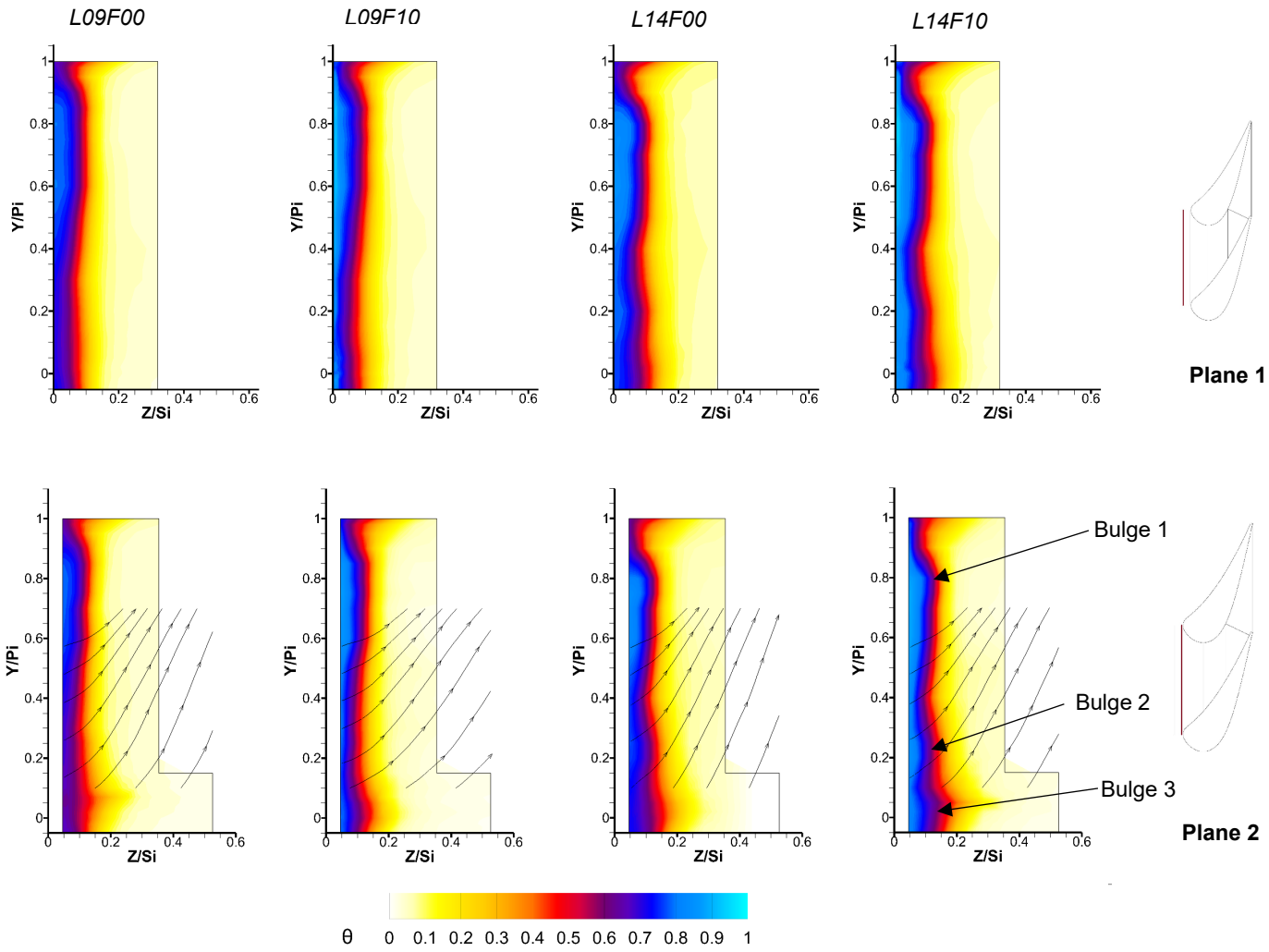

Figure 7.3.2 Thermal contours with streamline traces for L09 and L14 cases of planes 1 and 2

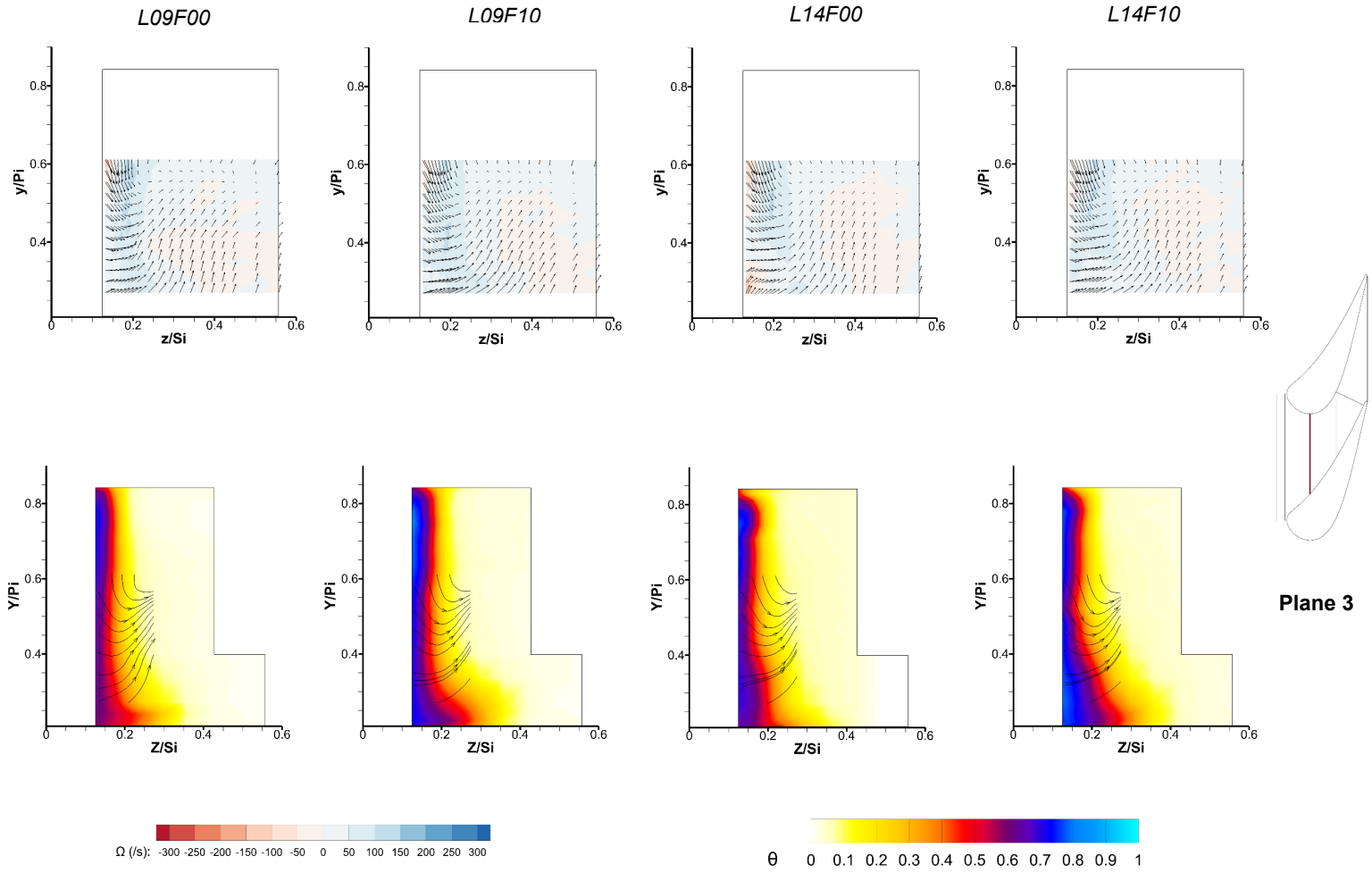

Figure 7.3.3 Vorticity contours with secondary velocity vectors and thermal contours with streamline traces for L09 and L14 cases of plane 3

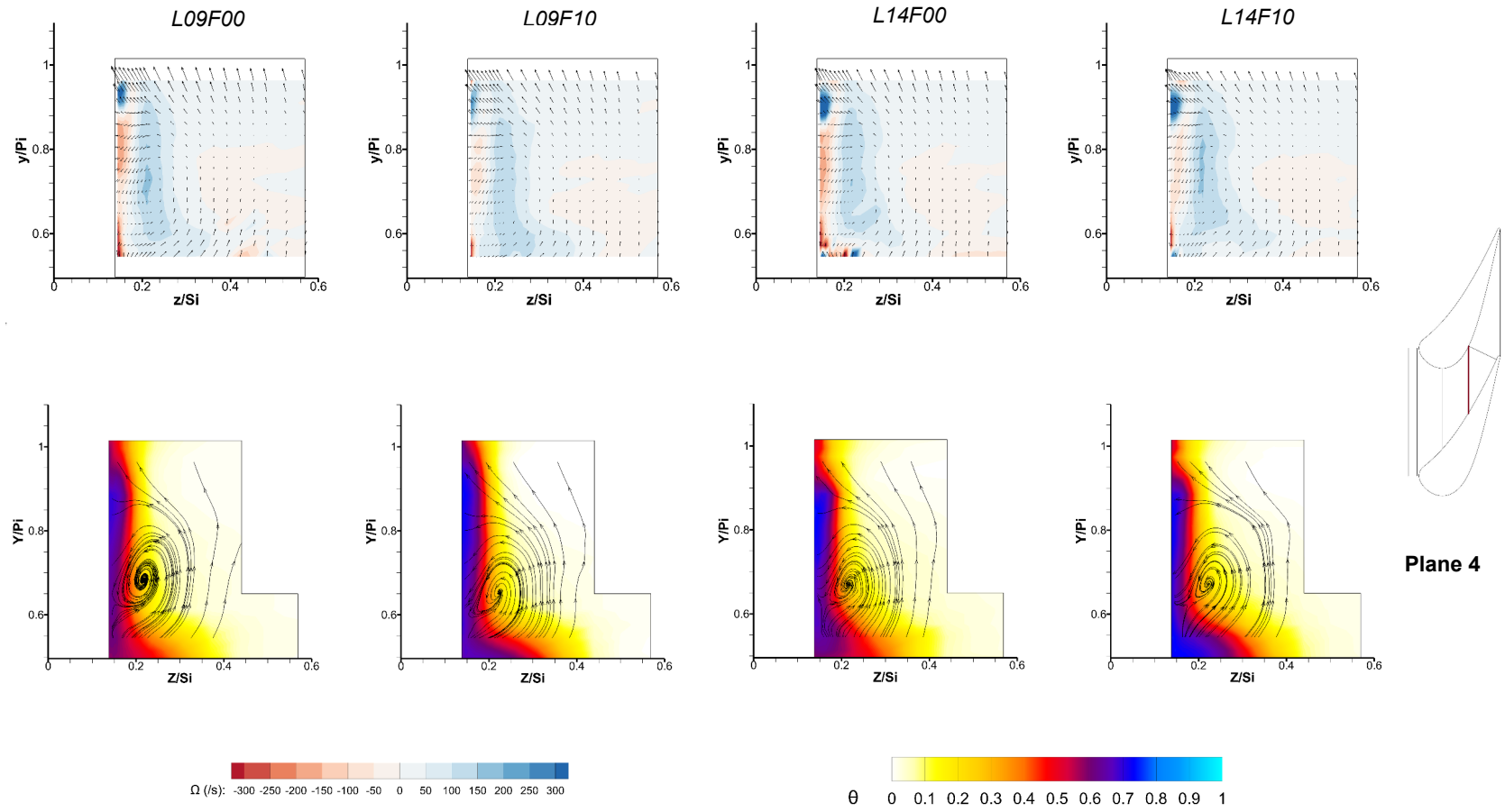

Figure 7.3.4 Vorticity contours with secondary velocity vectors and thermal contours with streamline traces for L09 and L14 cases of plane 4

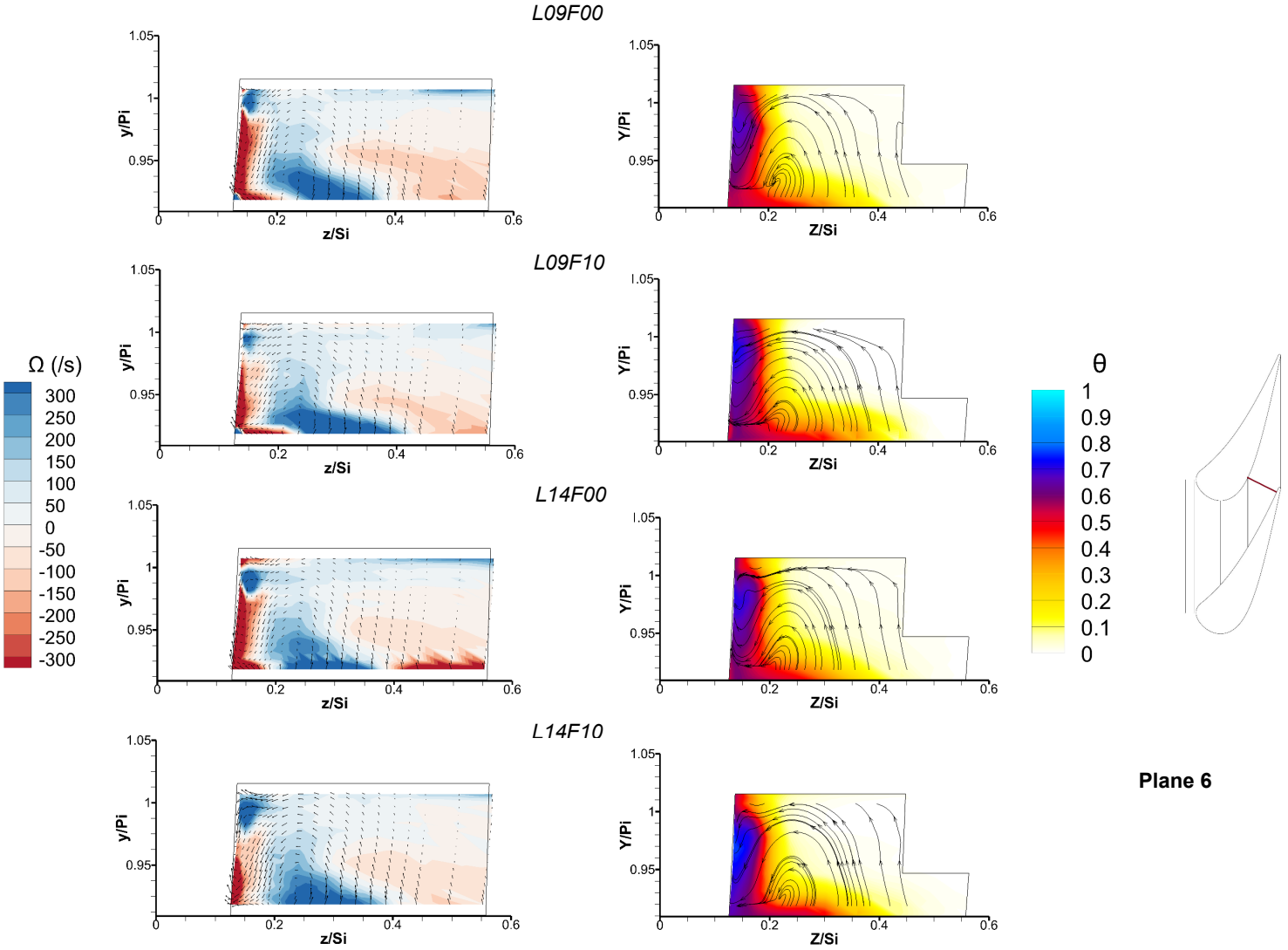

Figure 7.3.5 Vorticity contours with secondary velocity vectors and thermal contours with streamline traces for L09 and L14 cases of plane 6

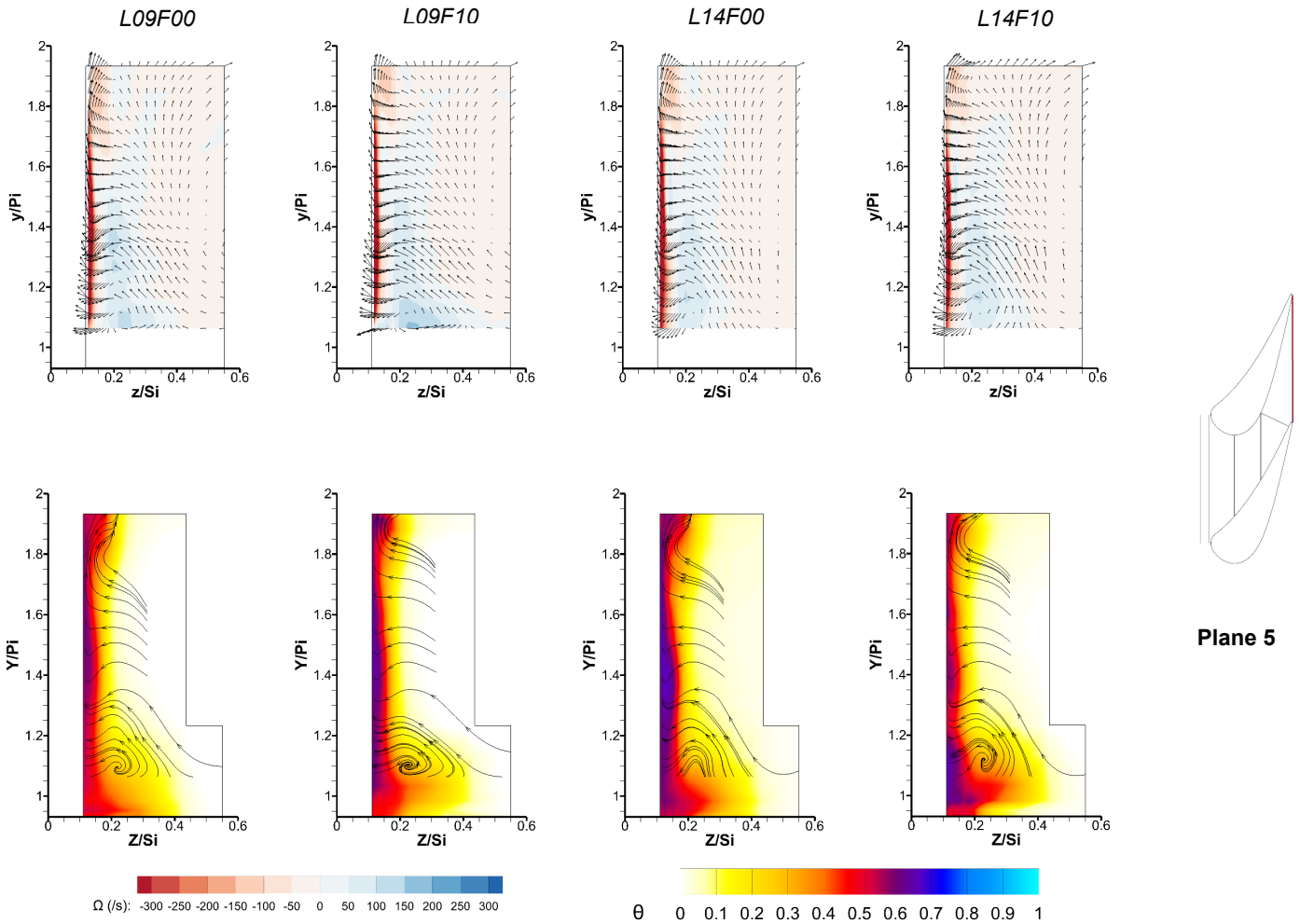

Figure 7.3.6 Vorticity contours with secondary velocity vectors and thermal contours with streamline traces for L09 and L14 cases of plane 5

Plane 3

The results for plane 3 are shown in fig. 7.3.3. The most striking difference between the three cases of different louver coolant flow rates is the location of the impingement vortex. For the L04 cases, the vortex center and its size are clearly visible; however, for the L09 and L14 cases, the center of the vortex is not seen, and the effects of the vortex can be seen only by looking at the secondary flow vectors. To ensure that the impingement vortex is present in these cases, vorticity contours were plotted. Mildly positive vorticity can be seen near the endwall, indicating that the impingement vortex effects are present. This supports the hypothesis made earlier that the location of the impingement vortex has shifted vertically, beyond the measurement zone, for the L09 and L14 cases. When the L09 and L14 cases' vorticity contours are compared, this positive vorticity is neither larger nor more intense in the L14 cases than in the L09 cases, indicating that the impingement vortex is little affected by the changes in louver cooling flow rate.

Although aerodynamic measurements were not taken near the suction surface, horseshoe vortex effects can be seen in the thermal contours. For all cases, the small coolant blob, suggesting mixing, can be seen at the same location and over about the same area. This suggests that the horseshoe vortex has not changed much in this plane with changes in louver coolant MFR. Small hints of endwall cross-flow are present in the vorticity contours of the L14 cases, but the L09 cases do not show negative vorticity near the endwall. This may be because the impingement vortex is stronger upstream in the passage. Decay of the impingement vortex from plane 3 to the exit plane was observed in a preceding section. The strong impingement vortex on this plane is suppressing the endwall cross-flow on this plane, although these flows start to appear on the downstream planes, as seen before.

It is seen that the impingement vortex also causes coolant spreading on the pressure surface. As the strength of the vortex is not affected, the coolant spreading is not expected

to change. The lack of change in the spanwise distance of coolant coverage can be seen in the thermal contours. This serves also as a minor verification that the impingement vortex is present in the L09 and L14 cases, even though it is not clearly visible.

Plane 4

Aero-thermal contours for plane 4 are plotted in fig. 7.3.4. The vorticity contours for L09 and L14 cases are also presented. It is seen that there is some increase in the spread of positive vorticity as well as some increase in the intensity of positive vorticity as the louver coolant MFR is increased. The streamlines of L04 cases show a less intense impingement vortex, based on the more rapid circulation pattern seen in the L09 and L14 cases. Unfortunately, the vorticity contours for the L04 cases are not available, so this cannot be said with absolute certainty.

Near the suction surface-endwall corner, the effects of the suction leg of the horseshoe vortex are seen in the thermal contours in the form of decreased coolant film thickness. This decrease in coolant film thickness is observed in bothL04 and L14 cases. The corresponding vorticity contours show that the intensity of the horseshoe vortex increases with increases in louver coolant MFR. Also, as observed before, the increase in film coolant MFR decreases the intensity of the horseshoe vortex. It is surprising that the two coolant streams have opposite effects on passage aerodynamics. This seeming discrepancy can be explained by discussing the louver coolant momentum. For the L09 cases, the louver coolant momentum is not high enough for penetrating into the mainstream, which shields the film coolant flow and, in turn, decreases the effects of both the horseshoe vortex and the endwall cross-flow, by the mechanism explained in the preceding section. But, when the louver coolant MFR is increased, the louver coolant has a tendency to penetrate and mix with the mainstream. This reduces the shielding effect, making the film coolant more prone to lift off of the endwall. This, in turn, decreases

opposition to cross-flow effects and the horseshoe vortex, for higher louver coolant flow cases. Both of these changes can be clearly seen in the vorticity contours. The more intense horseshoe vortex also causes the coolant mixing seen in the thermal contours at the same location.

Signs of the passage vortex are seen also in the vorticity contours along the suction surface. More prominently, thermal contours show substantially decreased film coolant thickness above the coolant blob formed by the horseshoe vortex. Clearly, there is coolant lifting off the endwall and moving toward the midspan along the suction surface, due to the passage vortex. This scenario is based on the decreased coolant effectiveness near the suction-side-endwall corner. The L04 cases do not show this lift-off while the L09 cases show that this lift-off is not as strong as in the L14 cases, suggesting that the passage vortex is strengthened with increases in louver coolant flow rate. This can again be attributed to the higher momentum of louver coolant leading it to move from endwall to midspan, a direction opposite to the sense of rotation of the impingement vortex. As this effect is not very dominant, it is probably getting suppressed in the region with high positive vorticity, i.e. the region significantly affected by the impingement vortex. However, near the suction surface, the louver coolant may cause a decrease in intensity of the impingement vortex which, indirectly, would cause an increase in passage vortex intensity. It was not possible to take the aerodynamic data near the suction surface and, therefore, verification of louver coolant acting against the impingement vortex from the vorticity contours cannot be made. Nevertheless, the thermal contours are supporting this hypothesis.

The pressure surface coolant spread is, once again, the same for all the cases. The vorticity strengths near the pressure surface for all cases shown in fig. 7.3.4 are comparable as well. This is confirming that the impingement vortex strength is not

changing with changes in louver coolant MFR. This is because, although the louver coolant is increased, the effusion coolant (which has about 5 times the flow rate of the louver coolant) is the same for all cases. Therefore, as the louver coolant changes, the local features near the endwall are affected but not those features that are prominent in the spanwise direction, mainly the formation of the impingement vortex.

Plane 6

Results for the streamline-normal plane 6 are shown in fig. 7.3.5. The impingement vortex has increased, compared to those of plane 4, significantly in intensity for all the cases. The cross-sectional area near the throat is very small compared to that of plane 4 and, therefore, the impingement vortex has decreased in size and increased in intensity, which can be seen in the vorticity contours. The streamlines also show that the effect of this vortex is across the whole pitch. Both the F00 and F10 cases show that intensities of the vortices are the same and so are the sizes, showing again that the impingement vortex is not affected much by changes in louver coolant flow rate. Also, for all cases in the vicinity of z/Si = 0.4, a mildly negative vorticity is seen near the pressure side. However, based on the streamlines, the flow on plane 6 eventually becomes influenced by the impingement vortex and starts moving toward the endwall.

In terms of the horseshoe vortex and endwall cross-flow, the trends on this plane are complementing the trends seen on plane 4. Both the horseshoe vortex and the cross-flow increase in their intensities with an increase in louver coolant flow rate, due to the high momentum of the louver coolant blowing into the mainstream rather than following the impingement vortex direction near the suction surface-endwall corner. This, as explained before, causes the passage vortex to become stronger. The negative vorticity near the suction surface for the L14F00 case is an indication of a growing passage vortex. Quite possibly, the same vorticity may exist in the L14F10 case, but it may be lying in the region

very close to the suction wall where aerodynamic data cannot be taken. When the thermal contours for cases L09F00 and L14F00 are compared, one sees a decrease in coolant thickness at the same locations where negative vorticity is observed. For the L09F10 and L14F10 cases, the same observation can be made.

No changes to coolant spreading rate along the pressure surface were seen with increases in louver coolant flow rate. As the pressure-surface end of this plane is practically at the trailing edge, it can be concluded pressure surface cooling is insensitive to changes in louver coolant MFR. Although cooling the pressure surface has not been the primary objective of introducing any of the coolant streams, this information is still useful toward modifying pressure surface cooling schemes in the future.

Plane 5

Figure 7.3.6 shows contours for plane 5, which is the passage exit plane. The intensity of the impingement vortex has decreased as compared to that of plane 6, as the cross-section area increase has stretched the vortex in the pitchwise direction. The center of the vortex is at the same location for all cases, except for case L14F00, which probably has its center somewhere in the wake region. The impingement vortex affects flow in the pitch-wise direction up to about y/Pi = 1.6 for all cases, showing that vortex stretching is of the same extent for every case.

The horseshoe vortex has completely disappeared after plane 5. This can be attributed to the increasing effect of the passage vortex which, in turn, was caused by weakening of the impingement vortex. Still, a region of almost zero vorticity exists near where the horseshoe vortex had appeared in upstream planes. The flow in this region is probably influenced by two opposite directions of rotation due to the passage vortex and the horseshoe vortex, resulting in a near-zero vorticity. The increase in intensity and, more importantly, the size of the passage vortex, are seen prominently in this plane. The

passage vortex effects are seen clearly beyond y/Pi = 1.7, for all cases. As seen in the upstream planes, the intensity of the passage vortex increases with increases in the louver coolant flow rate. Also, the streamlines show turning of the coolant flow due to the passage vortex. Endwall cross-flow is very uniform in the region below the passage vortex, more than seen on any of the upstream planes. Also, the cross-flow merges directly into the passage vortex due to not having the horseshoe vortex. This can be seen in the vorticity contours where the vorticity along the endwall is entirely negative for the first time. The nature of the passage vortex and the cross-flow, seen in this plane, resemble that which is seen in a conventional cascade, though the intensities of these effects are much lower in the current study. The lower intensity of these effects show that the combustor coolant injection is helping cool the endwall and vane surfaces.

Chapter 8. Results and Discussion: Surface Effectiveness Measurements

8.1. Order of Presentation

The previous chapter explained how the coolant streams interact in the vane passage. This interaction decides how the coolant is spread on various surfaces in the vane passage. This chapter will present and discuss the cooling of the endwall as well as the pressure and suction surfaces of the vanes. The three subsections in this chapter talk about thermal contours on the endwalls, pressure surfaces and suction surfaces. Under each subsection, the effects of changing the film coolant flow rate are explained first, followed by the effects of changing the louver coolant flow rate.

8.2. Endwall Thermal Contours

The endwall contours for all cases are shown in fig. 8.2.2. The film coolant flow rate increases from left to right in the figure while the louver coolant flow rate increases from top to bottom. The total MFR of the all coolant flows (which is the sum of flow rates of effusion coolant, louver coolant and film coolant divided by the mainstream flow rate at the exit of the nozzle) for each case are noted in the boxes. These numbers are color coded where the same color indicates an approximately equal amount of net coolant flow rate. This is done to show performance as dependent on cooling effectiveness and net flow rate. Similar to the in-field measurements' discussion, these contours will be first discussed with respect to changing the film coolant MFR and then discussed with respect to changing the louver coolant MFR.

Effects of Changing the Film Coolant Mass Flow Ratio

As previously discussed, the in-field measurements show that the louver coolant shields the film coolant, helping it to remain near the endwall region. Therefore, for the entire passage, an increase in the coolant effectiveness is expected with increasing film coolant. A significant increase is seen in the cases with film coolant present when compared to the F00 cases. However, further increase in film coolant beyond a point does not help much in increasing cooling effectiveness near the trailing edge. Near the leading edge, a significant increase in the coolant effectiveness is seen when L09F10 and L09F15 or L14F05 and L14F10 are compared. In this region, the film coolant momentum is significantly affecting the passage aerodynamics. But, as the trailing edge region is the one which is difficult to cool, the coolant effectiveness in that region is important. For this region, the highest film coolant flow rate cases show only marginal improvement over the medium film coolant flow rate cases. This, once again, shows that, although film coolant is necessary to cool the endwall, it is helpful only up to a certain value, beyond which the effect of increasing its flow rate becomes negligible.

Upstream in the passage, non-uniformity in the pitch-wise direction, for the L09 cases, is decreasing with increasing film coolant flow rate. This is because the higher film coolant momentum of these cases resists passage turning, tending to make coolant flow be in the axial direction. In the in-field measurements, it was seen that, earlier in the passage, the endwall cross-flow was suppressed by the momentum of film coolant. This serves as a verification of the pitch-wise uniformity in coolant distribution. But, more downstream (beyond plane 3, x/C_{ax}= 0.289), cross-flow was observed, with increasing intensity. This is complemented by the tendency of the coolant to move toward the suction side, as seen in the increased endwall coolant effectiveness near the suction side, versus the pressure side. A similar observation regarding coolant uniformity can be made also for the L14

cases. However, for the L04 cases, the uniformity in pitch-wise direction is hardly seen. This is because the louver coolant MFR of 0.37% is not enough for providing shielding for the film coolant and, therefore, the film coolant in cases L04F10 and L04F15 follows the turning passage rather than tending to remain axial. This displays the inability louver coolant for shielding in the L04 cases and shows why a higher louver coolant flow rate is desired.

Due to suppression of the passage vortex, coolant doesn't migrate to the suction side until almost the end of the passage (explained in section 7.2). This is seen in the endwall contours as well. It is also known that the impingement vortex increases in intensity with increasing film coolant flow rate, which would also mean that more coolant tends to remain near the pressure surface (due to the direction of rotation of the impingement vortex). In general, the pressure side region of the endwall is seen to be cooled with higher effectiveness with increasing film coolant flow rate. It is also seen that, although most of the coolant tends to remain on the pressure surface, some highly effective coolant is still present near the suction surface for the entire passage. This may be an indication of a horseshoe vortex suction leg. This vortex moves coolant along the suction surface and on the endwall near the suction surface, creating a thin layer of coolant near this region. For the L09 cases, endwall coolant effectiveness near the pressure and suction surfaces has similar values for all cases, increasing with increases in film coolant flow rate. For the L14 cases, endwall cooling effectiveness near the suction surface decreases with increasing film coolant flow rate. This indicates that endwall cross-flow suppression is increasing with increases in impingement vortex strength, which is caused by the increase in film coolant flow rate. It can be said that the endwall near the pressure surface has similar cooling effectiveness values irrespective of film coolant flow rate, while the endwall cooling effectiveness near the suction surface increases for the L04 cases, remains about the

same for L09 cases, and decreases for the L14 cases, with increasing film coolant flow rate.

In most of the L09 and L14 cases, small, low-effectiveness spots can be seen near x/C_{ax} = 0.6 (indicated in fig. 8.2.2). Aerodynamic contours at these locations (planes 4 and 7) show that these spots are near where the effects of the impingement vortex are decreased, and the passage vortex is driving the coolant away from the endwall toward the midspan (based on the vorticity and secondary vectors plots presented and discussed in section 7.2). Therefore, the endwall is deprived of coolant, creating a very small spot with low effectiveness (shown in fig. 8.2.1). Theoretically, these spots should exist on every plane of every case that shows the passage vortex. But, as this spot is small, the measurement locations must be very close to it to capture this feature. It is suspected that that is the reason for this effect to not be seen in the L09F10 case and be seen only on planes 4 or 7 for the rest of the cases.

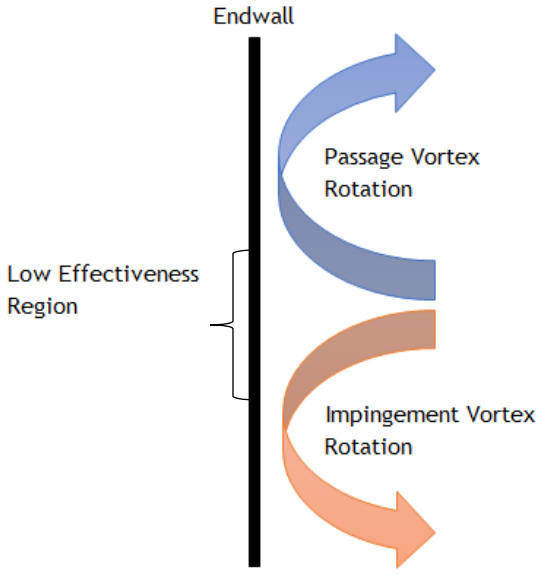

Figure 8.2.1 Cause of the low effectiveness spots on the endwall

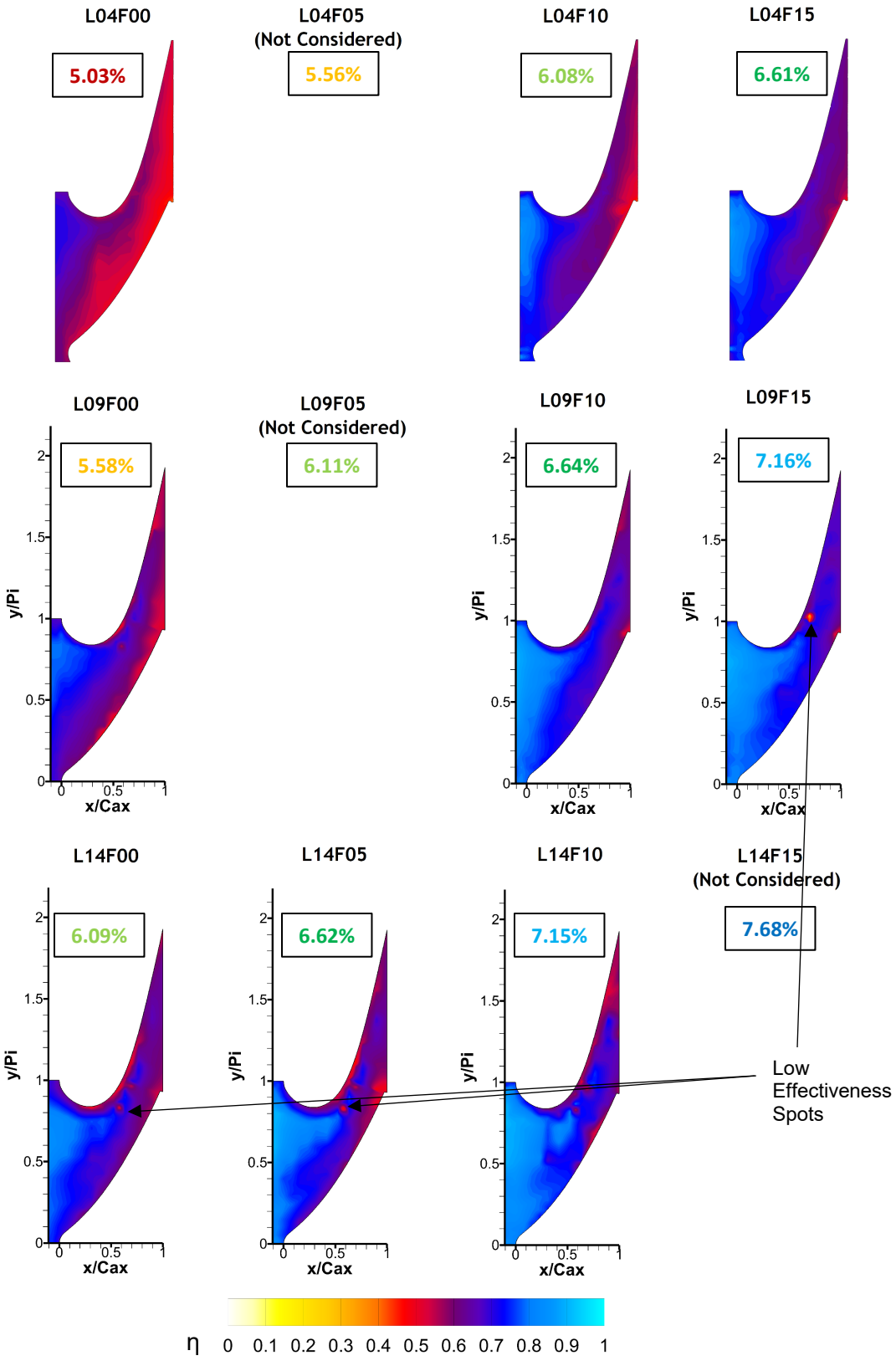

Figure 8.2.2 Endwall Cooling Effectiveness. The L04 cases (in the top row) are referenced directly from [40].

Effects of Changing the Louver Coolant Mass Flow Ratio

For the F00 cases, the overall endwall effectiveness increases with increasing louver coolant flow rate, from the L04 cases to the L14 cases. However, it was seen in the in-field thermal measurements in section 7.3 that the effectiveness values near the endwall were lower for the L14 cases than for the L09 cases, due to penetration of coolant streams into the mainstream. This looks like a discrepancy in the trend of cooling effectiveness. But it should be noted that when the film coolant is present, it helps the louver coolant to penetrate the mainstream. Therefore, the tendency for louver coolant to penetrate is much lower in the no-film-coolant-injection cases (F00 cases). When the F10 cases are compared, the endwall near the trailing edge region, for the L09 cases, is seen to be more effectively cooled than for the L14 cases. This shows that, for higher louver coolant and film coolant flow rates, both the louver coolant and the film coolant are penetrating into the mainstream, which leads to a decrease of coolant effectiveness on the endwall. This shows that increasing the louver coolant flow rate beyond a point results in reduced cooling performance on the endwall.

The observation made regarding pitchwise uniformity of coolant in the earlier part of this section can be made with respect to changes in the louver coolant flow rate as well. The uniformity increases with increasing louver coolant flow rate, as seen in the F00 and F10 cases. This confirms an observation made in section 7.3 that the louver coolant is not directly participating in forming the impingement vortex but is affected by it. Like the film coolant stream, the louver coolant stream with higher momentum also resists passage turning, providing more uniform shielding to the film coolant stream.

The comparison of the F10 cases also reveals that decreases of coolant effectiveness across the passage are more rapid in case L04 than in the L09 or L14 case. This is, once again, due to louver coolant not being able to shield the film coolant well in the L04 cases

but can do so in the L09 cases. Also, for the L14 cases, the higher momentum of louver coolant makes coolant penetrate the mainstream, reducing the shielding effect near the trailing edge, as seen by lower coolant effectiveness near the trailing edge in the L14F10 case, compared to the L09F10 case. Therefore, the L09 cases show the best overall performance when the effects of changes in louver cooling flow rate are studied.

The above discussions show that increases of both film coolant and louver coolant flow rates beyond a certain value are detrimental to cooling performance. When all endwall contours are compared, it is seen that the most optimum performance is in the L09F10 case. This case shows no rapid deterioration of coolant effectiveness across the passage, a good cooling effectiveness near the trailing edge without any coolant lift-off, comparable cooling performance near both suction and pressure side regions and high values of coolant effectiveness overall. The only case that gives a better performance than this case is the L09F15 case, but the increase in performance is only marginal and requires more louver coolant flow rate.

8.3. Vane Pressure Surface Thermal Contours

As the coolant coverage along the pressure surface was observed in the thermal contours of the in-field measurements in chapter 7, thermal measurements along the pressure surface were expected to reveal much new information about coolant coverage. Figure 8.3.1 shows the pressure surface thermal contours for all L09 and L14 cases measured in this study.

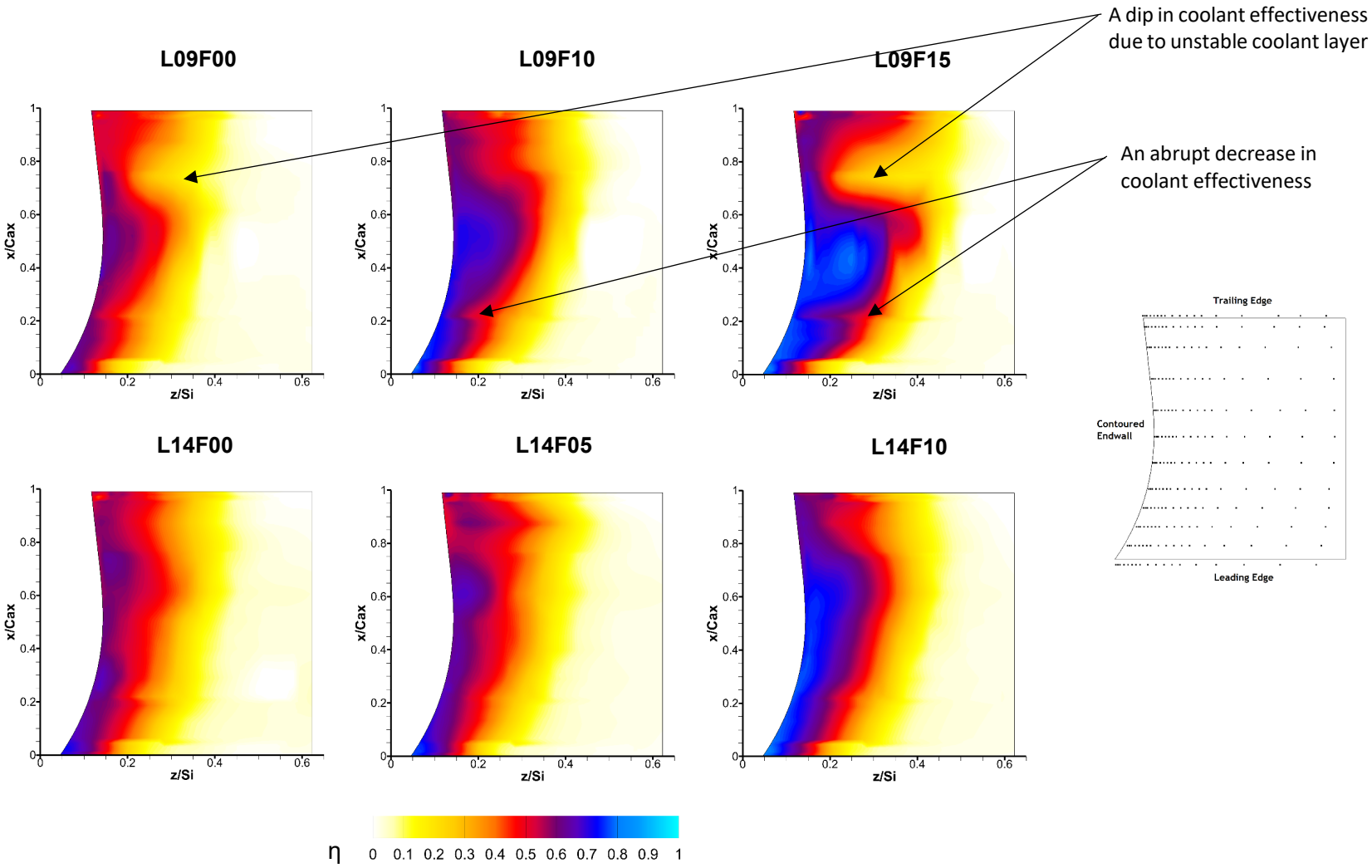

Figure 8.3.1 Vane pressure surface effectiveness for L09 and L14 cases

Effects of Changing the Film Coolant Mass Flow Ratio

The overall cooling effectiveness on the pressure surface near the endwall region can be seen to increase with an increase in film coolant flow rate for both the L09 and L14 cases. As expected, in the F00 cases, the impingement vortex is not helped by film coolant flow and thus shows much lower cooling effectiveness. Interestingly, the increases in the cooling effectiveness from L09F10 to L09F15 and from L14F05 to L14F10 are also substantial, to $x/C_{ax} = 0.6$. This proves that film coolant directly impinging on the pressure surface is not migrating toward the suction side due to the impingement vortex and is helping in increasing the vortex strength.

Although the coolant effectiveness is increasing with increasing film coolant flow rate, the coolant spread in the spanwise direction is not increasing much. This is showing that the impingement vortex is not growing much with increases in film coolant flow rate, an observation made in section 7.2. A small dip in coolant effectiveness near $x/C_{ax} = 0.22$ (indicated in fig. 8.3.1) can be seen prominently in cases L09F10 and L09F15, with hints of presence in the remaining cases. However, aerodynamic data near this region are not measured and, thus, this minor feature cannot be explained. There may also be a chance that the rather abrupt change in cooling effectiveness is a result of the data interpolation technique used. In any case, this feature is concentrated in a very small region and doesn't seem to affect coolant effectiveness of other regions on the pressure surface.

For the L09 cases, around $x/C_{ax} = 0.7$, a decrease in coolant effectiveness is seen for all film cooling flow rates. It can be seen that this is only slightly downstream of the location where the endwall contour has changed from being convex to being concave. Therefore, this appears to be an effect of instability of the coolant layer due to curvature of the endwall. This instability is causing a circulation region only in the location where the louver coolant stream resides as the film coolant stream seems to be attached to the endwall

(based on the axial uniformity of coolant effectiveness very close to the endwall throughout the passage). The louver coolant is mixing due to the circulation, causing a decrease in coolant effectiveness slightly away from the endwall, seen most prominently and indicated in the cases of L09F00 and L09F15 in fig. 8.3.1. Also, for both L09 and L14 cases, it can be seen that this decrease in effectiveness is increasing with increasing film coolant flow rate. This corroborates the observation made in section 8.2 that the film coolant is helping the louver coolant penetrate the mainstream. The film coolant pushing louver coolant further away from the endwall means that the instability of the louver coolant will increase, possibly showing a more rapid response to this instability. Therefore, as the L09F15 case has the maximum film cooling flow rate, it is showing the steepest decrease in cooling effectiveness downstream of $x/C_{ax} = 0.65$.

It should be noted that strengthening of the impingement vortex by continuous impingement of coolant streams (mechanism 3 of the formation of the impingement vortex, explained in chapter 2) will be present only upstream of $x/C_{ax} = 0.75$, due to the geometry of the vane passage. This means that beyond this location, the impingement vortex starts to decrease in intensity. This was observed in the vorticity contours and discussed in sections 7.2 and 7.3. Therefore, although not seen clearly in the thermal contours, a decrease in pressure surface cooling effectiveness is expected even without a contoured endwall, as more and more coolant migrates toward the suction side, with the decrease in strength of the impingement vortex. As the results of both the coolant layer instability and weakening of the impingement vortex are the same, their effects cannot be distinguished in the thermal contours.

Effects of Changing the Louver Coolant Mass Flow Ratio

It has been noted multiple times that louver coolant is not helping in increasing the impingement vortex intensity and, therefore, the coolant spread across the pressure

surface is not expected to change much by increasing the louver coolant flow rate. This is verified in the effects of changing louver coolant flow rates in cases F00 and F10 (see fig. 8.3.1). The effectiveness is more in the L14 cases than in the L09 cases, as more coolant is introduced in the L14 cases. This increase is significant in the upstream part of the passage and becomes very small near the trailing edge as the coolant is getting mixed into the mainstream or is moving toward the suction side.

The coolant layer instability effect explained earlier is also affected by changes in louver coolant flow rate. Mainly, a delayed response to endwall curvature is seen in the L14 cases when compared to the L09 cases. This can be seen by observing the location of the coolant mixing region close to the trailing edge for the L14 cases, as compared to x/C_{ax} = 0.7 for the L09 cases. This is because the momentum of the louver coolant is higher for the L14 cases, making it go further downstream before experiencing coolant layer instability and the formation of a blob of mixed coolant. This delay means that the coolant effectiveness is more uniform for the L14 cases across the whole passage.

The above discussions show that increasing the film coolant flow rate also increases the cooling effectiveness of the pressure surface. This trend is different than the coolant effectiveness trend seen on the endwall. The endwall cooling effectiveness decreased beyond a certain level of film cooling flow rate. Also, the coolant layer instability, caused by endwall contouring, is delayed in the L14 cases almost until the end of the passage. However, even with the presence of this instability, the coolant effectiveness below z/Si = 0.2 remains above 0.4 across the whole passage. Therefore, optimum cases (if only cooling of the pressure surface is considered) are L09F10 and L14F10. Between them, only a marginal performance rise is seen in the L14F10 case, with the cost of additional louver coolant flow rate. Therefore, L09F10 should be able to provide the cooling needs, especially since it also shows optimum performance for endwall cooling.

8.4. Vane Suction Surface Thermal Contours

In conventional cascades, due to migration of coolant from pressure surface to suction surface as a result of the passage vortex, the suction surface is cooled more substantially than the pressure surface is cooled. As the passage aerodynamics change by combustor coolant introduced in the current study, it is important to record the coolant coverage on the suction surface as well. Figure 8.4.1 shows the suction surface thermal contours for all L09 and L14 cases.

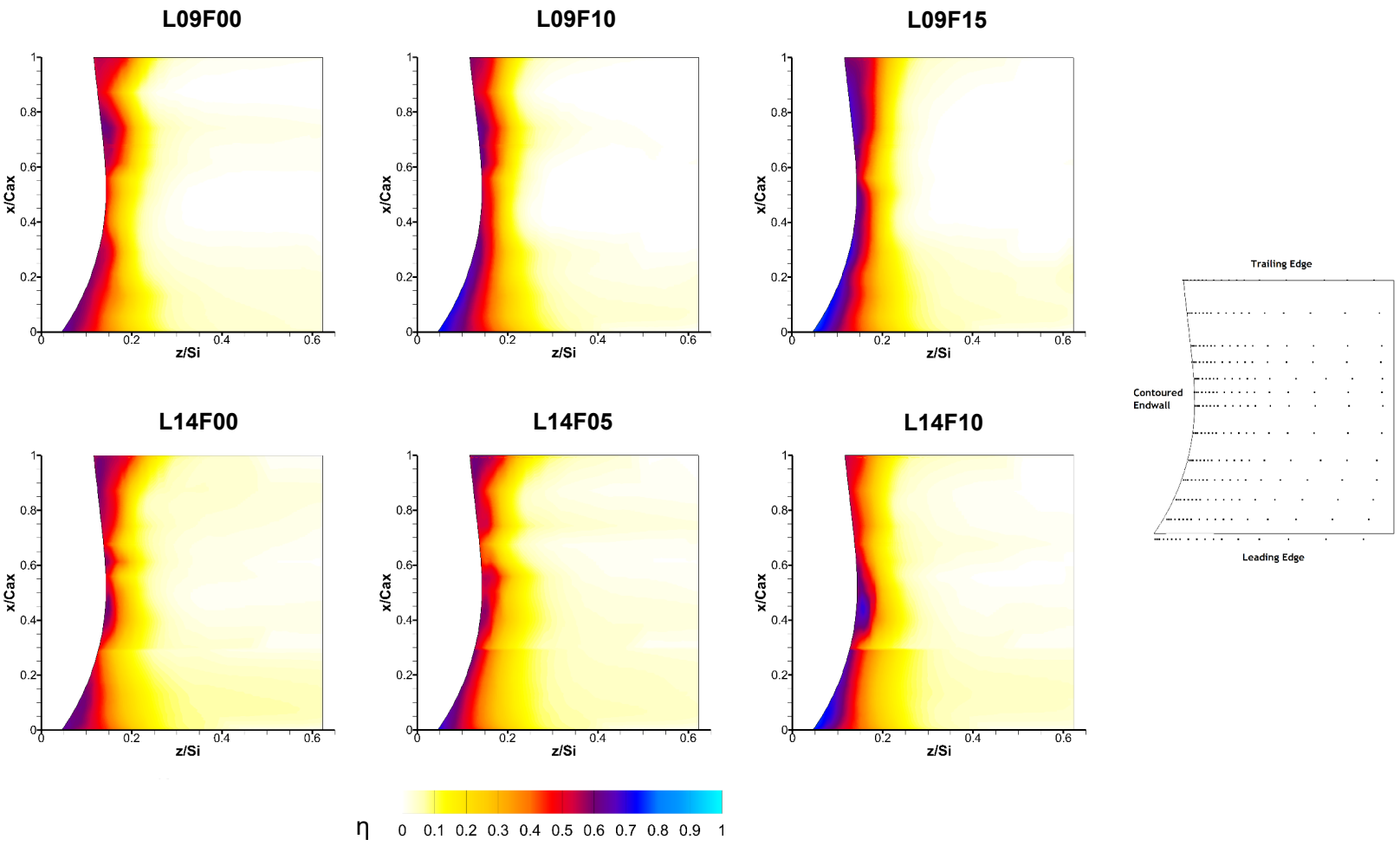

Figure 8.4.1 Vane pressure surface effectiveness for L09 and L14 cases

Effects of Changing the Film Coolant Mass Flow Ratio

The features seen on this surface are explained in the order they appear, from leading to trailing edge. For all cases, near the endwall-suction-surface corner, coolant effectiveness is the highest of the entire surface. This region has louver and film (except the F00 cases) coolant streams directly impinging on the suction surface. Due to the geometry of the vanes (see fig. 5.3.2), this direct impinging is present only until the axial location of plane 3, which is around $x/C_{ax} = 0.3$. This relates to the extent of a region of thick coolant layer near the suction-surface-endwall corner. When the F00 cases are compared with the cases with film injection, a small yet highly effective coolant layer can be seen near the endwall in the upstream region of the passage. This shows that the louver coolant is shielding the film coolant, which helps to retain its effectiveness. In the case of L09, the extent of this highly effective coolant layer is present to $x/C_{ax} = 0.38$ for the L09F10 case but $x/C_{ax} = 0.55$ for the L09F15 case. This is mostly because more coolant is introduced in the F15 case, which means that the coolant effectiveness of the film coolant decreases less rapidly as one moves downstream, for the F15 cases. A small discontinuity near $x/C_{ax} = 0.35$ can be seen, which may be a result of the interpolation technique used. But the neighboring points indicate that the contour at that location will probably be continuous.

In section 7.2, the suction leg of the horseshoe vortex is seen prominently across the passage. This vortex rotates flow from the suction surface toward the endwall and then downward toward the pressure surface. This can lead to a decrease in the coolant thickness on the suction surface. Therefore, for all cases, the coolant layer thickness decreases from $x/C_{ax} = 0.4$ to $x/C_{ax} = 0.6$, most prominently seen in cases L09F00 and L09F10. For the L09 cases, the F00 case shows more rapid thinning of the coolant layer as the highly effective coolant layer formed by the film injection is absent in this case. For

the L14 cases, thinning is present and coolant effectiveness near the endwall in this region increases with increasing film coolant flow rate.

However, as one moves closer to the trailing edge, the coolant layer thickens. This is because, the passage vortex effects have started to appear near the suction surface (also discussed in section 7.2). This vortex is moving coolant away from the endwall across the suction surface toward the mid-span. Therefore, very close to the trailing edge, the coolant layer is seen to be increasing in the spanwise direction. It was seen before that the passage vortex strength is directly dependent on the impingement vortex strength which, in turn, is dependent on the film coolant flow rate. With increasing film coolant flow rate, a decrease in passage vortex strength was observed in the in-field measurements. Therefore, the coolant layer thickness near the trailing edge is also decreasing with increasing film cooling flow rate.

The coolant layer instability effect due to endwall contouring, seen in the pressure surface measurements, is not seen here. This is because the coolant layer thickness on suction surface is much smaller than on the pressure surface and, therefore, the coolant layer is not affected by contouring, and coolant mixing seen on the pressure surface is not seen on the suction surface.

Effects of Changing the Louver Coolant Mass Flow Ratio

It is seen before that all major features present in the passage have been tied to the impingement vortex. As there is little change in the impingement vortex with changes in louver coolant flow rate, very similar thermal contours are observed when the F00 and F10 cases are compared. The thickness of the coolant layer near the leading edge (involving direct impingement of coolant) as well as near the trailing edge (involving passage vortex effects) are almost equal. A small coolant blob not present in the L09 cases is seen in all L14 cases near $x/C_{ax} = 0.45$. Unfortunately, aerodynamic data near

this region are not measured and therefore flow vectors and vorticity near this region are not known. However, the only major change seen when the in-field measurements of L09 and L14 cases are compared near the suction surface is the strength of the horseshoe vortex (see vorticity plots in section 7.2). Therefore, this coolant blob is probably an effect of migration of coolant along the suction surface toward the endwall. As the horseshoe vortex increases in strength with increases in louver coolant flow rate, it is probable true that the coolant blob appears only for the L14 cases.

If one looks at all the suction surface contours in a general sense, it is seen that the contours have not changed much in their pattern. This is further proof that the coolant migration toward the suction surface is avoided for almost the entire passage, due to the impingement vortex.

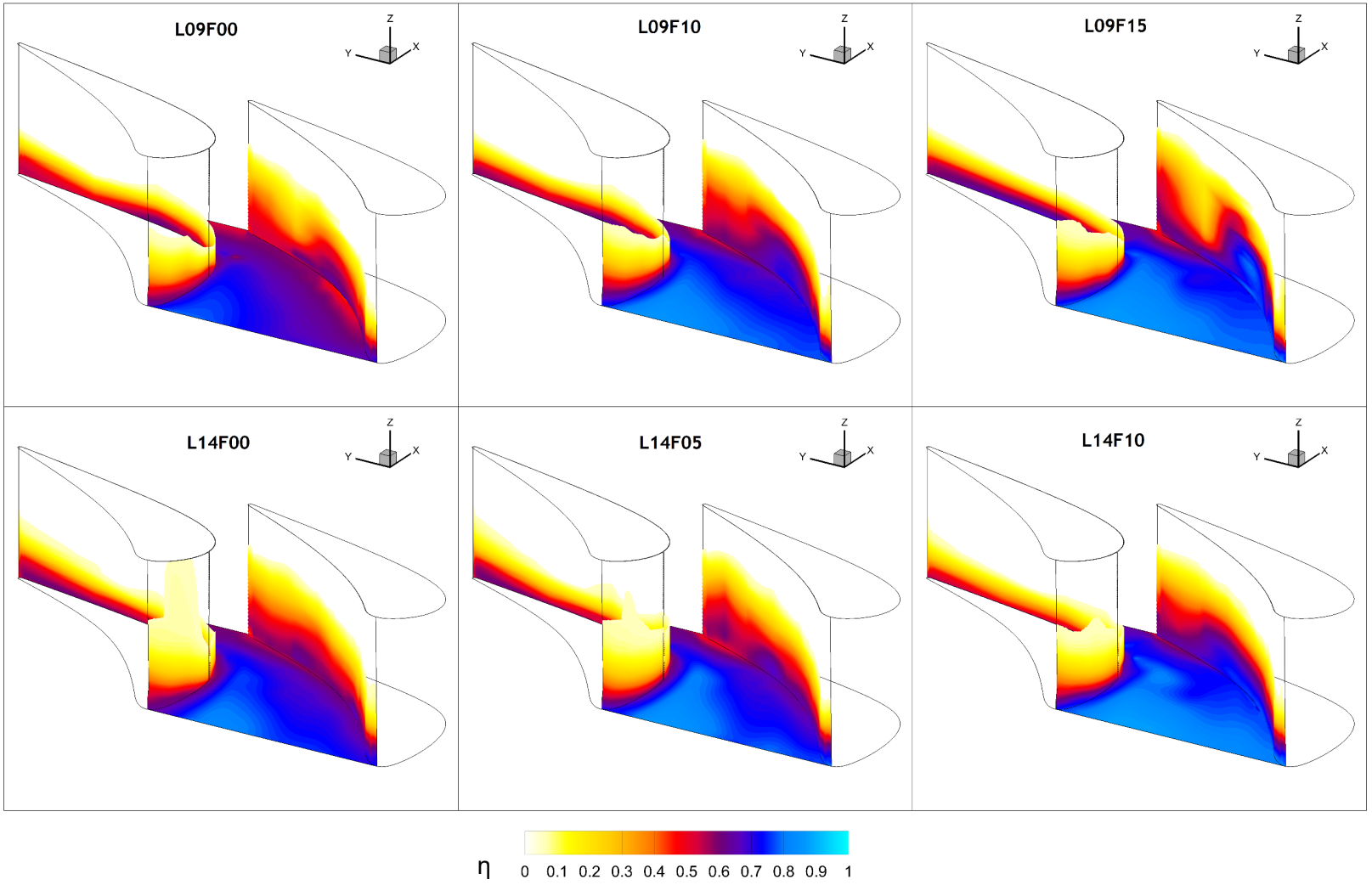

Figure 8.4.2 Coolant Effectiveness for all surfaces for L09 and L14 cases

Figure 8.4.2 shows the cooling effectiveness for all surfaces for the L09 and L14 cases. This figure is used as a summary to point out the major features seen on the endwall and vane surfaces across all cases. The louver coolant is shielding the film coolant and indirectly helping keep the endwall cooled over the whole passage. An increase in the film coolant beyond a certain value does not seem to give much increase in endwall cooling effectiveness. Increases in louver coolant flow rate beyond a certain value show slightly decreased performance on the endwall due to the louver coolant stream penetrating the mainstream.

Due to the rotation direction of the impingement vortex, the pressure surface is cooled much better than the suction surface. This cooling improves with higher film coolant flow rates. The pressure surface is cooled for the entirety of the passage and, although the cooling effectiveness drops near the trailing edge due to weakening of the impingement vortex, it still has a very high value. On the other hand, the suction surface thermal contours do not change much with changes in louver or film cooling flow rates. The coolant layer on the suction surface is very thin to almost the trailing edge. Near the trailing edge, the coolant is spreading more in the spanwise direction (z) than seen in the upstream regions. This is because of the passage vortex.

If all these cases were compared in terms of cooling provided for the three surfaces, L09F10 seems to be the optimum. This case provides uniform cooling on the endwall as well as good cooling on both the pressure surface and the suction surface.

Chapter 9. Conclusions

The experimental study presented in this report was conducted to understand the influence of multiple coolant streams upstream of a first-stage nozzle guide vane on cooling the endwall and vane surfaces. Flow inside a turbine vane is highly three-dimensional and coolant addition further complicates it. But coolants streams are necessary to keep various components from melting. Significant information is presented in the literature that deals with the cooling of these surfaces, but very few studies have considered the effect of the combustor coolant on cooling various surfaces inside a vane passage. The higher flow rates of the combustor coolants, compared to the film coolant flows designed specifically for cooling the endwall, significantly affect the flow physics in the passage. The interaction of the several coolant streams and their interactions with the mainstream are also important to understand the cooling effectiveness provided by this coolant. The current study addresses these questions. An engine-representative combustor simulator, providing high Reynolds number, high turbulence intensity and engine-comparable turbulence length scales, was used for measurements. The combustor coolant streams, which comprise of effusion and louver coolant, and film coolant streams were also introduced in the vane passage to create correct engine conditions downstream of the combustor section of the test facility. The endwall was axisymmetrically contoured as it has been proven that the secondary losses are decreased in a contoured-endwall vane passage.

The first objective was to understand the coolant interaction and transport through the vane passage. Therefore, in-field velocity and temperature measurements were taken at multiple locations throughout the passage. To find the effect of changing the louver coolant mass flow ratio (MFR), three different MFRs (0.37%, 0.92% and 1.43%) were considered.

For each of these three cases, the film coolant MFR was also varied for three different values, 0%, 1% and 1.5% for the first two cases and 0%, 0.5% and 1% for the last case, to see how the interaction between the louver coolant and film coolant changed with their flow rates. The second objective was to understand how the coolant interactions affected cooling on the endwall. Additionally, it was suspected that the vane surfaces also received coolant coverage. Hence, thermal measurements were taken on the endwall and the vane surfaces.

The results indicate that the impingement vortex was a dominant feature throughout the passage for every case. Its presence diminished the passage vortex and its effects throughout the vane passage. As the pressure leg of the horseshoe vortex doesn't migrate toward the suction surface until the latter part of the passage, the suction leg of the horseshoe vortex was observed upstream of the throat region, something which is not usually seen. Despite the impingement vortex, coolant near the endwall experienced the cross-flow from pressure surface to suction surface. Also, the impingement vortex helped in driving coolant toward the mid-span near the pressure surface, thereby cooling the pressure surface, a region notorious for getting the least amount of cooling. No significant change in intensity of the impingement vortex was observed when the louver coolant flow rate was increased. This shows that this vortex is almost exclusively a result of the effusion coolant flow. On the other hand, when the film coolant flow rate was increased, the coolant coverage span on the pressure surface and the impingement vortex strength were slightly increased, showing that the film coolant affected the impingement vortex. Also, the increase in the film coolant flow rate showed a decrease in endwall cross-flow and a decrease in the intensity of the suction leg of the horseshoe vortex, due to the coolant momentum resisting the endwall cross-flow and the horseshoe vortex. Although, not very

significant, these decreases play a role in affecting the coolant distribution on the endwall and the vane surfaces.

All cases having film coolant injection showed significantly better performance than the no-film-coolant injection cases. This is not only because the former cases had more net coolant injection, but because the film coolant is injected almost as a wall jet and if it remains attached to the endwall until the end of the passage, it gives very good performance. The success of the film coolant not mixing with the mainstream was found to be dependent on mass flow rate of the louver coolant. For low louver coolant flow rate, the inadequate momentum of the louver coolant made itself mix with the mainstream, exposing the film coolant to the mainstream as well, which reduced the endwall cooling effectiveness. On the other hand, for very high louver coolant flow rates, the high momentum of the louver coolant jet penetrated the mainstream, again exposing the film coolant to the mainstream. However, for a moderate louver coolant flow rate, the louver coolant neither diffused into nor penetrated the mainstream, providing a shielding effect for the film coolant throughout the passage, showing very uniform and highly effective cooling performance. Also, as the louver coolant flow rate increases, the endwall cooling performance in the early part of the passage started becoming uniform in the pitchwise direction. This uniformity is caused due to the high momentum of the coolant which adds resistance to passage turning. The increase in film coolant flow rate, for any louver coolant flow rate case, did not provide a similar increase in the coolant effectiveness. In fact, at the trailing edge, the endwall cooling effectiveness varied only marginally as the film coolant flow rate was increased. The case having a high louver coolant flow rate and a high film coolant flow rate actually showed worse overall endwall cooling performance than the case with moderate coolant flow rates.

The most surprising result of this study was the coolant coverage seen on the vane pressure surface. The impingement vortex has rotation opposite to that of the passage vortex and the continuous impinging of the film coolant keeps it from migrating toward the suction side. This effect not only keeps the coolant streams from migrating but also spreads them along the pressure surfaces. It was seen that the pressure surface was cooled over 20% of its span for almost the entire passage, for all cases. This percentage was not affected significantly by changes in coolant flow rate and, therefore, can possibly be an effect of effusion coolant, which was not varied in this study. Also, an instability in the coolant layer was observed due to endwall contouring, which decreased pressure surface cooling at downstream locations, although it was not severe in most of the cases. As seen in the case of endwall cooling, increases in the coolants flow rates beyond a certain point led to coolant lift off from the pressure surface due to excess momentum, resulting in lower surface cooling performance.

On the suction surface, there was a thin coolant film near the endwall region for the upstream part of the passage. This was a result of direct impingement of film coolant on the suction surface, which was not influenced by the other vortices in the passage. Also, in the downstream part of the passage, coolant effectiveness started to rise. This was due to passage vortex effects that were seen at the end of the passage. No significant differences in coolant spread were seen for any of the cases on the suction surface, because the most dominant feature of the passage, the impingement vortex, did not allow most of the coolant to migrate toward the suction surface for any of the cases.

The detailed in-field measurements presented in this thesis provide an understanding of the cooling effectiveness measured on the endwall and vane surfaces. The variety of cases gives a general idea for the range of the coolant flow rates that will provide optimum cooling performance. The results are expected to help in designing new endwall cooling

schemes as well as pressure surface cooling schemes, which will include the effects of the upstream cooling features present in an actual engine. The effect of changes in the effusion coolant flow rate should be studied as the next step of this study, as it was found to be instrumental in formation of the impingement vortex. As the results were strongly influenced by the geometry of the combustor-turbine interface, similar analyses for different types of interfaces can be very helpful in understanding coolant transport and performance in a vane passage.

References

1. R. Sedney, C. W. Jr. Kitchens, “The Structure of Three-Dimensional Separated Flows in Obstacle, Boundary Layer Interactions”, AGARD-CP-168 on Flow Separation, 1975
2. R. J. Goldstein, J. Karni, “The Effect of a Wall Boundary Layer on Local Mass Transfer from a Cylinder in Crossflow”, Journal of Heat Transfer, vol. 106, no. 2, p. 260, May 1984
3. L. S. Langston, “Crossflows in a Turbine Cascade Passage”, J. Eng. Power, vol. 102, no. 4, p. 866, Oct. 1980
4. O.P. Sharma, T.L. Butler, “Prediction of endwall losses and secondary flows in axial flow turbine cascades”, Trans. ASME J. Turbomachinery, 109, 229-236, 1987
5. R. J. Goldstein, R. A. Spores, “Turbulent Transport on the Endwall in the Region Between Adjacent Turbine Blades”, J. Heat Transfer, vol. 110, no. 4a, p. 862, Nov. 1988
6. H. P. Wang, S. J. Olson, R. J. Goldstein, E. R. G. Eckert, “Flow Visualization in a Linear Turbine Cascade of High Performance Turbine Blades”, J. Turbomach., vol. 119, no. 1, p. 1, Jan. 1997
7. J. D. Denton, "Loss Mechanisms in Turbomachines", ASME J. Turbomachinery, Vol. 115, pp. 621-656, 1993
8. S.W. Burd, “Secondary Flow and Heat Transfer Control in Gas Turbine Inlet Nozzle Guide Vanes”, PhD thesis, University of Minnesota, 1998
9. J. S. Ewen, F. W. Huber, J. P. Mitchell, “Investigation of the Aerodynamic Performance of Small Axial Turbines”, ASME Paper No. 73-GT-3, 1973
10. A. W. H. Morris, R. G. Hoare, “Secondary Loss Measurements in a Cascade of Turbine Blades with Meridional Wall Profiling”, ASME Paper No. 75-WA/GT-13, 1975

11. F. C. Kopper, R. Milanot, M. Vancot, “Experimental Investigation of Endwall Profiling in a Turbine Vane Cascade”, AIAA J., vol. 19, no. 8, pp. 1033–1040, Aug. 1981
12. L. P. Timko, “Energy Efficient Engine: High Pressure Turbine Component Test Performance Report”, NASA CR-168289, 1982
13. R. J. Boyle, J. E. Haas, “Comparison of Experimental and Analytical Performance for Contoured Endwall Stators”, AIAA Paper 82-1286, 1982
14. D. L. Tipton, “Experimental Investigation of Turbine Endwall Contouring”, Detroit Diesel Allison Report AX0400 174, General Motors Crop. AVRADCOM Tech. Report 81-D-19, 1981
15. S. H. Moustapha, R. G. Williamson, “Effect of Two Endwall Contours on the Performance of an Annular Nozzle Cascade”, AIAA Journal Vol. 24 No. 9 pp. 1524-1530, 1985
16. M. G. Rose, “Non-axisymmetric Endwall Profiling in the HP NGV’s of an Axial Flow Gas Turbine”, ASME Paper 94-GT-249, 1994
17. S. W. Burd, T. W. Simon, “Flow Measurements in a Nozzle Guide Vane Passage with a Low Aspect Ratio and Endwall Contouring”, J. Turbomach., vol. 122, no. 4, p. 659, Oct. 2000
18. J. D. Piggush, T. W. Simon, “Flow Measurements in a First Stage Nozzle Cascade Having Endwall Contouring, Leakage, and Assembly Features”, ASME. J. Turbomach. 2012;135(1):011002-011002-11
19. M. F. Blair, “Experimental Study of Heat Transfer and Film Cooling on Large-scale Turbine Endwalls”, ASME Journal of Heat Transfer, 96:524–529, 1974
20. C. H. Sieverding, P. Wilputte, “Influence of Mach Number and Endwall Cooling on Secondary Flows in a Straight Nozzle Cascade”, American Society of Mechanical Engineers, Paper 80-GT-52, May 1980

21. L. J. Goldman, K. L. McLallin, “Effects of Endwall Cooling on Secondary Flows in Turbine Stator Vanes”, AGARD, CPP-214, 1977
22. T. E. Biesinger, D. G. Gregory-Smith, “Reduction in Secondary Flows and Losses in a Turbine Cascade by Upstream Boundary Layer Blowing”, American Society of Mechanical Engineers, Paper 93-GT-114, May 1993
23. S. Friedrichs, H. P. Hodson, W. N. Dawes, “Aerodynamic Aspects of Endwall Film-Cooling”, Journal of Turbomachinery, Vol. 119, Oct. 1997, pp. 786–793
24. M. Papa, V. Srinivasan, R. J. Goldstein, “Film Cooling Effect of Rotor-Stator Purge Flow on Endwall Heat/Mass Transfer”, ASME. J. Turbomach. 2011;134(4):041014-041014-8. doi:10.1115/1.4003725
25. S.W. Burd, T.W. Simon, “Effects of Slot Bleed Injection Over a Contoured Endwall on Nozzle Guide Vane Cooling Performance: Part 1 – Flow Field Measurements”, ASME (Paper), 2000-GT-199, 2000
26. L. A. El-Gabry, R. Saha, J. Fridh, T. Fransson, “Measurements of Hub Flow Interaction on Film Cooled Nozzle Guide Vane in Transonic Annular Cascade”, ASME. J. Turbomach. 2015;137(8):081004-081004-9
27. P. P. Schuepbach, R. S. Abhari, M. G. Rose, J. J. Gier, “Influence of Rim Seal Purge Flow on the Performance of an Endwall-Profiled Axial Turbine”, ASME. J. Turbomach., 2010; 133(2):021011-021011-10. doi:10.1115/1.4000578
28. M. H. Alqefl, Y. Kim, H-K. Moon, L. Zhang, T. W. Simon, “Numerical Study of Contoured Endwall Flow and Heat Transfer with Combustor Coolant and Film Cooling Flows for a Turbine Nozzle Guide Vane”, Proceedings of ASTFE 4th Int. Workshop on Heat Trans. 2017, Las Vegas, NV, USA, TFEC-IWHT2017-18417
29. K. Takeishi, M. Matsuura, S. Aoki, T. Sato, “An Experimental Study of Heat Transfer and Film Cooling on Low Aspect Ratio Turbine Nozzles”, ASME Journal of Turbomachinery, 112:488–496, 1990

30. M. Y. Jabbari, K. C. Marston, E. R. G. Eckert, R. J. Goldstein, “Film Cooling of the Gas Turbine Endwall by Discrete-hole Injection”, Journal of Turbomachinery, 118:278, 1996

31. A. A. Thrift, K. A. Thole, S. Hada, “Effects of Orientation and Position of the Combustor-Turbine Interface on the Cooling of a Vane Endwall”, J. Turbomach., vol. 134, no. 6, p. 061019, Nov. 2012

32. S. W. Burd, C. J. Satterness, T. W. Simon, “Effects of Slot Bleed Injection over a Contoured Endwall on Nozzle Guide Vane Cooling Performance: Part 2 – Thermal Measurements,” ASME (Paper), 2000-GT-200, 2000

33. R. Erickson, T. W. Simon, “Effects of Stator/Rotor Leakage Flow and Axisymmetric Contouring on Endwall Adiabatic Effectiveness and Aerodynamic Loss”, Heat Transf. Res., vol. 42, no. 1, pp. 45–64, 2011

34. F. Ornano, T. Povey, “Experimental and Computational Study of the Effect of Momentum-Flux Ratio on High Pressure NGV Endwall Cooling Systems”, Proceedings of ASME Turbo Expo 2017, Charlotte, USA GT2017-64229

35. W. F. Colban, K. A. Thole, G. G. Zess, “Combustor Turbine Interface Studies—Part 1: Endwall Effectiveness Measurements”, ASME. J. Turbomach. 2003;125(2):193-202. doi:10.1115/1.1561811

36. W. F. Colban, A. T. Lethander, K. A. Thole, G. G. Zess, “Combustor Turbine Interface Studies—Part 2: Flow and Thermal Field Measurements”, ASME. J. Turbomach. 2003;125(2):203-209. doi:10.1115/1.1561812

37. Hermanson KS, Thole KA. Effect of Nonuniform Inlet Conditions on Endwall Secondary Flows. ASME. J. Turbomach. 2002;124(4):623-631. doi:10.1115/1.1505849

38. R. Saxena, M. H. Alqefl, Z. Liu, H-K. Moon, L. Zhang, T. Simon, “Contoured Endwall Flow and Heat Transfer Experiments with Combustor Coolant and Gap Leakage

Flows for a Turbine Nozzle Guide Vane," Proceedings of ASME Turbo Expo 2016, Seoul, Korea, GT2016-56675

39. M. H. Alqefl, Y. W. Kim, H.-K. Moon, L. Zhang, T. W. Simon, "Aerodynamic Measurements and Analysis in a First Stage Nozzle Guide Vane Passage with Combustor Liner Cooling, Slot Film Cooling and Endwall Contouring", Proceedings of ASME Turbo Expo 2018, Oslo, Norway, GT2018-76345
40. M. H. Alqefl, "Aero-Thermal Aspects of Endwall Cooling Flows in a Gas Turbine Nozzle Guide Vane", PhD Thesis, University of Minnesota, 2019
41. R. J. Roback, R. P. Dring, "Hot Streaks and Phantom Cooling in a Turbine Rotor Passage: Part 1 — Separate Effects", ASME. Turbo Expo: Power for Land, Sea, and Air, Volume 1: Turbomachinery, 1992: V001T01A042. doi:10.1115/92-GT-075
42. R. J. Roback, R. P. Dring, "Hot Streaks and Phantom Cooling in a Turbine Rotor Passage: Part 2—Combined Effects and Analytical Modeling", ASME. J. Turbomach. 1993;115(4):667-674. doi:10.1115/1.2929301
43. L. Zhang, J. Yin, K Liu, H.-K. Moon, "Effect of Hole Diameter on Nozzle Endwall Film Cooling and Associated Phantom Cooling", ASME. Turbo Expo: Power for Land, Sea, and Air, Volume 5B: Heat Transfer, 2015: V05BT12A016. doi:10.1115/GT2015-42541
44. S.-J. Li, S.-F. Yang, J.-C. Han, L. Zhang, H.-K. Moon, "Turbine Blade Surface Phantom Cooling from Upstream Nozzle Trailing-Edge Ejection", Journal of Thermophysics and Heat Transfer, 2016, Vol.30(4), pp.770-78
45. K. Du; Z. Li, J. Li, B. Sunden, "Influence of the Upstream Slot Geometry on the Endwall Cooling and Phantom Cooling of Vane Suction Side Surface", Applied Thermal Engineering, Vol. 121, pp.688-700, 2017
46. K. Du, L. Song, J. Li, B. Sunden," Effects of the Mainstream Turbulence Intensity and Slot Injection Angle on the Endwall Cooling and Phantom Cooling of the Vane

Suction Side Surface", International Journal of Heat and Mass Transfer, Vol.112, pp.427-440, September 2017

47. R. Oke, "Measurements in a Gas Turbine First Stage Nozzle Guide Vane Cascade with Film Cooling and Endwall Contouring", PhD Thesis, University of Minnesota, 2001
48. J. D. Piggush, "An Experimental Investigation of Endwall Leakage Flows and Misalignment in Gas Turbine Nozzle Guide Vane", M.S. Thesis, University of Minnesota, 2005
49. R. D. Erickson, "Experimental investigation of disc cavity leakage flow and hub endwall contouring in a linear rotor cascade", M.S. Thesis, University of Minnesota, 2010.
50. A. Ayaskanta, "Experimental investigation of the effect of engine representative combustor exit temperature profile and disc cavity leakage flow on the film cooling of contoured Hub Endwall of a high pressure gas turbine rotor cascade", M.S. Thesis, University of Minnesota, 2013.
51. R. Saxena, "Experimental Cascade Simulation of First Stage High Pressure Gas Turbine with Effects of Leakage Flow and Contouring on Endwall Film Cooling", M.S. Thesis, University of Minnesota, 2015.
52. M. H. Alqefl, "An Experimental and Numerical Investigation of Endwall Aerodynamics and Heat Transfer in a Gas Turbine Nozzle Guide Vane with Slot Film Cooling", M.S. Thesis, University of Minnesota, 2016
53. N. S. Sharp, S. Neuscamman, Z. Warhaft, "Effects of Large-scale Free Stream Turbulence on a Turbulent Boundary Layer", Phys. Fluids, vol. 21, no. 9, p. 095105, Sep. 2009
54. S.-W. Lee, H.-G. Kwon, B.-K. Park, "Effects of Combustor-level High Free-stream Turbulence on Blade-surface Heat/Mass Transfer in the Three-dimensional Flow

Region Near the Endwall of a High-turning Turbine Rotor Cascade", J. Mech. Sci. Technol., vol. 19, no. 8, pp. 1347–1357, 2005

55. G. W. Burns, M. G. Scroger, M. C. Croarkin, W. F. Guthrie, and G. F. Strouse, "Temperature-Electromotive Force Reference Functions and Tables for the Letter-designated Thermocouple Types Based on the ITS-90", N.I.S.T., 1993
56. A. L. Treaster, A. M. Yocum, "The Calibration and Application of Five-hole Probes", ISA Trans., 18, 23–34, 1979.
57. Hall, BF, and T Povey. "The Oxford Probe: An Open Access Five-hole Probe for Aerodynamic Measurements", Measurement Science and Technology, Vol. 28.3, 2017
58. L. V. King, "On the Convection of Heat from Small Cylinders in a Stream of Fluid: Determination of the Convection Constants of Small Platinum Wires with Applications to Hot-wire Anemometry", Philosophical Transactions of the Royal Society of London, Vol. 214, pp. 373–432, 1914
59. "TSI Thermal Anemometry Probes Catalog", TSI Inc.
60. D. J. Wilson, "An Experimental Investigation of the Mean Velocity, Temperature and Turbulence Fields in Plane and Curved Two-dimensional Wall Jets: Coanda Effect", PhD Thesis, University of Minnesota, 1970
61. J. O. Hinze, "Turbulence", 2nd Edition, McGraw-Hill, 1975
62. T. von Karman, "Progress in Statistical Theory of Turbulence", Proceedings of the National Academy of Sciences, Nov. 1948
63. F. E. Ames, R. J. Moffat, "Heat Transfer with High Intensity, Large Scale Turbulence: The Flat Plate Turbulent Boundary Layer and the Cylindrical Stagnation Point", Report No. HMT-44, Stanford University, 1990
64. F. E. Ames, "The Influence of Large-scale High-intensity Turbulence on Vane Heat Transfer", ASME. J. Turbomach. 1997; 119(1):23-30. doi:10.1115/1.2841007

Appendix A. Uncertainty Analysis

The calculation of uncertainties of the results presented in chapters 6 through 8 is shown in this appendix. Instrumentation information can be found in chapter 4. It is not possible to calculate the uncertainty for every measured location in the vane passage due to the volume of data recorded, but as the parameters being measured have different values, the uncertainties for all measured locations are not the same. However, the range of measured parameters is not very large and, thus, an uncertainty measured at a random location can be said to be approximately equal to the mean uncertainty of any locations. Additionally, as seen in chapters 7 and 8, the analysis performed in this report is more qualitative in nature than quantitative and a very high accuracy of the measured quantities was not essential in drawing conclusions. Still, the uncertainty calculations are presented to accompany the experimental results.

The Monte Carlo method (MCM) for propagation of uncertainties was used to evaluate uncertainties in measurements. A brief explanation of the method is given here, which is extracted from Coleman and Steele [a]. For each of the parameters that can bring uncertainty to the experiment, measured values (called nominal values) are first collected. Then, a standard deviation for each parameter is either decided upon (based on observations) or assumed. Then, a probability distribution function for every parameter is chosen (a normal distribution was chosen for all calculations in this study) and the distribution plot is generated. Then, a random sample of each parameter is chosen from these distributions and the final result is calculated. This process is repeated for a large number of times (5000 iterations for this study) and then the final results of all these iterations are compiled. This compilation can now be used to form a probability distribution of the final results (again, normal distribution for this study) and the standard deviation and

mean of the final results can be extracted. The uncertainty calculation procedure for each of the major results is explained now:

Endwall Effectiveness and Temperature Recovery Coefficient

Thermocouples were used to measure the temperatures, which were normalized in either the endwall effectiveness or the in-field recovery temperature coefficient. The uncertainty was calculated based on (i) the inherent uncertainty in the thermocouple, (ii) the uncertainty in measuring the temperature by the data acquisition unit, Agilent 34970A, (iii) the uncertainty in the calibration setup, (iv) the curve-fit error in the curve generated by the calibration to evaluate temperatures and (v) the error in not maintaining effusion coolant and film coolant temperatures to be exactly the same. The standard deviations for all these parameters are tabulated in table A.1.

Table A.1 Uncertain parameters in the temperature measurements

Error parameter	***Standard deviation***	***Notes***
Type E thermocouple measurement uncertainty	*0.33 °C*	*Assumed after comparing with a thermometer measurement*
Data acquisition unit	*0.0167 °C*	*Given in equipment user guide [b]*
Calibration setup	*0.02 °C*	*Assumed based on the setup*
Calibration curve-fit error	*-*	*Integrated in the final result implicitly*
Coolant temperature mismatch	*0.067 °C*	*Constrained during measurements*

Based on the standard deviations, a normal distribution was plotted for each parameter and results were calculated (see equations A.1 and A.2 for definitions of the parameters). The data used for these calculations were taken on plane 3 in the endwall-suction surface region, chosen at random. The mean and standard deviation for the temperature recovery

coefficient, θ, was 0.7256 and 0.0312. Therefore, the result for this location would be 0.7256 ± 0.0624. This gives an uncertainty of ±8.5% within the 95% confidence interval.

$$\eta = \frac{T_{(x,y,z)} - T_\infty}{T_C - T_\infty} \qquad Equation\ A.1$$

$$\theta = \frac{T_{(x,y,z)} - T_\infty}{T_C - T_\infty} \qquad Equation\ A.2$$

In-field Velocity Components

A five-hole probe was used to measure the velocity components of the passage flow. Three types of results were used to plot the aerodynamic measurements: (i) absolute velocity of the flow, (ii) magnitudes of the velocity vectors projected onto the pitch-span (y-z) plane and (iii) angles of the vectors mentioned in (ii) relative to the span (z) axis. Result types (ii) and (iii) can be seen in the vorticity contour plots and a representative vector is plotted in fig. A.1. The velocity vector magnitude, V_S and the vector angle, β are defined as follows:

$$V_S = V * \sqrt{cos^2(\gamma) * sin^2(\alpha) + sin^2(\gamma)} \qquad Equation\ A.3$$

$$\beta = \tan^{-1}\{\cot(\gamma) * \sin(\alpha)\} \qquad Equation\ A.4$$

Where V is the absolute velocity of the flow, α is the pitch angle and γ is the yaw angle.

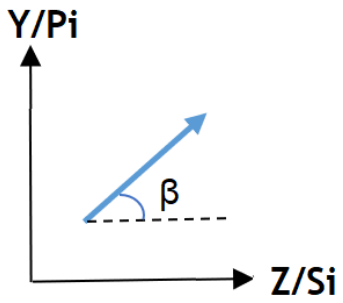

Figure A.1 A typical projection of velocity vector seen in plotted results. The length of the vector is equal to the magnitude of the velocity and β is the angle the vector makes with z-axis

The uncertainties involved in calculation of flow components are as follows: (i) the error in measuring the voltage by the data acquisition unit, Agilent 34970A, (ii) the error in curve-fitting the measured voltage into pressure measured by a transducer, (iii) the error in the calibration setup of the transducer, and (iv) the error in the contour-fit interpolation used for calculating the pressure coefficients. The standard deviations are reported in table A.2. The data used for calculations were chosen randomly from the mid-span, mid-pitch region of plane 6.

Table A.2 Uncertain parameters in the in-field velocity measurements

Error parameter	***Standard deviation***	***Notes***
Data acquisition unit	*20 μV*	*Given in equipment user guide [b]*
Curve-fit error for transducer	*-*	*Integrated in the final result implicitly*
Transducer calibration setup	*8 Pa*	*Assumed based on the manometer used for calibration*
Contour-fit error for five-hole probe	*(a) 0.5 degree for pitch and yaw (b) 0.02 for Cp*	*Assumed after testing random locations on the calibration setup and comparing measured values with contour-calculated values*

The Monte Carlo method gave the uncertainties as follows:

1. *Absolute Velocity:* The mean velocity was measured to be 68.94 $m.s^{-1}$ with a standard deviation of 0.862 $m.s^{-1}$. This makes the uncertainty in the absolute velocity, when measured with a five-hole probe, to be ±2.5% within the 95% confidence interval.
2. *Flow Vectors Projection*: This uncertainty can be reported in two parts: an uncertainty in the magnitude of the flow vector and an uncertainty in the angle of the vector with z-axis. The mean of the flow vector magnitude was found to be 11.96 $m.s^{-1}$ with a standard deviation of 0.349 $m.s^{-1}$. This makes the uncertainty to be ±5.8% within the

95% confidence interval. The mean flow vector angle, β, was calculated to be -29.6° while the standard deviation was 1.55°. This gives a rather large uncertainty of ±3.1°. But it should be noted that this angle is calculated using both pitch and yaw angles. If the uncertainty of only the pitch or yaw angle is considered, it is about ±2°, which is only slightly higher than the uncertainties reported for flow angles in the literature.

High-frequency Approach Flow Velocity

Hot-wire anemometry was used to take the approach flow velocity measurements to characterize the flow leaving the combustor. The calibration setup was from an experiment by Wilson [c] (discussed in section 4.3.2) and the uncertainty for the setup was taken from his thesis. Therefore, the hot-wire uncertainty calculation involves uncertainties due to (i) voltage measurement by the data acquisition unit (ii) calibration setup and (iii) calibration curve fit. The hot-wire calibration equation used during measurements is shown below:

$$u^{0.492} = 2.006 * V^2 - 2.906 \qquad Equation\ A.5$$

Where u is the flow velocity (m.s^{-1}) and V is the measured voltage (V).

Table A.3 Uncertain parameters in the high-frequency approach flow velocity

Error parameter	***Standard deviation***	***Notes***
Data acquisition unit	*20 μV*	*Given in equipment user guide [b]*
Calibration setup	*4.6 mV*	*Given by Wilson [c]*
Hot-wire calibration curve fit	*-*	*Integrated in the final result implicitly*

The uncertain parameters for the hot-wire measurements are compiled in table A.3. The mean velocity was 13.829 m.s^{-1} and the standard deviation was 0.264 m.s^{-1}. The uncertainty based on this standard deviation was calculated to be ±3.8% within the 95% confidence interval.

The uncertainties for all major reported results are compiled in table A.4:

Table A.4 The uncertainties of various measured parameters

Instrument	***Quantity***	***Unit***	***Mean***	***Standard deviation***	***Uncertainty (%)***
Thermocouple	*θ and η*	*-*	*0.726*	*0.031*	*8.5*
Five-hole Probe	*Absolute velocity*	*$m.s^{-1}$*	*68.94*	*0.86*	*2.5*
	Projected flow magnitude	*$m.s^{-1}$*	*11.96*	*0.35*	*5.8*
	Projected flow angle	*°*	*-29.6*	*1.55*	*10.5*
Hot-wire probe	*Absolute velocity*	*$m.s^{-1}$*	*13.83*	*0.26*	*3.8*

Note once again that these uncertainties were evaluated at a randomly chosen location (a different location for every instrument) and therefore they will not be exactly equal for all locations in the passage. Nonetheless, they give a good idea about the uncertainty of the plots presented in the results sections. As most of the conclusions drawn do not use the exact quantities but rather address general trends, the uncertainties in these experiments are suitable.

References

a. H. W. Coleman, W. G. Steele, “Experimentation, Validation, and Uncertainty Analysis for Engineers”, 3rd edition, John Wiley & Sons, 2009

b. Agilent 34970A/34972A Data Acquisition / Switch Unit User’s Guide

c. D. J. Wilson, “An Experimental Investigation of the Mean Velocity, Temperature and Turbulence Fields in Plane and Curved Two-dimensional Wall Jets: Coanda Effect”, PhD Thesis, University of Minnesota, 1970